# Multi-Qubit Gates and Quantum-Enhanced Deliberation for Machine Learning using a Trapped-Ion Quantum Processor

DISSERTATION

zur Erlangung des Grades eines Doktors

der Naturwissenschaften

vorgelegt von

M.Sc. Theeraphot Sriarunothai

eingereicht bei der Naturwissenschaftlich-Technischen Fakultät
der Universität Siegen
Siegen 2018

| | |
|---|---|
| Gutachter der Dissertation: | Prof. Dr. Christof Wunderlich<br>Prof. Dr. Mario Agio |
| Gutachter der Disputation: | Prof. Dr. Christof Wunderlich<br>Prof. Dr. Mario Agio<br>Prof. Dr. Otfried Gühne<br>Prof. Dr. Ivor Fleck |
| Datum der Disputation: | 13.11.2018 |

Gedruckt auf alterungsbeständigem holz- und säurefreiem Papier
Printed on aging resistant, wood-free, and acid-free paper

*“Dicebat Bernardus Carnotensis nos esse quasi nanos gigantium humeris insidentes, ut possimus plura eis et remotiora videre, non utique proprii visus acumine, aut eminentia corporis, sed quia in altum subvehimur et extollimur magnitudine gigantea”*

*“Bernard of Chartres used to say that we were like* ***dwarfs seated on the shoulders of giants****. If we see more and further than they, it is not due to our own clear eyes or tall bodies, but because we are raised on high and upborne by their gigantic bigness.”*

*John of Salisbury (Metalogicon (1159) bk. 3, ch. 4)*

# Zusammenfassung

Die Entwicklung eines großmaßstäblichen, fehlertoleranten Quantencomputers ist ein zentrales Ziel der Forschung im Bereich der Quanteninformation. Die Verfügbarkeit eines solchen Gerätes könnte nicht nur eine große Zahl an Forschungsfeldern grundlegend beeinflussen, sondern auch die Gesellschaft insgesamt. Ein Quantencomputer könnte quantengestützte Algorithmen anwenden, um Probleme zu lösen, die mit einem klassischen Rechner nicht praktikabel zu bewältigen sind. Eine zentrale Herausforderung stellt die Qualität logischer Quantengatter dar, sowie mögliche Fehler, die währenddessen auftreten.

In dieser Arbeit werden zunächst die Untersuchung und Verbesserung der *Fidelity* von Quantengattern in einem ionenfallenbasierten Quantencomputer vorgestellt. Dabei handelt es sich um einen Quantenprozessor in kleinem Maßstab, der auf lasergekühlten Ionen in einer makroskopischen linearen Paul-Falle basiert. Quantenbits (Qubits) werden durch Pseudospins der Ionen realisiert, indem atomare Hyperfeinzustände in einem Magnetfeldgradienten nach dem Schema Magnetfeldgradienten-induzierter Kopplung (MAGIC) genutzt werden. Quantenzustände einzelner Ionen werden mithilfe von Radiofrequenz (RF) - Feldern manipuliert, wobei die Adressierung im Frequenzraum erfolgt.

Diese Arbeit beschreibt mehrere Aspekte der Untersuchung und Verbesserung der *Fidelity* von Bell-Zuständen, die ein essentieller Bestandteil von Quantengattern ist. (i) Wir haben Seitenbandkühlung eines einzelnen Ions bis nahe an den Bewegungsgrundzustand mit RF-Feldern erreicht, die minimale Bewegungsanregung lag bei 0.30(12) Phononen. Diese Technik zur Kühlung wird anschließend auf ein Zwei-Ionen-System ausgeweitet und durch die Realisierung wird die sympathetische Kühlung eines Ionenkristalls mittels RF Seitenbandkühlung gezeigt. (ii) Wir haben mögliche Ursachen für die Dephasierung der Qubits zusammengestellt und untersucht. Dies sind Limitierungen bei der Steuerung der Qubits, Fluktuationen magnetischer Felder, Fluktuationen elektrischer Felder und die Folgen, wenn sich Ionen in angeregten Bewegungszuständen befinden. (iii) Unter Verwendung von Sequenzen zur dynamischen Entkopplung, die Qubits vor Dephasierung schützen, haben wir die Grenzen dieser Technik in numerischen Simulationen und mit Experimenten untersucht, bei denen wir für einen Bell-Zustand eine *Fidelity* von 0.95(3) erreicht haben.

Die Umsetzung all dieser Verbesserungen erlaubte den grundsätzlichen Nachweis eines quantengestützten *Learning Agent*, der den Entscheidungsprozess innerhalb des *Reinforcement Learning* Modells – ein Lernschema für maschinelles Lernen – beschleunigt. Die Entscheidungszeit des Quanten-*Learning Agent* konnte im Vergleich zum klassischen Pendant, quadratisch verbessert werden. Wir haben gezeigt, dass der Algorithmus $\mathcal{O}(\epsilon^{-0.57(5)})$ Schritte benötigt, anstelle von $\mathcal{O}(\epsilon^{-1})$, wobei $\epsilon$ die Wahrscheinlichkeit darstellt, aus der Wahrscheinlichkeitsverteilung des Lernprozesses eine Aktion zu erhalten. Diese Demonstration hebt das Potential eines Quantencomputers in den

Bereichen maschinellen Lernens und der künstlichen Intelligenz hervor, die zu einer grundlegenden Komponente für moderne autonome Maschinen geworden sind. Weiterhin haben wir einige Voraussetzungen für ein statisches Quantenregister anhand eines Systems aus vier Ionen behandelt. Schließlich werden vorläufige Demonstrationen von Quantenzustandstransfer vorgestellt.

# Abstract

During last decades, the development of large-scale fault-tolerant quantum computers has been a central aim of research in quantum information processing. The availability of such a device could fundamentally impact not only a large number of research fields but also the whole of society. A quantum device could perform quantum-enhanced algorithms to solve problems, which are practically inaccessible using a classical machine. A key challenge lies in qualities of quantum logic gates and any errors occurring during their execution.

In this work, the investigation and improvements on the quantum-gate fidelity of an ion-trap-based quantum computer are presented. This is a small-scale quantum processor based on laser-cooled ions in a macroscopic linear Paul trap. Quantum bits (qubits) are realized by the ions' pseudo-spins using ionic hyperfine states in a static magnetic field gradient following the MAgnetic Gradient Induced Coupling (MAGIC) scheme. Quantum states of individual ions are manipulated using radio frequency (RF) radiation and addressing in frequency space.

This work reports the investigation and improvement of the Bell-state fidelity, which is an essential ingredient of quantum gates, in several aspects. (i) We have achieved sideband cooling on a single ion near the motional ground state using RF radiation with a minimum motional excitation of 0.30(12) phonons. The cooling technique is also extended to a two-ion system. This realization shows sympathetic cooling using RF sideband cooling of an ion crystal. (ii) We have outlined and explored possible sources of qubit dephasing, which are limitations of qubit control, fluctuations of magnetic fields, fluctuations of electric fields, and consequences of ions being in motionally excited states. (iii) Using dynamical decoupling sequences to protect from qubit dephasing, we have explored the limitations of this technique in numerical simulations and experiments, in which we have achieved a Bell-state fidelity of 0.95(3).

The implementation of all these improvements allowed the proof-of-principle demonstration of a quantum-enhanced learning agent to speed up the deliberation process within the reinforcement learning paradigm – a learning scheme in the field of machine learning. The deliberation time of the quantum learning agent has been quadratically improved with respect to its classical counterpart. We have demonstrated that the algorithm takes $\mathcal{O}(\epsilon^{-0.57(5)})$ steps instead of $\mathcal{O}(\epsilon^{-1})$, where $\epsilon$ represents a probability to sample an action in the probability distribution of the learning process. This demonstration highlights the potential of a quantum computer in the fields of machine learning and artificial intelligence, which have grown into fundamental components for modern autonomous machines. Furthermore, we have discussed some prerequisite elements for a static quantum register using four ions. In addition, preliminary demonstrations of quantum state transfer have been presented.

# Contents

# 1

# Introduction

It is now a very exciting time in the field of quantum information processing: a so-called *noisy intermediate-scale quantum* (NISQ) machine [1] is expected to become available soon. These NISQ machines or quantum computers contain *quantum bits* (*qubits*) as an information unit, in the range of 50-100 qubits with noise in quantum logic gates. NISQ machines cannot be simulated by classical devices with the most powerful existing digital supercomputers. This number of qubits is a significant milestone in realizing a large-scale quantum computer. The consideration of NISQ devices concerns not only the number of qubits but also the quality of quantum gates and the gate operation times. The reliability of quantum gates limits the computational power. Quantum computers are expected to be more powerful than current digital computers, for example, in optimization problems, which might be a study of complex molecules leading to developments of, for instance, new drugs, new types of materials, and many more.

Quantum information processing is a field of study, which is a combination of quantum physics, computer science, mathematics, and chemistry. Quantum mechanics, established during the first half of the 20th century, explains the nature of objects such as atoms, and of small amounts of energy such as photons (particles of light). The understanding of quantum mechanics leads to developments of, for example, laser systems, transistors, and semiconductor devices [2]. Computing theory explores how efficiently problems can be solved on a model of computation through the use of algorithms. The Turing machine [3] is one of the computation models in a mathematical abstraction. This machine serves as a mathematical model of modern digital computers.

Digital computers made possible efficiently storing data[1], communication as an internet, or even performing complex mathematical computations enabling the study of artificial intelligence as of today. Digital information is interpreted by a series of states of switches, or logic gates, such that for each switch is either open or closed. These states are the elementary pieces of information and they are called *bits*. Each bit can be only in two possible states, referred to as logical 0 or logical 1. This assignment makes two clearly distinct states that give a safety range for reliability when the sys-

---

[1] Here, the efficiency means a large amount of data can be stored in a small physical space. For example, a USB stick storage can store information of more than 2000 books.

tem is exposed to some kind of noise, electric field fluctuations as an example. A qubit imitates a classical bit using a two-state quantum-mechanical system. Nevertheless, quantum systems allow the qubit to be in both states of logical 0 and 1 at the same time, which is called quantum *superposition*. This property can be used to implement *quantum parallelism*. Moreover, two or more qubits can exhibit a non-classical correlation between them, which is called *entanglement*. That is, if a measurement is performed on a particle of an entangled pair, the outcome of the measurement on the first particle will also affect the outcome of the measurement on the second particle and vice versa. Throughout this dissertation, a system of several qubits is called a *quantum register*, for example, a quantum register of eight qubits is a quantum byte.

In 1982, Richard P. Feynman showed that any quantum-mechanical system cannot be simulated efficiently with a classical computer, but presumably could be with a potential quantum computer [4]. Here, efficiency means that the computational time does not scale exponentially with the size of the simulated system. Feynman coined the term *quantum computer* for a simulator governed by the laws of quantum physics to efficiently simulate the behavior of many-body quantum systems. In 1985, David Deutsch presented the concept of a *universal quantum computer* [5]. It would have many outstanding properties which are not achievable by any classical machine such as *quantum parallelism* and *entanglement*. A quantum computer with these properties has the potential to outperform a classical computer. In 1993, Ethan Bernstein and Umesh Vazirani theoretically predicted the existence of quantum computers [6]. Later in 1994, Peter Shor mathematically proved that a quantum computer can outperform a classical computer [7, 8]. The *Shor algorithm*, designed to run on a future quantum computer, can find the prime factorization of any integer efficiently, which could rapidly crack the current cryptography schemes (such as RSA encryption) implemented for banking, other sensitive transactions, and secured communications. The speedup of the large number factorization algorithm not only showed the potential of computational power, but also increased attention outside of academia given the numerous applications. In 1996, another powerful algorithm was devised by Lov Grover [9]. *Grover algorithm* can perform searching unstructured databases efficiently.

It was evident that a quantum computer would be a useful device, although the mentioned investigations were still theoretical. In 1996, David P. DiVincenzo outlined five requirements for building a quantum computer [10]. These requirements are later known as the *DiVincenzo's criteria* [11]:

1. A scalable physical system with well-characterized quantum registers.

2. The ability to initialize the state of the quantum registers to a simple fiducial state.

3. A long lifetime of the quantum-state dynamics of quantum registers, much longer than the gate operation time.

4. A universal set of quantum gates, so any quantum algorithm can be constructed.
5. An individual readout of a quantum register.

In addition, if quantum computers are connected over a distance, then quantum channels for exchanging quantum information must be established and two further conditions must be satisfied:

6. The ability to interconvert stationary and flying quantum registers.
7. The ability to faithfully transmit flying quantum registers between desired locations.

Since then, many physical systems have been tried to satisfy these conditions such as trapped atomic ions [12–14], trapped neutral atoms [15, 16], superconducting circuits [17], single photons [18], quantum dot [19], vacancy-center system [20]. However, the quantum computer can currently overtake the classical computer only in term of the complexity of the information size but not the calculating time.

A trapped-ion system is one of the earliest physical implementations considered to be a candidate for a scalable quantum computer [21]. It is currently the most successful architecture in terms of qubit connectivity and the success probabilities for the implemented circuits [22]. Two electronic states of an ion can be used as 0 and 1 states of the qubit. Several species of atomic ion have been used for trapping and quantum information processing such as calcium [23], ytterbium [24–27], magnesium [28], barium [29, 30], strontium [31], mercury [32], beryllium [21], and cadmium [33]. Ions are electrodynamically confined, and electromagnetic radiation is used to individually control internal degrees of freedom of each ion. An interaction between ions, which is a coupling within a quantum register, occurs through collective motional excitations. The use of laser pulses could limit the quality of quantum logic gates due to two technical challenges. The challenges are the enormous number of individually controlled and stabilized lasers as well as beam focusing to each ion without unintended excitation to its neighbor ions when building a large-scale quantum computer. The trapped-ion systems have certain advantages over other physical systems because they have extremely long coherence times compared with the other mentioned architectures [34–37], abilities to demonstrate entanglement of large numbers of qubits [38–40], high fidelity state preparation and readout [41, 42], as well as highest gate fidelity for universal quantum logic operations [21, 43–45].

In 2001, a trapped-ion system with the use of long-wavelength radiation, instead of lasers for qubit-state manipulation, was proposed [46, 47]. Using radio-frequency (RF) pulses instead of laser pulses, the technical challenges can be circumvented by high-quality RF sources from commercially available devices. However, the use of long-wavelength radiation leads to two main problems. First, the long wavelength is on the scale of centimeters, which cannot be focused on individual ions on the scale of microns. Second, the momentum kick to excite motional modes is too small which limits the coupling between ions. These problems have been solved by an introduction of a magnetic field gradient in addition to an electrodynamical trap, enabling individual addressing of ions when they are encoded in magnetic field-sensitive states. The magnetic field gradient then enhances the coupling between the internal and external[2] degrees of freedom of an ion and hence the coupling between ions. Alternatively, another approach using RF radiation was proposed in 2008, which is based on oscillating magnetic fields [48]. This approach can also be used in quantum information processing with trapped ions [49].

Using long-wavelength radiation together with a magnetic field gradient, individual addressing of a single ion in the frequency domain was experimentally demonstrated for the first time [50, 51]. An advantage of the use of RF pulses was demonstrated by the probabilities of unintended excitation to neighboring ions [52, 53]. The coupling between internal and external degrees of freedom of an ion was also demonstrated [51]. To experimentally prove the coupling between ions, another setup was developed, and it validated the long-range couplings between two and three ions [27]. This experimental setup also showed that the coupling strength can be controlled by adjusting the trap potential [27]. Furthermore, the magnetic field gradient allows cooling a single ion to near its motional ground state with RF radiation [54–57]. The positive and negative couplings between ions can be further controlled by encoding a quantum register into different Zeeman hyperfine levels [58]. The long-range interaction between ions grants the multiple-qubit logic gates via the mutual couplings of a multi-ion system which can speed up a quantum algorithm [58].

A key challenge to build a large-scale and fault-tolerant quantum computer, which can become a universal quantum computer, lies in error and quality of quantum logic gates. Quantum states are fragile as they are easily perturbed by noise. Several methods to protect information against noise have been considered, as well as methods to retrieve information already lost. First, quantum registers could be protected against fluctuations by making individual qubits more robust to noise by using dressed states, which have been realized by ions [34, 59]. This technique has improved the coherence time of a single quantum memory by two orders of magnitude. Furthermore, two-qubit gates have been experimentally demonstrated using dressed states [60]. Second, quantum registers could be topologically protected by using non-Abelian quantum phases of matter [61], which is a theoretical concept to realize a *topological quantum computer* proposed by Alexei Kitaev in 1997. Collective composite particles, known as *non-Abelian anyons*, might be formulated by a group of elementary particles. Anyons are quasiparticles confined in a three-dimensional space-time, which are possible to braid allowing for implementation of a quantum circuit. These make qubits robust against fluctuations that act on individual particles locally. The error threshold of a topological qubit system has been estimated at $7.5 \times 10^{-3}$ per source of preparation, gate,

---

[2] The external degree of freedom is the same as the collective motional excitation.

storage, and detection [62]. An evidence of non-Abelian anyons was experimentally observed in a fractional quantum Hall effect system [63], however, this is not conclusive [64]. Third, *quantum error correction* can be performed repetitively to retrieve quantum information from errors [65, 66], which has been considered to be used in the future when the quality of quantum gates is at the sufficient level. In practice, if we do not want to mostly spend operation time on quantum error correction, the error threshold must not be exceeded, which has been estimated to be $1 \times 10^{-4}$ [67]. Exploring ways to improve the fidelity of quantum logic gates with a view to reaching and overcoming the fault-tolerant computation threshold is one of the topics pursued in this work.

Over recent years, the ideas between quantum information processing and artificial intelligence have been united as quantum artificial intelligence or quantum machine learning [68]. Until then, artificial intelligence and machine learning have become essential components of modern automated machines using enormous data processing via a massive load of classical processors. This is hence of fundamental and practical interest to determine how quantum information processing and autonomously learning machines can mutually benefit from each other. Quantum computation grants the advantages for quantum machine learning algorithms advancing classical methods of machine learning [69], which will be presented later in this dissertation. In a similar manner, applying classical methods of machine learning also grant a possibility to improve and analyze physical implementations of quantum system [70, 71].

Now the field of quantum information processing shifts from purely scientific studies to industrial technologies. Therefore, it demands not only physicists, but also specialists from several branches of knowledge, including computer scientists, engineers, mathematicians, vacuum technicians, and electricians.

Even though a universal quantum computer does not exist yet, NISQ devices could still help to perform complex simulations. Using computing power gained by a NISQ device, we could have applications corresponding to optimization problems, for example, a better understanding of complex materials such as high-temperature superconductors, biomedical simulation to personalize medical treatments, optimizing logistic supply chains for ultra-efficient solutions, or even advancing artificial intelligence and robotics.

In the coming years, if a quantum version of a conventional supercomputer could be built, it could rapidly disrupt the nowadays digital security, which is responsible for protecting, for example, online transactions, banking information, and digital communications. The so-called *post-quantum cryptography*[3] [72] is studied in parallel to prevent security scrambling from quantum cyberattacks. In addition, quantum random-number generators [73] could instantaneously deliver completely unpredictable digits by nature for enhancing encryption.

---

[3] It is also known as quantum-proof, quantum-safe, or quantum-resistant cryptographic algorithm.

It must be noted that building a hardware to realize a universal quantum computer is only half of the story. Developments of algorithms and software to create an interface between a physical implementation and users are other fields of study to be explored. A comprehensive catalog of known quantum algorithms and their original references together with short summaries can be found in Ref. [74].

In this dissertation, the experiments are described on trapped ionic atoms of ytterbium-171 in a static magnetic field gradient to perform quantum information processing using long-wavelength radiation. Our experimental setup uses a *static quantum register* as a quantum processor. This means that the linear chain of ions is trapped in a trap with non-segmented electrodes and the quantum operations are performed without the ion-shuttling technique. Our quantum processor has crosstalks below the fault-tolerant threshold. It also has long-range interactions, which can be turned on/off or changed their sign by RF pulses. In this work, several quantum algorithms have been implemented, namely controlled-NOT gate, Bell-state gate, SWAP gate, quantum reflecting projective simulation, and teleportation, where the main focus is on improving the fidelity of elementary quantum gates. The implementation of all these improvements allows demonstrating a basic unit of a decision-making process using a small-scale quantum processor paving a path to quantum artificial intelligence. After a review of the theoretical foundations essential for understanding our system in chapter 2, the setup and methods are explained in chapter 3 and 4, respectively. Subsequently, the investigation results are described. Chapter 5 presents results of decreasing the motional excitation of the ion crystal to close to its motional ground state. Chapter 6 shows the investigation of noise sources limiting the lifetime of our quantum register. The extension of the lifetime of a quantum register protected by dynamical pulse sequences as well as the limitations of this technique are discussed in chapter 7.

All improvements lead us to chapter 8 which explains about realizing a quantum-enhanced algorithm used in machine learning which quadratically boosts learning process. This highlights a path of NISQ devices, which could potentially break through the performance of conventional supercomputers in the next few years. Furthermore, a quantum system using more than two qubits is presented in chapter 9 introducing preliminary results of the quantum information transfer within the same static quantum register.

# 2

# Quantum Information using Trapped Ions

Quantum systems can store more information than a classically physical system, offering additional resources for computation. They have a potential to solve problems inaccessible to conventional computers due to the memory size and the computing time. This chapter is a short summary of the theoretical foundations of quantum information processing in general using trapped ions for storing and manipulating quantum information, i.e. as a quantum processor. The detailed descriptions of ion-trap-based realizations of a quantum information processor have been theoretically investigated in Refs. [46, 47, 75]. The ion-trap-based approach is used in this work. The other approaches have been mentioned in the introduction.

## 2.1 Quantum Information

### 2.1.1 Quantum Bits

In classical computing the storage and manipulation are described in terms of discrete states. The smallest unit of classical information, represented by two possible states, is termed binary digit or short *bit*. It is usually represented by 0 and 1 for any physical two-state system. A quantum computing also operates on two possible states, called *qubit* (or quantum bit). A qubit is represented by either the state $|0\rangle$ or $|1\rangle$, but allows, in contract to classical states, for a *superposition*. That means the general state of a qubit can be described by

$$|\Psi\rangle = a|0\rangle + b|1\rangle, \tag{2.1}$$

where $a$ and $b$ are complex normalized coefficients such that $\sqrt{|a|^2 + |b|^2} = 1$. The coefficients can be phrased using angles, such that normalization is automatically

**Figure 2.1: Bloch sphere representation of a single qubit.** The blue arrow is a superposition state to be represented, which can be described by a polar angle $\theta$ and an azimuthal angle $\phi$. Black arrows are the projections on the $z$-axis and the $xy$-plane. In a dynamic system, the coefficients from equation (2.1) are functions of time, as $a = a(t)$ and $b = b(t)$. The state vector of a superposition precesses around the $z$-axis unless it is transformed. (All Bloch spheres are generated by QuTiP [77].)

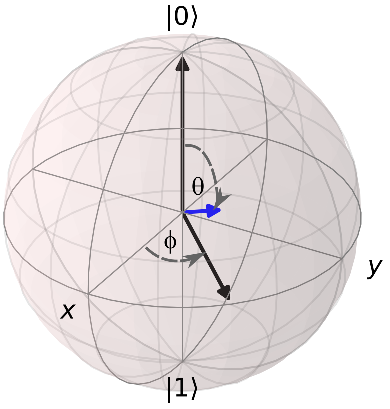

fulfilled,

$$|\Psi\rangle = \cos\left(\frac{\theta}{2}\right)|0\rangle + e^{i\phi}\sin\left(\frac{\theta}{2}\right)|1\rangle. \tag{2.2}$$

Here $\theta$ and $\phi$, corresponding to real values, define a point on the surface of the unit three-dimensional sphere, called the Bloch sphere [76], see Fig. 2.1. It can visualize the state of a single qubit, while multiple qubits are not easily visualized.

For a system of $N$ qubits, we can write states in the form $|x_1,x_2,...,x_N\rangle$ or $|x_1\rangle \otimes |x_2\rangle \otimes ... \otimes |x_N\rangle$, where $x_i$ can be either 0 or 1. These states are called the computational basis states, which are specified by $2^N$ complex coefficients[1].

If the state vector cannot be specified because of insufficient information, but the probabilities $p_i$ for being in a state $|\psi_i\rangle$ are known, then another representation of a state of a single qubit can be used, the so-called density matrix [76]

$$\rho = \sum_i p_i |\psi_i\rangle\langle\psi_i|. \tag{2.3}$$

This represents a statistical mixture of states. When $p_i = 1$, the state becomes pure, otherwise the system is in a *mixed state*.

### 2.1.2 Quantum Computation

The evolution time of a quantum state is governed by the time evolution operator which is related to the Hamiltonian of the system. This can be described by the language of quantum computation. There are elementary quantum gates to manipulate the quantum information, which can be categorized by single-qubit gates and multi-qubit gates.

---

[1] Complex coefficients are sometime called amplitudes.

### Single-qubit Gates

A change of the quantum state of a qubit can be defined as a rotation operator, which rotates a state vector on the Bloch sphere. The operator can be expressed by

$$R_{\hat{n}}(\theta) = \exp\left(-\mathrm{i}\frac{\theta}{2}(\hat{n}\cdot\vec{\sigma})\right), \tag{2.4}$$

where $\hat{n}$ represents a three-dimensional unit vector of the rotation axis, $\theta$ represents the rotation angle, and $\vec{\sigma}$ represents a vector of Pauli matrices. The well-known Pauli matrices are

$$\sigma_x \equiv \begin{pmatrix} 0 & 1 \\ 1 & 0 \end{pmatrix}; \qquad \sigma_y \equiv \begin{pmatrix} 0 & -\mathrm{i} \\ \mathrm{i} & 0 \end{pmatrix}; \qquad \sigma_z \equiv \begin{pmatrix} 1 & 0 \\ 0 & -1 \end{pmatrix}. \tag{2.5}$$

In principle, the Pauli matrices are defined together with a basis, in this case, that $\begin{pmatrix} 0 \\ 1 \end{pmatrix}$ has $\langle\sigma_z\rangle = -1$. In our experiment, the single-qubit manipulation is performed on the ion's carrier resonance transition at the frequency $\omega_C$, for which an intuitive picture can be obtained in a frame co-rotating with the radio frequency (RF) field. In the dipole approximation, and after the so called *rotating wave approximation*, a single spin driven with a RF pulse at $\omega_C$ with amplitude or the Rabi frequency $\Omega$ is transformed by

$$\begin{aligned} R(\theta,\phi) &= \exp\left[\mathrm{i}\frac{\Omega t_{\mathrm{RF}}}{2}(\sigma_x\cos\phi - \sigma_y\sin\phi)\right], \\ &= \exp\left[\mathrm{i}\frac{\theta}{2}(\sigma_x\cos\phi - \sigma_y\sin\phi)\right], \end{aligned} \tag{2.6}$$

where $t_{\mathrm{RF}}$ is the pulse duration, $\theta = \Omega t_{\mathrm{RF}}$, and $\phi$ is the phase of the RF pulse. In a multi-qubit system, we have an index $(j)$ indicating the qubit to be manipulated

$$R^{(j)}(\theta,\phi) = \exp\left[\mathrm{i}\frac{\theta}{2}(\sigma_x^{(j)}\cos\phi - \sigma_y^{(j)}\sin\phi)\right]. \tag{2.7}$$

From equation (2.6), a $\pi/2$-pulse with phase $\phi = \pi$ will perform a $\pi/2$ rotation about $\hat{x}$, and is also denoted as $R_x(90)$ or for short as $X$. A negative rotation about $\hat{x}$, denoted as $R_x(-90)$ or $\bar{X}$, is obtained by phase $\phi = 0$. Similarly, a $\pi/2$-pulse with phase $\phi = \pi/2$ will perform a $\pi/2$ rotation about $\hat{y}$ denoted as $R_y(90)$ or $Y$ and rotation with phase $\phi = -\pi/2$ is denoted as $R_y(-90)$ or $\bar{Y}$. For multi-qubit systems, an index $(j)$ is used as subscript to indicate the qubit to be interacted with, e.g. $\bar{X}^{(j)}$.

Since the rotation about $\hat{z}$ is not directly achievable in our experiment, two decomposition components are expressed as

$$R_z^{(j)}(\pm\theta) = X^{(j)} R_y^{(j)}(\pm\theta) \bar{X}^{(j)} = \bar{X}^{(j)} R_y^{(j)}(\mp\theta) X^{(j)}, \tag{2.8}$$

$$= Y^{(j)} R_x^{(j)}(\mp\theta) \bar{Y}^{(j)} = \bar{Y}^{(j)} R_x^{(j)}(\pm\theta) Y^{(j)}. \tag{2.9}$$

A Hadamard gate[2], denoted by $U_{\mathrm{H}}$, is also a common single-qubit gate. It is represented in the circuit as

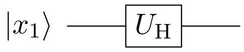

, where the circuit is read from left to right and the state $|x_1\rangle$ is an initial state and it will be transformed by $U_{\mathrm{H}}$. The matrix representation of a Hadamard gate is expressed as

$$U_{\mathrm{H}} = \frac{1}{\sqrt{2}} \begin{pmatrix} 1 & 1 \\ 1 & -1 \end{pmatrix}. \tag{2.10}$$

In our pulse scheme the Hadamard gate can be expressed as [78]

$$U_{\mathrm{H}}^{(j)} = e^{\mathrm{i}\pi/2} R^{(j)}(\frac{\pi}{4}, -\frac{\pi}{2}) \left(X^{(j)}\right)^2 R^{(j)}(\frac{\pi}{4}, \frac{\pi}{2}), \tag{2.11}$$

with the global phase $e^{\mathrm{i}\pi/2}$ being not measurable, and therefore irrelevant.

### Multi-qubit Gates

One of the frequently used two-qubit gates is the controlled-NOT (CNOT) gate. It flips a target qubit conditionally on the state of a control qubit. The CNOT gate ($U_{\mathrm{CNOT}}$) can be described by

$$U_{\mathrm{CNOT}}^{(C,T)} = \begin{pmatrix} 1 & 0 & 0 & 0 \\ 0 & 1 & 0 & 0 \\ 0 & 0 & 0 & 1 \\ 0 & 0 & 1 & 0 \end{pmatrix}, \tag{2.12}$$

where the superscript first index $C$ indicates the control qubit and the second index $T$ indicates the target qubit. This also comes with a basis, namely ($C$,$T$) ordered

(00)
(01)
(10)
(11).

---

[2] The Hadamard transform is also known as the Walsh-Hadamard transform.

The physical implementation will be described later in section 7.1.2. CNOT gates and single-qubit gates can create any arbitrary two-level gates of $n$ qubits [76, 79], hence, these gates are universal for quantum computation.

The CNOT gate and the Hadamard gate can generate the so-called *Bell states.* Bell states are examples of entangled states. Entangled states are defined as states that cannot be written as a product of single qubit states. These states show correlation between qubits. The Bell states are generated by $U_{\text{Bell}} = U_{\text{CNOT}}^{(C,T)} U_{\text{H}}^{(C)}$ in the following circuit.

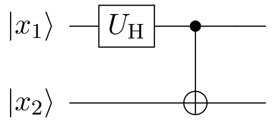

Then, the Bell states are generated by four initial states,

$$|00\rangle \xrightarrow{U_{\text{Bell}}} |\Phi^+\rangle = \frac{1}{\sqrt{2}}(|00\rangle + |11\rangle), \tag{2.13}$$

$$|01\rangle \xrightarrow{U_{\text{Bell}}} |\Psi^+\rangle = \frac{1}{\sqrt{2}}(|01\rangle + |10\rangle), \tag{2.14}$$

$$|10\rangle \xrightarrow{U_{\text{Bell}}} |\Phi^-\rangle = \frac{1}{\sqrt{2}}(|00\rangle - |11\rangle), \tag{2.15}$$

$$|11\rangle \xrightarrow{U_{\text{Bell}}} |\Psi^-\rangle = \frac{1}{\sqrt{2}}(|01\rangle - |10\rangle). \tag{2.16}$$

In our ion trap, the coupling between qubits does not only exist between two nearest neighbors but also between all qubits within the same ion crystal via long range interactions. This allows mutual couplings to form multi-qubit gates, in which the gate time of a quantum algorithm can be reduced [58].

### 2.1.3 Quantum Measurement

To readout the populations in a local basis, the measurement performed on qubits is a *projective measurement*, where each qubit is either detected in the state $|0\rangle$ or $|1\rangle$. A projective measurement or a state selective detection is described by projection operators $M_m$ acting on the state $|\Psi\rangle$ with eigenvalues $m$ = 0,1 [76]. The qubit observable operators are given by

$$M_0 = |0\rangle\langle 0|, \qquad M_1 = |1\rangle\langle 1|. \tag{2.17}$$

For a superposition state as in equation (2.1), the probability either to obtain the result 0 or 1 after a projective measurement is then

$$p(0) = \langle\Psi|0\rangle\langle 0|\Psi\rangle = |a|^2, \tag{2.18}$$

$$p(1) = \langle\Psi|1\rangle\langle 1|\Psi\rangle = |b|^2, \tag{2.19}$$

respectively. After the projective measurement, the state becomes

$$|\Psi'\rangle = \frac{M_m|\Psi\rangle}{\sqrt{p(m)}}, \tag{2.20}$$

which means the measured state stays in either the state $|0\rangle$ or $|1\rangle$ without the phase factor.

For a two-qubit system, the state is given by

$$|\Psi\rangle = a|00\rangle + b|01\rangle + c|10\rangle + d|11\rangle, \tag{2.21}$$

where $\sqrt{a^2 + b^2 + c^2 + d^2} = 1$. The probability of the projective measurement of the first and the second qubit to obtain the result 0 for both qubit is given by

$$p^{(1,2)}(00) = \langle\Psi|(M_0^{(1)} \otimes M_0^{(2)})^\dagger (M_0^{(1)} \otimes M_0^{(2)})|\Psi\rangle = |a|^2. \tag{2.22}$$

The other probabilities in a two-qubit system are given by

$$p^{(1,2)}(01) = \langle\Psi|(M_0^{(1)} \otimes M_1^{(2)})^\dagger (M_0^{(1)} \otimes M_1^{(2)})|\Psi\rangle = |b|^2, \tag{2.23}$$

$$p^{(1,2)}(10) = \langle\Psi|(M_1^{(1)} \otimes M_0^{(2)})^\dagger (M_1^{(1)} \otimes M_0^{(2)})|\Psi\rangle = |c|^2, \tag{2.24}$$

$$p^{(1,2)}(11) = \langle\Psi|(M_1^{(1)} \otimes M_1^{(2)})^\dagger (M_1^{(1)} \otimes M_1^{(2)})|\Psi\rangle = |d|^2. \tag{2.25}$$

Similarly, the projective measurement can be extended to $N$ qubits.

## 2.2 Trapped Ions

There are several approaches to confine charged particles. Two very common devices in quantum optics and atomic physics are the so-called *Penning trap* [80, 81] and *Paul trap* [82]. They are based on either static electric and magnetic fields or static and dynamic electric fields, respectively. Originally, the Paul trap was used in the field of mass spectrometry, however, it became widely used in the field of precision measurement and then quantum information processing.

The experiment in this dissertation uses a linear Paul trap to confine ionized atoms [83], shown in Fig. 2.2. The trap consists of four blade electrodes and two endcap electrodes.

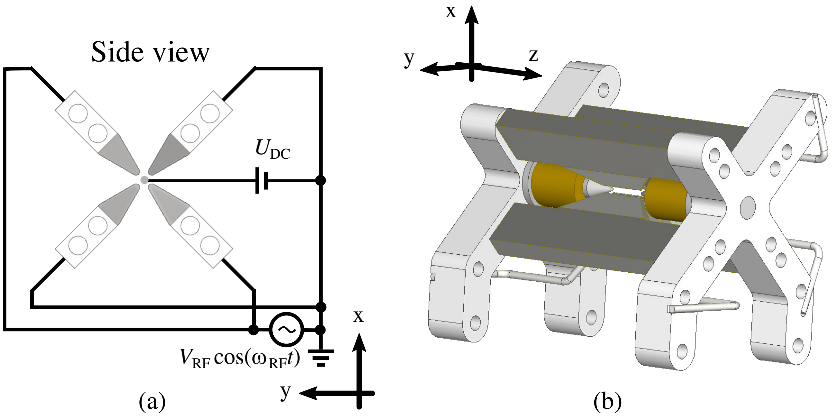

**Figure 2.2: Our linear Paul trap.** (a) The wiring of the electrodes is shown. An alternating voltage $V_{\text{RF}}\cos(\omega_{\text{RF}}t)$ is applied to two diagonally opposite blade electrodes. The other two blade electrodes are connected to the electric ground. The endcap electrodes are connected to a DC voltage. (b) The 3D model of a macroscopic Paul trap shows the ion confinement along $z$-axis. On the endcap electrodes, two cylindrical permanent magnets, indicated by yellow, generate the magnetic-field gradient along the trap axis.

An alternating voltage (AC) $U_0 + V_{\text{RF}}\cos(\omega_{\text{RF}}t)$ is applied to two diagonally opposite blade electrodes. The other two blade electrodes are connected to the electric ground. Here the AC voltage has amplitude $V_{\text{RF}}$, frequency $\omega_{\text{RF}}$, and offset potential $U_0 = 0$. Therefore, the quadrupole potential near the center of the trap, with the electrode separation $2r_0$, is approximated as

$$\Phi_r(x,y,t) = \alpha\frac{V_{\text{RF}}\cos(\omega_{\text{RF}}t)}{2r_0^2}(x^2 - y^2), \tag{2.26}$$

with the geometry factor $\alpha$ specific to each trap and a charged particle of mass $m$ with charge $e$ in the $x$- and $y$-direction (or radial direction). The equations of motion have the form of the canonical Mathieu equation [82, 84]. The Mathieu equation gives either stable or unstable solutions, depending on the values of the so-called stability parameters $a$ and $q$ in the sense that unstable solutions will diverge for infinite (absolute) times. The stability parameters are given as

$$a = \frac{4e\alpha U_{\text{DC}}}{m\omega_{\text{RF}}z_0^2}, \tag{2.27}$$

$$q = \frac{2eV_{\text{RF}}}{m\omega_{\text{RF}}z_0^2}. \tag{2.28}$$

The first stable solution has two components, large-amplitude slow oscillation (*secular motion*) and small-amplitude fast oscillation (*micromotion*). For $U_0 = 0$, the oscillation frequency of the secular motion is at the angular frequency

$$\omega_r = \omega_x = \omega_y = \frac{eV_{\mathrm{RF}}}{\sqrt{2}\omega_{\mathrm{RF}} m r_0^2}, \tag{2.29}$$

called the *radial trap frequency.*

Until this point, there is no confinement in the $z$-direction. The endcap electrode are supplied with a direct current (DC) voltage source with potential $U_{\mathrm{DC}}$, thus the potential around equilibrium can be approximated as harmonic potential as

$$\Phi_z(x,y,z) = \frac{\alpha U_{\mathrm{DC}}}{z_0^2}(z^2 - \frac{1}{2}(x^2 + y^2)), \tag{2.30}$$

where $z_0$ represents the distance between one of the endcap electrodes and the trap center and $\alpha = 0.15$ [83]. The oscillation frequency of the harmonic motion is at the angular frequency

$$\omega_z = \sqrt{\frac{2e\alpha U_{\mathrm{DC}}}{m z_0^2}}, \tag{2.31}$$

which corresponds the *axial trap frequency.* Hence, the total effective trapping potential is described by

$$\Phi(x,y,z,t) = \frac{1}{2} m\omega_r^2 (x^2 + y^2) + \frac{1}{2} m\omega_z^2 z^2. \tag{2.32}$$

When $N$ identical ions are trapped, the ion crystal arranges so that the center-of-mass lies at the trap center. The ion crystal stays in a linear string as long as the radial confinement is stronger than the axial confinement with

$$\frac{\omega_r}{\omega_z} > 0.73 N^{0.86}, \tag{2.33}$$

otherwise the crystal deforms to be zigzag [85] or even a three-dimensional crystal. For a harmonic trap, the spacing between neighboring ions increases towards the string ends. The equilibrium positions of ions $z_m^{(0)}$ can be determined by the dimensionless equilibrium position $u_m = z_m^{(0)}/l$ [86] as

$$u_m - \sum_{n=1}^{m-1} \frac{1}{(u_m - u_n)^2} + \sum_{n=m+1}^{N} \frac{1}{(u_m - u_n)^2} = 0, \qquad \forall m \in [1,N], \tag{2.34}$$

and the length scale $l$ with

$$l = \sqrt[3]{\frac{e^2 Z^2}{4\pi\epsilon_0 m \omega_z^2}}. \tag{2.35}$$

Here $Z$ represents the degree of ionization of ions, $m$ represents the mass of a single ion, and $\epsilon_0$ represents the vacuum permittivity. Because of the Coulomb interactions between ions in the harmonic trap, the displacements of ions will be coupled together and ions' collective oscillations can be described by normal modes. Numerical frequencies for $N = 2, \ldots, 10$ can be found in Ref. [86].

## 2.3 Ions and Magnetic-Field Gradient

To control qubits, several ion-trap experiments use lasers directly driving optical qubits [87–89] or hyperfine qubits [21, 90, 91] via Raman transitions. In the former case, the lasers need to be highly stable in frequency, intensity, and phase. Furthermore, in both cases, lasers must be tightly focused for addressing or individual manipulation of single ions, typically separated by a few microns. These requirements are extremely demanding.

Another approach is to directly work on hyperfine qubits using RF radiation to directly manipulate the hyperfine qubit states [46, 47, 75]. RF and microwave (MW) technologies are easier to handle than lasers. One could get RF and MW systems as commercially-available devices. Fields of stable frequency, amplitude, and phase are simpler to achieve. These can be stabilized on high-precision commercial atomic clocks and commercial frequency generators providing simple and accurate control fields. Earlier, RF radiation was not used for ion-trap quantum information processing because of two main reasons. Firstly, RF radiation cannot be focused down to micron spot size for individual addressing, due to its wavelength in the centimeter range and beyond. Secondly, RF radiation does not carry enough momentum to couple the internal state to the ion motion for conditional dynamics between ions. The spin-phonon coupling is mathematically described by the Lamb-Dicke parameter (LDP) $\eta$ as

$$\eta = k\Delta z, \tag{2.36}$$

where $k = 2\pi/\lambda$ represents the photon wave vector, $\Delta z = \sqrt{\hbar/2Nm\omega_z}$ represents the spatial spread of the ground state wave function of $N$ ions in a harmonic oscillator at mode $\omega_z$, and $\hbar$ represents the reduced Planck constant. The *Lamb-Dicke regime* is defined as $\eta \ll 1$. In our experiment the LDP for RF radiation is 5 orders of magnitude smaller than the LDP for a laser[3] which is used for manipulating a trapped ion via an

---

[3] For optical photons, the LDP is on the order of $10^{-1}$.

optical transition, indicating that the RF radiation hardly excites the motional modes unlike optical photons. However, both problems are solved by adding a magnetic-field gradient along the trap axis, enabling the ion addressability in the frequency domain and inducing the coupling between the internal and external dynamics of the ions [46, 47]. This technique is called ***MA**gnetic **G**radient **I**nduced **C**oupling* (MAGIC).

### 2.3.1 Ion Addressing with MAGIC

In the MAGIC scheme, hyperfine qubits are addressable and manipulated directly via RF radiation [51, 52]. Lasers are used only for cooling ions and readout of the states of ions. Generally, a static magnetic field lifts the degeneracy of the Zeeman sub-levels of ion's hyperfine ground state with respect to magnetic field strength. In a weak magnetic field limit, with the interaction of the external field being weaker than the hyperfine interaction, the energy shifts are described by the Zeeman effect. In a strong magnetic field limit, the energy shifts are described by the Paschen–Back effect, which is the second order perturbation correction. In an inhomogeneous magnetic field, the level shifts and therefore qubit splitting become position dependent and can thus be made different for each ion.

The Hamiltonian of the atomic hyperfine structure is given by [92]

$$H_{\text{hfs}} = A_{\text{hfs}} \frac{\boldsymbol{I} \cdot \boldsymbol{J}}{\hbar^2}, \tag{2.37}$$

$$\Delta E_{\text{hfs}} = \frac{1}{2} A_{\text{hfs}} K, \tag{2.38}$$

where $K = (F(F+1) - I(I+1) - J(J+1))$, $A_{\text{hfs}} = -\mu_B g_I b\hbar$ is called the *magnetic dipole hyperfine constant* with the magnetic field $b$ generated by the electronic shell at the position of the nucleus, $\mu_B$ represents the Bohr magneton, $g_I$ represents the nuclear spin Landé g-factor, $\boldsymbol{I}$ represents the nuclear spin operator, and $\boldsymbol{J}$ represents the fine-structure angular momentum. For the hyperfine ground state $^2\mathrm{S}_{1/2}$ of a $^{171}\mathrm{Yb}^+$ ion [93], the magnetic dipole hyperfine constant is determined as

$$\frac{A_{\text{hfs}}}{h} = 12\,642\,812\,118.466(2)\,\text{Hz}. \tag{2.39}$$

If the system is exposed to an external magnetic field $\boldsymbol{B}$, the interaction Hamiltonian for the Paschen–Back effect is given by [92]

$$H_B^{(\text{hfs})} = (g_J \mu_B \boldsymbol{J} - g_I \mu_N \boldsymbol{I}) \cdot \boldsymbol{B}. \tag{2.40}$$

Here $g_J$ represents the fine-structure angular momentum Landé g-factors, and $\mu_N$ represents the nuclear magneton. The lifted degeneracy, corresponding to the Paschen–Back hyperfine quantum number $m_F$, can be described by the Breit-Rabi formula with a nuclear spin of $I = 1/2$ for a $^{171}\mathrm{Yb}^+$ ion as [92, 94],

$$E_B^{(\pm)}(B,F,m_F) = -\frac{A_{\mathrm{hfs}}}{4} - g_I \mu_N m_F |\boldsymbol{B}| \pm \frac{A_{\mathrm{hfs}}}{2} \left(1 + 2m_F \xi |\boldsymbol{B}| + \xi^2 |\boldsymbol{B}|^2\right)^{1/2}, \quad (2.41)$$

where $\xi = (g_J \mu_B + g_I \mu_N)/A_{\mathrm{hfs}}$.

The addressing frequency of the state $|^2\mathrm{S}_{1/2}\,(F = 0)\,\rangle \leftrightarrow |^2\mathrm{S}_{1/2}\,(F = 1)\,\rangle$ due to the linear Zeeman effect in the magnetic-field gradient, $\boldsymbol{B} = \boldsymbol{B}(z)$, is given by

$$\begin{aligned} \omega(z) =& \frac{E_0 + \Delta E(z)}{\hbar} \approx \omega_0 + \frac{1}{2\hbar}(g_J \mu_B - g_I \mu_N) \Delta m_F |\boldsymbol{B}(z)|, && (2.42) \\ =& \omega_0 + \frac{1}{2\hbar}(g_J \mu_B - g_I \mu_N) \Delta m_F (B_0 + \partial_z B \cdot z). && (2.43) \end{aligned}$$

Here $\omega_0 = A_{\mathrm{hfs}}/\hbar$ represents the atomic ground state transition without external magnetic field. The magnetic field $\boldsymbol{B}(z)$ along the trap axis consists of an offset $B_0$ and a coordinate dependent part $\partial_z B$. Thus, the resonance frequencies of the $\sigma^{\pm}$-transition, $\Delta m_F = \pm 1$, of an ion depend on its position in the magnetic-field gradient, therefore the ion can be addressed in frequency space. The frequency difference between ions can be determined by

$$\Delta\omega(z_i,z_j) = \frac{1}{2\hbar}(g_J \mu_B - g_I \mu_N) \Delta m_F (\partial_z B \cdot \Delta z). \quad (2.44)$$

Using RF radiation for the qubit addressing, the crosstalk between neighboring and non-neighboring ions in a string of eight ions has been shown with a remarkable low level ($10^{-5}$) below the fault-tolerant limit [52].

### 2.3.2 Spin-Spin Coupling with MAGIC

Superimposing the position dependent Zeeman splitting, the harmonic trapping potential, and the Coulomb interaction result in a dependency of the equilibrium position of each ion on its internal state. When the internal state is changed, the ion will oscillate around its new equilibrium position similar to receiving a momentum kick. Therefore, the LDP is replaced by an effective LDP $\eta_{\mathrm{eff}}$, described by [75]

$$\eta_{\mathrm{eff}} = \frac{\Delta z \partial_z(\omega_\sigma(z))}{\omega_z}, \quad (2.45)$$

where $\omega_\sigma$ follows equation (2.43).

For a linear string of $N$ ions in a static magnetic-field gradient, the Hamiltonian is described by [75]

$$\tilde{H} = \frac{\hbar}{2}\sum_{n=1}^{N}\omega^{(n)}(z_0^{(n)})\sigma_z^{(n)} + \sum_{n=1}^{N}\hbar\omega_n(a_n^\dagger a_n) - \frac{\hbar}{2}\sum_{n<l}^{N}J_{nl}\sigma_z^{(n)}\sigma_z^{(l)}. \tag{2.46}$$

The first term represents the internal energy of $N$ ions, where the qubit resonance frequency $\omega^{(n)}$ is at its equilibrium position $z_0^{(n)}$. The second term shows the total energy of $N$ axial motional modes. The last term represents the spin-spin coupling (or $J$-coupling) due to the magnetic-field gradient. Here, the coupling between qubit $i$ and $j$ is the sum of the contributions from all normal modes with the vibrational frequency $\omega_n$,

$$J_{ij} \equiv \sum_{n=1}^{N}\omega_n\varepsilon_{ni}\varepsilon_{nj}. \tag{2.47}$$

The coupling strength $\varepsilon$, generalized as

$$\varepsilon_{nl} \equiv \eta_{\text{eff}}S_{nl} = \frac{\Delta z_n \partial_z \omega_l}{\omega_n}S_{nl}, \tag{2.48}$$

corresponds to the coupling strength of ion $l$ to the motional mode $n$ and $\Delta z_n = \sqrt{\hbar/2m\omega_n}$ characterizes the spatial extension of the wave function of the motional ground state corresponding to the vibrational frequency $\omega_n$ and the ion's mass $m$. The dimensionless matrix $S_{nl}$ expresses the scaled deviation of the ion $l$ from its equilibrium position by the motional excitation mode $n$.

Since the partial derivative of the internal energy of the ions always appears in pairs in the $J$-coupling between two spins, see equation (2.44) and (2.47), the sign of the coupling can be chosen by using qubits composed of different Zeeman sub-levels, experimentally demonstrated in Ref. [58]. The sign becomes negative when the magnetic quantum numbers $m_F$ are chosen differently. The coupling can even be 'switched off' when a qubit is chosen to be magnetic field independent.

## 2.4 Coherence of Trapped-Ion Qubit

The dynamics of a qubit in contact with its environment is characterized by *coherence time*, i.e. time in which the qubit must preserve its information. Therefore, the coherence time must be much longer than any gate time. This is one of the basic conditions for a quantum computer from DiVincenzo's criteria [11]. The coherence time can be described by the phase preservation of the superposition states. For a time exceeding the coherence time, the phase relation is completely random. This is also called the *dephasing* of the internal states. Hence, quantum information processing is reliable for any operation much shorter than the coherence time.

Since our qubit are encoded in a magnetic field-sensitive state, it is susceptible to any magnetic field fluctuations, which randomize the relative phase between the qubit states over time. The coherence time of a quantum system can be determined by the Ramsey measurement [95], which will be described in section 4.3.3. In addition, the coherence time of qubits can be extended using the dressed state, as experimentally demonstrated in Refs. [34, 59].

# 3

# Quantum Processor

This chapter describes the experimental setup used throughout this dissertation, which acts as a quantum processing unit. Modifications with respect to earlier work are also explained, as completely described in Refs. [54, 83, 96]: the RF radiation control is extended to work with multiple ions simultaneously, requiring synchronization between RF radiation sources. The imaging system is modified to reduce the magnification. The acousto-optic modulator (AOM) for the detection lasers is changed to reduce unwanted light scattering. The reference optical resonator is improved as well for locking stability. An upgrade for real-time image processing in the experimental control is described. In addition, a technique to counteract the drift of the ambient magnetic field is presented using active magnetic-field stabilization.

## 3.1 The $^{171}$Yb$^{+}$ Qubit

In our quantum processor, our qubits are encoded in the magnetic field-sensitive state of the hyperfine $^2\mathrm{S}_{1/2}$ ground state of $^{171}\mathrm{Yb}^+$ ions, whereas

$$|0\rangle \equiv |^2\mathrm{S}_{1/2}, F = 0\,\rangle, \tag{3.1}$$

$$|1\rangle \equiv |^2\mathrm{S}_{1/2}, F = 1, m_F = +1\,\rangle, \tag{3.2}$$

with an ion per qubit. The energy level structure is shown in Fig. 3.1. Ions are exposed to an offset magnetic field of approximately 0.5 mT, providing the Zeeman splitting of the state $|^2\mathrm{S}_{1/2}, F = 1\,\rangle$ large enough to distinguish between different $m_F$-states. By having a magnetic field gradient of approximately 19 T/m, the qubits can be individually addressed in frequency space via direct RF radiation near $2\pi \cdot 12.65\,\mathrm{GHz}$.

The hyperfine qubit state has a long lifetime, and therefore the longitudinal coherence time $T_1$, which denotes the decoherence from spontaneous emission of the magnetic dipole radiation, is negligible [97]. The main dephasing of our qubit is from the magnetic field inhomogeneity of the transverse coherence time $T_2^*$. Typically, the transverse coherence time is approximately 0.5 ms; therefore, we need techniques for protection of qubit states, either by using pulsed refocusing schemes or, alternatively,

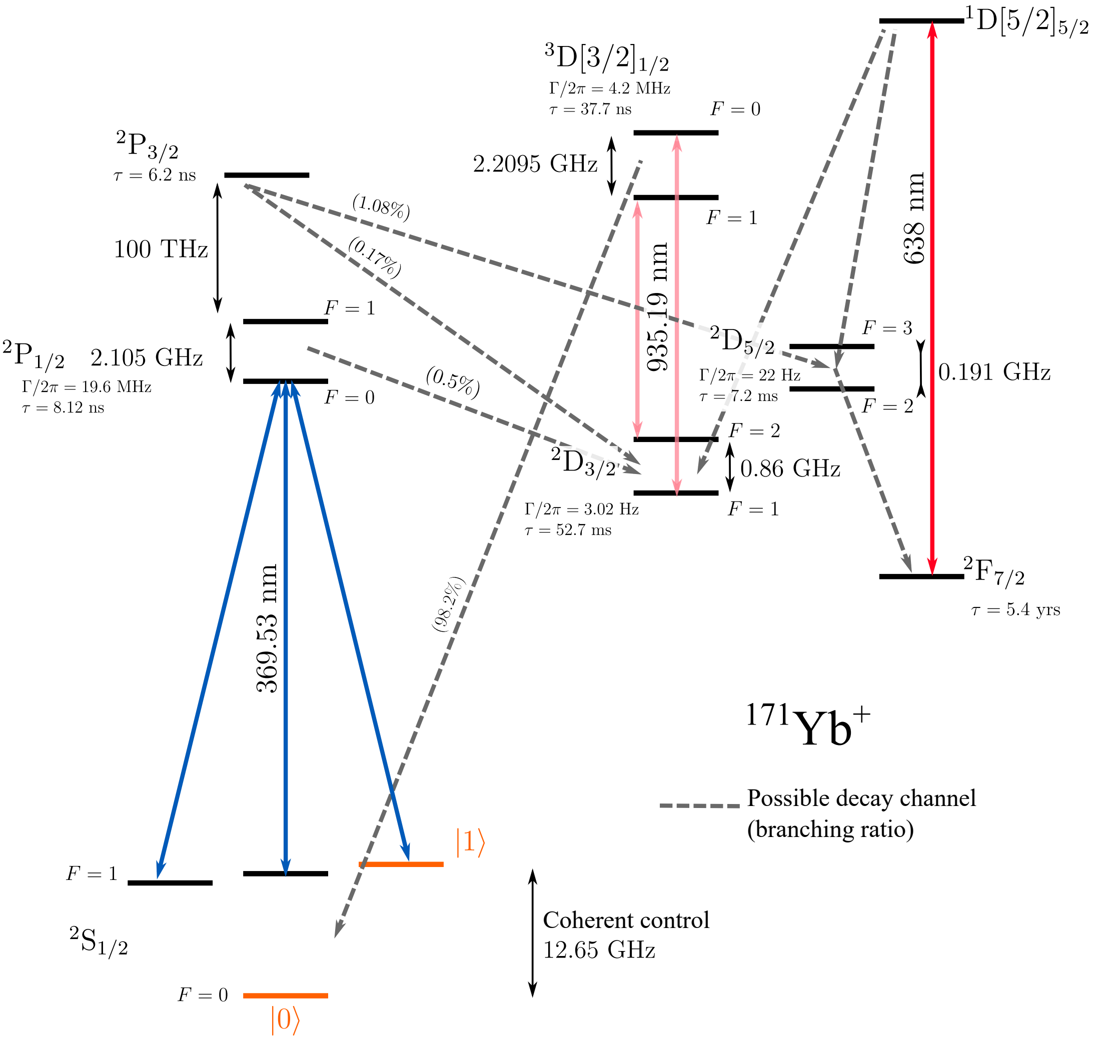

**Figure 3.1: Energy level structure of $^{171}$Yb$^+$.** The schematic, not to scale, shows optical transitions for Doppler cooling and repumping, indicated by colored arrows. Significant decay channels are shown by dashed lines. Numbers in round parentheses show the branching ratio for each possible channel. The main qubit states are highlighted in orange. More information and references can be found in appendix C.

using a continuously dressing field [34, 59, 60]. In this dissertation, we focus on pulsed refocusing schemes, also known as "dynamical decoupling pulses" [98, 99], which will be explained later in section 4.3.5.

Normally, the qubits are cooled using lasers with a two-step process to near their motional ground state, using Doppler cooling and sideband cooling (SBC). For Doppler cooling, the laser at 369 nm is near-resonantly driven to the transition $|^2\mathrm{S}_{1/2}\,(F=1)\,\rangle \leftrightarrow |^2\mathrm{P}_{1/2}\,(F=0)\rangle$ using red-detuning of 19 MHz, together with RF radiation at the transition between the state $|0\rangle$ and the state

$$|0'\rangle \equiv |^2\mathrm{S}_{1/2}\,(F=1, m_F=0)\,\rangle \tag{3.3}$$

at $2\pi \cdot 12.642\,819\,5\,\mathrm{GHz}$ ($\pi$-transition). The lasers at 935 and 638 nm are continuously driven to close the cooling process. More information and references can be found in appendix C. For sideband cooling, the laser at 369 nm is blue-detuned by 2.1 GHz, matching the transitions between $|^2\mathrm{S}_{1/2}\,(F=1)\,\rangle \leftrightarrow |^2\mathrm{P}_{1/2}\,(F=1)\rangle$. The RF radiation frequency is red-detuned by a motional mode frequency to decrease the motional excitation; more detailed discussion can be found in chapter 5. As a result, the two-step cooling prepares a single qubit with an average phonon number of 0.30.

## 3.2 Ion Trap and Vacuum Recipient

Ions are confined in a linear Paul trap, see Fig. 3.2, in an ultra-high vacuum (UHV) environment to isolate ions from background gas interactions. Detailed information concerning the macroscopic ion trap with a magnetic field gradient integrated can be found in Ref. [83]. The information also provides the vacuum recipient design as well as the measured geometric trap parameters.

Ions are confined using two potentials, a quadrupole potential and an approximated harmonic potential. The quadrupole potential, a radial trapping potential, is generated at a frequency of $2\pi \cdot 18.882\,\mathrm{MHz}$ with a power of approximately 16 W to the helical resonator, corresponding to a peak voltage of approximately 600 V coupling to two blades of the trap electrodes. That is, the quality factor of the RF resonator is measured as $Q' = 114$ [83]. Another two blades have no offset potential and are connected to ground. The axial trapping potential is approximately harmonic and generated by a DC voltage applied to the endcap electrodes. The DC voltage is generated by a linear DC power supply[1] and has a potential of 24.93 V.

On the endcap electrodes, there are two hollow cylindrical permanent magnets installed

---

[1] The endcap electrodes were previously supplied by two 12-V batteries. However, because of the discharging over time, we changed to a DC power supply to provide a constant potential over a long time period. Note that this change does not affect the coherence time of the bare state qubit.

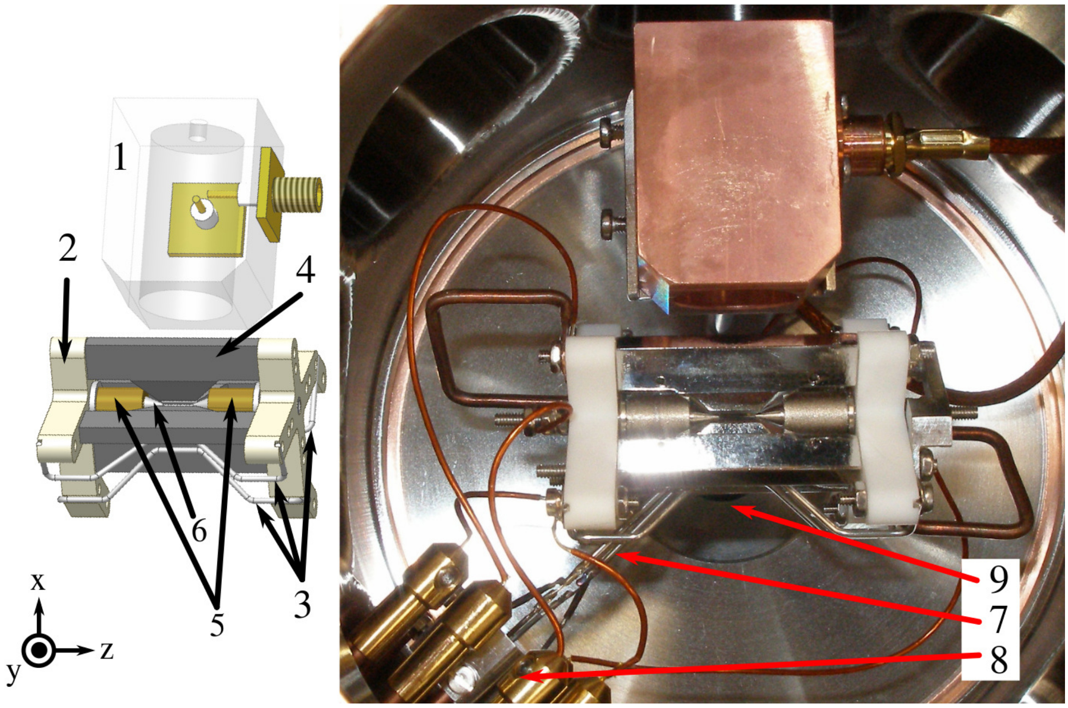

**Figure 3.2: Ion trap and vacuum recipient.** 1: RF antenna (OFHC copper). 2: Macor mounting. 3: Compensation electrodes (stainless steel 316L), namely RF-side, under RF-side, and under viewport windows. 4: RF electrodes (stainless steel 316L). 5: Permanent magnets (SmCo28). 6: Endcap electrodes (Iron). 7: Atomic ovens. 8: Electrical DC feedthrough interfaces. 9: RF feedthrough of a helical resonator.

[83]. These magnets are mounted facing each other with the same magnetic pole. They stay on the endcap electrodes without any rigid fixing; however, the magnetic force pushes the magnets against the endcap electrodes to keep them in place. They provide a static magnetic-field gradient, which is the main feature of this ion trap. The magnetic-field gradient of 19.105(5) T/m is generated along the endcap electrodes, which is also the quantization axis or $z$-axis.

The endcap electrodes have passive electrical RC filters to reduce AC noise. The filters have been optimized in Ref. [56] to achieve a heating rate reduction of two orders of magnitude. In addition, atomic ovens are also filtered with a passive electrical RC filter to prevent noise from the oven power supply. The heating rate is further discussed in section 5.4.

There are three compensation electrodes in addition to the ion trap electrodes. The electrodes are located at the RF feedthrough side, under the RF feedthrough side, and under the viewport windows; see Fig. 3.2 and Ref. [83, sec. 4.3]. Each of these compensation electrodes also has a passive electrical RC filter to prevent noise from the DC power supplies [54]. The current potential setting can be found in appendix I.4.

The ytterbium ovens are located underneath the trap perpendicularly orientated to an ionization laser [83], which co-propagates along with the other cooling lasers from the lower right corner of Fig. 3.2. Two ovens contain Yb I enriched with ytterbium isotopes 171 and 172, respectively. A detailed description of the ovens can be found in Ref. [100]. Ytterbium atoms are released from each oven by applying a current to heat the oven.

An ion getter pump is kept running to maintain the ultra-high vacuum, with a pressure below $1 \times 10^{-8}$ mbar. There is no pressure gauge in our experiment; therefore, we do not know the exact pressure.

## 3.3 RF Antenna

Our RF antenna is a copper[2] circular waveguide designed to transmit RF radiation at approximately 12.7 GHz. The detailed design and characteristics are described in Ref. [83, sec. 3.8]. This signal is used for a coherent control of the hyperfine ground state of $^{171}\mathrm{Yb}^{+}$ ions. The RF antenna is located inside the vacuum chamber near the trapped ion; see Fig. 3.2. Two orthogonal polarizations are possible regarding the orientation of the waveguide with respect to the magnetic field of the quantization axis. However, the achieved Rabi frequency of one of the two orthogonal polarizations perceived by ions is much less than the other, which is due to the trap electrode geometry and material acting similar to a RF polarizer. The signal generation is described in the following section.

## 3.4 RF Amplification Chain

In quantum information processing, high-precision coherent control of qubits is required because it is directly proportional to the fidelity of single-qubit gates, which has to exceed the fault-tolerant limit. In our system, the hyperfine qubit is controlled using RF pulses. That means we have to precisely control the frequency, amplitude, and phase of the RF pulse. The frequency source also has to maintain coherence throughout experimental sequences, which can be achieved by a versatile frequency generator (VFG) [101]. The VFG is capable of generating frequencies in the range of 1 to 150 MHz; however, the experiment operates at a frequency of approximately 12.6 GHz. The previous setup [83] has a single VFG-150 device mixed with a stable frequency at 12.568 GHz. Now, more frequency generators are added to the RF chain system to gain more control frequencies simultaneously. The components can be found in appendix B.

---

[2] This copper is an OFHC (oxygen-free high conductivity) type.

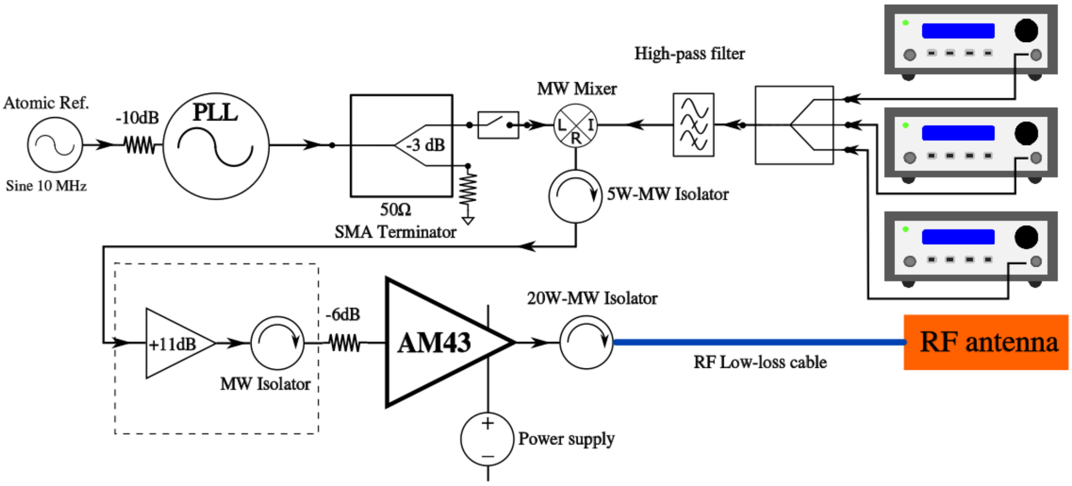

**Figure 3.3: Schematic of RF qubit-control chain.** Three qubit-control signals from three VFGs are combined by a 4-way power combiner and mixed using a single-sideband double-balanced mixer with a frequency of 12.568 GHz, which is generated by a phase-locked loop (PLL) oscillator. The PLL oscillator is also synchronized with the atomic clock reference. To be able to completely switch off the high frequency, a MW switch is installed before the mixer. After the mixer, the signals are in the range to manipulate the qubit transitions with controllable frequency, amplitude, and phase. The signal is amplified by a pre-amplifier as an option, indicated by the dashed box, and further amplified by a power amplifier (AM43). The isolators are inserted for back-reflection protection. Finally, the RF control signals are sent through a low-loss and phase-stable cable to the RF antenna. The components are given in more detail in appendix I.1.

In future experiments, at least three frequencies are required simultaneously; for example, to prepare qubits in the dressed-state basis, similar to Ref. [34]. Then, synchronization between all frequency generators is necessary to obtain zero phase relation between the generators. The synchronization procedure is performed according to Ref. [102]. The specific setup for this experiment is characterized in Ref. [103]. The timing synchronization to start any experiment already takes into account the 50-Hz signal of the power grid to have the same noise characteristics as the power grid.

The complete RF control chain is shown in Fig. 3.3. After three VFGs are synchronized, as described in Ref. [103], three control signals are combined by a 4-way power combiner, mixed with the accurate and stable 12.568 GHz signal generated by a dual loop phase-locked loop (PLL) oscillator. The PLL oscillator is synchronized with the atomic clock reference at 10 MHz. The PLL signal is split into two signals by a power splitter for future experiments, for example, preparation of dressed states, as mentioned in Ref. [103]. The second signal is currently terminated. The main signal can be switched on and off by a MW switch. The 12.568 GHz signal and the VFG signals are mixed by a single-sideband double-balanced mixer[3]. After the mixer, the signals

---

[3] In some experiments, a double-balanced MACOM M79 mixer is used.

are in the range of approximately 12.7 GHz, which can be used to manipulate the qubit transitions with controllable frequency, amplitude, and phase via VFGs. As an option, the signal is amplified by a pre-amplifier, indicated by the dashed box in Fig. 3.3. Then, the control signal is further amplified by a power amplifier (AM43)[4], which is supplied by a low-noise linear power supply (TOE 8851-16). The isolators are inserted for back-reflection protection. The attenuators are inserted to adjust the power to the desired level. Finally, the RF control signals are sent through a low-loss and phase-stable cable to the RF antenna.

## 3.5 Lasers

In this experiment, we primarily focus on the laser and RF radiation manipulation of $^{171}\mathrm{Yb}^+$ ions. The relevant transitions have been shown in section 3.1. There are several lasers with respect to the ytterbium ionic transitions. The laser with emission wavelength close to 369 nm is for cooling, preparation, and readout. The lasers with emission wavelengths close to 638 nm and 935 nm are for repumping to close the cooling cycle. The laser with emission wavelength close to 399 nm is for an ionization process. Lastly, the laser with emission wavelength close to 780 nm is frequency-stabilized using saturation spectroscopy in a rubidium cell and acts as a laser frequency reference.

Each laser is an external cavity diode laser (ECDL) using a reflective grating in the Littrow configuration [104] to be able to fine tune their frequency with a narrow bandwidth. More detailed designs and descriptions can be found in Refs. [105, 106]. All lasers are frequency-stabilized with optical resonators using a technique called side-fringe locking [104–106]. The optical resonator is discussed further in the next section.

To obtain knowledge concerning all laser wavelengths, all lasers are measured in a movable Michelson interferometer. A detailed description can be found in Refs. [83, 107]. The simultaneous detection of interference fringes from the reference laser near 780 nm and the laser of interest allows determination of their air-wavelength ratio. The frequency reference laser is frequency-stabilized with the crossover 2,3 transition[5] of the $^{87}$Rb D2-line using saturation spectroscopy in a rubidium gas cell. This laser is locked with a digital dual lock-in amplifier with a laser current modulation. The feedback is achieved by a piezoelectric transducer acting on its Littrow grating angle.

The lasers at 369 nm and 935 nm have light switches using acousto-optic modulators (AOMs) in a double-pass configuration [106]. This configuration allows very fast switching in the nanosecond regime, and it also allows changing a modulated fre-

---

[4] This device is in some experiments replaced by a Globes Elisra power amplifier.

[5] The crossover 2,3 frequency is half the sum of the $5^2S_{1/2}(F=2) \leftrightarrow 5^2P_{3/2}(F'=2)$ and $5^2S_{1/2}(F=2) \leftrightarrow 5^2P_{3/2}(F'=3)$ transitions.

quency without changing the beam propagation. The laser at 369 nm has two AOMs for modulated frequencies of −90 MHz and 960 MHz, respectively. These provide two overlapping UV laser beams for a shifted frequency of 2.1 GHz, which is used to initialize and sideband cool ions to the ground state.

From the state $^2P_{1/2}$ , the state $^2D_{3/2}$ can be reached with a branching ratio of 0.5 %. Therefore, the laser at 935 nm is used to close the cooling cycle. However, with hyperfine splitting, the state $^2D_{3/2}$ for both $F = 1$ and $F = 2$ cannot be depopulated simultaneously. Hence, an electro-optic modulator (EOM) is installed, providing an additional blue-detuned frequency of 3.07 GHz [54]. The EOM installation is also a key factor enabling success of the sideband cooling process. It prevents the population from staying in the long-life metastable state; in addition, it improves the detection fidelity of the bright state [54].

A new AOM[6] at a driving 90-MHz frequency for the laser at 369 nm improves the beam separation between the diffracted and non-diffracted beams from 4 mrad to 9 mrad. This removes the previously observed overlap of the zero and first diffraction orders, which can cause light-induced dephasing of the qubit [108], even for optimal beam alignment and switched-off AOM. Because of the AOM change, the in-house assembly AOM controller [106] is modified for a voltage-controlled oscillator (VCO) to drive frequencies around 90 MHz. The AOM calibration is adapted to account for the new setup. In Fig. 3.4, the calibration curve is shown, which is measured by applying a variable voltage to the VCO and measuring the frequency via a spectrum analyzer. The result is fitted by a degree-7 polynomial, and the fitting coefficients are shown in appendix I.2.

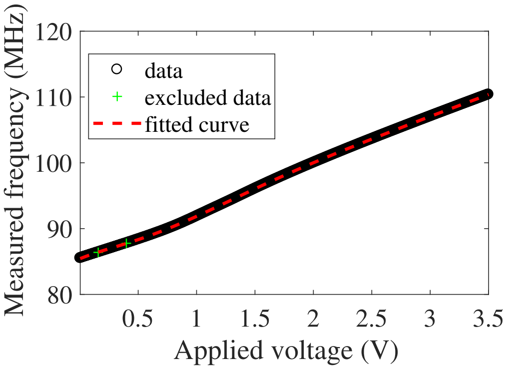

**Figure 3.4: New VCO calibration of the AOM control for the laser at 369 nm.** By applying a variable voltage to the VCO and measuring the frequency via a spectrum analyzer, the calibration curve is measured. The result is fitted by a degree-7 polynomial.

Furthermore, to improve the laser alignment on a daily basis, the pointing stability is improved by a fiber coupling. Formerly, the laser at 369 nm was guided in free-space to overlap with the other lasers using a beam-overlapping unit before injecting them into the vacuum chamber. This allowed for a walk-off of the 369 nm beam with respect to the other laser beams, as daily relocking of the ECDL affects the subsequent pointing.

---

[6] ISOMET 1206C-833

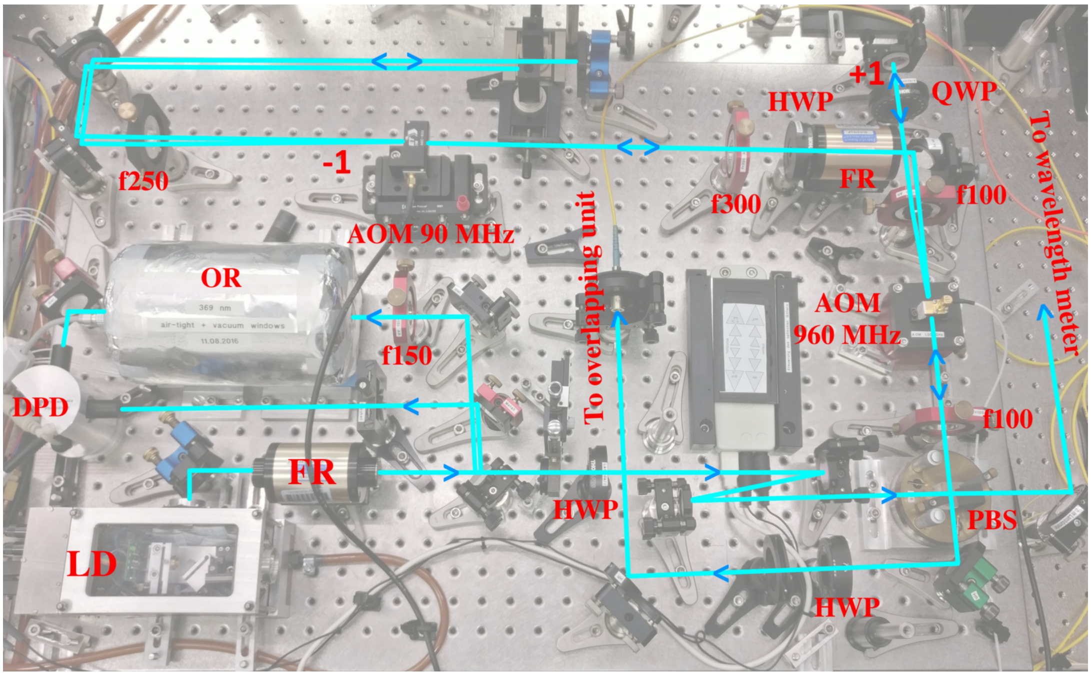

**Figure 3.5: Alignment of the laser at 369 nm.** The blue line shows laser beam trajectories, with arrow heads indicating directions. LD: laser diode, FR: Faraday rotator, OR: optical resonator, DPD: differential photo diode, f and a 3-digit number: plano-convex lens with an indicated focal length in mm, HWP: half-waveplate, PBS: polarizing beam splitter, QWP: quarter-waveplate. The laser exits the board via an optical fiber to the overlapping unit before being injected into the vacuum chamber.

Now, the laser at 369 nm is guided through a polarization-maintaining optical fiber[7] with collimators[8]. The current alignment for the laser at 369 nm is shown in Fig. 3.5. Before the laser is guided to the optical fiber to the overlapping unit, the powers of the 180 MHz-diffracted beam and the 1920 MHz-diffracted beam are 230 µW and 58 µW, respectively. After the overlapping unit, before being injected into the vacuum chamber, the powers of the 180 MHz-diffracted beam and the 1920 MHz-diffracted beam are 70 µW and 10 µW, respectively.

## 3.6 Optical Resonator

The optical resonator is based on a Fabry-Pérot interferometer with a piezo actuator, which allows for tuning of the resonator length and therefore its resonance frequency. It is further actively temperature-stabilized using a heating mat wrapped around an

---

[7] Thorlabs PM-S350MHP

[8] Schäfter+Kirchhoff 60FC-4-A11-01

air-tight aluminum housing and utilizing thermal insulation against environmental temperature drifts composed of styrofoam sheets and aluminum foil.

Previously, the fluorescence during detection was observed to fluctuate, even though the reading temperature of the active feedback temperature controller for the resonator for the laser at 369 nm is stable within ±2 mK. This indicates that the laser frequency drifts, regardless of the temperature, which suggests that the optical resonator is not completely air-tight as intended. The main reason for this is the electrical connectors on the housing lid, which up to now were not perfectly air-tight. Furthermore, the housing lids also have an access window each, which is attached to the lid by epoxy glue. Here, using a helium gas leaking test, we found that the application of epoxy glue is not reliable and might leave some small holes, which are not possible to be observed by the naked eye. Therefore, the housing lids of the resonator of the laser at 369 nm are redesigned. We choose a vacuum CF viewport[9] with a quartz glass window compatible with a UV laser. Each viewport is mounted to each resonator lid using M3 screws, with a rubber O-ring and vacuum grease applied between the contact. In addition, the electrical connectors are changed to an air-tight type[10]. The connectors are mounted with their own screw and washer with vacuum grease applied. A drawing of the new lids can be found in appendix H.1.

After changing the lids of the optical resonator for the laser at 369 nm, we have checked the performance. A single $^{172}\mathrm{Yb}^{+}$ ion is trapped and Doppler cooled to observe the fluorescence. The Doppler cooling laser is usually red-detuned by approximately 19 MHz from the resonance. If the fluorescence is directly observed and the frequency drifts towards lower wavelengths, the ion might not be cooled, and fluorescence cannot be observed. Alternatively, we can indirectly observe drifts by continuously adjusting the piezo potential of the cooling laser; therefore, the changing potential indicates the laser frequency drift. The sensitivity of the laser frequency to adjustment of the piezo voltage is $df/dU_{piezo} = 0.482\,\mathrm{MHz/mV}$ [106]. Fig. 3.6 shows the performance of the optical resonator with the new lids. The results are analyzed using the standard correlation function, which is given by [109]

$$\mathrm{corr}(X,Y) = \frac{\sum_i((x_i - \bar{x})(y_i - \bar{y}))}{\sqrt{\left(\sum_i(x_i - \bar{x})^2\right)\left(\sum_i(y_i - \bar{y})^2\right)}}. \tag{3.4}$$

There is no correlation between the laser frequency drift and the atmospheric pressure $P$ of our laboratory, indicating that the optical resonator is air-tight. However, there is a correlation between the laser frequency drift and the relative reading temperature of a sensor inside the optical resonator $\Delta T_{TEC}$, after optimizing to a better feedback PI signal the gain parameters of the temperature controller[11]. This shows that the main fluctuations of the fluorescence come from feedback oscillations of the temperature

---

[9] Kurt J. Lesker Company UV Quartz DN16CF VPZL-133Q.

[10] Lemo Gmbh HGG.1B.306.CLLSV and Lemo Gmbh HGP.00.250.CTLSV

[11] TEC setting: gain = 750000 and time constant = 50000

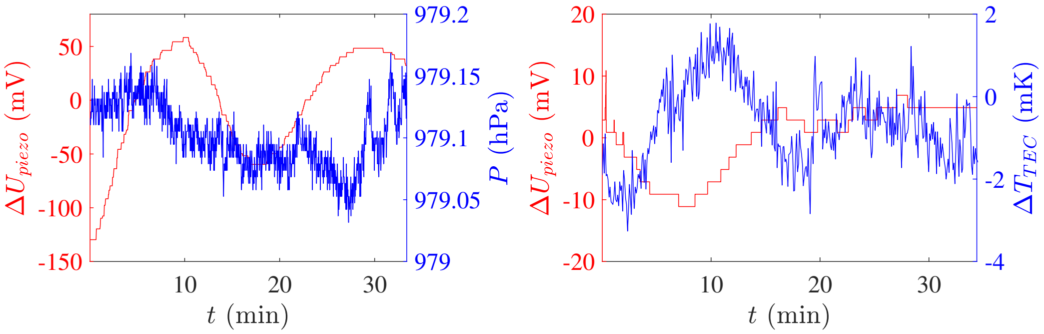

(a) (b)

**Figure 3.6: Performance of the optical resonator for the laser at 369 nm with new lids.** A single $^{172}\mathrm{Yb}^{+}$ is trapped and Doppler cooled to observe the resonance fluorescence. When the frequency of the Doppler cooling laser drifts, the detected fluorescence intensity changes. The deviation of the fluorescence can be used as an error signal for the feedback loop, which acts via the piezo voltage on the grating angle and is thus able to restore the fluorescence level and therefore a constant detuning to the atomic resonance. The sensitivity of the laser frequency to adjustment of the piezo voltage is $df/dU_{piezo} = 0.482\,\mathrm{MHz/mV}$ [106]. (a) The adjusted piezo potential $\Delta U_{piezo}$ and the measured pressure $P$ are plotted over time. There is no correlation between the piezo potential and the atmospheric pressure in our laboratory, in which the correlation coefficient (equation (3.4)) between the two data is given by $-0.06$. This corresponds to no correlation between the detected fluorescence intensity and the pressure, indicating the optical resonator is air-tight. (b) After optimizing the gain parameters of the temperature controller, the adjusted piezo potential $\Delta U_{piezo}$ and the relative reading temperature of a sensor inside the optical resonator $\Delta T_{TEC}$ are plotted over time. Here, the correlation coefficient between the two quantities is given by $-0.66$, with a delay time of 3.5 min, showing the limit of the temperature stabilization. Now, the main source of laser drift originates from residual temperature fluctuations of the reference cavity.

controller, which is at the limit of temperature stabilization.

## 3.7 Imaging System

The ion fluorescence is collected by a collimating lens system with a focal length of $f = 40\,\mathrm{mm}$, described in detail in Ref. [110], which combines a large numerical aperture of $NA = 0.4$ with a large diffraction-limited field of view of the area of a typical ion chain. After the collimating lens system, the imaging system is presented in detail in Refs. [54, 83]. The collimated light is focused onto the detector using a plano-convex lens. The focal length of the imaging lens is now reduced from $f = 1000\,\mathrm{mm}$ to $f = 500\,\mathrm{mm}$ to reduce the magnification from 25 to 12.5 accordingly while still keeping the light collection efficiency of 4 %. Unwanted scattering light is blocked by a mechanical structure consisting of blades and irises. The fluorescence is finally detected by either an electron multiplying CCD (EMCCD) camera or a photo-multiplier tube (PMT), distributed by a mirror or beam splitter [54].

The main reason for changing the magnification to 12.5 is to reduce the electronic noise from the EMCCD's super pixels. The assumption is that if we have a smaller active area on the EMCCD chip, the electronic noise of the detection processing and therefore the detection error would decrease. Previously, the ion fluorescence had a diameter of approximately 1-2 superpixels each, consisting of $8 \times 8$ pixels; this is changed now to approximately 1-2 superpixels, consisting of $4 \times 4$ pixels each. The observed detection error is not significantly different. Nevertheless, the image distortion caused by the imaging alignment is reduced with respect to the previous setup, in which ions appeared as a comet shape on the camera. In addition, the observation of light scattering on trap electrodes simplifies the laser alignment and thus the reduction of straylight, and therefore the background noise and detection error.

## 3.8 Experimental Control

Fig. 3.7 illustrates an overview of our experimental control during this dissertation. There are two computers for two different tasks; the first computer is used for generating experimental sequences and controlling all hardware. The second computer is used for recording a series of images from an electron multiplying CCD camera (EMCCD) and analyzing experimental results. In general, the hardware control is commanded via National Instruments LabVIEW, while the results are analyzed via self-developed scripts in MathWorks MATLAB.

The main control programs were originally developed during the theses [54, 83, 106]. Now we have cleaned some complicated parts of several experimental sequences, putting in sub-routines (sub-VIs) to be better able to understand program flows.

The main control hardware is a Jäger ADwin system, which is a real-time processor capable of outputting digital and analog signals, controlling the experimental timing precisely. The time resolution of ADwin's sequences is 25 ns [111]. The RF pulses, which are used for the qubit control, are controlled by an experimental sequence implementing VFGs from the control computer, as mentioned earlier in section 3.4. The time resolution of the VFG's sequences is 5 ns [101].

Originally, the EMCCD camera records the data stream through a USB port using the company-provided software, Andor Solis. Now, a frame grabber card, BitFlow Neon-CLB (Andor compatible hardware), is installed [112] to parallelly access the data stream via a Camera Link output. The data transfer from the EMCCD camera is modified to allow for real-time processing of images, as required for drift compensation (see section 4.4).

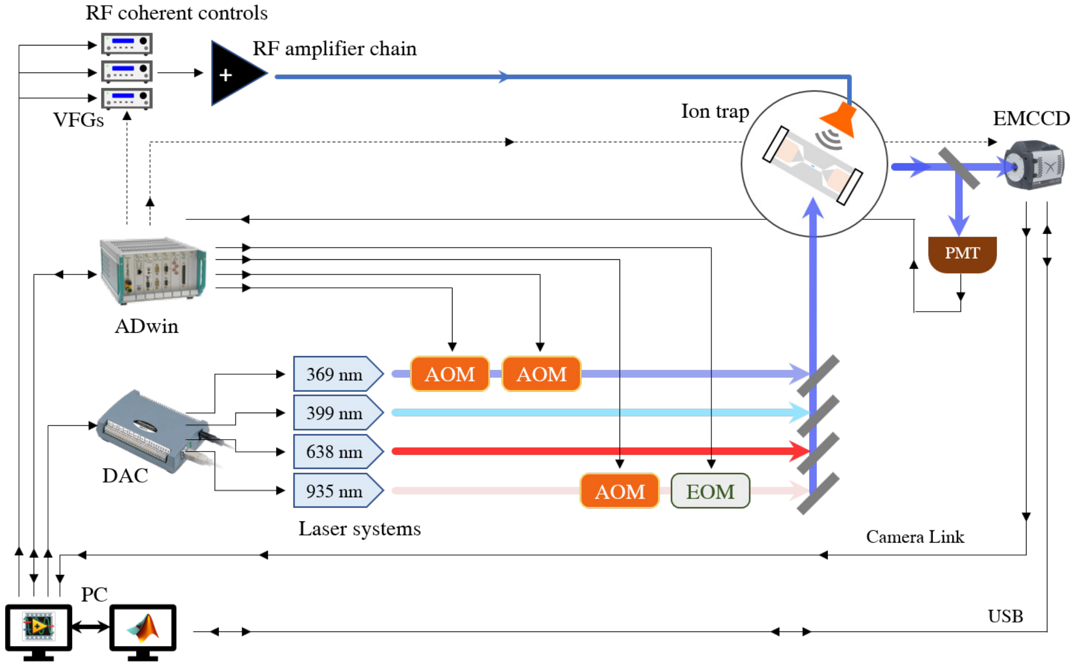

**Figure 3.7: Overview of the experimental control.** The schematic shows connections between experimental instruments. Solid lines represent either control or readout signals. Dashed lines represent trigger signals. Data flows are indicated by arrow directions. Two computers (PC) are used in our experiment; one is used for generating experimental sequences and controlling all hardware. The other computer is used for recording series of images from an electron multiplying CCD camera (EMCCD) and analyzing experimental results. The other components are listed as follows: DAC – digital-to-analog converter for generating piezo voltages of optical resonators; ADwin – real-time signal generation and data acquisition; VFG – versatile frequency generator; PMT – photo-multiplier tube; AOM – acousto-optic modulator; EOM – electro-optic modulator.

## 3.9 Active Magnetic-Field Stabilization

Because magnetic field noise is a dominant contribution to qubit coherence, an active stabilization is designed to counteract those noise components. The active magnetic-field stabilization is based on a feedback system consisting of a magnetic-field sensor, an analog PI feedback control, a current driver, and a set of coils. The main idea is to probe magnetic fields and nullify those fields by applying the appropriate current to the coils. Therefore, a magnetic-field sensor must perceive the same fields as seen by ions in the trap.

Here, the magnetic-field sensor was not initially integrated as a part of the trap inside the vacuum chamber. Hence, the probing sensor is placed as close as possible to the trap from the outside of the vacuum chamber, approximately 30 cm underneath the vacuum chamber, assuming the same noise contribution between the trap area and the neighbor area. In addition, the generated field must have a homogeneous magnetic-field area covering the probing and trapping area. Therefore, three pairs of rectangular coils in an *approximate Helmholtz configuration* are designed. The Helmholtz configuration is not fully satisfied because of the radial symmetry along the common axis.

### 3.9.1 Environmental Magnetic Field

Before designing a magnetic-field generation device, it is necessary to know the field magnitude to be compensated. Fig. 3.8 shows the relative magnetic field measured over several hours at a location approximately 30 cm underneath the vacuum chamber along the ion trap quantization axis. The maximum and the minimum give a magnitude of field fluctuations of approximately 4.5 µT. The coils are designed to generate compensation fields of 20 µT/A [113].

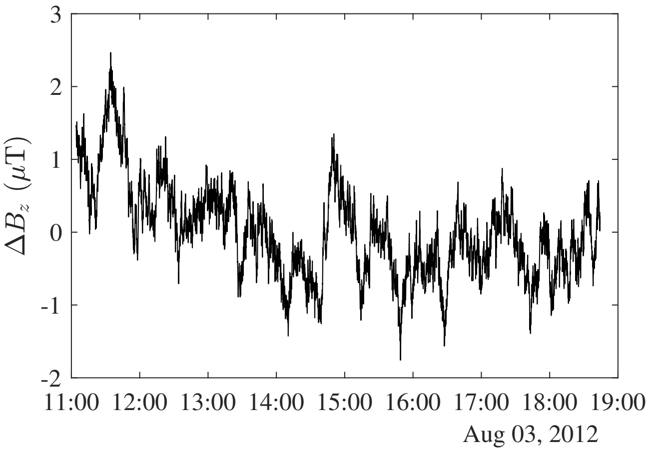

**Figure 3.8: Environmental magnetic field noise along the ion trap quantization axis.** A magnetic-field sensor is located approximately 30 cm underneath the vacuum chamber, aligned along the quantization axis, denoted by $z$-axis. (a) The relative magnetic field is plotted for several hours every few seconds. Two extrema show the peak-to-peak magnitude of field fluctuations of approximately 4.5 µT. The room temperature during the measurement is stable within $\Delta T = 0.2\,\mathrm{K}$.

### 3.9.2 Installation of Compensation Coils

To match the desired compensation fields to the existing noise, three rectangular coil pairs with the approximate Helmholtz configuration are constructed, as in the schematic shown in Fig. 3.9. The coil dimensions and separations are numerically calculated to approximately satisfy the Helmholtz configuration, shown in Ref. [113].

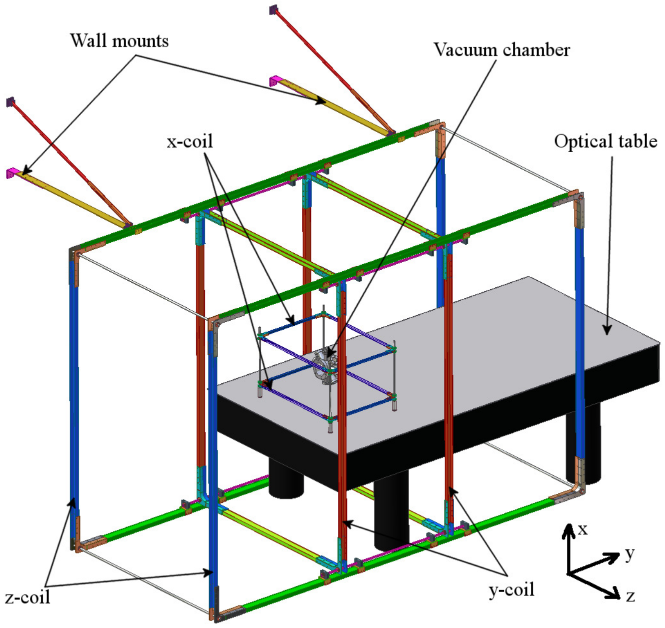

**Figure 3.9: A schematic of the magnetic-field compensation coils [113].** An aluminum frame surrounds the optical table, using the vacuum chamber as the center. The frame has two wall mounts as additional supports for windings of cable. The coils in the z-direction, z-coils, have dimensions of 3.40 × 2.38 $\mathrm{m}^2$, a separation of 1.50 m, and 35 turns. The y-coils have dimensions of 1.570 × 2.274 $\mathrm{m}^2$, a separation of 0.95 m, and 23 turns. The x-coils have dimensions of 0.80 × 0.60 $\mathrm{m}^2$, a separation of 0.375 m, and 9 turns. The z-coils and y-coils utilize a copper cable with a conducting cross-section of 1.5 $\mathrm{mm}^2$. The x-coils use a copper wire with a conducting cross-section of 0.5 $\mathrm{mm}^2$ (a diameter of 0.8 mm). The coils are designed for approximately 20 µT/A [113].

The coils in the $z$-direction, $z$-coils, have dimensions of $3.40 \times 2.38\,\mathrm{m}^2$, a separation of 1.50 m, and 35 turns. The $y$-coils have dimensions of $1.570 \times 2.274\,\mathrm{m}^2$, a separation of 0.95 m, and 23 turns. The $x$-coils have dimensions of $0.80 \times 0.60\,\mathrm{m}^2$, a separation of 0.375 m, and 9 turns. The $z$-coils and $y$-coils consist of a copper cable with a conducting cross-section of $1.5\,\mathrm{mm}^2$. The $x$-coils are composed of a copper wire with a conducting cross-section of $0.5\,\mathrm{mm}^2$ (a diameter of 0.8 mm).

### 3.9.3 Signal-Locking Module

The signal-locking module is a PI controller, as described in appendix F, which takes the error signal (the deviation from the magnetic field set point) and generates a control signal for the current supplies. The module is designed and assembled by Simon Spitzer. The detailed schematic can be found in appendix G.2. The summary of the module is illustrated in Fig. 3.10. A magnetic-field signal together with the set

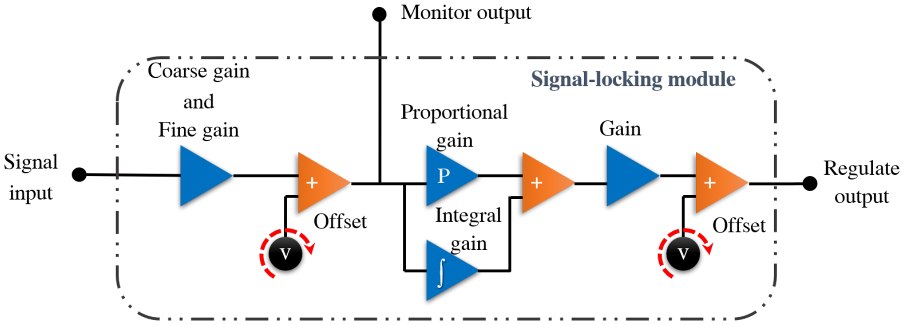

**Figure 3.10: The schematic of the signal-locking module.** The module is based on a PI controlled feedback loop mechanism [114]. The error signal is provided as a signal input to the module. The signal can be adjusted with a coarse gain, a fine gain, and a voltage offset. We can monitor the adjusted signal using a monitor output. The feedback loop is locked with respect to this signal. After that, the signal passes a proportional gain parallel to an integral gain. The total signal can further be amplified and adjusted by the last gain and offset before outputting it to a regulate output. Later, this output will be connected to a current driver.

point for the magnetic field, acting as an error signal, is provided to a signal input of the module. There are two stages of signal adjustments. The first stage is for the locking signal of the feedback loop. The second stage is for the signal level of a current driver. The first stage is adjusted with a coarse gain, a fine gain, and a voltage offset. At this point, there is a monitor output to observe the locking of the feedback loop. After that, the signal passes through a proportional gain and an integral gain unit. The total signal can still further be amplified and adjusted in the second stage with a gain and a voltage offset before outputting it to an output, called a regulate output.

### 3.9.4 Magnetic Field Feedback Loop

A three-dimensional magnetic-field sensor[12] measures the magnetic-field components along all three directions simultaneously. Three signal-locking modules (three PI controllers) take the magnetic-field sensor signals as their error signals. Then, each PI controller gives a modulation signal with respect to its proportional and integral gains to be amplified by a current driver, supplying one of the three coil pairs described previously. The current drivers are provided by the university electronics workshop[13]. The circuit can be found in appendix G.3. The active magnetic-field stabilization system is illustrated in Fig. 3.11[14].

In Fig. 3.12, the performance of the active stabilization is characterized by applying

---

[12] Either our in-house sensor, see appendix E, or a Bartington Mag-03MS500.

[13] Each driver is supplied by ±25 V.

[14] So far, there are devices to drive 2 axes. The $x$-direction, the perpendicular direction of the optical table, has not been installed because of the current optics elements.

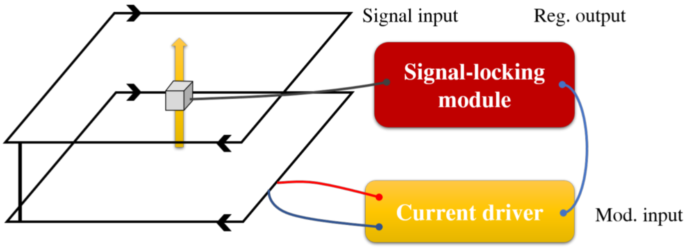

**Figure 3.11: A schematic of a single-axis magnetic field feedback loop.** A magnetic-field sensor measures the magnetic field in one direction located approximately 30 cm underneath the vacuum chamber. The signal is processed though a signal-locking module, as shown in Fig. 3.10. Then, the deviation output signal is sent to the modulation input of a current driver. The current is driven to a respective rectangular coil pair in the approximate Helmholtz configuration to counteract the measured magnetic field deviation. Compensation along the other 2 axes together requires another 2 feedback systems in a similar manner.

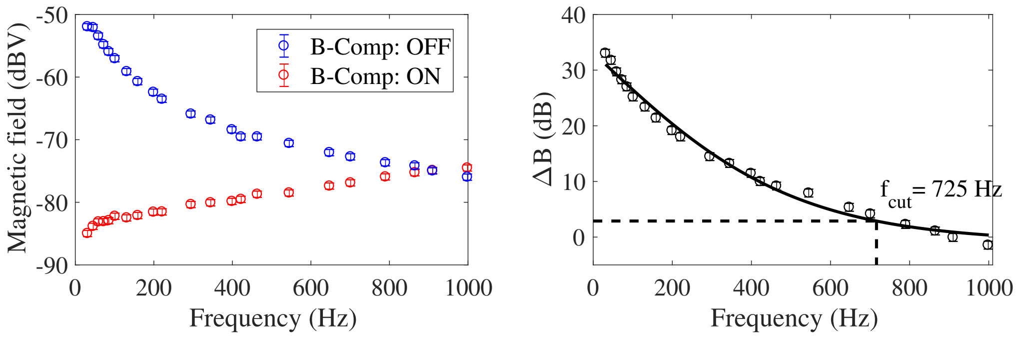

**(a)** **(b)**

**Figure 3.12: Artificially generated magnetic spectrum and the stabilization system [113].** As a test signal, a magnetic field is generated for a given frequency using a function generator through a one-turn coil, which is wrapped around one of the $z$-coils (see Fig. 3.9). (a) The magnetic-field sensor is placed approximately 30 cm underneath the vacuum chamber. The blue plot shows the measured magnetic field probed by the magnetic-field sensor at a given frequency when the signal is generated at that frequency. When the active magnetic field stabilization system is switched on, the red plot shows the measured magnetic field at the applied frequency. The errors on the measurement points are due to the average over the measuring time of approximately 30 s. (b) By subtracting the red from the blue data, the difference in magnetic field magnitude with and without the stabilization system is shown. The data are fitted by an exponential decay. At the 3-dB point, the frequency limit is at 0.73(11) kHz. This result shows the compensation limit of this active magnetic field stabilization.

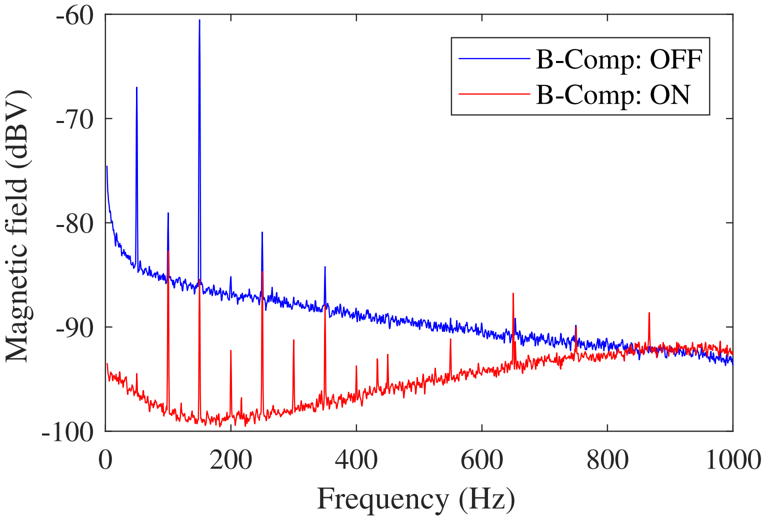

**Figure 3.13: Comparison between the magnetic-field spectrum in our laboratory when the stabilization system is switched on and off [113].** This test is only performed in the direction of the quantization axis. The blue data show the magnetic-field spectrum in our laboratory probed by the magnetic-field sensor, where the sensor location is approximately 30 cm underneath the vacuum chamber. The main components are at 50 Hz and 150 Hz. Smaller components are found at 100 Hz, 250 Hz, and 350 Hz. When the active stabilization is switched on, the magnetic-field spectrum is presented by the red data. The magnetic field magnitude is reduced as expected up to the frequency limit of approximately 0.7 kHz. Below 200 Hz, the magnetic field spectrum is reduced by more than 10 dB. The components of 50 Hz and 150 Hz are reduced by 27 dB and 24 dB, respectively.

an artificial noise for a given frequency and observing the compensation magnitude [113]. At the 3-dB point, the frequency limit is at 0.73(11) kHz. A similar performance can be seen from Fig. 3.13, showing the comparison of the magnetic-field spectrum with and without the active stabilization. Below 200 Hz, the magnetic field spectrum is reduced by more than 10 dB. The components of 50 Hz and 150 Hz are reduced by 27 dB and 24 dB, respectively.

## 3.10 Experimental Trap Parameters

### 3.10.1 Trap Frequencies

The axial and radial trap frequencies of our ion trap are determined by applying an AC voltage to a nearby electrode, which is one of the compensation electrodes, at a given frequency. When the applied frequency is close to either the axial or radial trap frequency, it will excite ions to oscillate in the trap. This technique is called

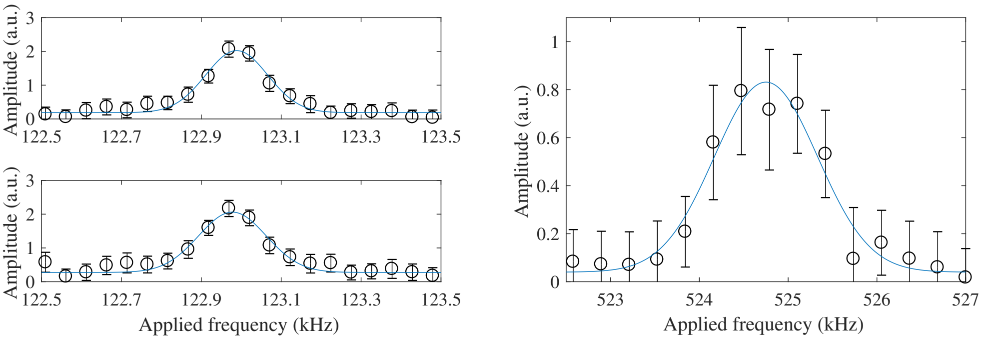

**(a)** **(b)**

**Figure 3.14: Tickle excitations.** (a) In a two-ion system, the frequency is applied close to the axial trap frequency. The upper and lower sub-figures indicate the excitations observed by two different ions. The deduced excitation frequencies fitted by a Gaussian function are $2\pi \cdot 122.989(7)$ kHz and $2\pi \cdot 122.978(10)$ kHz. (b) In a single-ion system, the frequency is applied close to the radial trap frequency. The deduced excitation frequency is $2\pi \cdot 524.75(8)$ kHz.

'tickle' excitation [115]. The AC voltage is applied by a function generator with a peak voltage of 1 V. The oscillation amplitude of ions can be determined using an exposure time of 0.4 s and averaging over 10 images. The ions show their trajectories by fluorescence from the long exposure time, which provide the oscillation amplitude of each ion. In Fig. 3.14a, the frequency is applied close to the axial trap frequency in a two-ion system, where the upper and lower sub-figures are excitation observed by different ions. The results are fitted by a Gaussian function. The deduced excitation frequencies are $2\pi \cdot 122.989(7)$ kHz and $2\pi \cdot 122.978(10)$ kHz. Both ions are excited by the same frequency within 2 standard deviations. In Fig. 3.14b, the frequency is applied close to the radial trap frequency in a single-ion system. In a similar fitting, the deduced excitation frequency is $2\pi \cdot 524.75(8)$ kHz.

### 3.10.2 Magnetic-Field Gradient

From equations (2.44), (2.35) and (2.34), the Zeeman shift of the $\sigma^+$-transitions of a four-ion system is plotted against the equilibrium position of ions, as shown in Fig. 3.15, using the axial trap frequency of $2\pi \cdot 122.984$ kHz. Therefore, the magnetic-field gradient is deduced to be 19.105(5) T/m.

**Figure 3.15: The Zeeman shift of ions' $\sigma^{+}$-transitions vs. the equilibrium positions.** The shifted frequency is compared with the frequency of the energy without an external magnetic field, where $\omega_0$ follows equation (2.39). The magnetic-field gradient is deduced to be 19.105(5) T/m at the axial trap frequency of $2\pi \cdot 122.984$ kHz.

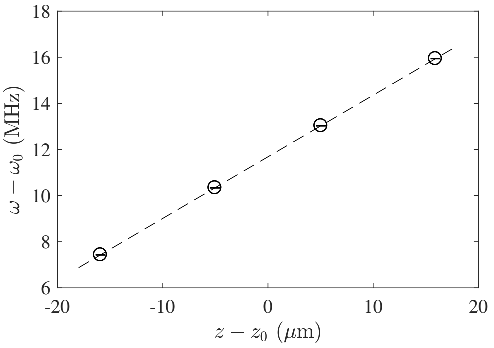

# 4

# Experimental Methods

This chapter explains the general methods and techniques for operating the experiment as carried out during this dissertation. It consists of preparing ions in the trap, the measurement structure in general, and basic experimental schemes to measure experimental parameters and qubit operations. Additionally, a technique to keep track of qubits' resonance is presented.

## 4.1 Ion Loading

Applying a current to an atomic oven enriched by either ytterbium-171 or ytterbium-172, Yb I (atomic ytterbium) is evaporated inside the vacuum chamber and can be ionized by a two-color photo-ionization [116]. The ionization process includes two steps. First, the transition $^1\mathrm{S}_0 \rightarrow {}^1\mathrm{P}_1$ of Yb I is excited by the laser at 398.9 nm. Second, the electron is further excited to the single-ionized state Yb II by another laser at $\lambda < 394\,\mathrm{nm}$. This step can be achieved above the ionization threshold by the laser at 369.5 nm, which is already present for ion cooling. For loading a single $^{171}\mathrm{Yb}^+$($^{172}\mathrm{Yb}^+$) ion, the typical current of 1.67 A (1.53 A) is applied. The mentioned currents give a loading time of approximately 5-10 minutes per ion. The loading process can be terminated by blocking the laser at 398.9 nm.

## 4.2 Measurement Structure

Any experimental sequence contains steps for ion cooling, initialization, arbitrary coherent manipulation, and readout, as shown in Fig. 4.1a. At the beginning, ions are left in the Doppler cooling state. A trigger, which is synchronized with the power grid, starts an experimental run. If desired, the ions are further cooled below the Doppler cooling temperature by employing the SBC process. Because of sympathetic cooling, when a part of the ion crystal is cooled, then the whole ion crystal is cooled down. A more detailed discussion of SBC can be found in chapter 5. The qubit manipulation consists of RF pulses and free evolution under the Hamiltonian that couples the ionic

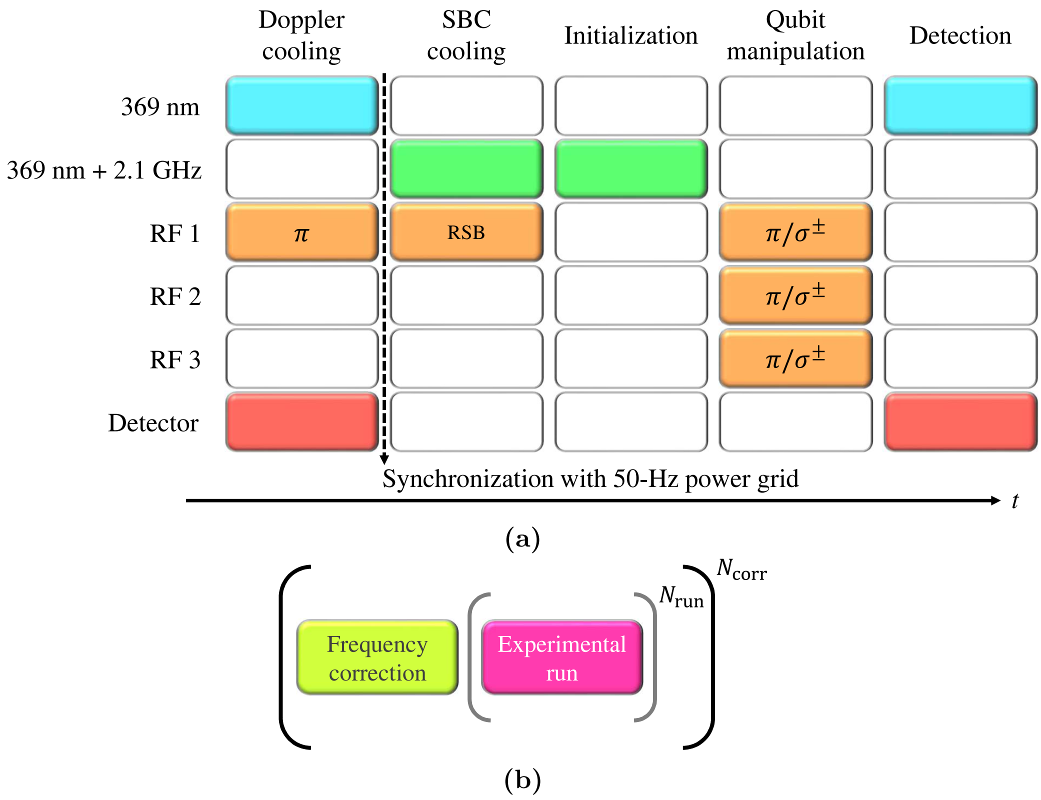

**Figure 4.1: Schematic of the experimental structure.** An experimental parameter is varied in steps for several runs, forming a repetition of an experimental sequence. (a) The structure of a single run, corresponding to a varying step in a repetition of a total measurement. Initially, an ion (or ions) is loaded and Doppler cooled in the trap. Every experimental run is synchronized with the 50-Hz signal from the power grid. If an experimental sequence requires a motional excitation level less than the Doppler cooling temperature, then sideband cooling (SBC) is applied with the RF signal using the red-detuned frequency with respect to motional modes. The qubits are then initialized to the state $|0\rangle$. The qubits are coherently manipulated using RF pulses and free evolution under the Hamiltonian that couples the ionic qubits (see equation (2.46)). The labels "$\pi$" and "$\sigma^{\pm}$" indicate that the frequency of the RF signal is set to the corresponding transition during the process. The label "RSB" means the RF signal is set to a red-sideband of a desired motional mode. The current setup can generate three RF signals simultaneously. Finally, the readout is performed using state-selective detection. (b) Complete schematic of a measurement sequence. After a few experimental runs $N_{\text{run}}$, the atomic resonance frequencies are updated by the frequency correction sequence, as described in section 4.4, which is typically performed every 40 s, reducing the effects of slow drifts. Both the frequency correction and the experimental runs are repeated for $N_{\text{corr}}$ blocks, forming the total repetition of a measurement sequence.

qubits according to equation (2.46). The ions can be simultaneously controlled by three RF signals to generate RF pulses with different frequencies. Finally, the readout is performed using state-selective detection. An experimental parameter is varied in steps for several runs, forming a repetition of an experimental sequence. The sequence is repeated until the desired level of statistics is obtained.

The measurement structure employs adaptive frequency correction, as will be described in section 4.4, and thus accounts for slow drifts of the atomic resonances of ions. This technique becomes essential when the total measurement duration reaches more than several minutes. The total measurement sequence is split into $N_{\mathrm{corr}}$ blocks interleaved with the frequency correction sequence, to keep updating the atomic resonance frequencies, after a few experimental runs $N_{\mathrm{run}}$. A frequency correction is typically performed every 40 s. In many cases, the effect of a variation of some experimental parameter is investigated, yielding even deeper nested sequences. An optimal rate of frequency correction requires further investigation.

### 4.2.1 Doppler Cooling

From the loading sequence or from heating processes during previous experimental runs, ions have high temperature corresponding to their kinetic energy. Laser cooling is utilized to stabilize ions, reducing their motion in the trap. The standard technique is Doppler cooling [117–121]. In our setup, the laser at 369 nm is red-detuned by approximately $2\pi \cdot 19\,\mathrm{MHz}$ from the optical dipole transition $|{}^2\mathrm{S}_{1/2}\,(F=1)\,\rangle \leftrightarrow |{}^2\mathrm{P}_{1/2}\,(F=0)\rangle$ together with RF resonantly driving the transition $|0\rangle \leftrightarrow |0'\rangle$. The detuned frequency takes the saturation broadening into account. When ions move toward the laser source, the Doppler effect leads to an increased scattering rate. Together with the momentum transfer during the absorption process, this establishes the so-called Doppler cooling. The Doppler cooling limit (Doppler temperature) [122]

$$T_D = \frac{\hbar\Gamma_{({}^2\mathrm{P}_{1/2})}}{2k_B} = \frac{\langle n_D\rangle \hbar\omega_z}{k_B} \tag{4.1}$$

can be achieved at the optimal detuning of $-\Gamma_{({}^2\mathrm{P}_{1/2})}/2$ from the resonance of the optical transition. Here, $\Gamma_{({}^2\mathrm{P}_{1/2})}$ represents the linewidth of the state $|{}^2\mathrm{P}_{1/2}\,\rangle$, $k_B$ represents the Boltzmann constant, and $\langle n_D\rangle$ represents the average phonon number at the Doppler temperature. Theoretically, our experiment has an average phonon number at the Doppler temperature for a ${}^{171}\mathrm{Yb}^{+}$ion of $\langle n_D\rangle = 19.9$, where $\omega_z = 2\pi \cdot 122.984\,\mathrm{kHz}$ and $\Gamma_{({}^2\mathrm{P}_{1/2})} = 2\pi \cdot 4.9\,\mathrm{MHz}$ [94]. The average phonon number can be further decreased to the motional ground state by employing sideband cooling. The experiments described in this dissertation do not always require starting from the motional ground state; therefore, the experiments usually are performed with ions near the Doppler temperature, unless specified otherwise.

### 4.2.2 Sideband Cooling

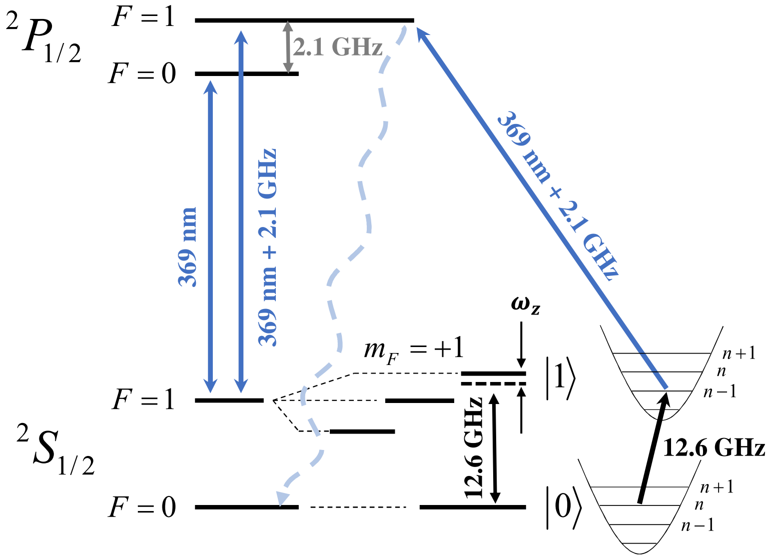

**Figure 4.2: RF sideband cooling cycle of a $^{171}$Yb$^+$ ion.** From the state $|0\rangle$, RF radiation red-detuned by the frequency of the ions' harmonic motion ($\omega_z$) is applied to perform sideband cooling. Simultaneously, the 369 nm laser, detuned by 2.1 GHz, is employed to resonantly drive the $|^2\mathrm{S}_{1/2}\,(F=1)\,\rangle \leftrightarrow |^2\mathrm{P}_{1/2}\,(F=1)\rangle$ transition, so that the ion radiates back to the state $|^2\mathrm{S}_{1/2}\,(F=0)\,\rangle$.

To further reduce the phonon level below the Doppler temperature, the sideband cooling technique is employed [117, 123]. Here, our sideband cooling is performed on an ion of the ion crystal by RF radiation [54, 56, 57], illustrated in Fig. 4.2. Starting the RF sideband cooling cycle, the ion is prepared by optical pumping into the $|^2\mathrm{S}_{1/2}\,(F=0)\,\rangle$ state by resonantly driving the transition between the $|^2\mathrm{S}_{1/2}\,(F=1)\,\rangle$ state and $|^2\mathrm{P}_{1/2}\,(F=1)\rangle$. Because the Lamb-Dicke parameter of this transition is $\eta \ll 1$, excitation and spontaneous decay usually do not change the motional state. The RF radiation is red-detuned to a motional sideband of an ion; therefore, the corresponding ion is excited to the $|^2\mathrm{S}_{1/2}\,(F=1, m_F=+1)\,\rangle$ state while the motional quantum number is simultaneously reduced by one. At this hyperfine level, there is no spontaneous emission; hence, optical repumping between $|^2\mathrm{S}_{1/2}\,(F=1)\,\rangle \leftrightarrow |^2\mathrm{P}_{1/2}\,(F=1)\rangle$ is necessary to incoherently repump to the state $|^2\mathrm{S}_{1/2}\,(F=0)\,\rangle$. For each sideband cooling cycle, a phonon is taken out of the ion state [124]. Further discussion concerning SBC will be carried out in great detail in chapter 5.

### 4.2.3 Qubit Initialization

The qubit initialization is necessary to put a qubit state into a well-defined state. This is one of the basic conditions for a quantum computer according to DiVincenzo's criteria [11]. The initialization process is performed by optical pumping into the state $|^2\mathrm{S}_{1/2}\,(F = 0)\,\rangle$ via the state $|^2\mathrm{P}_{1/2}\,(F = 1)\rangle$ [26, 125]. The optical pumping is performed on the transition $|^2\mathrm{S}_{1/2}\,(F = 1)\,\rangle \leftrightarrow |^2\mathrm{P}_{1/2}\,(F = 1)\rangle$ by the cooling laser blue-detuned by 2.1 GHz from the Doppler cooling transition. The laser is generated by an AOM, as mentioned in section 3.5. Because the state $|^2\mathrm{P}_{1/2}\,(F = 1)\rangle$ can decay to the state $^2\mathrm{D}_{3/2}$ with a branching ratio of 0.5 %, see Fig. 3.1 and section 3.5, the laser at 935 nm is necessary for the repumping process. The preparation efficiency with this technique is achieved at the lower bound efficiency of 0.9975 [96].

### 4.2.4 Coherent Qubit Manipulation

After a qubit is initialized by optical pumping, the actual qubit operations can be applied. The desired operations, either single-qubit rotations or multi-qubit gates, are performed by a series of RF pulses and free evolution times. During an evolution time, the qubits evolve with the $\sigma_z \otimes \sigma_z$-interaction (or the ZZ-interaction) as given by the spin-spin coupling or MAGIC Hamiltonian, see section 2.3.2. Basically, the manipulation sequence changes for different experiments while the other sequences are always kept the same. By varying the input parameters in a given number of steps for each run, a measurement is constructed by the total number of runs given by the number of steps and the number of repetitions of each step.

The standard RF pulse can be set by four parameters:

- Amplitude. The amplitude of the RF field defines the Rabi frequency.
- Duration $\tau$. The duration specifies a time interval or pulse time of a rectangular RF pulse. A $\pi$-pulse has a duration of $\tau_\pi = \pi/\Omega$ and a $\pi/2$-pulse has a duration of $\tau_{\pi/2} = \pi/(2\Omega)$.
- Frequency $\nu$. The frequency of the RF pulse addresses an individual qubit, which might have a detuning $\delta$ with respect to the atomic resonance.
- Phase $\phi$. The phase is set relative to the current phase.

### 4.2.5 State-Selective Detection

The final step of every experimental sequence run is the readout of the final state of qubits. This is the projection onto the computational basis $\{|0\rangle,|1\rangle\}$ of each qubit. The global laser beam drives the electric dipole transition $|^2\mathrm{S}_{1/2}\,(F = 1)\,\rangle \leftrightarrow |^2\mathrm{P}_{1/2}\,(F = 0)\rangle$, similar to the Doppler cooling but without the RF radiation, so that only ion(s) in the state $|1\rangle$ at the end of the experimental sequence can couple to the laser. The near-resonance fluorescence of a single ion or multiple ions is driven, continuously absorbing and emitting photons. For ion(s) in the state $|0\rangle$, only off-resonant excitation and background scattering photons can be measured. We use an electron multiplying charged coupled device (EMCCD) camera, Andor iXon Ultra EMCCD camera, to obtain spatially resolved fluorescence imaging of the ion crystal, which allows the fluorescence and therefore excited-state population of all ions to be obtained simultaneously.

After EMCCD image acquisition, the brightness of ions is interpreted as the excitation probability to detect the state $|1\rangle$ (the bright state). There are several steps to be performed [112]: background correction, ion identification, post selection, labeling the state of ions' fluorescence, and calculation of the excitation probability.

**Background correction.** During an experiment, background images are taken by preparing ions in the dark state to take the background illumination into account. The background image correction subtracts pixel by pixel for each image taken for data analysis.

**Ion identification.** Using images with the background image correction subtracted, the regions of interest are identified for each individual ion. Each ion may have fluorescence intensity distributed over multiple pixels because of the current imaging system; see section 3.7. It has proven to be a reasonable threshold to select pixels that range among the brightest 30 % as the bright areas.

**Post selection.** Some images are discarded by the post selection of the analysis of Doppler cooling images. In some events, ions do not stay in either the state $|^2\mathrm{S}_{1/2}\rangle$ or $|^2\mathrm{P}_{1/2}\rangle$, causing no detected fluorescence. In these events, we assume that ions are not manipulated as expected; therefore, the images corresponding to these events are discarded.

**Labeling the state of ions' fluorescence.** Detecting resonance fluorescence on a closed transition for a fixed time results in a double Poissonian distribution, in which two average numbers correspond to the dark and the bright average numbers of the distribution. For the current light collection efficiency, any two Poissonian distributions $\mathcal{P}(\lambda,n)$ for any $\lambda$, $\lambda'$ overlap, resulting in ambiguity of detected events in the overlapping region. The probabilities are not inclined clearly to any of the two Poissonians. The double-threshold method [126, 127] is employed to discard cases that do not clearly distinguish between the dark and bright events, as shown in Fig. 4.3. The double-threshold method is given in detail in Ref. [128]. A preliminary experiment is performed to define a lower and upper threshold by constructing two separate intensity histograms of an ion prepared in the dark or bight state and discarding the ambiguity region for 10 % of each histogram. The upper limit of the dark state before the discarded region defines the lower threshold $t_D$. The lower limit of the bright state before the discarded region defines the upper threshold $t_B$. Nevertheless, there is a finite (but now lower) probability that dark events exist that are erroneously identified as bright, and vice versa.

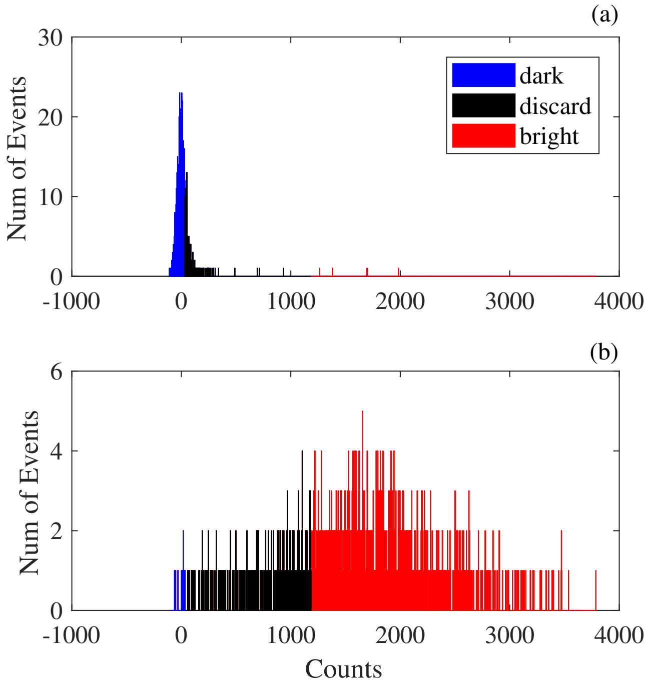

**Figure 4.3: The double threshold method.** An ion is prepared in the dark or bight state. The fluorescence of each state is used to construct an intensity histogram. (a) The histogram of the ion in the dark state. (b) The histogram of the ion in the bright state. The ambiguity region is removed by taking 10 % of each histogram. The upper limit of the blue region in (a) defines the lower threshold. The lower limit of the red region in (b) defines the upper threshold. Events with count numbers in between these two thresholds are discarded. The detection error is determined by the count outside the range between two thresholds by erroneous identification, that is, events marked in red in the dark (upper) distribution and events marks in blue in the bright (lower) distribution.

**Calculation of the excitation probability.** Evaluating an experiment for all repetitions ($N$) results in $N_D$ identified as dark events and $N_B$ identified as bright events, where the dark/bright events are identified by photon counts lower/greater than the threshold $t_D/t_B$. Therefore, the probability to measure bright events is described by

$$P_{\tilde{B}} = \frac{N_B}{N_B + N_D}. \tag{4.2}$$

The probability to falsely identify a dark event as a bright event is represented by $d_D$. Correspondingly, the probability to falsely identify a bright event as a dark event is represented by $d_B$. These false identification probabilities allow us to obtain the real probability of finding the ion in the state $|0\rangle$ ($P_D$) and $|1\rangle$ ($P_B$) as [128]

$$\begin{pmatrix} P_B \\ P_D \end{pmatrix} = \begin{pmatrix} 1 - d_B & d_D \\ d_B & 1 - d_D \end{pmatrix}^{-1} \begin{pmatrix} P_{\tilde{B}} \\ P_{\tilde{D}} \end{pmatrix}. \tag{4.3}$$

The probability density distribution $\rho(P_B|N_B,N)$ of the probability $P_B$ for a given number of projections to the bright state $N_B$ is given by [129]

$$\rho(P_B|N_B,N) = \frac{P_B^{N_B}(1 - P_B)^{N-N_B}}{\mathcal{B}(N_B + 1,N - N_B + 1)}, \tag{4.4}$$

where

$$\mathcal{B}(N_B + 1,N - N_B + 1) = \int_0^1 p^{N_B}(1 - p)^{N-N_B}\mathrm{d}p \tag{4.5}$$

denotes the beta function. The uncertainty of the excitation probability $P_B$ following equation (4.4) is given by the statistical error obtained by the variance of the measured data [129],

$$\sigma_P = \sqrt{\mathrm{Var}(P_B)} = \sqrt{\frac{N(N_B + 1) - N_B^2 + 1}{(N + 2)^2(N + 3)}}. \tag{4.6}$$

It must be noted that the mentioned detection error cannot be distinguished from the qubit initialization; see section 4.2.3. Therefore, this error is usually called state preparation and measurement (SPAM) error.

For a $M$-state system, each state probability is counted by a number of event $k_m$ outcomes as $m$. Now, the uncertainty of each $M$-state probability is determined by [129]

$$\sigma_{P_m} = \sqrt{\mathrm{Var}(P_m)} = \sqrt{\frac{(k_m + 1)(N + M - (k_m + 1))}{(N + M)^2(N + M + 1)}}. \tag{4.7}$$

The uncertainty of a two-qubit system ($M = 4$) becomes

$$\sigma_{P_m} = \sqrt{\frac{(k_m+1)(N+4-(k_m+1))}{(N+4)^2(N+5)}}. \tag{4.8}$$

The detection fidelity when preparing a single ion in the state $|0\rangle$ or $|1\rangle$ is measured as

$$P_{\tilde{D}} = 0.997(11) \qquad P_{\tilde{B}} = 0.990(12). \tag{4.9}$$

The statistical errors represent one standard deviation for 1500 repetitions. For a two-ion system, the detection fidelity of each individual ion is measured as

$$P^{(1)}_{\tilde{D}} = 0.995(12), \qquad P^{(1)}_{\tilde{B}} = 0.979(11), \tag{4.10}$$

$$P^{(2)}_{\tilde{D}} = 0.995(12), \qquad P^{(2)}_{\tilde{B}} = 0.978(11). \tag{4.11}$$

The statistical errors represent one standard deviation for 2000 repetitions. From these results, our detection fidelities show asymmetric fidelity. That is, the fidelity of detecting the state $|1\rangle$ is less than that of the state $|0\rangle$. This is due to the fact that the cooling and detection cycle is not closed and because of the branching ratio to the state $|^2\mathrm{D}_{3/2}\rangle$ from the state $|^2\mathrm{P}_{1/2}\,(F=1)\rangle$, which leaves the detection cycle, and the far-detuned excitation to the state $|^2\mathrm{P}_{1/2}\,(F=1)\rangle$ and $|^2\mathrm{P}_{3/2}\rangle$; see Fig. 3.1.

## 4.3 General Experimental Sequences

In the following section, a collection of basic measurement schemes frequently used throughout this dissertation is presented.

### 4.3.1 RF-Optical Double-Resonance Spectroscopy

The addressing frequency of individual qubits can be determined by the coherent RF-optical double-resonance spectroscopy. A Doppler-cooled ion is initialized in the state $|0\rangle$; see section 4.2.3. Thereafter, the qubit is manipulated by an RF pulse of a fixed duration with a varying frequency, in which the frequency range is assumed near the qubit resonance. Ideally, the pulse duration corresponds to the duration of a $\pi$-pulse, which in the present state of the experiment is in the range of $10-20\,\mu$s. Then, state-selective detection is observed; see section 4.2.5. The sequence is repeated for various RF frequencies to construct a spectrum. For measurement of multiple qubits, the sequence can take several RF pulses with various frequency ranges. Each pulse

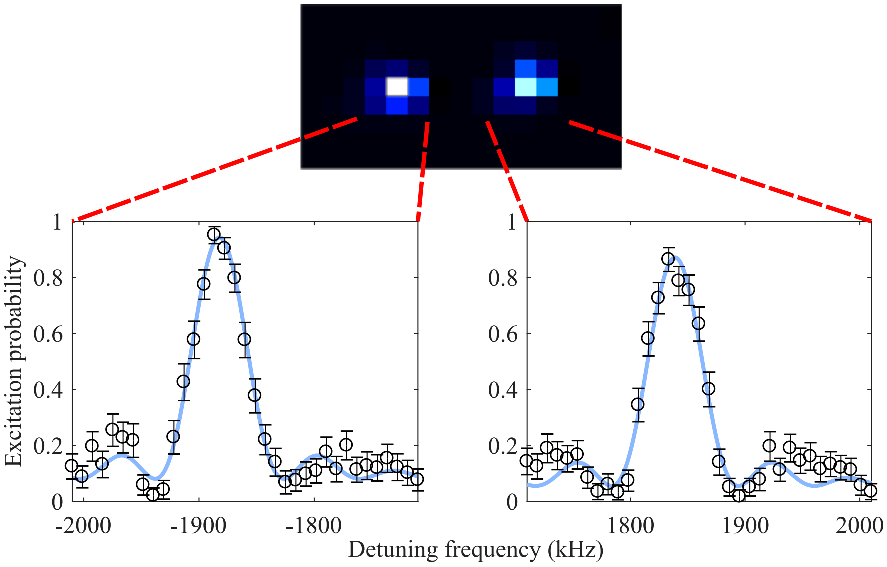

**Figure 4.4: RF-optical double-resonance spectra of a two-ion crystal.** Doppler-cooled ions are initialized in the state $|00\rangle$. The RF manipulation is applied on each ion by varying the frequency around the respective $\sigma^{+}$-transition. The duration of the RF pulses is set to 16 µs, close to the duration of a $\pi$-pulse. The $x$-axes show the detuning frequency with respect to the frequency between the two resonances. The deduced resonance frequencies are $2\pi \cdot 12\,646\,857.9(8)$ kHz and $2\pi \cdot 12\,650\,579.0(8)$ kHz, respectively. The error bars represent statistical errors within one standard deviation for 70 repetitions. For each ion, the excitation probability at its resonance frequency does not reach unity because the chosen pulse duration does not exactly correspond to a $\pi$-pulse. These results are obtained from Doppler-cooled ions, where the observed Rabi oscillation is damped from the motional excitation; see section 5.2.1. Moreover, the excitation probabilities of the resonance frequencies from both ions are not equal, indicating the difference in their Rabi frequencies. This result is probably due to a difference in the RF radiation perceived by the two ions because of the orientation of the RF antenna with respect to the trap quantization axis and/or the interference of the reflected RF from the vacuum recipient. This does not matter here, as we are interested in detuning the resonance frequency.

has a frequency range near one of the qubit resonances.

For a frequency range smaller than the axial frequency, the sideband spectra cannot be observed. The excitation probability of a qubit can be mathematically described by the Rabi model as [104]

$$P_{|1\rangle} = |\langle 1|R(\Omega\, t{,}0)|0\rangle|^2 = \frac{\Omega^2}{\Omega^2+\delta^2}\sin^2\left(\frac{\sqrt{\Omega^2+\delta^2}}{2}t\right), \tag{4.12}$$

where the unitary operator $R$ follows equation (2.6), $\Omega$ represents the Rabi frequency of the qubit transition, $\delta$ represents the detuning frequency of the RF pulse with respect to the qubit resonance, and $t$ represents the pulse duration. By taking the motional excitations into account, the resonance spectrum is further discussed in section 5.2.2. The acquired addressing frequencies can be used later for adaptive frequency correction to measure the frequencies more precisely, as described in section 4.4. The experimental result of an RF-optical double-resonance spectroscopy with 2 ions is shown in Fig. 4.4. The deduced resonance frequencies are $2\pi \cdot 12\,646\,857.9(8)$ kHz and $2\pi \cdot 12\,650\,579.0(8)$ kHz, respectively.

### 4.3.2 Rabi Oscillation Measurement

Here, the Rabi oscillation [130] is observed using the addressing carrier frequency of the $|0\rangle \leftrightarrow |1\rangle$ transition. The oscillation signal gives the Rabi frequency, which will be used to define the pulse duration of a $\pi/2$-pulse and a $\pi$-pulse. Instead of varying the frequency of the RF pulse as in the RF-optical double-resonance spectroscopy, the frequency is set to the qubit resonance and the duration of the RF pulse is varied. For measurement of multiple qubits, the sequence can also manipulate multiple resonance frequencies to associate with each qubit resonance, resulting in a Rabi oscillation for each ion.

Using a Doppler-cooled ion, damping of the Rabi oscillation can be observed because of the dependence of the Rabi frequency on the motional state and the population of various motional levels in a thermal state. We will continue to discuss the motional excitation in section 5.2.1 and 5.4. Therefore, for a better determination of the Rabi frequency, the ion is sideband-cooled before RF manipulation. The experimental results of the Rabi oscillation will be presented later; see Fig. 5.7.

In a case of a non-resonantly applied frequency, the contrast of the oscillation signal is limited. The maximum excitation probability is reduced by $(\Omega/\Omega_R)^2$, and the oscillation frequency is accelerated compared with the resonant case expressed by the generalized Rabi frequency $\Omega_R = \sqrt{\Omega^2 + \delta^2}$.

### 4.3.3 Ramsey Measurement

The Ramsey method [95] was originally designed to find the resonance frequency of an atomic transition by means of an atomic clock. Here, the Ramsey-interference experiment is a straightforward method to investigate the qubit coherence time. In the context of quantum information processing, a Ramsey experiment consists of two $\pi/2$-pulses with a free evolution time between the pulses. A Doppler-cooled (or sideband-cooled) ion is initialized in the state $|0\rangle$. The first $\pi/2$-pulse puts the qubit into an equal superposition, in which it is maximally susceptible to dephasing errors. The state evolves during an evolution according to the Hamiltonian describing the physical system; see equation (2.46). Finally, the second $\pi/2$-pulse interrogates the final

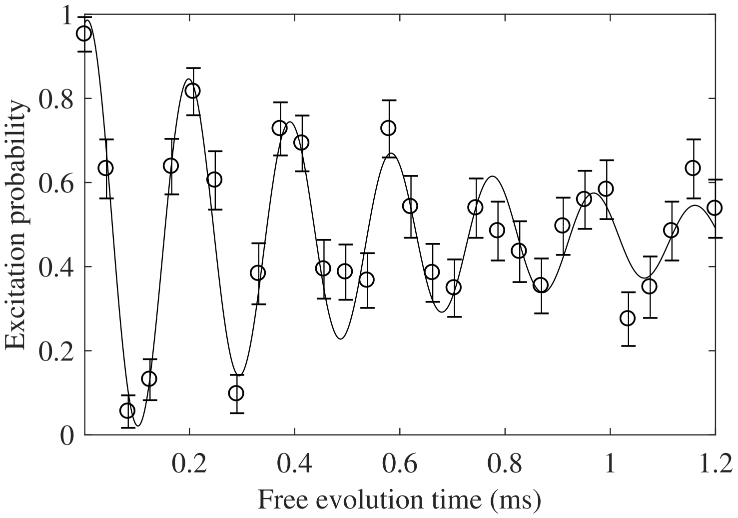

**Figure 4.5: Ramsey oscillation of a single ion.** A sideband-cooled ion is initialized in the state $|0\rangle$. The manipulation is applied to the $\sigma^+$-transition. The first $\pi/2$-pulse with phase 0 brings the qubit to a superposition state. The free evolution time is varied with a detuned frequency of $2\pi \cdot 4.5\,\mathrm{kHz}$. The second $\pi/2$-pulse with phase 0 brings the qubit to the state $|1\rangle$. The deduced transverse coherence time $T_2^*$ is 0.62(8) ms. The error bars represent statistical errors within one standard deviation for 60 repetitions.

state. If there is no dephasing during the free evolution time, the second RF pulse will bring the qubit to the state $|1\rangle$ ($|0\rangle$) when the second pulse is applied, with a relative phase 0 ($\pi$) compared with the first RF pulse. When there is dephasing, the superposition state randomly acquires phase shifts during the free evolution time. Then, the population will not be perfectly transferred by the second RF pulse, resulting in a damped oscillation for the excitation probability. The Ramsey experiment with a sideband-cooled ion is shown in Fig. 4.5. The deduced transverse coherence time $T_2^*$ is 0.62(8) ms.

### 4.3.4 Spin-Echo Pulse

The spin-echo pulse is a technique originally invented in the field of nuclear magnetic resonance [131]. It can compensate detuning frequencies and fluctuations on a time scale slower than the free evolution time $\tau$. A spin-echo experiment is a Ramsey-type experiment with an additional correcting $\pi$-pulse as a refocusing pulse in the middle of the free evolution time $\tau$. Here, we also use a spin-echo experiment as a method to investigate the qubit coherence time. The principle can be understood by a time reversal of the corresponding evolution caused by a $\pi$-pulse (a spin echo pulse or a NOT gate). A spin-echo experiment is illustrated in Fig. 4.6. A qubit is initialized

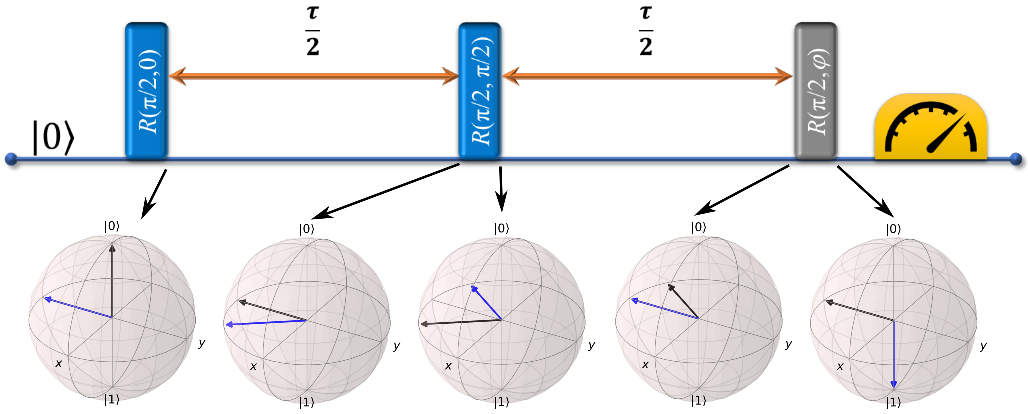

**Figure 4.6: The experimental sequence of a spin-echo experiment.** A superposition state of a qubit is initialized by a $\pi/2$-pulse from the state $|0\rangle$. The phase of the superposition state shifts because of drifts of the qubit splitting during a free evolution time of $\tau/2$ for a phase $\xi$. A spin echo pulse rotates the state, obtaining the qubit state with a reversed phase. The qubit state evolves with another evolution time of $\tau/2$ with the reversed phase. Another $\pi/2$-pulse brings the qubit state to the state $|1\rangle$ if the phase $\varphi = 0$ is applied. The lower part visualizes the Bloch vector at a given state, where the black arrow represents the previous state and the blue arrow represents the current state.

in a superposition state by a $\pi/2$-pulse. The phase of the superposition state shifts because of drifts of the qubit splitting during a free evolution time of $\tau/2$, which can be represented by a rotation of the Bloch vector of angle $\xi$ on the equator. A $\pi$-pulse with phase $\pi/2$, acting as a spin echo pulse, rotates the Bloch vector around the $y$-axis by angle $\pi$. The Bloch vector evolves with another evolution time of $\tau/2$ with a reversed phase to compensate the phase from noise. Another $\pi/2$-pulse brings the Bloch vector to the state $|1\rangle$ if the phase 0 is applied, and to the state $|0\rangle$ if the phase $\pi$ is applied. The experimental results of the spin-echo experiment will be presented in Fig. 6.1b.

### 4.3.5 Dynamical Decoupling Pulses Sequence

Dynamical decoupling (DD) [98, 99] is a dynamical control technique used to refocus the phase of quantum states. It is also known as the *bang bang* method. The DD sequence is an active technique to protect quantum states against noise. The basic idea is to use unitary control operations that impose a time dependence interaction with environmental noise, which can be achieved by a series of $\pi$-pulses with the same phase for the simplest case. The main variables used to design DD sequences are the intervals between pulses and the phase of pulses, where the phase corresponds to the orientation of the rotation axis in the $xy$-plane of the Bloch sphere.

One of the most basic DD sequences is the Carr-Purcell-Meiboom-Gill (CPMG) sequence [132], which can be viewed as repetitions of spin-echo pulses. This sequence consists of $N$ $\pi$-pulses with a total evolution time of $T$. The CPMG-XY sequence is described as [133]

$$[\tau\,(\pi)_{\phi_2}\,\tau\,\tau\,(\pi)_{\phi_1}\,\tau]^{N/2}\,, \tag{4.13}$$

where the phases $\phi_i$ of the decoupling pulses follow $\left(0, \frac{\pi}{2}\right)$ and $\tau = T/(2N)$. Note that sequences are read from right to left. When the CPMG-XY sequence is repeated with $N = 4$, it is called the XY-4 sequence.

Another sequence is based on a nesting of phases, called concatenated dynamic decoupling of the order $n$ (CDD-$n$) [134]. The CDD-$n$ sequence is described as [135]

$$\text{CDD-}n = C_n = \left[\sqrt{C_{n-1}}\,\tau\,(\pi)_{\phi_2}\,\tau\,C_{n-1}\,\tau\,(\pi)_{\phi_1}\,\tau\,\sqrt{C_{n-1}}\,\tau\right]^2, \tag{4.14}$$

where the phases $\phi_i$ also follow $\left(0, \frac{\pi}{2}\right)$ and CDD-1 = XY-4 = $\left[\tau\,(\pi)_{\phi_2}\,\tau^2\,(\pi)_{\phi_1}\,\tau\right]^2$.

One of the fault-tolerant sequences based on several different rotation axes is called the Knill-DD (KDD) sequence [135].

$$\text{KDD}_\varphi = \left[\tau\,(\pi)_{\phi_5+\varphi}\,\tau^2\,(\pi)_{\phi_4+\varphi}\,\tau^2\,(\pi)_{\phi_3+\varphi}\,\tau^2\,(\pi)_{\phi_2+\varphi}\,\tau^2\,(\pi)_{\phi_1+\varphi}\,\tau\right], \tag{4.15}$$

where the phases $\phi_i$ follow $\left(\frac{\pi}{6}, 0, \frac{\pi}{2}, 0, \frac{\pi}{6}\right)$. To further increase the fault tolerance, the KDD sequence can be concatenated by

$$\text{KDD} = \left[\text{KDD}_{\varphi+\pi/2}\text{KDD}_\varphi\right]^2. \tag{4.16}$$

The last decoupling scheme discussed here is the family of so-called arbitrarily accurate pulse sequences, which includes the universally robust (UR) DD sequence [136]. It compensates for imperfections of experimental parameters to an arbitrary order. The UR sequence is described as

$$(\text{UR-}n)^N = \left[\tau\,(\pi)_{\phi_n}\,\tau^2\,\cdots\,\tau^2\,(\pi)_{\phi_2}\,\tau^2\,(\pi)_{\phi_1}\,\tau\right]^N, \tag{4.17}$$

where $n$ represents the number of pulses per sequence and the phases $\phi_i$ also follow

$$\phi_k^{(n)} = \frac{(k-1)(k-2)}{2}\Phi^{(n)} + (k-1)\phi_2, \tag{4.18}$$

$$\Phi^{(4m)} = \pm\frac{\pi}{m}, \qquad \Phi^{(4m+2)} = \pm\frac{2m\pi}{2m+1}, \tag{4.19}$$

in which $\phi_2$ and the sign ± can be chosen as desired. Some examples of phases for UR

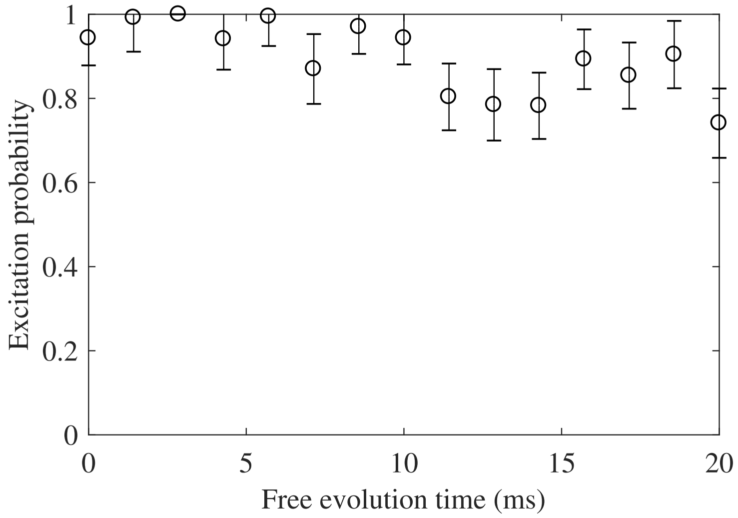

**Figure 4.7: Ramsey experiment with DD pulses in a two-ion system.** The Ramsey experiment has a final $\pi/2$-pulse with the phase 0 to obtain the final population at the state $|1\rangle$. It is performed on the magnetic field-sensitive transition of one of the ion crystal. During the evolution time, the DD pulses are applied using the KDD sequence of 80 $\pi$-pulses only on the manipulated ion. The Rabi frequency in this experiment is $2\pi \cdot 30.45\,\mathrm{kHz}$. The excitation probability shows no significant decay until approximately 10 ms. The other ion is left unprotected in the state $|0\rangle$, and the measured excitation probability is 0.017(9). The error bars represent statistical errors within one standard deviation for 50 repetitions.

sequences are shown as follows:

$$\text{UR-10:}\quad \left(0,\, \frac{4\pi}{5}, \frac{2\pi}{5}, \frac{4\pi}{5}, 0,\, 0,\, \frac{4\pi}{5}, \frac{2\pi}{5}, \frac{4\pi}{5}, 0\right), \tag{4.20}$$

$$\text{UR-14:}\quad \left(0, \frac{6\pi}{7}, \frac{4\pi}{7}, \frac{8\pi}{7}, \frac{4\pi}{7}, \frac{6\pi}{7}, 0, 0, \frac{6\pi}{7}, \frac{4\pi}{7}, \frac{8\pi}{7}, \frac{4\pi}{7}, \frac{6\pi}{7}, 0\right). \tag{4.21}$$

One might concatenate a UR sequence and apply for example a UR sequence with 140 $\pi$-pulses as 10 repetitions of a UR-14 sequence.

For a two-ion system, the experimental result of the Ramsey experiment with DD pulses is shown in Fig. 4.7. The RF manipulation is performed on the magnetic field-sensitive transition of one of the ion crystal. The DD pulses are applied using the KDD sequence of 80 $\pi$-pulses only on the manipulated ion to protect its state during the evolution time. The excitation probability shows no significant decay until approximately 10 ms, which means this sequence can protect the qubit longer than the time needed for a CNOT gate. The other ion is left unprotected in the state $|0\rangle$. The excitation probability of the unprotected ion is 0.017(9). It has a small excitation probability, which might due to the far-detuned excitation of the readout process.

## 4.4 Adaptive Frequency Correction

Our qubits are encoded in magnetic field-sensitive states, which are affected by environmental magnetic field noise. One of the noise components is a slow drift of the qubit transition frequency on the scale of one minute, which can be accounted for by repeatably measuring atomic resonance frequencies and re-calibrating driving frequencies. Originally, atomic resonance frequencies in our experiment were measured by RF-optical double-resonance spectra, which will be described in section 4.3.1. The degree of precision depends on the number of repetitions. Each measurement cycle, containing a sequence to measure a single data point in the RF-optical double-resonance spectrum, is limited to 20 ms/cycle because of the 50-Hz synchronization. That means that measurement of a resonance spectrum with an error of a few kilohertz may easily require a minute or more. This measurement time can be reduced by so-called two-point frequency measurements, which are described in detail in Ref. [112]. The resonance drift in the second or minute range is also a typical problem for the field of optical atomic clocks [137]. A similar technique for atomic clocks, called the servo loop, has been realized in Refs. [138–140]

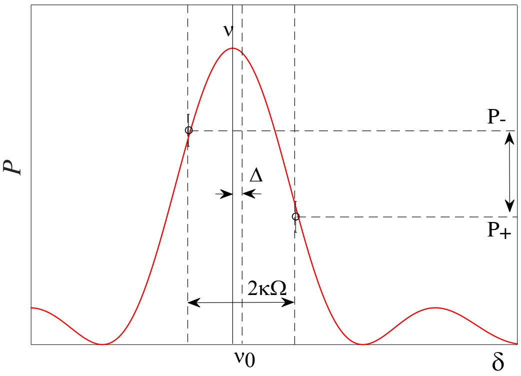

**Figure 4.8: Two-point addressing frequency measurement [112].** The red curve represents the excitation probability $P$ of an RF-optical double resonance spectrum for a varying detuning frequency $\delta$ from a hyperfine transition. Frequency $\nu_0$ indicates the last known resonance frequency, while frequency $\nu$ is the instantaneous resonance. This means that the correction to be applied is the offset frequency $\Delta$. A two-point measurement takes two excitation probabilities ($P_+$ and $P_-$) for a spreading frequency of $2\kappa\Omega$ symmetrically around $\nu_0$ and infers $\Delta$ from $P_+$ and $P_-$ by inverting equation (4.22).

The resonance determination requires two measurement points of the excitation probabilities ($P_+$ and $P_-$), as its name suggests. The two points are chosen with a priori knowledge of the addressing frequency using a spreading frequency of $2\kappa\Omega$, see Fig. 4.8, where $0 < \kappa < 1$ represents a separation parameter and $\Omega$ represents the Rabi frequency of the corresponding resonance transition. To determine an offset frequency $\Delta$, an error signal $g(\Delta)$ as a function of the offset frequency is defined as

$$g(\Delta) = \frac{P_+ - P_-}{P_+ + P_-}. \tag{4.22}$$

This function is calculated in advance, providing inverse mapping to the offset frequency when we have a value of $g(P_+, P_-)$, where $P_\pm = P_\pm(\delta = (\Delta \pm \kappa)\Omega)$.

The offset frequency is unique within a limited mapping area of $|\Delta| \leq \min((1-\kappa)\Omega, \kappa\Omega)$. If the resonance frequency is not in this mapping area, then a full RF-optical double resonance spectrum is required to provide a new guess parameter.

The typical parameters are $\kappa = 0.7$, each $P_{\pm}$ has 75 repetitions, and the two-point measurement is repeated in 2 steps for a large and small Rabi frequency. The small Rabi frequency can narrow down the resonance transition, obtaining a smaller error compared with the high Rabi frequency. These 2-step measurements allow us to determine a resonance frequency precisely, causing a remaining addressing error within a few hundred Hertz of the 12.65-GHz transition within a few seconds of measuring time. This technique can be interleaved with other experimental sequences to actively re-calibrate the qubit transitions during a measurement. This is especially beneficial for long experimental sequences, which are prone to the detrimental effects of slow drifts.

# 5

# Near Ground-State Cooling

Cooling beyond the Doppler limit of trapped atomic ions and neutral atoms close to their motional ground state is an essential tool and often a prerequisite in quantum optics and quantum information experiments. To date, the best known results to my knowledge for ground-state cooling using the sideband cooling (SBC) technique are reported in Ref. [141] and Ref. [142] for a trapped ion and neutral atom, respectively. These achievements are indicated by motional ground state occupation probabilities of 99.9% and 99% for ions at an axial trap frequency of $2\pi \cdot 4.51\,\text{MHz}$ and for neutral atoms at a radial trap frequency of $2\pi \cdot 100\,\text{kHz}$, respectively.

For a realization of (near-)ground state cooling in typical traps, atomic transitions in the optical regime have been used, as they provide a sufficiently large Lamb-Dicke Parameter (LDP). The coupling between the internal and motional states of a single trapped ion [143] and an atom [144, 145] have been experimentally demonstrated.

In this chapter, our technique uses RF radiation to drive the atomic sidebands together with a repumping laser [54]. A detailed investigation of RF sideband cooling applied to bare ionic states of $^{171}\text{Yb}^{+}$ in a static magnetic-field gradient is reported. The focus is on one- and two-ion crystals. This work continues from Refs. [54, 56] and has been published in Ref. [57].

## 5.1 Radio-Frequency Sideband Cooling

First, a single $^{171}\text{Yb}^{+}$ion is considered in the Doppler-cooled state, as described in section 4.2.1. To further reduce the phonon level below the Doppler limit, the sideband cooling technique is employed using RF radiation, as described in section 4.2.2. The frequency of the RF radiation is red-detuned by the angular trap frequency $\omega_z = 2\pi \cdot 117\,\text{kHz}$ relative to the state $|1\rangle$. When taking the AC light shift [146] into account when applying the detuned RF field, the applied frequency for sideband cooling deviates from the trap frequency, where the trap frequency is at $2\pi \cdot 122.984\,\text{kHz}$, as shown in section 3.10.1. For each sideband cooling cycle, a phonon is taken out of the ion state [124]. In this model, the sideband cooling process can be described by rate equations.

### 5.1.1 The Rate Equation Model

The scattering rate limits how fast the ion is cooled. In a two-level system, the cooling rate depends on the occupation of the excited level $\rho_{ee}$ and the decay rate of the given level $\Gamma$. The excited level occupation can be described as [122]

$$\rho_{ee} = \frac{|\Omega|^2/4}{\Delta^2 + |\Omega|^2/2 + \Gamma^2/4}, \tag{5.1}$$

where $\Omega$ represents the Rabi frequency driving the ion between the ground state and the excited state, $\Delta$ represents the detuned frequency to the driving transition, and $\Gamma$ represents the decay rate of the excited state. In the non-linear coupling regime, the Rabi frequencies $\Omega_{n,n+k}$ of the transition $|0{,}n\rangle \leftrightarrow |1{,}n+k\rangle$, where the first entry indicates the atomic transition and the second entry indicates the phonon number, are determined by [147]

$$\begin{aligned} \Omega_{n,n+k} &= \Omega_{n+k,n}, \\ &= \mathrm{e}^{-\eta^2/2}\eta^k \Omega_0 L_n^k(\eta^2)\sqrt{\frac{n!}{(n+k)!}}, \end{aligned} \tag{5.2}$$

with the pure electronic Rabi frequency $\Omega_0$, non-negative integers $n$ and $k$, the effective LDP $\eta$ (see equation (2.45)), and the generalized Laguerre polynomial

$$L_n^k(x) = \sum_{j=0}^{n} (-1)^j \binom{n+k}{n-j} \frac{x^j}{j!}, \tag{5.3}$$

of order $n$. With the limit of small $\eta$, $\Omega_{n,n-1} \approx \Omega_0 \eta \sqrt{n}$. From this point, we will drop the subscript from the pure electronic Rabi frequency. The cooling rate, which is dependent on the motional excitation, can then be expressed as

$$\begin{aligned} \mathcal{R}_c &= \Gamma \rho_{ee}, \\ &= \Gamma \frac{(\Omega\eta\sqrt{n})^2}{2(\Omega\eta\sqrt{n})^2 + \Gamma^2}, \end{aligned} \tag{5.4}$$

where the first red sideband frequency is resonantly driven. When the ground state is reached, there is no motional excitation ($n = 0$), as well as no fluorescence from decay of the excited state. However, on the hyperfine level of $^{171}\mathrm{Yb}^+$ ions, the cooling process cannot be modeled as a two-level system because there is no optical spontaneous emission of the qubit excited state. The qubit excited state is then coupled to another auxiliary fast decay transition to change the decay rate of the excited state ($\Gamma \rightarrow \Gamma'$).

Therefore, the motional ground state can be reached; see Fig. 5.1a and Fig. 5.1b. The resulting decay rate $\Gamma'$ is in the limit of low saturation and is given by [148]

$$\Gamma' = \frac{\Omega_{e,aux}^2}{(\Gamma_{aux,e} + \Gamma_{aux,g})^2 + 4\Delta_{e,aux}^2}\Gamma_{aux,e}, \tag{5.5}$$

$$= \frac{\Omega_{e,aux}^2}{4\Gamma_P}. \tag{5.6}$$

Here, $\Omega_{e,aux}$ represents the Rabi frequency driven between the qubit excited state $|1\rangle$ and the auxiliary state $|aux\rangle$, $\Gamma_P$. $\Gamma_{aux,e} = \Gamma_{aux,g}$ represent the decay rates from the auxiliary state to the states $|1\rangle$ and $|0\rangle$, ${}^2\mathrm{P}_{1/2}\,(F = 1)$, which have a lifetime of 8.12(2) ns, corresponding to the decay of $2\pi \cdot 19.6\,\mathrm{MHz}$ [149]. $\Delta_{e,aux}$ represents the detuning from the first motional sideband frequency, which is zero when the frequency is at the resonance. Later, $\Omega_{e,aux}$ is replaced by $\Omega_L$ to denote the Rabi frequency of the optical transition ${}^2\mathrm{S}_{1/2}\,(F = 1) \leftrightarrow {}^2\mathrm{P}_{1/2}\,(F = 1)$. The prominent cooling processes are illustrated in Fig. 5.1c, which are either the red-sideband frequency of the qubit excited state or the auxiliary state and decay to the ground state to reduce a motional level. Thus, the prominent cooling processes are given by [121]

$$\mathcal{R}_{c,1} = \Gamma' \frac{(\Omega\eta\sqrt{n})^2}{2(\Omega\eta\sqrt{n})^2 + \Gamma'^2}, \tag{5.7}$$

$$\mathcal{R}_{c,2} = \Gamma'_{RSB} \frac{\Omega^2}{2\Omega^2 + {\Gamma'_{RSB}}^2 + 4\omega_z^2}, \tag{5.8}$$

where $\Gamma'_{RSB} = \frac{(\Omega_L\tilde{\eta}\sqrt{n})^2}{4\Gamma_P}$, $\tilde{\eta} = k\cos\theta_L\sqrt{\hbar/2m\omega_z}$ represents the LDP of the optical transition, $k = 2\pi/\lambda$ represents the photon wave vector, and $\theta_L$ represents the laser propagation direction with respect to the trap quantization axis.

Even though the motional ground state can be reached, the heating process can limit the sideband cooling process, as illustrated in Fig. 5.1d. The prominent heating processes are either the blue-sideband frequency of the qubit excited state or the auxiliary state and decay to the ground state to gain a motional level. Therefore, the prominent heating processes are given by [121]

$$\mathcal{R}_{h,1} = \Gamma'_{BSB} \frac{\Omega^2}{2\Omega^2 + {\Gamma'_{BSB}}^2 + 4\omega_z^2}, \tag{5.9}$$

$$\mathcal{R}_{h,2} = \Gamma' \frac{(\Omega\eta\sqrt{n+1})^2}{2(\Omega\eta\sqrt{n+1})^2 + \Gamma'^2 + 4(2\omega_z)^2}, \tag{5.10}$$

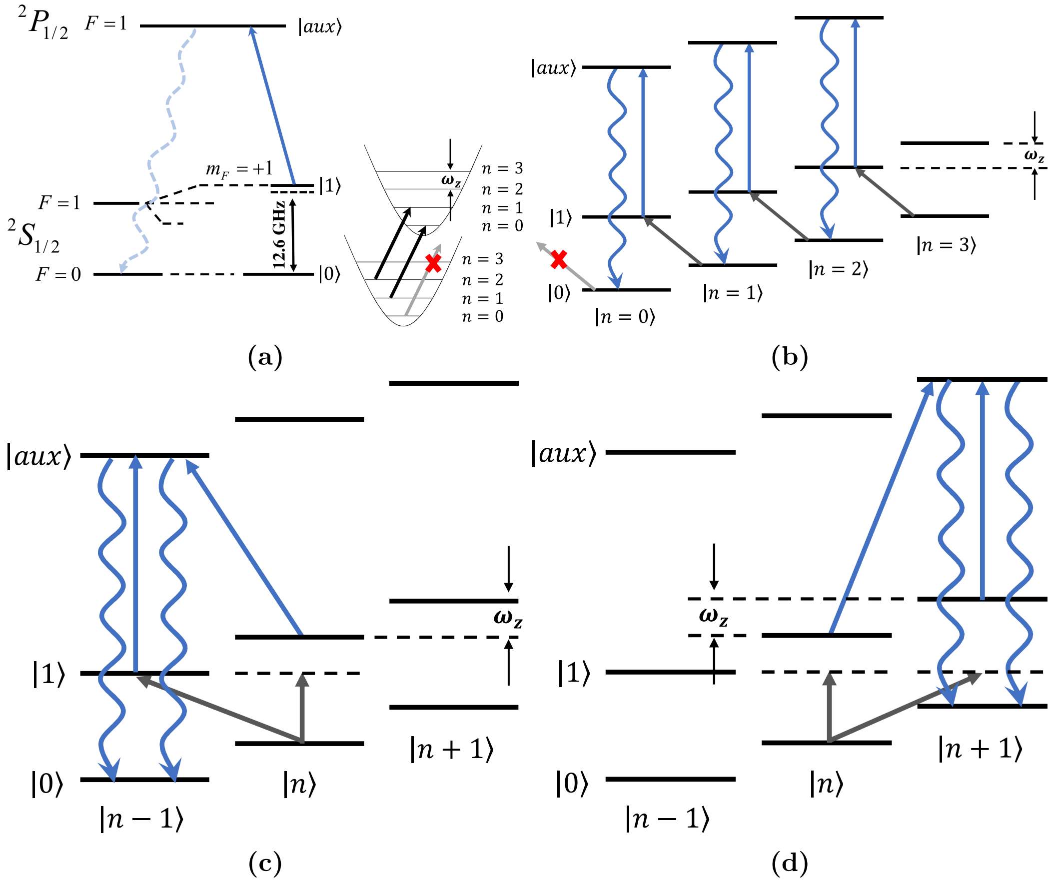

**Figure 5.1: Sideband cooling cycle to achieve the motional ground state [121, 148].** (a) The ground state can be reached by reducing the motional excitation level with red-detuned RF radiation. After achieving the motional ground state, there is no further fluorescence because it is not possible to drive to the $(m_F = +1)$ level of the ${}^2\mathrm{S}_{1/2}$ $(F = 1)$ state indicated by a red cross. (b) The cooling cycle is considered to be a $\Xi$ (cascade) configuration with a strong dipole transition of the auxiliary state $|aux\rangle$ and the state $|0\rangle$. Similarly, when reaching the motional ground state, there is no further fluorescence. (c) Two prominent cooling processes in a cascade configuration are either the red-sideband frequency of the qubit excited state or the auxiliary state and decay to the ground state to reduce a motional level. (d) Similarly, two prominent heating processes in a cascade configuration are either the blue-sideband frequency of the qubit excited state or the auxiliary state and decay to the ground state to gain a motional level.

where $\Gamma'_{BSB} = \frac{(\Omega_L \tilde{\eta}\sqrt{n+1})^2}{4\Gamma_P}$. The steady state of the rate equation is calculated as

$$\dot{p_0} = p_1(\mathcal{R}_{c,1} + \mathcal{R}_{c,2}) - p_0(\mathcal{R}_{h,1} + \mathcal{R}_{h,2}), \tag{5.11}$$

$$\dot{p_1} = -\dot{p_0}, \tag{5.12}$$

such that $p_0$, $p_1 = 1 - p_0$ represent the phonon occupation probabilities for states $|n = 0\rangle$ and $|n = 1\rangle$, respectively. This will give the cooling limit of the SBC process. Generally, the rate equation is described by [148]

$$\begin{aligned}\dot{p_n} =&(n+1)(\mathcal{R}_{c,1} + \mathcal{R}_{c,2})p_{n+1} - ((n+1)(\mathcal{R}_{h,1} + \mathcal{R}_{h,2}) + n(\mathcal{R}_{c,1} + \mathcal{R}_{c,2}))p_n \\ &+ n(\mathcal{R}_{h,1} + \mathcal{R}_{h,2})p_{n-1}.\end{aligned} \tag{5.13}$$

Using the rate equation model, the sideband cooling process is simulated and is shown in Fig. 5.2. The simulation scripts can be found in appendix D.1. The simulation parameters are similar to the laboratory parameters, including an axial trap frequency $\omega_z$ of $2\pi \cdot 117.5\,$kHz, a magnetic-field gradient of 19 T/m, and an initial average phonon $\langle n \rangle$ of 100. The SBC process is applied for 60 ms while changing the Rabi frequency of the qubit transition and the repumping laser. This is shown in Fig. 5.2a by a contour

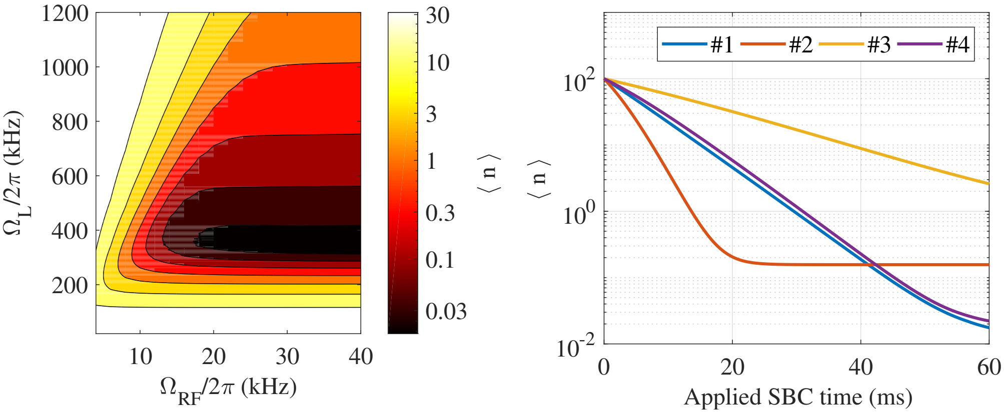

**(a)** **(b)**

**Figure 5.2: Sideband cooling simulation using the rate equation model.** (a) The simulation makes use of the laboratory parameters, which are an axial trap frequency $\omega_z$ of $2\pi \cdot 117.5\,$kHz, a magnetic-field gradient of 19 T/m, and an initial average phonon $\langle n \rangle$ of 100. The sideband cooling process is applied for 60 ms. The area for phonons smaller than 0.05 corresponds to $\Omega_{RF}/2\pi > 16\,$kHz and $\Omega_L/2\pi$ between 302 kHz - 470 kHz. (b) Some simulation samples are shown here. The average phonon is plotted as a function of the duration of time sideband cooling is applied, where #1 has $\Omega_{RF}/2\pi = 40\,$kHz and $\Omega_L/2\pi = 338\,$kHz, #2 has $\Omega_{RF}/2\pi = 40\,$kHz and $\Omega_L/2\pi = 630\,$kHz, #3 has $\Omega_{RF}/2\pi = 18\,$kHz and $\Omega_L/2\pi = 888\,$kHz, and #4 has $\Omega_{RF}/2\pi = 20\,$kHz and $\Omega_L/2\pi = 360\,$kHz. The lowest attainable phonon is at 0.018, from simulation #1 (blue line).

plot of the motional excitation level after sideband cooling of 60 ms. The lowest phonon number area ($\langle n \rangle < 0.05$) can be found at the Rabi frequency of the qubit transition $\Omega_{RF}/2\pi > 16\,\text{kHz}$ and the Rabi frequency of the repumping laser $\Omega_L/2\pi$ in the range of 302 kHz - 470 kHz. The contour plot shows that the sideband cooling process to achieve the ground state requires optimal intensities of either the coherent RF control radiation or the repumping laser. That is, the Rabi frequency of the qubit transition cannot be too small because it will slow down the cooling process, and the same applies to the Rabi frequency of the repumping laser. However, when the Rabi frequency of the repumping laser is too high, the probability for off-resonant excitation becomes higher, and the occupation probability of the motional ground state will decrease.

In Fig. 5.2b, the phonnon number is plotted against the applied sideband cooling time from 4 different sets of Rabi frequencies. The simulation set #1 (blue) has $\Omega_{RF}/2\pi = 40\,\text{kHz}$ and $\Omega_L/2\pi = 338\,\text{kHz}$. This setting gives the lowest phonon number of 0.018 from the simulation parameter ranges. This means that the SBC needs to be applied for at least 60 ms to achieve the lowest average phonon number. The Rabi frequencies of the other three sets are $\#2 : \Omega_{RF}/2\pi = 40\,\text{kHz}$ and $\Omega_L/2\pi = 630\,\text{kHz}$, $\#3 : \Omega_{RF}/2\pi = 18\,\text{kHz}$ and $\Omega_L/2\pi = 888\,\text{kHz}$, and $\#4 : \Omega_{RF}/2\pi = 20\,\text{kHz}$ and $\Omega_L/2\pi = 360\,\text{kHz}$. Simulation #2 shows a better cooling rate but it cannot achieve a lower phonon number in the end, indicating that off-resonant excitation probability limits the occupation probability of the motional ground state; see equation (5.8) and (5.10).

The simulation suggests that a higher cooling rate can be achieved by increasing the intensity of the repumping laser; however, it will decrease the occupation probability of the motional ground state. In practice, the ion will have more heating processes that might come from electronic noise from neighboring devices. Then, we should decide the level of the occupation probability of the motional ground state in which the intensity of the repumping laser can be higher. That is, we can shorten the cooling time by reducing the occupation probability of the motional ground state.

### 5.1.2 Experimental Procedure

To diagnose the cooling state of the ion, a generic pulse sequence is utilized, as shown in Fig. 5.3. Each measurement point includes the following experimental sequence: (A) Doppler cooling, (B) sideband cooling, (C) qubit preparation to the state $|0\rangle$, (D) coherent RF manipulation, and (E) detection using an EMCCD camera. In the diagnosis of the motional excitation state, a simple RF pulse is applied, varying either pulse durations or frequencies that are detuned from the qubit transition. The experimental sequence is repeated until reaching the desired statistical error for each data point.

Theoretical determination of motional excitation is discussed in the next section. In

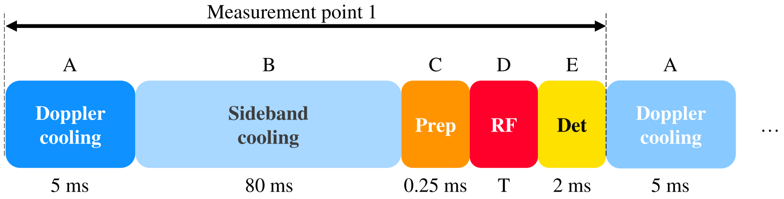

**Figure 5.3: The experimental pulse sequence of the SBC experiment.** The motional excitation is deduced from the measurements to obtain Rabi oscillations and motional sideband spectra after cooling. These measurements consist of (A) Doppler cooling, (B) sideband cooling, (C) preparation of qubit state $|0\rangle$, (D) coherent RF manipulation, and (E) detection. The operation times of each sequence are indicated. The coherent RF manipulation uses the variable time $T$.

this work, two different coherent experiments are considered.

## 5.2 Determination of Motional Excitation for a Single Ion

To verify the result of the sideband cooling process, two different coherent experiment were performed to determine the average phonon number after sideband cooling.

(i) Rabi oscillations can be observed after applying the sideband cooling to determine the motional excitation state. Rabi oscillations are driven directly to the resonant transition $|0\rangle \leftrightarrow |1\rangle$. The pulse duration of the RF pulse at the transition resonance frequency is varied, forming a Rabi oscillation signal. The damping of the Rabi oscillation can be observed. This is due to the phonon level dependency of the Rabi frequency, which can be used to determine the average phonon $\langle n\rangle$ [150].

(ii) An RF-optical double-resonance spectrum is observed by varying the RF pulse frequency. This measures the excitation probability as a function of RF frequency for a given pulse duration. The RF frequency is varied around the $|0\rangle \leftrightarrow |1\rangle$ transition after preparing an ion in state $|0\rangle$ and applying sideband cooling. The pulse duration is selected to enhance the probability of exciting the red and blue sidebands. The excitation of the red and blue sidebands can be used to determine the average phonon $\langle n\rangle$.

### 5.2.1 Determination of Motional Excitation by Damping of Rabi Oscillation

In the Lamb-Dicke regime, the frequency of the $|0\rangle \leftrightarrow |1\rangle$ transition depends on the motional excitation state of the ion. This causes damping of Rabi oscillations, enabling

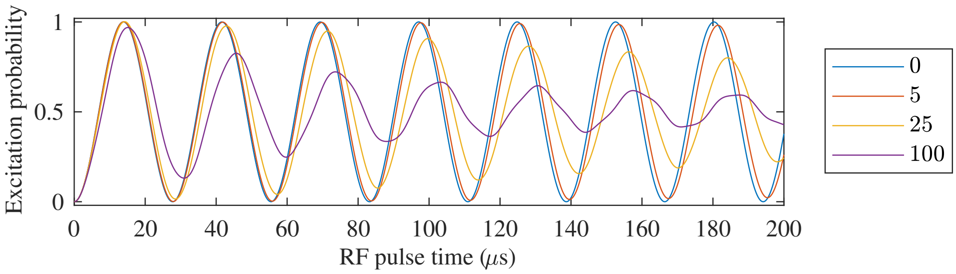

**(a)** Carrier

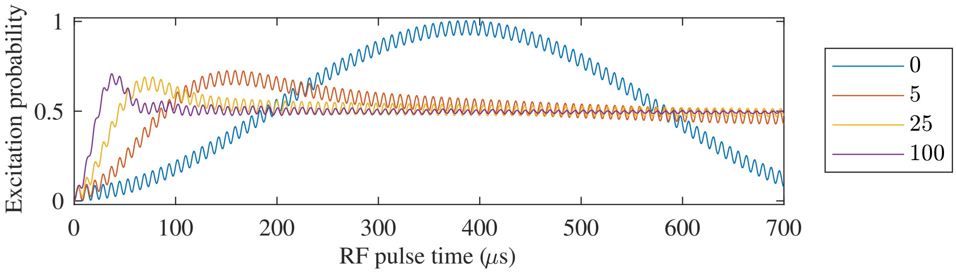

**(b)** BSB

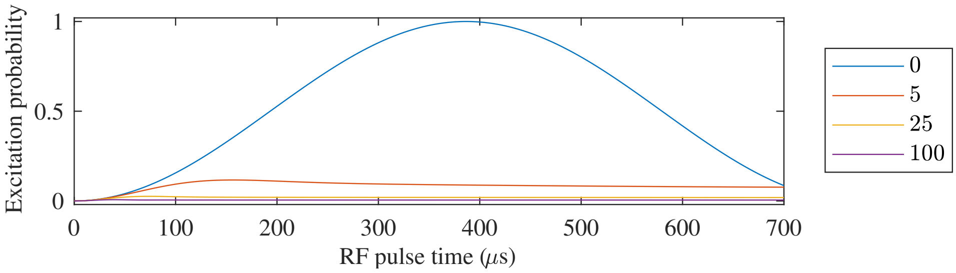

**(c)** Comparing BSB and RSB

**Figure 5.4: Simulated Rabi oscillations for different average phonon numbers.** The calculation of the Rabi oscillations uses average phonon numbers, as indicated by the legend. The calculation is based on a Rabi frequency of $2\pi \cdot 36\,\text{kHz}$ and an axial trap frequency of $2\pi \cdot 117.5\,\text{kHz}$. The excitation probability corresponds to the probability of finding the ion in state $|1\rangle$ when the RF radiation is set on the qubit resonance, namely the carrier frequency (a) or on the blue sideband frequency (b). The Rabi oscillations on the carrier frequency show fast amplitude damping for high phonon levels, starting from the second oscillation period. In (b), a small and fast oscillation is caused by non-resonant excitation from the carrier transition. The probabilities of excitation on the blue-sideband frequency are damped very fast with high phonon numbers. They give more clear visualization when the ion has motional excitation of only a few phonons. (c) From the excitation probabilities using the blue sideband frequency (as in (b)) and the red sideband frequency (not shown), the comparison probability is shown by the blue-sideband excitation subtracted from the red-sideband excitation. The subtraction shows that the two probabilities are approximately the same when the phonon number is high. This result means that the motional excitation of high phonon numbers cannot be accurately determined from the excitation probabilities of the two sidebands.

us to map the motional state or the average phonon number $\langle n \rangle$. The Rabi oscillation at the carrier frequency is given by [122]

$$P_{|1\rangle} = \frac{1}{2}\left(1 - \sum_{n=0}^{\infty} p_n(T) \cos\left(\Omega_{n,n} t\right)\right), \tag{5.14}$$

where the excitation probability $P_{|1\rangle}$ is the probability of finding the ion in state $|1\rangle$. The Rabi oscillation is driven by the pulse duration $t$ and distributed by the thermal distribution $p_n(T)$. The probability of thermal distribution is given by

$$p_n(T) = \frac{1}{\langle n \rangle_T + 1}\left(\frac{\langle n \rangle_T}{\langle n \rangle_T + 1}\right)^n, \tag{5.15}$$

considering the phonon number $\langle n \rangle_T$ at temperature $T$, as mentioned in the Doppler cooling limit in section 4.2.1. In the non-linear coupling regime, the Rabi frequencies $\Omega_{n,n+k}$ are shown in equation (5.2). The effective LDP is defined in equation (2.45) using information from equation (2.44), where the magnetic-field gradient along the quantization axis $\partial_z B = 19\,\mathrm{T/m}$, the ${}^{171}\mathrm{Yb}^{+}$ ion-mass $m = 2.84 \times 10^{-25}\,\mathrm{kg}$, and the axial trap frequency $\omega_z = 2\pi \cdot 117.48\,\mathrm{kHz}$. Using the mentioned parameters, the LDP in our experiment is given by $\eta_{\mathrm{eff}} = 0.036$.

The average phonon number can be determined by measuring the excitation probability and using equation (5.14) to fit the measured result. Note that the sum theoretically runs to infinite phonon numbers, but in the fitting routine runs up to ten times the expected average phonon numbers, where the probability of finding these phonon numbers or higher is negligible.

Some examples for different average phonon numbers are shown in Fig. 5.4. The Rabi oscillations on the carrier frequency show fast amplitude damping for high phonon levels, starting from the second oscillation period. By driving with the blue-sideband frequency, the small and fast oscillations are observed together with the Rabi oscillations. These are due to non-resonant excitation from the carrier transition. The probabilities of excitation on the blue-sideband frequency give more clear visualization when the ion has a motional excitation of only a few phonons. The subtraction between the excitation from the blue-sideband to the red-sideband excitation to compare between the two probabilities is also shown, which shows that the two probabilities are approximately the same when the phonon number is high. This result means that the motional excitation of high phonon numbers cannot be accurately determined from the excitation probabilities of the two sidebands.

### 5.2.2 Determination of Motional Excitation by Resonance Spectrum

Another method to determine the motional excitation state of an ion is to consider the RF-optical double resonance spectrum. By keeping the duration of the RF pulse constant, the RF frequency is varied around the sidebands of the $|0\rangle \leftrightarrow |1\rangle$ transition, after the ion is prepared in the ground state $|0\rangle$. For the carrier, the probability of finding the ion in the excited state is given by [122]

$$P_C(\delta,T) = \sum_n^{\infty} p_n(T) \frac{\Omega_{n,n}^2}{\Omega_{n,n}^2 + \delta^2} \sin^2\left(\frac{\sqrt{\Omega_{n,n}^2 + \delta^2}}{2} t\right), \tag{5.16}$$

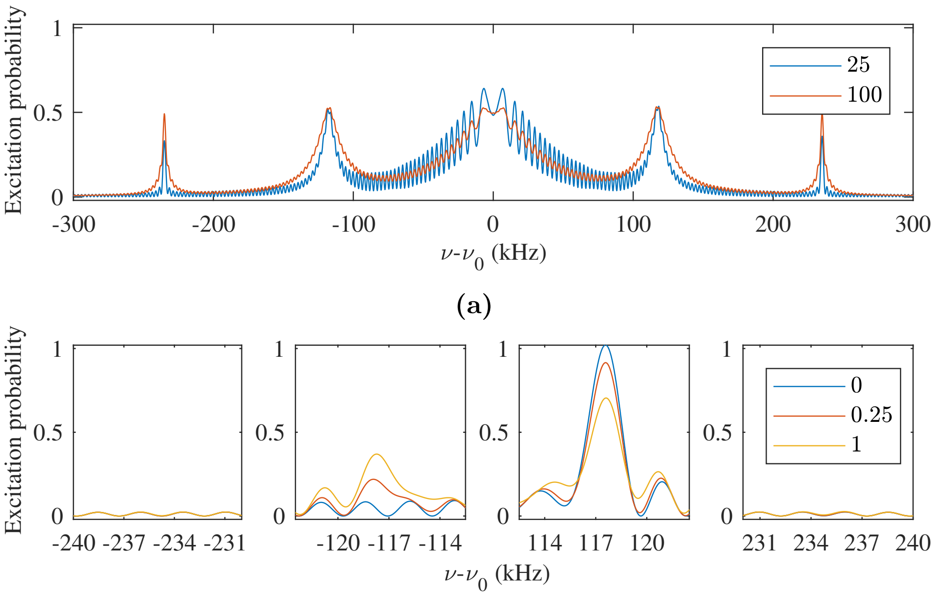

**(a)**

**(b)**

**Figure 5.5: Simulated resonance spectra for different average phonon numbers.** The calculation of the RF resonance spectra uses average phonon numbers, as indicated by the legend. It is based on a Rabi frequency of $2\pi \cdot 36\,\text{kHz}$, an RF pulse duration of $400\,\mu\text{s}$, and an axial trap frequency of $2\pi \cdot 117.5\,\text{kHz}$. (a) The excitation probability is with respect to the detuned RF radiation of the qubit resonance in a full spectrum. (b) As in (a), but focusing on the first and second sidebands. There is no visible excitation on the second sidebands when the phonon number is below 1.

where $\delta$ is the RF pulse detuning from the $|0\rangle \leftrightarrow |1\rangle$ resonance. For the blue sideband of the $k^{\text{th}}$ order, the excitation probability $P_B^k(\delta{,}T)$ is given by

$$P_B^k(\delta{,}T) = \sum_n^{\infty} p_n(T) \frac{\Omega_{n+k,n}^2}{\Omega_{n+k,n}^2 + (\delta - k\omega_z)^2} \sin^2\left(\frac{\sqrt{\Omega_{n+k,n}^2 + (\delta - k\omega_z)^2}}{2} t\right), \tag{5.17}$$

where $\Omega_{n+k,n}$ is with respect to equation (5.2). The probability of excitation through the red sideband $P_R^k(\delta{,}T)$ is proportional to the excitation through the blue sideband and determined by

$$P_R^k(\delta{,}T) = \left(\frac{\langle n\rangle_T}{1 + \langle n\rangle_T}\right)^k P_B^k(-\delta{,}T). \tag{5.18}$$

To determine the average phonon number by considering all excitation probabilities up to the second-order sidebands, the excitation probability $P_{|1\rangle}$ is given by

$$P_{|1\rangle}(\delta{,}T) = P_C(\delta{,}T) + \sum_{k=1}^{2}\left(P_R^k(\delta{,}T) + P_B^k(\delta{,}T)\right). \tag{5.19}$$

Some examples of simulated $P_{|1\rangle}(\delta{,}T)$ for different average phonon numbers are shown in Fig. 5.5. When more ions are considered, all motional modes also have to be taken into account; therefore

$$P_{|1\rangle}(\delta{,}T) = P_C(\delta{,}T) + \sum_{mode}\sum_{k=1}^{2}\left(P_R^k(\delta{,}T) + P_B^k(\delta{,}T)\right). \tag{5.20}$$

The average phonon number is determined by measuring the excitation probability of the resonance spectrum and fitting with either equation (5.19) or equation (5.20).

## 5.3 Optimal Duration of the SBC process

Next, the optimal duration for applying the SBC process is discussed. This is due to the fact that a cold system is desirable, without spending too much time on the cooling sequence.

During the sideband cooling process, the photon can only be scattered by reaching the state $|1\rangle$. When the motional ground state is reached, there is no excitation probability through the red sideband; therefore, there is no fluorescence scattering. Using the calibrated intensity of the optical repumping laser [54] and an RF frequency set to the red sideband, the fluorescence scattering observed during the sideband cooling process

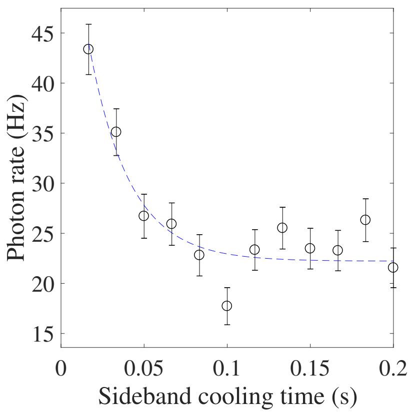

**Figure 5.6: Determination of the optimal time for the sideband cooling process.** By observing the fluorescence rate during the sideband cooling process when the RF frequency is set at the red sideband transition, the optimal time can be obtained. The Rabi frequency at the carrier frequency is measured at $\Omega = 2\pi \cdot 46.0(1)\,\mathrm{kHz}$ and an intensity of $2.3(4)\,\mathrm{W/m^2}$ for the repumping laser. The decay constant deduced from the exponential fit is $25(8)^{-1}\ \mathrm{ms}^{-1}$. The optimal duration of sideband cooling is chosen as 80 ms, where the scattering decay approaches its asymptote. The error bars represent statistical errors within one standard deviation for 1200 repetitions.

is as shown in Fig. 5.6. The optimal duration of sideband cooling is chosen as 80 ms, where the scattering decay approaches its asymptote. Further discussion of this topic can be found in Ref. [56].

## 5.4 Cooling of a Single Ion

Further discussion regarding cooling of a single ion is presented in the following section. Two methods, a decay of Rabi oscillations and a sideband spectrum of the RF-optical double resonance spectrum, are considered to deduce the motional excitation level.

From the Rabi oscillation measurement, the average phonon number immediately after Doppler cooling is 91(5), as shown in Fig. 5.7a. To extract the average phonon number, the fitting is performed with the theoretical excitation probability given in section 5.2.1. The SBC process uses the RF radiation on the first red sideband frequency and an intensity of $0.21(4)\,\mathrm{W/m^2}$ of the repumping laser. At the location of the ion, the laser is focused to a waist of $144(3)\,\mu\mathrm{m}$ [106] with a power of $0.11(2)\,\mu\mathrm{W}$ measured outside the entrance viewport of the vacuum chamber. The Rabi frequency at the carrier frequency is measured at $\Omega = 2\pi \cdot 39.47(4)\,\mathrm{kHz}$. Applying the SBC for 80 ms, the phonon number is reduced to 1.71(15), as shown in Fig. 5.7b.

From the RF-optical double resonance spectrum, the blue and red sidebands are both clearly visible when an ion is highly motionally excited. When the ion is cooled close to the motional ground state, the resonance of the red sideband is strongly reduced [117]. After Doppler cooling, the average phonon number is 65(22), as shown in Fig. 5.8a. To extract the average phonon number, fitting is performed with the theoretical excitation probability given in section 5.2.2. The fit shows the measured motional frequency $\omega_z$ of $2\pi \cdot 117.48(11)\,\mathrm{kHz}$. For a Doppler-cooled ion, the motional excitation is at a high level. This leads to a larger error for the fitting routine because the phonon number extracted

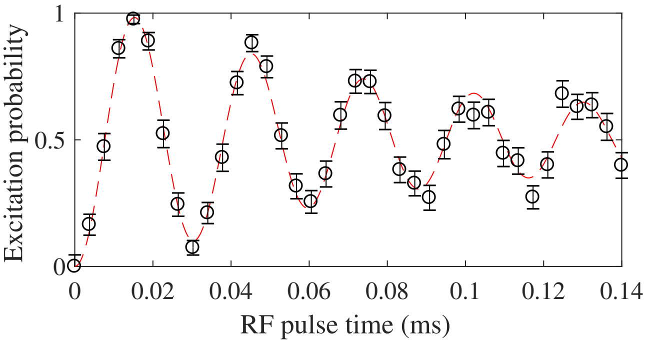

**(a)** Doppler cooling

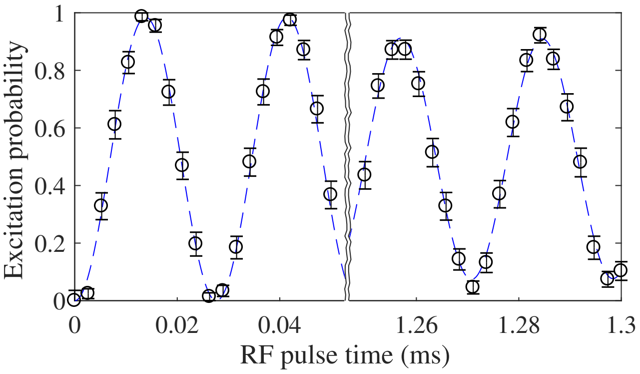

**(b)** Sideband cooling

**Figure 5.7: Determination of the average phonon number by Rabi oscillations** The Rabi oscillations are driven resonantly between the $|0\rangle \leftrightarrow |1\rangle$ transition. (a) Without any SBC process, the ion is only Doppler-cooled before the measurement of the Rabi oscillation. The deduced average phonon number is $\langle n \rangle = 91(5)$. (b) RF sideband cooling applied for a duration of 80 ms, and the Rabi oscillation sequences are carried out at two different pulse-time windows. The windows correspond to an applied RF pulse duration of $0-50\,\mu\text{s}$ (left) and $1.25-1.30$ ms (right). The deduced average phonon number is $\langle n \rangle = 1.71(15)$. The error bars represent statistical errors within one standard deviation for 125 repetitions.

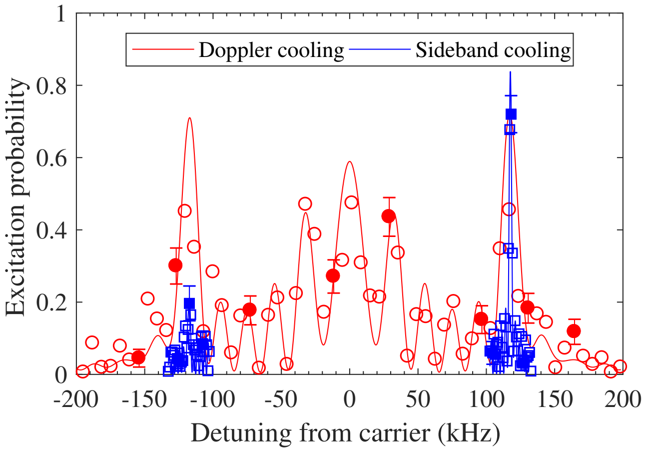

**(a)**

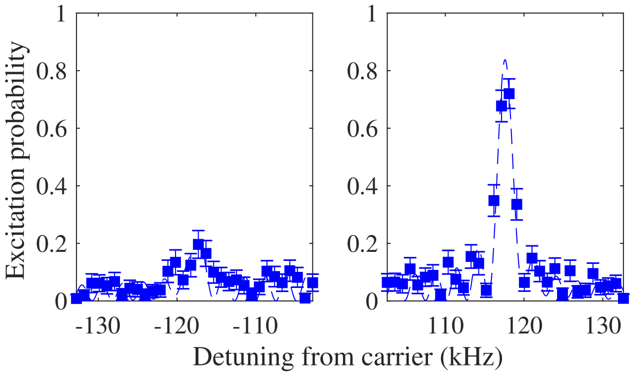

**(b)**

**Figure 5.8: RF-optical double resonance spectrum of a single ion.** (a) After Doppler cooling (red data points and red solid line), an RF pulse of 55 µs is used to measure the RF-optical double resonance spectrum. An additional RF sideband cooling of 80 ms is applied on a Doppler-cooled ion, and an RF pulse length of 400 µs is used to measure the RF-optical double resonance spectrum (blue). These measurements focus primarily on the first sidebands. The red sideband is significantly suppressed after sideband cooling. The average phonon numbers deduced from the fits are $\langle n \rangle = 65(22)$ (red) and $\langle n \rangle = 0.30(12)$ (blue). (b) This plot is a zoom-in view of the sideband-cooled ion in (a). The upper plot shows error bars only for a few selected data points for clarity. The error bars represent statistical errors within one standard deviation for 100 repetitions.

from the spectrum depends on the ratio between the excitation probabilities close to unity on the red and blue sidebands; see Fig. 5.4c and Fig. 5.5a. Error reduction can be performed for particularly large numbers of repetitions. After the SBC, the phonon number inferred from the RF resonance spectrum is reduced to 0.30(12); see Fig. 5.8b.

From the two described approaches, there is a discrepancy in the deduced average phonon numbers after the sideband-cooling cycle in the range of a few phonons. The discrepancy can be understood as a change in the qubit resonance frequency over time. In the current setup, the magnetic field-sensitive transition regularly drifts by approximately 2−3 Hz/s, which can lead to accumulation of approximately 50−100 Hz for a single measured data point. A reduction of the contrast of Rabi oscillations is then caused by a large number of repetitions, as well as the inaccuracy of the deduction of the motional excitation level. In contrast, even though drift causes a reduction in the excitation probabilities of the motional sidebands, the deduction of the motional level remains significantly unaffected, as it depends on the ratio of excitation probabilities between the sidebands. Therefore, the phonon number deduced by observing the decay of Rabi oscillations is considered as an upper limit for the actual average phonon number, and the RF resonance spectrum is used for more accurate results.

To estimate the lowest attainable average phonon number from the sideband cooling

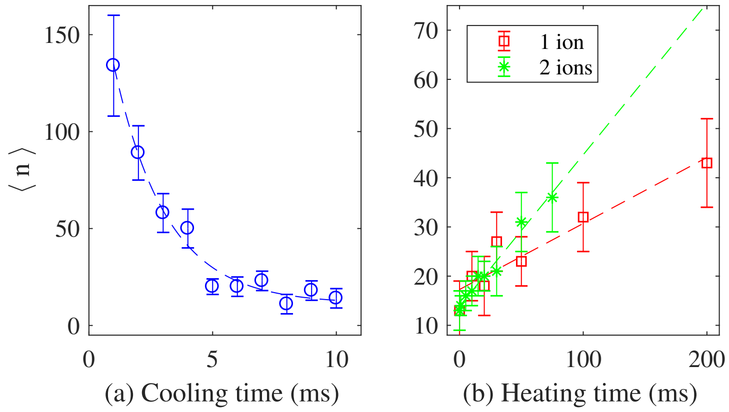

(a) Cooling time (ms)

(b) Heating time (ms)

**Figure 5.9: Determination of the cooling and heating rates for a single ion.** (a) After the ion is initially Doppler-cooled, the average deduced phonon number from a Rabi oscillation is plotted as a function of the sideband cooling time. The exponential fit shows a sideband cooling rate of 0.47(6) $\mathrm{ms}^{-1}$ [54]. (b) After 15 ms of sideband cooling, all cooling processes were switched off and the ion was left in the trap for a given time to gain temperature from the environment. The linear fit shows a heating rate of 0.13(2) $\mathrm{ms}^{-1}$ for a single-ion system (square) [56]. For a two-ion system (star), sideband cooling is applied for 50 ms on the COM mode of the refrigerant ion, and the linear fit shows a heating rate of 0.30(2) $\mathrm{ms}^{-1}$. The error bars represent statistical errors within one standard deviation of 35 repetitions.

technique, the heating rate and the cooling rate of the ion system need to be considered. The theoretical prediction can be determined by

$$\langle n \rangle = \frac{R_H}{(R_{SBC} - R_H)}, \tag{5.21}$$

where $R_H$ is the heating rate and $R_{SBC}$ is the sideband cooling rate of a single ion [121]. The cooling rate can be measured by observing Rabi oscillations to extract average phonon numbers as a function of the sideband cooling time; see Fig. 5.9a. The cooling process indicates an exponential decay of the phonon number with time and shows a sideband cooling rate $R_{SBC}$ of $0.47(6)\,\mathrm{ms}^{-1}$ from an exponential fit [54]. For the heating rate measurement, the ion is first cooled by the sideband cooling for 15 ms; then, all cooling processes are switched off, letting the ion heat up for varying durations before observing Rabi oscillations. The result (red plot) is shown in Fig. 5.9b. The linear fit shows the heating rate $R_H$ of $0.13(2)\,\mathrm{ms}^{-1}$ for a single-ion system [56]. According to these two rates, the theoretical limit of sideband cooling is estimated to be $\langle n \rangle = 0.37(10)$. In Fig. 5.8, the single-ion experiment shows an average phonon number of $\langle n \rangle = 0.30(12)$ after sideband cooling. This agrees well with the theoretical limit calculated from the heating and cooling rates.

As one might notice, the phonon number at the Doppler-cooled state in Fig. 5.9a is higher than the one in Fig. 5.7a. This is due to a higher heating rate, primarily caused by electronic noise, at the time of taking the data shown in Fig. 5.9a. After applying additional low-pass filters to suppress noise components in the DC voltages applied to the trap electrodes, the heating rate was subsequently reduced. More information can be found in Refs. [56, 96].

## 5.5 Cooling of Two Ions

In what follows, the SBC process is discussed with respect to a two-ion system. The cooling is performed on one of the two ions. Thus far, the discussion has focused on a single ion. Now, the sideband cooling technique is extended to a two-$^{171}\mathrm{Yb}^+$ ion Coulomb crystal; see Fig. 5.10. Thus, the effective LDPs are adjusted for multiple harmonic-oscillator modes [86, 151].

For cooling of two or more ions, the cooling applied on one of ions can cool the other ions through collisions. This effect is called sympathetic cooling. The cooling ion is referred to as the coolant or refrigerant ion, and the other ion is known as the target ion. Sympathetic cooling for a system that is larger than a single ion has been considered and demonstrated with respect to different aspects, for example, two identical ions employing laser radiation (e.g., [152]), or two different isotopes of the same ion species (e.g., [153]), or two different ion species (e.g., [28, 154]). In

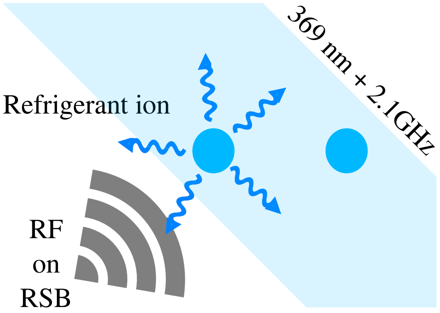

**Figure 5.10: Illustration of SBC in a two-ion system.** In a two-ion Coulomb crystal, the left ion participates in the sideband cooling cycle with the RF radiation at the red sideband (RSB) frequency of the left ion; therefore, it is referred to as the coolant or refrigerant ion. The right ion is sympathetically cooled through the refrigerant ion and hence referred to as the target ion.

this section, a complementary demonstration using RF sideband cooling to achieve sympathetic cooling is presented.

In a two-ion crystal, there are two normal modes of vibration: a center-of-mass (COM) mode, and a stretch (STR) mode. In the COM mode, the ions oscillate in phase; in the STR mode, the ions oscillate 180° out of phase. The effective LDP for two ions in our experiment is $\eta_{\text{eff}}^{\text{COM}} = \eta_{\text{eff}}/\sqrt{2} = 0.0254$ and $\eta_{\text{eff}}^{\text{STR}} = \eta_{\text{eff}}/\sqrt{2\sqrt{3}} = 0.0193$. From the axial secular frequency of a single ion, $\omega_z = 2\pi \cdot 117.48(11)\,\text{kHz}$, the motional mode of the COM mode is expected to be $\omega_z$, and that of the STR mode is $\omega_{\text{STR}} = \sqrt{3}\omega_z = 2\pi \cdot 203.48\,\text{kHz}$. However, by measuring the RF-optical double resonance spectrum, the motional frequencies of both modes are determined to be $\omega_{\text{COM}} = 2\pi \cdot 117.23(5)$ and $\omega_{\text{STR}} = 2\pi \cdot 209.54(14)\,\text{kHz}$[1], e.g., Fig. 5.11, following the same procedure as described in section 5.4. These deviations can be described by the AC-stark effect [146] because RF radiation is applied during the RF-optical double resonance spectroscopy. Furthermore, the shifted frequency may be caused by the imperfection of micromotion compensation. Ions can be displaced from the trap center by any residual micromotion, resulting in a coupling between the axial and radial modes [155] and leading to a shift in the axial motional mode frequencies [28, 156].

The magnetic field-insensitive transition $|0\rangle$ and $|0'\rangle$ is used to Doppler-cool a single ion. For a two-ion crystal, this transition for each ion is slightly shifted by a few kilohertz because of the second-order Zeeman shift. Thus, the average frequency between the two RF resonance frequencies for two ions is used to Doppler-cool the ions. After Doppler cooling, the average motional excitation levels for the COM and STR modes are measured using the RF-optical double resonance spectra of the respective modes. The red and blue sidebands of the respective frequency modes give average phonon numbers of $\langle n_{\text{COM}} \rangle = 64(23)$ and $\langle n_{\text{STR}} \rangle = 11(5)$, as shown in Tab. 5.1. The COM mode, which has a higher heating rate compared with the STR mode, may experience a larger coupling to stray electric fields [157, 158], so that $\langle n_{\text{COM}} \rangle > \langle n_{\text{STR}} \rangle$.

After the ions are Doppler cooled, RF sideband cooling by tuning the red sideband resonance RF radiation to the COM mode of one of the two ions is applied. The

---

[1] Here, the trap frequencies are obtained as the average of several results during data acquisition for two-ion measurements.

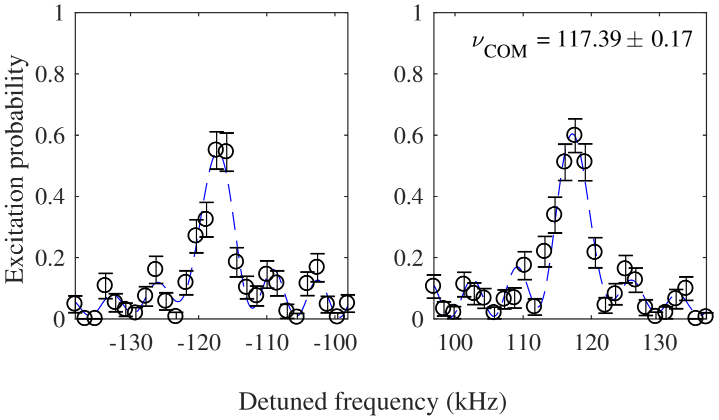

**(a)** center-of-mass mode

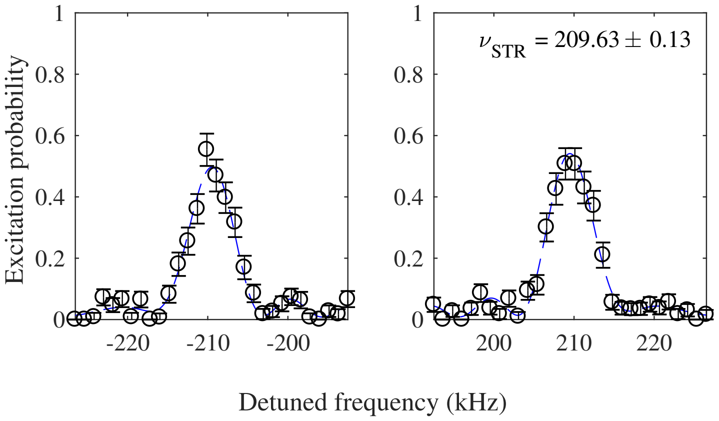

**(b)** stretch mode

**Figure 5.11: RF-optical double resonance spectrum of two-ion system.** The RF frequency is applied, focusing on the sidebands. These two plots are not at the ground state to precisely measure the sideband excitation. The sideband cooling is applied for a few milliseconds to affect approximately 10 phonons. (a) Center-of-mass (COM) mode. (b) Stretch (STR) mode.

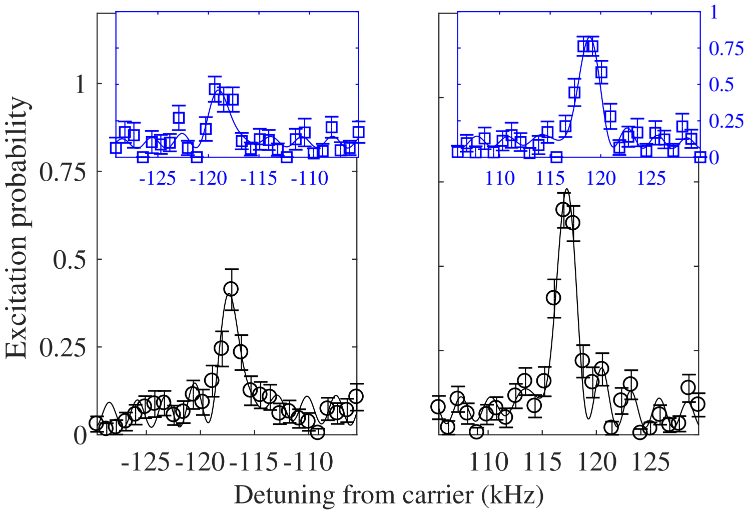

**Figure 5.12: Demonstration of sympathetic cooling using two identical isotopes of the same ion species.** The black plot and the blue plot represent the sideband spectra of the COM mode of the refrigerant ion (circles) and the target ion (squares), respectively. After applying the SBC process, the refrigerant ion and the target ion have average phonon numbers of 1.1(4) and 1.0(6), respectively. The error bars represent statistical errors within one standard deviation for 100 repetitions.

SBC is applied for 80 ms using an intensity of 0.57(4) W/m$^2$ for the repumping laser. This corresponds to a power of 0.30(2) µW measured outside the vacuum chamber. The sideband spectra of the refrigerant ion, indicated with circular marks in Fig. 5.12, give an average phonon number $\langle n_{\text{COM}}^{refrigerant} \rangle$ of 1.1(4). Conversely, by measuring the target ion (square markers), the average phonon number of the target ion after sideband cooling only the refrigerant ion is $\langle n_{\text{COM}}^{target} \rangle = 1.0(6)$. The motional excitation between the two ions is not significantly different, as expected, because only one COM mode exists in the oscillator.

**Table 5.1:** Summary of average phonon number achieved with or without sideband cooling applied to different motional modes in a two-ion system. No experimental result is available for a blank entry.

| Cooling (on ion) | Refrigerant ion | | Target ion | |
|---|---|---|---|---|
| | COM | STR | COM | STR |
| Doppler cooling (both) | 64(23) | 11(5) | 62(20) | 15(8) |
| SBC on COM (Refrigerant ion) | 1.1(4) | - | 1.0(6) | - |
| SBC on STR (Refrigerant ion) | - | 3.2(1.1) | - | 4.2(1.7) |

In addition to considering the COM mode, the STR mode is also studied. After Doppler cooling, the RF sideband cooling is tuned to the STR mode of the red sideband resonance. Similar to the study of the COM mode, the SBC is also applied for 80 ms, but using an intensity of 8.16(4) $\mathrm{W/m^2}$ for the repumping laser. The sideband spectra of the refrigerant ion give an average phonon number $\langle n_{\mathrm{STR}}^{refrigerant}\rangle$ of 3.2(11); see also Tab. 5.1. The sideband spectra of the target ion give an average phonon number $\langle n_{\mathrm{STR}}^{target}\rangle$ of 4.2(17). The phonon numbers observed from the two ions are compatible within the error bars, demonstrating efficient sympathetic cooling.

Moreover, the heating rate for a two-ion system is measured. The heating rate study starts with two Doppler-cooled ions, after which RF sideband cooling is applied on the COM mode of the refrigerant ion for 50 ms. After allowing the ions to heat up by switching off all cooling processes for a given amount of time, the RF-optical double resonance spectra for different heating times are measured. Observation of the Rabi oscillation decay is not suitable for a multiple-ion system because it is not possible to distinguish between different motional modes. The result (green plot) is shown in Fig. 5.9b. A linear fit shows a heating rate $R_{H,COM}^{2\ ions}$ of 0.30(2) $\mathrm{ms^{-1}}$.

## 5.6 Summary of Experimental Results and Outlook

In this chapter, we presented a detailed investigation of near-ground state cooling of a single and two trapped atomic ions. This technique employs simple RF sideband cooling using ions exposed to a static magnetic-field gradient. The current achievement is at the theoretical limitation because of the heating rate of 0.13(2) $\mathrm{ms^{-1}}$ for a single ion at the axial trap frequency of $2\pi \cdot 117.48(11)$ kHz in the current setup. In this work, there are two methods to determine the average phonon number, which are observation of the Rabi oscillation decay and the sideband spectrum. The lowest attainable motional excitation is at the average phonon number of 0.30(12), which is translated to a motional ground state occupation probability of 77 % using the probability obtained by $p_0$ of equation (5.15). With the noise present in the lab causing a drift in the qubit resonance, the observation of the Rabi oscillation decay is more suitable for probing a high motional excitation, and the sideband spectrum is more suitable for probing a low motional excitation in a single-ion system. Observation of the Rabi oscillation decay is not suitable for a multiple-ion system because it is not possible to distinguish between different motional modes. Furthermore, this study is the *first demonstration of sympathetic sideband cooling using RF radiation* in a two-ion crystal. This complements the conventional approaches of laser cooling.

Additionally, the experimental demonstration is performed at a relatively low secular trap frequency regime, which is also often encountered in neutral atom traps. The method demonstrated here is expected to be useful for future experiments in the ion and atom trapping communities, given the widespread use of hyperfine transitions in many neutral atom and ion experiments and the easy availability of commercial RF tools. This method is cost-effective when compared with Raman laser techniques.

The presented demonstration makes use of a single RF frequency to perform the SBC process. To be more efficient regarding SBC, multiple frequencies can be employed to cool all motional modes simultaneously. This will increase the cooling rate for a multi-ion crystal and could improve the ground state occupation. However, combining multiple frequencies with a power combiner reduces the power of each frequency, if a passive power combiner is used.

One of the cooling limitations in these proof-of-principle experiments is the heating rate of an ion crystal. Because an RF power of approximately 15 to 20 W is applied to the trapping electrodes, the electrodes can heat up to more than 370 K [159]. The electrode temperature contributes to the heating rate [160, 161]. The electrode heating can be improved by changing to a material with a better conductivity, e.g., titanium [159] instead of stainless steel (316L) [83], and sapphire [159] instead of macor [83] to match thermal conductivity. In a new trap design, the electrode distances can be adjusted to provide a higher magnetic-field gradient, which will improve the cooling efficiency by increasing the LDP [124]. Other setups using two-dimensional and three-dimensional micro-structured traps utilizing microfabrication technology have achieved static magnetic-field gradients of 36 T/m [162] and 16.3(9) T/m [163], using integrated permanent magnets or current wires, respectively. A dynamic magnetic-field gradient of 35.3(4) T/m has also been demonstrated in Ref. [49]. Additionally, a proposal in Ref. [13] is expected to achieve a magnetic-field gradient of 150 T/m.

Ref. [54, Sec. 5.3] reports the results of a study of the motional excitation level when varying the Rabi frequency of the RF radiation and intensity of an optical repump laser during the SBC process. This suggests that an increase in the Rabi frequency of the RF radiation will improve the achievable ground state cooling. However, the increasing power caused by the increasing Rabi frequency can be limited by the axial secular trap frequency. A far-detuned excitation is most likely when the Rabi frequency becomes too high compared with the trap frequency. Therefore, one might consider performing the SBC process in a coherent method using composite narrow-frequency pulses [164] to prevent far-detuned excitation when utilizing higher Rabi frequencies.

# 6

# Investigation of Qubit Dephasing

To realize a large-scale universal quantum computer, quantum bits are required to be very well controlled so that quantum information can be processed correctly. A trapped ion system, which is a well-established platform, is a candidate to be a quantum computer [76, 165–167]. However, trapped ion qubits are susceptible in particular to dephasing from interactions with the environment. These interactions cause phase randomization of a quantum superposition state. Qubit dephasing, an uncontrolled and unwanted mechanism, limits the realization of high-fidelity conditional quantum gates, e.g., a unitary controlled-NOT gate. The CNOT gate is an elementary gate for arbitrary quantum algorithms [168]. One technique to overcome qubit dephasing is the dynamical decoupling technique, explained in section 4.3.5, using either a continuous or pulsed style [34, 59, 99, 169]. However, it is advantageous and preferable if noise sources are individually identified and suppressed. This will reduce any overhead techniques required for qubit protection. In this chapter, detailed investigations of the qubit dephasing of trapped ion qubits exposed to a static magnetic-field gradient are presented.

## 6.1 Observation of Qubit Dephasing

From the superposition state of the magnetic field-sensitive state $|^2\mathrm{S}_{1/2}\,(F=1, m_F = +1)\,\rangle$, a qubit has been observed to dephase rapidly compared with a two-qubit gate time. The measurement used to observe the coherence time is a Ramsey-type measurement, as explained in section 4.3.3. The decay of a Ramsey fringe or a Ramsey oscillation infers the qubit coherence time $T_2^*$. Previously, our system had a qubit coherence time of 0.2(1) ms [83, 96, 99]; see Fig. 6.1a. In addition, a Ramsey-type measurement with a spin echo $\pi$-pulse is also performed to determine the coherence time. In this case, at half of the free evolution time, a resonant $\pi$-pulse with a relative phase of $\pi/2$ is applied. A spin echo pulse can compensate for a small possible detuning of the qubit transition with respect to the Rabi frequency. The spin echo

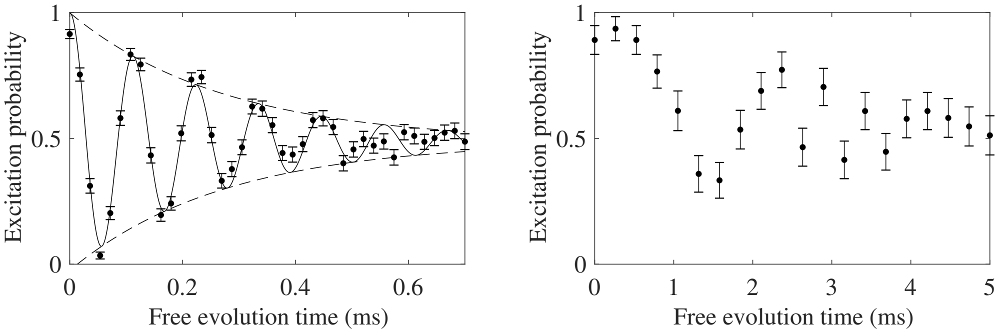

**(a)** Ramsey oscillation **(b)** Spin echo measurement

**Figure 6.1: Ramsey-type measurement to determine the coherence time.** (a) A Ramsey oscillation with respect to the free evolution time is measured on the magnetic field-sensitive $\sigma^+$-transition. The deduced coherence time $T_2^*$ is 0.27(4) ms. The error bars represent statistical errors within one standard deviation for 350 repetitions. (b) A Ramsey-type measurement with a spin echo $\pi$-pulse is measured against the free evolution time. This measurement gives a longer coherence time as a result of noise correction by a spin echo pulse. The error bars represent statistical errors within one standard deviation for 100 repetitions.

pulse can also compensate for noise components of a few hundred hertz[1]. Without qubit dephasing, the last pulse of the Ramsey sequence brings the excitation probability always to one. As can be seen in Fig. 6.1b, the excitation probability drops and spreads between 0.5 ms and 3 ms. A clear minimum is found at 1.4 ms. This minimum indicates a strong noise component at 0.36 kHz because the excitation probability is less than 0.5 [170]. After some evolution time, the excitation probability stays at 0.5 because of the loss of phase information for the qubit.

Using a spin echo pulse, the qubit coherence time can be extended to a few milliseconds. Nevertheless, this is significantly small compared with the time required to realize a single CNOT gate, which is approximately 5 ms. To neglect the effect from qubit dephasing, the qubit coherence time is expected to be much longer than the time needed for coherent operations. Therefore, the possible causes of fast dephasing are investigated.

One could compare the measured coherence time to a similar setup, which has a comparable magnetic-field gradient. A similar behavior is observed, and the dephasing is also approximately 0.2 ms [59]. On the contrary, the coherence time is approximately 5 ms and significantly longer in the experiment of Ref. [171], in which there is no magnetic-field gradient. If fluctuations of magnetic fields do exist, then a change in the magnetic field leads to a change in the resonant frequency of the magnetic field-sensitive $\sigma^+$-transition (or $\sigma^-$-transition), in which qubits are encoded. The

---

[1] The free evolution time of 2 ms (1 ms) corresponds to 250 Hz (500 Hz); see equation (7.22) and the paragraph therein.

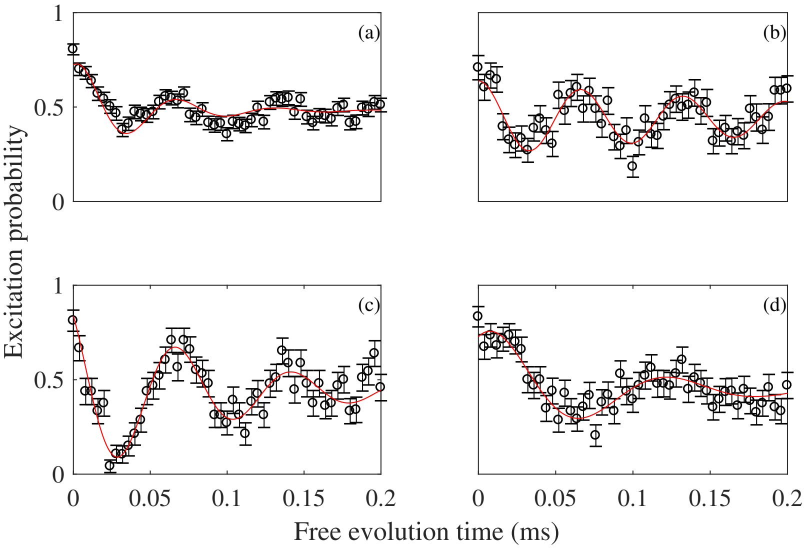

**Figure 6.2: Frequency drift of a Ramsey oscillation measurement.** (a) The Ramsey oscillation is measured and has no contrast after a free evolution of approximately 70 µs. The deduced oscillation frequency is $2\pi \cdot 15.5(15)$ kHz. The error bars represent statistical errors within one standard deviation for 200 repetitions. The total measurement takes approximately 15 min. This result is split into individual results of 50 repetitions each. The first three sets are shown in (b), (c), and (d), respectively. (b) The first 50-repetition analysis shows an oscillation frequency of $2\pi \cdot 15.1(7)$ kHz. (c) The second 50-repetition analysis shows an oscillation frequency of $2\pi{\cdot}13.3(6)$ kHz. (d) The third 50-repetition analysis shows an oscillation frequency of $2\pi \cdot 8.8(11)$ kHz. The error bars in (b), (c), and (d) represent statistical errors within one standard deviation for 50 repetitions. The results in (b), (c), and (d) show that the qubit addressing frequency is shifted over the measuring time, resulting in misinterpretation of the qubit coherence time. Adaptive frequency correction can minimize this problem by keeping up with the drift of the addressing frequency.

magnetic-field fluctuation can be expressed as phase damping [172]. According to our experimental parameters, the qubit transition frequency is related to the magnetic field shift as 14 kHz/µT (or 1.4 MHz/G). For fluctuations of electric fields, ions can be spatially moved by electric forces from nearby electrodes. Ions are moved under a static magnetic-field gradient of 19 T/m; then, the qubit transition frequency is also shifted. The qubit transition frequency with respect to the ion displacement is $263\,\mathrm{Hz\,nm^{-1}}$.

Interpretation of the Ramsey-type measurement is required to accumulate sufficient statistics. To achieve a precise statistic, the measurement time can be quite long, up to 15 to 30 min per measurement. By analyzing a long measurement of Ramsey oscillation, as shown in Fig. 6.2, we find that the complete measurement gives a very short coherence time, while the coherence time is improved when taking a fraction of the total measurement. Furthermore, different measurement fractions provide different Ramsey detuning frequencies, which indicates a slow drift of the qubit transition

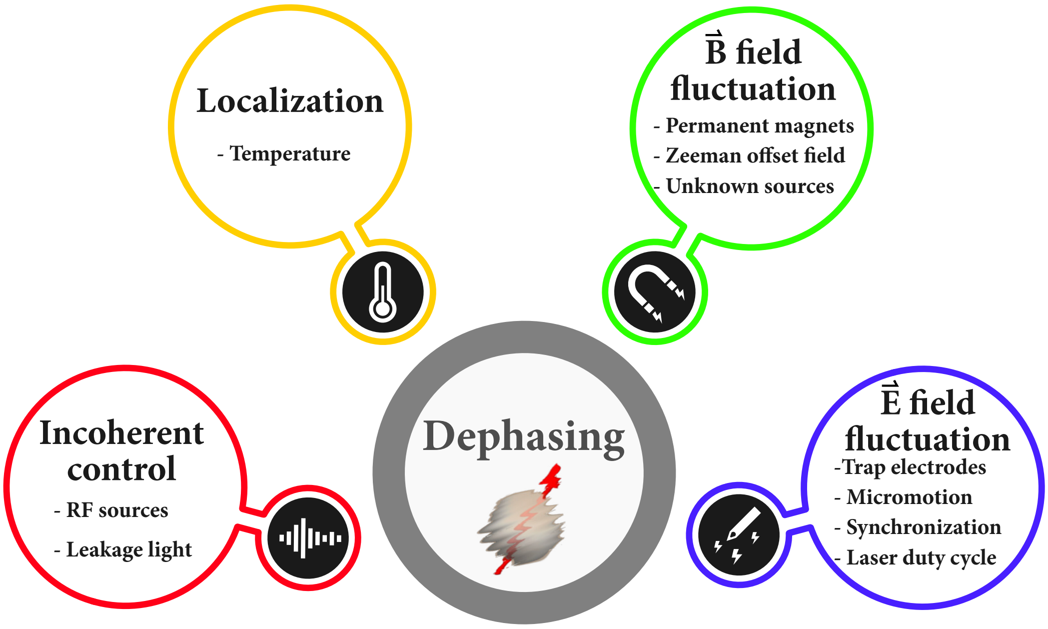

**Figure 6.3: Mind map for the discussion of possible causes of rapid dephasing.** There are four possible causes in our consideration: Incoherence of the qubit control, qubit localization, magnetic field fluctuation, and electric field fluctuation. These effects may be caused by laboratory devices, for example, the source for the qubit manipulation, magnetic-field noise caused by neighboring devices, and electric-field noise caused by the fluctuation of the supplied signals. Furthermore, some physical processes, such as micromotion, leakage light, ion temperature, and laser duty cycle, could be responsible for dephasing.

frequency. A slow drift of the qubit transition could lead to misinterpretation of the qubit coherence time. In Ref. [96], a slow drift of the qubit transition frequency for a single ion was observed. The frequency drift was significant when an ion was freshly loaded. The frequency drift was greater than 120 kHz over 20 min. Even after the frequency reached a stable level, it still changed slowly, in the range of 50 kHz. By employing adaptive frequency correction [112], also described in section 4.4, the experimental time can be decreased to a smaller time interval before changing to a new qubit addressing frequency. This can remove some slow drift when the frequency correction is performed often enough.

In what follows, we discuss possible potential noise sources, which might limit the qubit coherence time. The overview is based on a mind map, shown in Fig. 6.3. In our consideration, there are four possible causes: (i) incoherence of the qubit control, (ii) qubit localization, (iii) magnetic field $\mathbf{B}$ fluctuation, and (iv) electric field $\mathbf{E}$ fluctuation. Our investigation is performed using Ramsey-type measurements, similar to Fig. 6.1.

## 6.2 Incoherence of Qubit Control

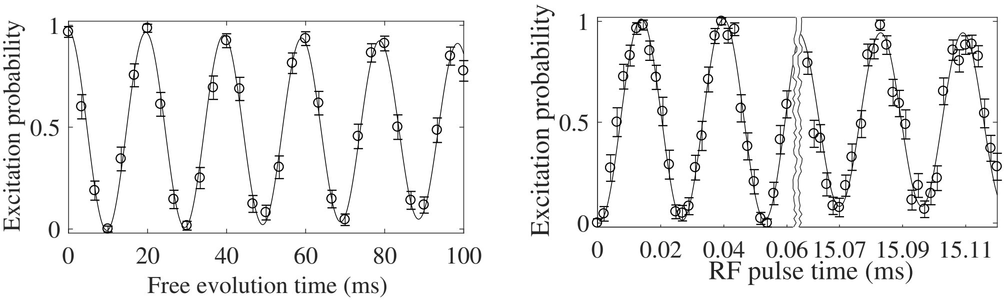

**(a)** Ramsey oscillation

**(b)** Rabi oscillation

**Figure 6.4: Ramsey and Rabi oscillations on the magnetic field-insensitive $\pi$-transition.** (a) Ramsey oscillations on the magnetic field-insensitive transition. The error bars represent statistical errors within one standard deviation for 80 repetitions. At the time for a CNOT gate of approximately 5 ms, the Ramsey oscillation contrast is above 0.99. (b) Rabi oscillations on the magnetic field-insensitive transition, measured in two windows separated by 15 ms. The error bars represent statistical errors within one standard deviation for 65 repetitions. At the time for a CNOT gate of approximately 5 ms, the Rabi oscillation contrast is at 0.95. These results indicate that the coherent RF generation system is not the cause of fast dephasing of the magnetic field-sensitive qubit.

Qubits are operated using RF pulses to coherently drive the hyperfine transition. The RF source is investigated as one of the possible sources of dephasing. The RF radiation is generated by a chain of frequency components, as described in section 3.4. When the generating RF pulse has insufficient phase stability, fast dephasing of qubits would result. We can test the RF generation by observing the magnetic field-insensitive $\pi$-transition ($|^2\mathrm{S}_{1/2}\,(F = 0)\,\rangle \leftrightarrow |^2\mathrm{S}_{1/2}\,(F = 1, m_F = 0)\,\rangle$). A Ramsey measurement is obtained with the $\pi$-transition and provides a coherence time of greater than 200 ms; see Fig. 6.4a. This coherence time is more than three orders of magnitude longer than the 0.2(1) ms determined for the $\sigma^+$-transition. Moreover, a Rabi oscillation is observed with a contrast of greater than 87 % for a duration longer than 15 ms; see Fig. 6.4b. We conclude that the RF generating source is not the cause of dephasing, as the same RF system is employed whether qubits are encoded by the $\pi$-transition or the $\sigma^+$-transition.

Furthermore, during coherent qubit manipulation, which is normally achieved solely with RF pulses, there is the possibility of stray laser light (or leakage light) being present at the ions' location because of an incompletely blocked detection laser. The leakage light can cause light-induced decoherence [108]. However, the coherence of the Ramsey oscillation of the $\pi$-transition is measured to be greater than 200 ms, as mentioned earlier, indicating that the leakage light is not our concern on the time scale of a few milliseconds. Conversely, the leakage light becomes crucial when the coherent control time reaches the second or minute scale [37]. On this time scale, the leakage light can be completely removed by a mechanical shutter.

## 6.3 Fluctuation of Magnetic Field

Here, the noise caused by the fluctuation of magnetic fields is discussed. Because of the ions' environment, the possible noise sources are the magnets for the magnetic-field gradient, the coils for the magnetic field offset for the Zeeman splitting, and unknown sources.

The total magnetic field in the area of ion confinement is produced by a pair of permanent magnets mounted on the end cap electrodes, see Fig. 3.2 in section 3.2; three pairs of Helmholtz coils mounted around the vacuum recipient; and other interfering devices in the neighborhood. In this section, the discussion is of possible causes of fast dephasing resulting from the magnetic field noise.

The Helmholtz coils provide offset fields to lift the degeneracy of hyperfine ground state $|^2\mathrm{S}_{1/2}\,(\mathrm{F}{=}1)\rangle$ to define the quantization axis of the transitions. The magnetic field of the Helmholtz coils also compensates for earth's magnetic field and the magnetic field caused by the vacuum pump (the ion getter pump). The ion getter pump generates several hundred microteslas in the ion confinement area. The Helmholtz coils can generate magnetic field noise when there is a fluctuation in the applied current. The coil pair, which generates the magnetic field along the quantization axis (or $z$-axis), has a field proportional to the applied current of $1788\,\mu\mathrm{T/A}$ by design [83]. The coil pairs perpendicular to the optical table ($x$-axis) and along the optical viewport ($y$-axis) have a field proportional to the applied current of $300\,\mu\mathrm{T/A}$ and $596\,\mu\mathrm{T/A}$, respectively. To investigate the possible influence of coils on the qubit coherence, the $z$-axis coil pair were not supplied with current, while the other two coil pairs for the perpendicular directions still received current to compensate for the perpendicular fields. In this scenario, the magnetic field along the quantization axis at the ion confinement area is caused by the cylindrical permanent magnets and the ion pump. Let $B_z$ is the magnetic field along the trap axis, and $B_\perp$ is the magnetic field perpendicular to the trap axis. Then, the total magnetic field can be expressed as

$$\begin{aligned} B =& \sqrt{B_z^2 + B_\perp^2} \\ =& B_z\sqrt{1+\left(\frac{B_\perp}{B_z}\right)^2}. \end{aligned} \tag{6.1}$$

The current stability is better than 0.25 mA, which means that the possible influence is on the order of a few hundred nanoteslas. Because $B_\perp \ll B_z$, $B_\perp$ is on the order of a few hundred nanoteslas and $B_z$ is on the order of several hundred microteslas, the

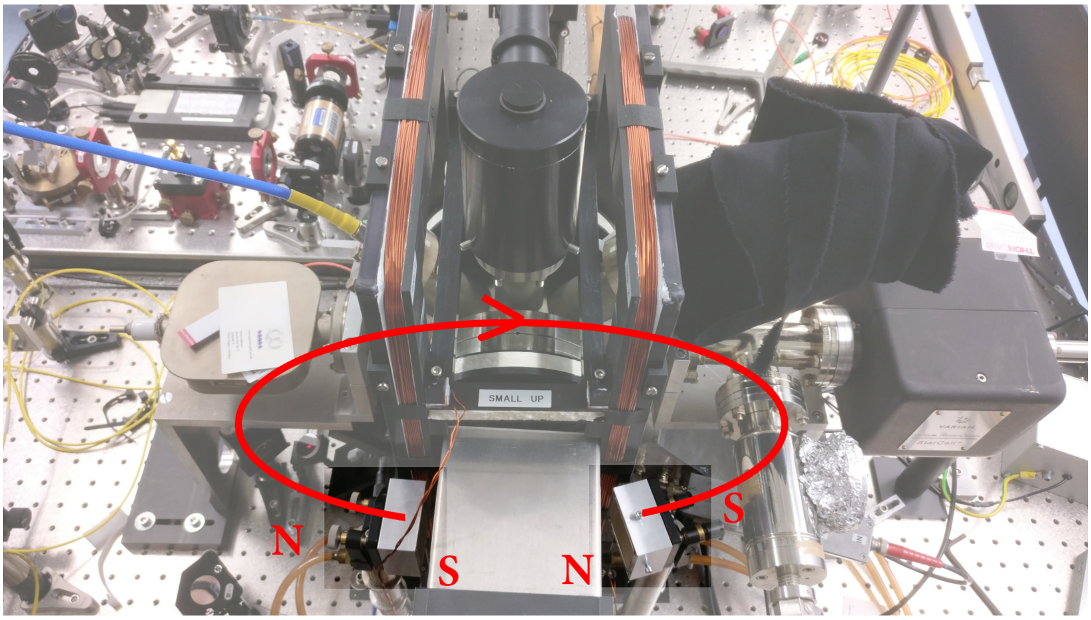

**Figure 6.5: Installation of two permanent magnets.** Instead of generating a magnetic field from the Helmholtz coils, an offset field can be generated by these magnets. They are made of Neodymium (grade N42). Each magnet has dimensions of $40 \times 40 \times 20\,\mathrm{mm}^3$. The field magnitude is verified by the addressing frequency of a single ion. The coherence time is again investigated, and no significant change is observed.

total magnetic field can be approximated as

$$B \approx B_z \left[ 1 + \frac{1}{2} \left( \frac{B_\perp}{B_z} \right)^2 \right]. \tag{6.2}$$

In this configuration, the fluctuations of the perpendicular coils are several orders of magnitude smaller; hence, the magnetic field in the ion confinement area is almost independent of the current fluctuations of the coils. The coherence time is investigated, as in Fig. 6.1, and no significant change is observed. Thus, it is concluded that the Helmholtz coils are not the cause of fast dephasing. It may be noted that the current drivers of the Helmholtz coils are also compared between the in-house-made devices and a commercial device (Toellner TOE 8733-2)

To further discard the magnetic field along the $z$-axis while keeping a comparable offset field, two permanent magnets are installed to replace the Helmholtz coils along this direction, as shown in Fig. 6.5. The coherence time is again investigated, as in Fig. 6.1, and no significant change is observed.

Another possibility as a source of magnetic field fluctuation is all of the neighboring laboratory electrical equipment. The existing magnetic field noise in the vicinity

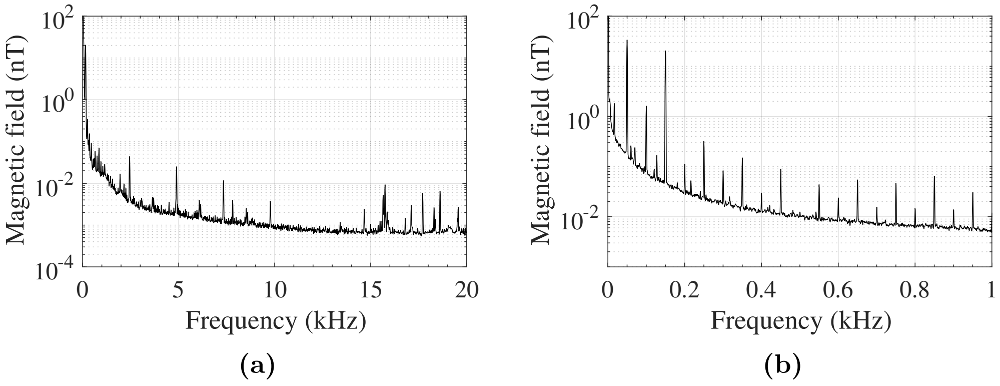

**Figure 6.6: Magnetic field noise spectrum along the quantization axis [113].** The magnetic field is probed using a compensation coil along the quantization axis. The spectra are averaged internally using a spectrum analyzer (Advantest R9211B) for 100 repetitions. (a) The noise spectrum is measured up to 20 kHz. (b) The noise spectrum is focused up to 1 kHz. The harmonics of 50 Hz are the main contributions.

of the vacuum recipient is investigated by probing the noise spectrum with different magnetic-field sensors. For more details, see Ref. [113]. The significant noise components were observed at 50 Hz and its harmonics, see Fig. 6.6, with a strength below 0.1 µT. To counteract these noise components, together with other ambient magnetic fields, an active magnetic field stabilization system is designed and employed in this experiment. Specific details of this system are given in section 3.9. The magnetic field generated by the active stabilization system is homogeneous over a few tens of centimeters because of the large dimensions of the Helmholtz configuration coils. The dominating frequency components can be suppressed by 25 to 30 dB; see Fig. 3.13. Using Ramsey measurements with a spin echo pulse similar to Fig. 6.1b, the coherence time $T_2^{SE}$, considered to be the time for the excitation probability to drop to 0.5, is improved by a factor of approximately three, as shown in Fig. 6.7. Nevertheless, the coherence time (without the spin echo pulse) $T_2^*$ remains the same as that observed by Ramsey oscillations, regardless of whether the active magnetic field stabilization system is used or not. One reason for this may be that the magnetic sensor, which is a probe of the stabilization system, may perceive different magnetic fields compared with the ion confinement area. There are some signals that could not be compensated. Currently, the magnetic sensor cannot be placed inside the vacuum chamber, which would require opening up the vacuum chamber. For this reason, the stabilization system cannot compensate for all magnetic fields experienced by ions. Therefore, it can be stated that the various sources causing the 50-Hz noise component and its harmonics are not the cause of fast dephasing when the trigger to the power grid is appropriately applied.

Another potential cause of dephasing is the permanent magnets themselves. These permanent magnets provide a magnetic-field gradient to induce spin-spin coupling.

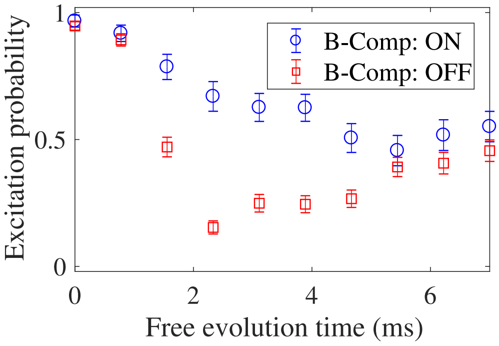

**Figure 6.7: Ramsey measurement with active magnetic field stabilization.** Ramsey measurements are observed with a spin echo pulse, similar to Fig. 6.1b. The measurement is performed once with active magnetic field stabilization, denoted 'B-Comp: ON', and once again without active compensation, denoted 'B-Comp: OFF'. The coherence time $T_2^{SE}$, considered to be the time for the excitation probability to drop to 0.5, is improved by a factor of approximately three. The error bars represent statistical errors within one standard deviation for 120 repetitions.

They are located close to the trapped ions ($\approx$ 5.7 mm). The magnets are hollow cylinders mounted on the endcap electrodes of the trap. They stay on the endcap electrodes without any rigid fixing. It is therefore possible that the magnets vibrate relative to the endcap electrodes. This results in the motion of ions in the magnetic-field gradient, and the small fluctuations originating from them may not be detected by the magnetic field sensor outside the vacuum recipient. If the two magnets oscillate with an amplitude of 10 nm, the change in the magnetic field in the gradient is 0.19 µT, which corresponds to an addressing frequency shift of 2.7 kHz. Therefore, vibrations with a frequency of a few hundred hertz to a few hundred kilohertz can potentially lead to dephasing.

Additionally, the permanent magnets can have their own noise as a possible cause of dephasing. For a magnetic material, when the temperature is not at absolute zero, there is fluctuation of magnetization of the domains, which can be considered magnetic noise. As the temperature of permanent magnets increases, so does the noise, before they become demagnetized. Because we have a power of approximately 16 W applied to the trap RF electrodes, it is likely that the magnets become hot, as mentioned in Ref. [159]. In a vacuum recipient, black body radiation is an only way to reduce the heat, which is why the temperature of trap electrodes can be substantially high (>370 K [159]). Obviously, this temperature can also be coupled to the permanent magnets on the nearby endcap electrodes. Because of the rising temperature, the magnetization of the domains could be fluctuate more, which is potentially a cause of dephasing. So far, to my knowledge, there has been no experimental study regarding the temperature dependency of the near-field fluctuation from magnetic materials. Recently, other groups have demonstrated that changing the materials of trap electrodes and mounting systems can reduce the trap temperature by an order of magnitude, which is in the room-temperature regime [159]. The materials are changed from stainless steel and macor to titanium and sapphire, respectively. Such a change may help reduce the noise from permanent magnets.

## 6.4 Fluctuation of Electric Field

In what follows, the noise from the fluctuation of electric fields is discussed. The possible sources include all electrodes near the ion confinement area, the shift in the ion's position resulting from charging by the UV laser, and the ion's micromotion.

In a Paul trap, the ions are confined using static and dynamic electric fields; see sections 2.2 and 3.2. Ions are charged particles experiencing a force from any electric field $\mathbf{E}$ as $\mathbf{F} = q\mathbf{E}$, where $q$ denotes the charge of the ion. Additional electric fields will generally change the equilibrium position of an ion in the trapping potential. Any change in position in the existing magnetic-field gradient effectively results in a change in the magnetic field experienced by the ion, thus causing dephasing. Moreover, noise components with frequencies near the axial and radial trap frequencies have been demonstrated to have the greatest impact on the motion of ions [122, 150]. These frequency components can excite harmonic motion of the ions. This in turn is counteracted by cooling. Therefore, this excitation would be evident as a change in coherence time when changing the cooling. This means that noise components in the frequency range of 110 to 130 kHz and 500 to 600 kHz can be a potential cause of dephasing. This noise could come from any electrode in the trap, which includes the endcap electrodes, trap RF electrodes, and compensation electrodes.

To characterize the electric field fluctuations that lead to a change in ion position, the heating rate of a single ion is measured, as explained in section 5.4. Here, an ion is cooled by RF sideband cooling and then left alone, without any cooling mechanism. During the time without cooling, electric field fluctuations lead to random movement of the ion. Thus, the ion becomes hot. By diagnosing the motional excitation level, the heating rate is obtained. In a previous work [54], the heating rate was initially determined to be $1.4(3)\,\mathrm{ms}^{-1}$ at the axial trap frequency of $2\pi \cdot 124\,\mathrm{kHz}$. Then, low pass RC filters with a cut-off frequency of 1.25 Hz were installed to passively filter the DC potentials applied to the endcap electrodes, together with better ground connections for neighboring power supplies, thereby reducing the heating rate to $0.13(2)\,\mathrm{ms}^{-1}$ at the axial trap frequency of $2\pi \cdot 122.984\,\mathrm{kHz}$ for a single-ion system; see section 5.4 and Ref. [56]. The heating rate is improved by an order of magnitude; however, the improvement does not result in an enhancement of coherence time. Therefore, this would likely mean that on the $\frac{1}{1.25\,\mathrm{Hz}}$ timescale, the electric field noise of the DC potential electrodes could be a cause of dephasing.

Another source of time-varying electric fields is the cooling laser duty cycle, discussed in Ref. [96, appendix G]. The cooling laser, which is a UV laser, can charge the exposed electrodes because of the photoelectric effect. The electrostatic charge on the electrodes results in the displacement of ions. The ions can experience a magnetic field shift because of this movement. The drift rate was on the order of 10 kHz/min in Ref. [96]. Recently, we found from our previous laser alignment that the lasers

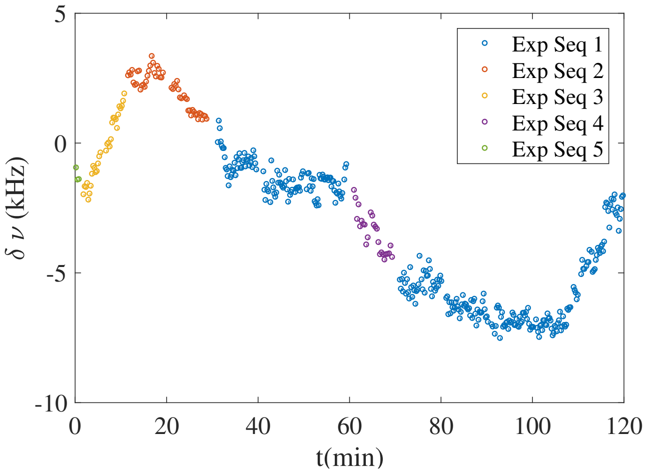

**Figure 6.8: Relative addressing frequency of the magnetic field-sensitive transition of an ion of a four-ion crystal.** The addressing frequencies are relative to the first measured addressing frequency. Over two hours, several coherent experimental sequences are measured. The sequences are (i) state preparation and detection measurement, (ii) Rabi oscillation measurement on an ion of a four-ion crystal, (iii) Rabi oscillation measurement on three ions of a four-ion crystal, (iv) two-qubit Bell-state creation, and (v) Ramsey measurement on an ion of a four-ion crystal. There is no observed jump in the addressing frequencies between different coherent sequences. The error bars, too small to be seen, represent statistical errors within one standard deviation for 75 repetitions.

were hitting the trap RF electrodes, resulting in high background photon counts. The photon count rate could be up to several thousand counts per second (sometimes up to ten thousand counts per second), as observed with a beam splitter before a photomultiplier tube. Hence, after improving the alignment, the fluctuation amplitude of the addressing frequency is less than 10 kHz over two hours, see Fig. 6.8 and Ref [112], while it was approximately 50 kHz over an hour in the past [96, appendix G].

In a Paul trap, ions can have unwanted movement because of micromotion. This movement lets ions experience a magnetic field shift because of the trapping magnetic field. In an ideal linear Paul trap, it occurs perpendicular to the trapping axis. According to the Gauss law of magnetism in Maxwell's equations,

$$\overrightarrow{\nabla} \cdot \boldsymbol{B} = \partial_x B_x + \partial_y B_y + \partial_z B_z = 0, \tag{6.3}$$

the magnetic-field gradient along the trap axis ($\partial_z B_z \neq 0$) also leads to a gradient along the perpendicular axis. The gradient perpendicular to the trap axis is half of the gradient along the trap axis because of symmetry. For this reason, the micromotion effectively leads to a change in the magnetic field experienced by the ions. The micromotion frequency corresponds to the frequency of $2\pi \cdot 18.9\,\text{MHz}$ of the RF trap drive. The changing magnitude is proportional to the amplitude of micromotion in the

**Figure 6.9: Ramsey contrast and micromotion amplitude vs. applied voltage on the "RF-side" compensation electrode.** The electrode distance to the ion position is approximately 18.4 mm [83]. The contrast in the Ramsey fringe remains unchanged over a voltage range of approximately 40 V. However, a clear optimum voltage resulting in the lowest micromotion can be found.

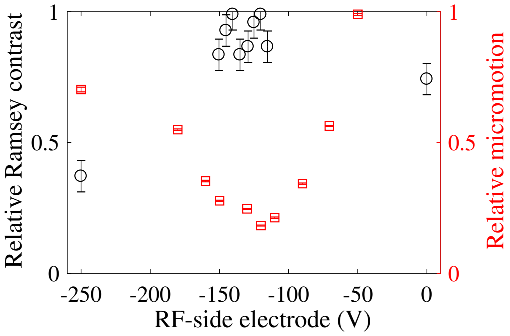

magnetic-field gradient. In addition, we do not have an ideal Paul trap, which means there could be additional axial micromotion. The influence of micromotion on the coherence time is also investigated. The micromotion can be measured by recording the arrival times of photons on a photo-multiplier using a time-to-digital converter (TDC)[2]. The procedure to measure the micromotion is described in Ref. [83]. By moving the ion position using a DC potential applied to a compensation electrode (RF-side), Ramsey-type measurement with a spin echo pulse is observed. The free evolution time is kept fixed at 2.0 ms. The contrast in a Ramsey fringe is normalized to maximum when the micromotion is minimized, as shown in Fig. 6.9. It turns out that the observed variation of the contrast is comparable with a constant value considering the error bars over a voltage range of 40 V, while the micromotion amplitude is exactly a clear minimum at a voltage of $-120$ V.

To further exclude micromotion as the cause of fast dephasing, a synchronization trigger circuit is developed to synchronize with the RF trap drive frequency ($2\pi \cdot 18.9$ MHz); more details can be found in Ref. [56]. This synchronization using a trigger circuit works similar to the 50-Hz synchronization of the laboratory power grid. This synchronization trigger circuit allows us to synchronize the trap drive and the laboratory power grid, simultaneously. The synchronization diagram is shown in Fig. 6.10. Instead of immediately starting the experimental sequence, the circuit waits for the rising edge of a signal that is synchronized with the trap drive. Thus, each experimental sequence is synchronized with the RF trap drive and the power grid. The 50-Hz synchronization can be shifted by a maximum of 53 ns, in which the 50-Hz synchronization is still effective because the period of the power grid is 20 ms. Observation of the coherence time remains unchanged. For these reasons, micromotion can be discarded as the cause of dephasing.

---

[2] Fast Com Tec GmbH P7888 PCI TDC unit

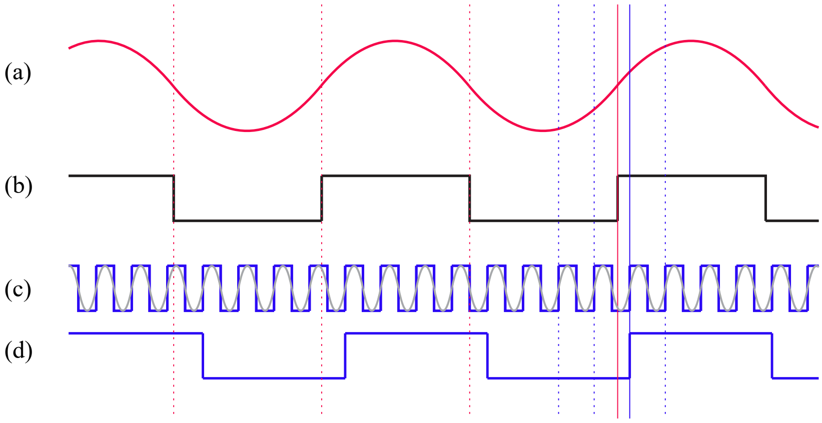

**Figure 6.10: A not-to-scale synchronization signal diagram** [56]. (a) The 50-Hz signal of the laboratory power grid is shown as a sine curve. (b) The original trigger circuit card provides the corresponding TTL signal of the power grid signal. (c) This is a similar circuit to (b) but for an RF trap drive frequency of $2\pi \cdot 18.9\,\mathrm{MHz}$. The synchronization signal, as a TTL signal, waits for the rising edge of the trap drive frequency after receiving the trigger from the power grid. Then, the last signal is used to start the experimental sequence, allowing both synchronizations.

## 6.5 Ion Localization

The spatial wave function of a trapped ion can be described by the quantum harmonic oscillator model. The delocalization of an ion in a magnetic-field gradient leading to a drift in the qubit resonances may explain fast dephasing. The delocalization is measured by the expansion of the wave function, quantified by the width of the wave function. The spatial wave function as a function of coordinate $z$ is generally described by [173]

$$\psi_n(z) = (2^n n!)^{-1/2} \left(\frac{m\omega_z}{\pi\hbar}\right)^{1/4} \exp\left(-\left(\sqrt{\frac{m\omega_z}{\hbar}}z\right)^2/2\right) H_n\left(\sqrt{\frac{m\omega_z}{\hbar}}z\right), \tag{6.4}$$

where $H_n(\xi)$ represents a Hermite polynomial of order $n$ and $n$ denotes the oscillator excitation. The motional excitation of an ion in the pseudopotential can be described by a thermal distribution,

$$p_n(n) = \frac{1}{\langle n\rangle + 1}\left(\frac{\langle n\rangle}{\langle n\rangle + 1}\right)^n, \tag{6.5}$$

where $\langle n\rangle$ denotes the average motional excitation level. Fig. 6.11 shows the localization probabilities for different average motional excitations of 0, 1, 10, and 100 phonons. The calculation uses an axial trap frequency of $2\pi \cdot 122.984\,\mathrm{kHz}$. It is obvious that a lower thermally excited ion is more localized than a highly thermally excited

**Figure 6.11: Localization probability of a thermally excited ion in a quantum mechanical harmonic oscillator potential.** An average excitation of 0, 1, 10, or 100 phonons is shown. The potential is characterized by an axial trap frequency of $2\pi \cdot 122.984\,\text{kHz}$. The localization of cooler ions is much narrower.

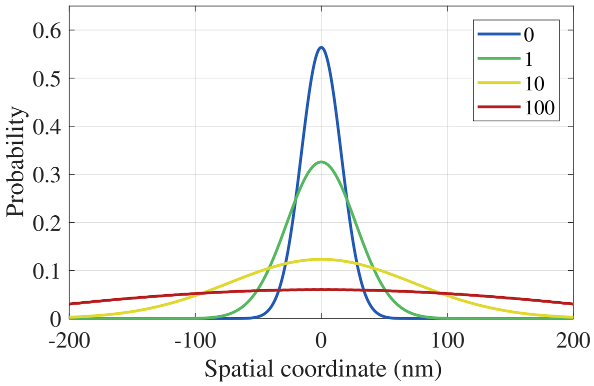

ion. To investigate whether the temperature of trapped ions affects the coherence time, an experiment is performed, as shown in section 5.4. A single ion is either cooled to the Doppler limit ($\langle n \rangle = 91$) or close to the motional ground state ($\langle n \rangle = 0.30$), after which the Ramsey experiment is performed to observe the coherence time. There is no significant change in coherence time observed from the result of near-ground state cooling. This result is expected because the location of the center of mass of an ion is independent of motional excitation; therefore, there is no change in its addressing frequency. It can be concluded as expected that the ion localization is not the cause of fast dephasing.

## 6.6 Summary of Investigations and Open Questions

From the investigation of qubit dephasing, the RF generation system for qubit coherent control, the light-induced decoherence, and the Zeeman splitting magnetic field generated by either the Helmholtz coils or the permanent magnets (N42) can be completely ruled out as possible sources of dephasing. Furthermore, unknown sources of magnetic noise up to 700 Hz can be compensated for using active magnetic field stabilization. However, it is not possible to place the current magnetic sensor inside the vacuum chamber where ions are located. The active stabilization might not compensate for the exact same field experienced by ions for this reason. Micromotion compensation and passive filtering of DC potentials lowered the heating rate and thereby improved the general stability of the experiment, but not as a dephasing source. The coherence time is also similar when an ion is cooled close to the motional ground state. It is important to note that a very similar experimental apparatus without a strong magnetic-field gradient exhibits a significantly longer coherence time [171]. This indicates that there might be a correlation between coherence time and the ion's motion in the magnetic-field gradient, which has not yet been fully explored.

The suspicion about the vibration of the permanent magnets (SmCo28), used for generating the magnetic-field gradient, still needs to be investigated. It is possible to do so when we need to open the vacuum recipient. We should redesign the trap to be able to mount the permanent magnets rigidly to avoid relative motion between trap electrodes and magnets.

The randomness of the magnetization of magnetic material resulting from the temperature is also an open question. We can study the magnetic material temperature and its effect on the qubit coherence time. Moreover, changing the material of the trap, as discussed in section 5.6, is likely to improve the electrodes' temperature, which might reduce the randomness of the magnetization and improve the qubit coherence time.

When multiple ions are manipulated to perform a quantum gate, two or more frequencies are used simultaneously. The ions will be affected by the addressing frequencies of their neighborhood, which are shifted by approximately a few megahertz. In this case, ions would experience an AC-stark shift, resulting in a systematic error in the detuning of the addressing frequencies. We should investigate this matter in the future. This effect could be one of the limitations of our quantum gate fidelity.

# 7

# Investigation of Two-Qubit Gates

A two-qubit controlled-NOT gate is an elementary gate for quantum algorithms [168]. To perform a complex quantum algorithm, we must have good two-qubit gates because, in general, a quantum algorithm requires a large number of high-fidelity two-qubit gates to be able to perform real-world operations. This also applies to preparing multi-partite entangled states. Thus, the infidelity of these quantum gates limits the number of coherent operations. In our MAGIC scheme, the two-qubit entangled gate between two nearest neighbors had a fidelity of 0.63(3) [83], which could be achieved with the help of dynamical decoupling (DD) pulse sequences. However, the qubit coherence time extended using DD sequences was still too short compared with the two-qubit gate time, by more than an order of magnitude. The previous achievement was just barely enough to prove the existence of quantum entanglement but not to perform a complicated quantum algorithm. In this chapter, the improved fidelity of the two-qubit gate is shown. The limitations associated with the use of dynamical decoupling pulse sequences is also considered here.

## 7.1 Two-Ion Measurement Methods

### 7.1.1 *J*-Coupling Measurement

From the Hamiltonian in equation (2.46), the time evolution operator in a rotating frame with an RF field is described by

$$U_{zz}(t) = e^{J_{kl} t \sigma_z^{(k)} \sigma_z^{(l)}/2}. \tag{7.1}$$

The $J$-coupling measurement technique is fully explained in Ref. [96], which also covers systems with more than two qubits. For a two-ion system, $J_{12}$ can be determined by a Ramsey-type measurement, as shown in Fig. 7.1. Two Doppler-cooled ions are further cooled by sideband cooling and then initialized in the state $|0\rangle^{(1)}|0\rangle^{(2)}$. One of the ions is prepared in a superposition state by a $\pi/2$-pulse at the respective resonance frequency. At the same time, the other ion, acting as a control qubit, is either left in the state $|0\rangle$ or prepared in the state $|1\rangle$ by a $\pi$-pulse. Then, the qubits evolve according

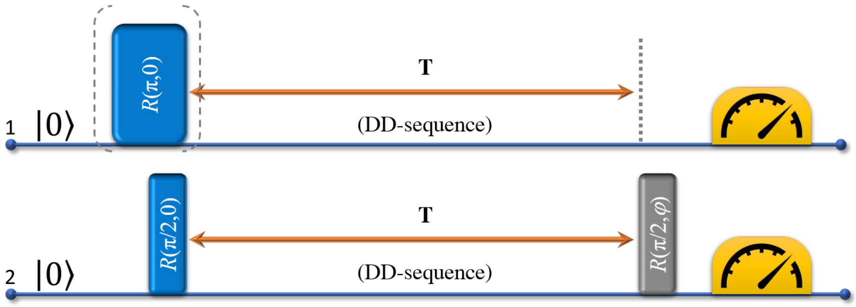

**Figure 7.1: The experimental sequence of a $J$-coupling experiment.** A superposition state for qubit 2 is initialized by a $\pi/2$-pulse from the state $|0\rangle$. Qubit 1 is either left in the state $|0\rangle$ or prepared in the state $|1\rangle$ by a $\pi$-pulse. During a conditional evolution time $T$, qubit 2 evolves according to equation (7.1). Each qubit is also protected by a DD sequence applied simultaneously. Another $\pi/2$-pulse is applied to qubit 2 with the varying phase $\varphi$. The Ramsey fringe can be observed, and the $J$-coupling can be deduced from the obtained phase via $\Delta\varphi = |J\tau|$.

to equation (7.1) for an evolution time $\tau$. That is, the ion in the superposition state will precess, conditioned on the state of the other ion, whereas the ion in either the $|0\rangle$ or $|1\rangle$ state will not change its state. During this evolution time, both ions can be protected against noise using a DD sequence applied to each ion simultaneously. Finally, a $\pi/2$-pulse with a varying phase is applied to the ion in the superposition to acquire Ramsey fringes. The obtained phase, conditioned on the state of the other ion for a given evolution time, can be used to deduce the $J$-coupling from $\Delta\varphi = |J\tau|$. The experimental results will be shown later; see Fig. 7.9.

### 7.1.2 Bell-State Generation

Before the Bell state $|\Phi^+\rangle$ can be realized, conditional dynamics for a two-qubit system must be performed. This is a CNOT gate, in which a target qubit is inverted only when the control qubit is in state $|1\rangle$. In the MAGIC scheme, the evolution operator from equation (7.1) can be rewritten as

$$U_{zz}(\vartheta) = e^{\vartheta\sigma_z^{(k)}\sigma_z^{(l)}/2}, \tag{7.2}$$

where $\vartheta = |J_{kl}t|$. Therefore, a two-qubit CNOT gate must fulfill the phase shift as [27]

$$\vartheta = |J_{12}\tau_{\text{CNOT}}| = \frac{\pi}{2} \qquad \Rightarrow \qquad \tau_{\text{CNOT}} = \frac{\pi}{2|J_{12}|}. \tag{7.3}$$

Thus, a CNOT gate ($U^{(1,2)}_{\mathrm{CNOT,AK}}$), where qubit 1 is a control qubit and qubit 2 is a target qubit, can be expressed as [27]

$$U^{(1,2)}_{\mathrm{CNOT,AK}} = R^{(2)}\left(\frac{\pi}{2},\frac{3\pi}{2}\right) U_{zz}\left(\frac{\pi}{2}\right) R^{(2)}\left(\frac{\pi}{2},0\right). \tag{7.4}$$

However, we cannot directly implement this expression, as the qubit coherence time does not exceed the gate time by orders of magnitude. Hence, a DD sequence with $N$ $\pi$-pulses is interleaved with the CNOT gate as

$$\begin{aligned} U^{(1,2)}_{\mathrm{CNOT,AK}} &= R^{(2)}\left(\frac{\pi}{2},\frac{3\pi}{2}\right) DD^{(1,2)} R^{(2)}\left(\frac{\pi}{2},0\right), && (7.5)\\ DD^{(1,2)} &= \left[U_{zz}\left(\frac{\pi}{4N}\right) R^{(1,2)}\left(\pi,\varphi_N\right)\cdots R^{(1,2)}\left(\pi,\varphi_2\right) U_{zz}\left(\frac{\pi}{2N}\right) R^{(1,2)}\left(\pi,\varphi_1\right) U_{zz}\left(\frac{\pi}{4N}\right)\right]^N. && (7.6) \end{aligned}$$

The CNOT gate in a two-ion system using the MAGIC scheme was first demonstrated in Ref. [27] and is discussed in detail in Ref. [83].

Even though the result for the two-state probabilities of the mentioned CNOT gate is correct as expected, the phase relation between two qubits is not correct, which can be seen from equation (7.4) (with a shifted global phase) as

$$\begin{aligned} U^{*(1,2)}_{\mathrm{CNOT}} &= \exp\left(-\mathrm{i}\frac{\pi}{4}\right) U^{(1,2)}_{\mathrm{CNOT,AK}}, && (7.7)\\ &= \begin{pmatrix} 1 & 0 & 0 & 0\\ 0 & -\mathrm{i} & 0 & 0\\ 0 & 0 & 0 & 1\\ 0 & 0 & +\mathrm{i} & 0 \end{pmatrix}. && (7.8) \end{aligned}$$

Here, the wrong phase relation between two qubits can be fixed by adding a rotation around the $z$-axis. Therefore, the correct implementation follows

$$\begin{aligned} U^{(1,2)}_{\mathrm{CNOT}} &= \mathrm{e}^{(-\mathrm{i}\pi/4)} R^{(2)}\left(\frac{\pi}{2},\frac{3\pi}{2}\right) R^{(2)}_z\left(\frac{-\pi}{2}\right) R^{(1)}_z\left(\frac{+\pi}{2}\right) U_{zz}\left(\frac{\pi}{2}\right) R^{(2)}\left(\frac{\pi}{2},\frac{\pi}{2}\right), && (7.9)\\ &= \mathrm{e}^{(-\mathrm{i}\pi/4)} \bar{Y}^{(2)} R^{(2)}_z\left(\frac{-\pi}{2}\right) R^{(1)}_z\left(\frac{+\pi}{2}\right) U_{zz}\left(\frac{\pi}{2}\right) Y^{(2)}, && (7.10)\\ &= \begin{pmatrix} 1 & 0 & 0 & 0\\ 0 & 1 & 0 & 0\\ 0 & 0 & 0 & 1\\ 0 & 0 & 1 & 0 \end{pmatrix}. && (7.11) \end{aligned}$$

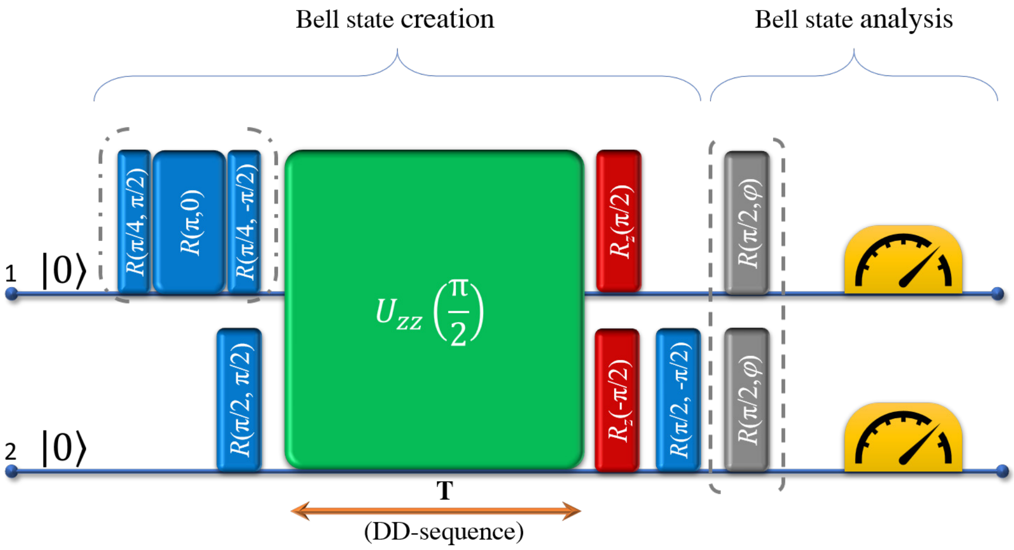

**Figure 7.2: The experimental sequence to create and characterize a Bell state in a two-qubit system.** Both qubits are initialized in the state $|00\rangle$. A Hadamard gate is applied to qubit 1, indicated by the RF pulses in the dot-dash parentheses. The rest of the sequence is the CNOT gate, as expressed in equation (7.9). During a conditional evolution time $T$, qubit 2 evolves according to equation (7.2). Each qubit is protected by a DD sequence applied simultaneously. Then, state-selective detection is performed. Here, the final state is expected to be $|00\rangle \xrightarrow{U_{\mathrm{Bell}}} 1/\sqrt{2}(|00\rangle + |11\rangle)$. In addition, the parity oscillation signal can be measured by adding another $\pi/2$-pulse applied to each qubit with a varying phase $\varphi$, denoted by gray pulses.

Then, the two-qubit Bell gate is expressed as

$$\begin{aligned} U_{\mathrm{Bell}} &= U^{(1,2)}_{\mathrm{CNOT}}\, U^{(1)}_{\mathrm{H}}, && (7.12)\\ &= \mathrm{e}^{(-\mathrm{i}\pi/4)} \bar{Y}^{(2)} R^{(2)}_z\left(\frac{-\pi}{2}\right) R^{(1)}_z\left(\frac{+\pi}{2}\right) U_{zz}\left(\frac{\pi}{2}\right) Y^{(2)}\, U^{(1)}_{\mathrm{H}}, && (7.13) \end{aligned}$$

where a Hadamard gate $U_{\mathrm{H}}$ is described in equation (2.11). This correction is important when the Bell gate or CNOT gate acts as a subroutine for another quantum algorithm.

The experimental scheme to prove the existence of a Bell state is shown in Fig. 7.2. The routines discussed before are thought to yield the state $|00\rangle \xrightarrow{U_{\mathrm{Bell}}} 1/\sqrt{2}(|00\rangle + |11\rangle)$, where state-selective detection is performed for each qubit. This results in the non-classical correlation of two-state probabilities on a computational basis, $P_{00}$, $P_{01}$, $P_{10}$, and $P_{11}$. The parity is given by [174]

$$\Pi_z = P_{00} + P_{11} - (P_{01} + P_{10}). \tag{7.14}$$

When another $\pi/2$-pulse with a varying phase $\varphi$ is applied to each qubit (depicted in gray in Fig. 7.2), this results in non-classical correlations on another basis. The parity oscillates as

$$\Pi(\varphi) = V\cos(2\varphi), \tag{7.15}$$

where $V$ represents the parity oscillation amplitude. Therefore, the Bell-state fidelity is calculated as [174]

$$F_{\text{Bell}} = \frac{\Pi_z + 1}{4} + \frac{V}{2}. \tag{7.16}$$

The experimental result will be shown in Fig. 7.11.

## 7.2 Coherent Operations and Dynamical Decoupling Pulses

When a DD pulse sequence is used in a coherent operation, the DD pulse sequence can act as a selective frequency filter. This is due to equidistant pulses as a characteristic of DD pulse sequences. This means if noise at certain frequencies matches at certain evolution times, then the contrast shows a reduction; see Fig. 7.3. The experiment is performed as a Ramsey experiment with the final $\pi/2$-pulse at the phase 0, in which the excitation probability is expected to be unity. On the magnetic field-insensitive transition ($\pi$-transition), the excitation probability of the Ramsey experiment, which interleaves the free evolution time with a KDD pulse sequence of 100 $\pi$-pulses, does not show a reduced probability. In contrast, the Ramsey experiment on the magnetic field-sensitive transition ($\sigma^+$-transition), interleaved with 10 sets of a UR-10 sequence (100 $\pi$-pulses), shows a significant reduction at 1.2 ms. In addition, the reduction does not depend on the DD sequence. DD sequences using CPMG-XY, CDD-3, KDD, and UR sequences have been tested, and there is always some reduction[1] when the experiment is performed on either the $\sigma^+$-transition or on the $\sigma^-$-transition.

To further investigate the reduced excitation probability, another Ramsey experiment with a fixed evolution time and varying phase of the final $\pi/2$-pulse is performed, as shown in Fig. 7.4. During the free evolution time, a DD pulse sequence is incorporated using 10 sets of a UR-10 sequence. Fig. 7.4a shows the reduction of the excitation probability in the Ramsey experiment at approximately 0.2 and 0.4 ms. Taking the evolution time of 0.3947 ms, where the excitation is reduced, to another Ramsey experiment, shown in Fig. 7.4b, the Ramsey experiment is measured by varying the phase of the final $\pi/2$-pulse. The Ramsey contrast vanishes. When an evolution time that

---

[1] The reduction is not always present at 1.2 ms, depending on the number of pulses applied in a DD sequence.

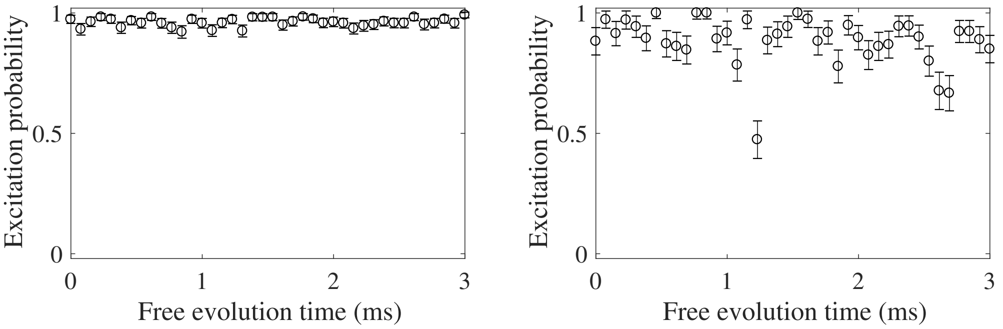

**(a)** $\pi$-transition **(b)** $\sigma^+$-transition

**Figure 7.3: Ramsey experiment using a single ion with DD pulses.** The Ramsey experiment has a final $\pi/2$-pulse with phase 0 to obtain the final population at the state $|1\rangle$. (a) The Ramsey experiment is performed on the magnetic field-insensitive transition ($\pi$-transition). During the free evolution time, the DD pulses are applied using the KDD sequence of 100 $\pi$-pulses. The Rabi frequency in this experiment is at $2\pi \cdot 77.58\,\text{kHz}$. The error bars represent statistical errors within one standard deviation for 150 repetitions. (b) The Ramsey experiment is performed on the magnetic field-sensitive transition ($\sigma^+$-transition) with 10 sets of a UR-10 sequence (100 $\pi$-pulses). The Rabi frequency in this experiment is at $2\pi \cdot 62.29\,\text{kHz}$. The error bars represent statistical errors within one standard deviation for 50 repetitions. Some magnetic field noise components cannot be compensated for, indicated by the reduction of the excitation probability.

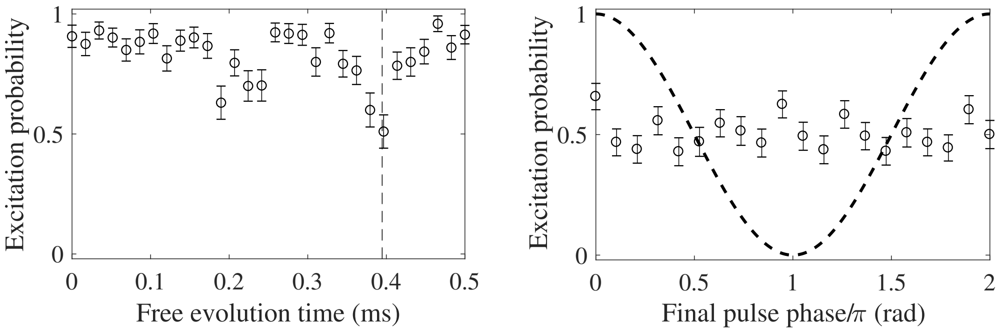

**(a)** **(b)**

**Figure 7.4: Ramsey experiment focusing on the evolution time of the reduced excitation probability.** (a) The Ramsey experiment is performed using 10 sets of a UR-10 pulse sequence. The Rabi frequency of $2\pi \cdot 60.22\,\text{kHz}$ is applied. The error bars represent statistical errors within one standard deviation for 75 repetitions. There are two significant reductions, at approximately 0.2 and 0.4 ms. The dashed line is marked at 0.3947 ms, where the excitation probability drops to 0.5. (b) The Ramsey experiment is measured using a final $\pi/2$-pulse with varying phase. In this experiment, the free evolution time is fixed at 0.3947 ms, in which 10 sets of a UR-10 pulse sequence are interleaved. The error bars represent statistical errors within one standard deviation for 100 repetitions. The dashed line corresponds to an expected fringe. Thus, this result indicates that the Ramsey oscillation is completely destroyed.

does not show a reduction is chosen, the Ramsey contrast with the varying phase is comparable to the excitation probability in Fig. 7.4a. This indicates a magnetic noise component corresponding to the time between $\pi$-pulses, which is responsible for the qubit dephasing.

The interpretation of information from the reduction of the Ramsey contrast can be described by a quantum metrology feature called a quantum lock-in amplifier. In the context of a quantum lock-in amplifier [170], the probe phase is mixed with an oscillating signal, assuming the probe is coupled both to a signal $S(t)$ and noise $N(t)$ by

$$H_{int} = M(t)\frac{\sigma_z}{2}, \tag{7.17}$$

where $M(t) = S(t) + N(t)$ and $\sigma_j$ represent the Pauli matrices. For a lock-in measurement, the signal is modulated as

$$S(t) = S_0 \cos\left(2\pi f_m + \varphi\right), \tag{7.18}$$

where $f_m$ is a frequency in noise $N(t)$ and $\varphi$ is a constant phase. When the probe phase is mixed with an oscillating signal, then

$$H = \frac{1}{2}\left(M(t)\sigma_z + \Omega(t)\sigma_y\right). \tag{7.19}$$

When $\Omega(t)$ is applied periodically and synchronized with the signal $S(t)$, then the phase is accumulated to coherently add up the signal. The random phase is also accumulated, but noise $N(t)$ is averaged away. The probe is prepared in a superposition using a $\pi/2$-pulse, which is characterized by the probability of finding the probe in the excited state $P_{|1\rangle}$ and the superposition relative phase $\phi_{lock-in}$. The quantum lock-in signal is measured at time $T$ by

$$\phi_{lock-in} = \frac{1}{\hbar}\int_0^T dt M(t)\cos\left(\frac{1}{\hbar}\int_0^t dt'\Omega(t')\right), \tag{7.20}$$

$$1 - P_{|1\rangle} = \frac{1}{\hbar}\int_0^T dt M(t)\sin\left(\frac{1}{\hbar}\int_0^t dt'\Omega(t')\right). \tag{7.21}$$

Here, $\hbar$ represents the reduced Planck's constant. A train of $N$ $\pi$-pulses with equidistant $\tau_{arm}$ is applied. Ideally,

$$\Omega(t) = \sum_{n=1}^{N}\delta(t - n\tau)\pi, \tag{7.22}$$

where $\delta(t)$ denotes the Dirac delta function; hence, the cosine term in equation (7.20) becomes a square waveform with a period of $2\tau_{arm}$, and the sine term in equation (7.21) vanishes. Thus, the measured signal is modulated by a frequency $f_m = 1/2\tau_{arm}$ and

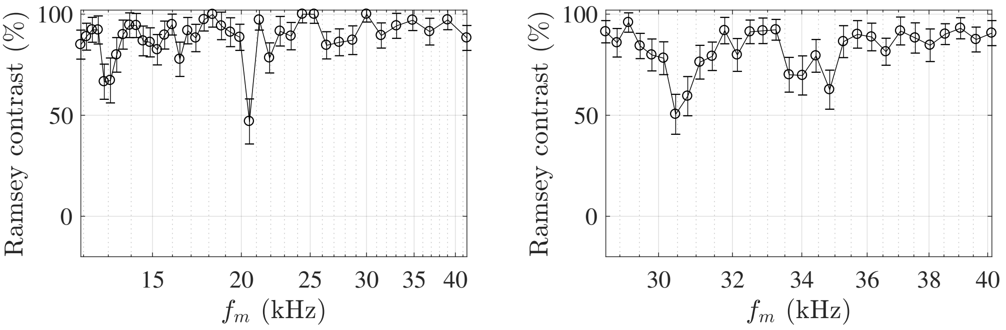

**(a)** **(b)**

**Figure 7.5: Ramsey contrast versus DD-pulse band-pass frequency.** (a) A replot of Fig. 7.3b in terms of the noise spectrum corresponding to the $\pi$-pulse interval in a DD sequence. The significant magnetic noise components are at 12.9 and 21.5 kHz. (b) A replot of Fig. 7.4a. The significant magnetic noise components are at 30.5 and $\sim$ 34 kHz. The lines are to guide the eye.

is in phase with the ion oscillation, $\varphi = 0$.

Generally, our Ramsey experiments are depicted by a plot of the excitation probability against the free evolution time, excluding the duration of RF pulses. From Fig. 7.3b, we correct the time of RF pulses and replot to the quantum lock-in signal, as shown in Fig. 7.5a. The Ramsey contrast reduction at 1.2 ms, as mentioned before, corresponds to the frequency component at 21.5 kHz. A replot of Fig. 7.4a is shown in Fig. 7.5b. The Ramsey contrast reduction at 0.3947 ms corresponds to the frequency component at 30.5 kHz. One might notice that even these two plots have some overlapping of measured frequencies, but Fig. 7.5a does not show the component of $\sim$ 30 kHz as in Fig. 7.5b. These two data sets were measured on two different days, which might be a reason for the different noise components. However, within a single day, we also obtain different noise components. Therefore, this indicates the noise environment changes over time.

To achieve good fidelity when realizing a two-qubit gate, we should consider the $\pi$-pulse interval and the width of a $\pi$-pulse to avoid the noise spectrum with respect to the two-qubit gate time. A straightforward way to accomplish this is using a two-qubit gate time, which corresponds to the $J$-coupling between two ions, and changing the number of pulses during a DD sequence. Furthermore, one might attempt to determine and eliminate those noise components to be able to perform better experiments.

## 7.3 Dynamical Decoupling Pulses and Composite Pulses

When a DD pulse sequence is applied, a single pulse infidelity can become a major concern. This is because there are a large number of $\pi$-pulses applied in a sequence, and errors can accumulate [99]. A practical method to improve a single pulse error for systematic error control is to apply composite pulses [175]. In this section, MATLAB numerical simulations are presented, assuming pulse length errors and qubit detuning frequency errors. The MATLAB scripts can be found in appendices D.2, D.3, and D.4.

The simulation is based on two experimental sequences: a Ramsey measurement and a Bell-state sequence. The examined pulse length errors are presented in terms of a relative pulse length error $\Delta L/L_0$. Similarly, the examined qubit detuning frequency errors are presented in term of a relative detuning with respect to a Rabi frequency $\delta/\Omega$. Here, the simulation is shown for both errors at 25 %. A typical pulse length error in the current setup is 0.15 %, and a typical detuning error is 0.8 %. Previously in [96], a typical pulse length error in the experimental setup was less than 5 %, and a typical detuning error was 20 %.

In a Ramsey measurement, as described in section 4.3.3, the simulation starts with a single qubit in the state $|0\rangle$. Then, the state is brought to $1/\sqrt{2}(|0\rangle + |1\rangle)$ by a $\pi/2$-pulse. At this point, the sequence either does nothing or takes a DD pulse sequence. Here, we provide an example of a DD pulse sequence of 10 sets of a UR-14 sequence, as mentioned in section 4.3.5. The ending pulse is also another $\pi/2$-pulse with a phase that can take the state population to unity. To overcome single pulse errors, composite pulses called "Broadband-1 pulse" (BB1) [176] are employed in the simulation. The BB1 sequence can replace an arbitrary pulse, making it less sensitive to pulse length error and detuning error.

The BB1 sequence consists of the error-correcting sequence $W$ as

$$W(\phi_0) = R(\pi,\phi_1 + \phi_0)R(2\pi,\phi_2 + \phi_0)R(\pi,\phi_1 + \phi_0). \tag{7.23}$$

Here, the phases of the single qubit rotation are chosen as

$$\phi_1 = \pm \arccos\left(-\frac{\theta}{4\pi}\right), \tag{7.24}$$

$$\phi_2 = 3\phi_1, \tag{7.25}$$

and $\phi_0$ represents the phase of the initial rotation. Therefore, the overall sequence follows

$$R^{BB1}(\theta,\phi_0) = R(\theta/2,\phi_0)W(\phi_0)R(\theta/2,\phi_0). \tag{7.26}$$

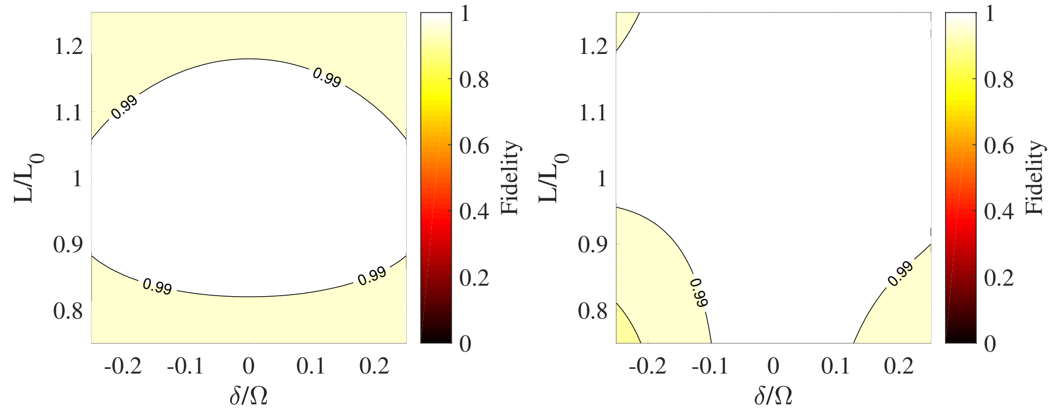

**(a)** rectangular $\frac{\pi}{2}$ pulse **(b)** BB1 $\frac{\pi}{2}$ pulse

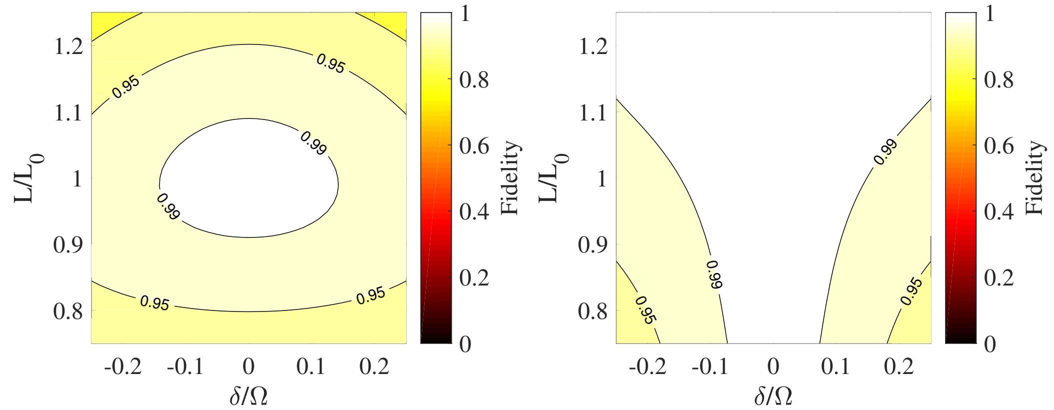

**(c)** rectangular $\pi$ pulse **(d)** BB1 $\pi$ pulse

**Figure 7.6: Numerical simulation of a single pulse with systematic control errors.** The contour plots show the single pulse fidelity expected for either a $\frac{\pi}{2}$ pulse or a $\pi$ pulse. $\Delta L/L_0$ denotes a relative pulse length error. $\delta/\Omega$ denotes a relative detuning with respect to the Rabi frequency. (a) A rectangular $\frac{\pi}{2}$ pulse. (b) A BB1 $\frac{\pi}{2}$ pulse. (c) A rectangular $\pi$ pulse. (d) A BB1 $\pi$ pulse. BB1 pulses show a broader area of 0.99 fidelity, including the pulse length error and the detuning error.

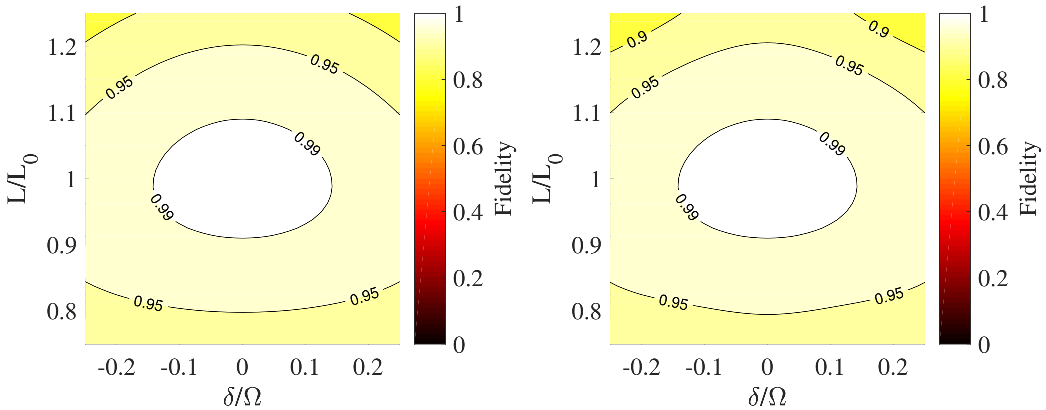

**(a)** Without any pulse

**(b)** DD pulse sequence

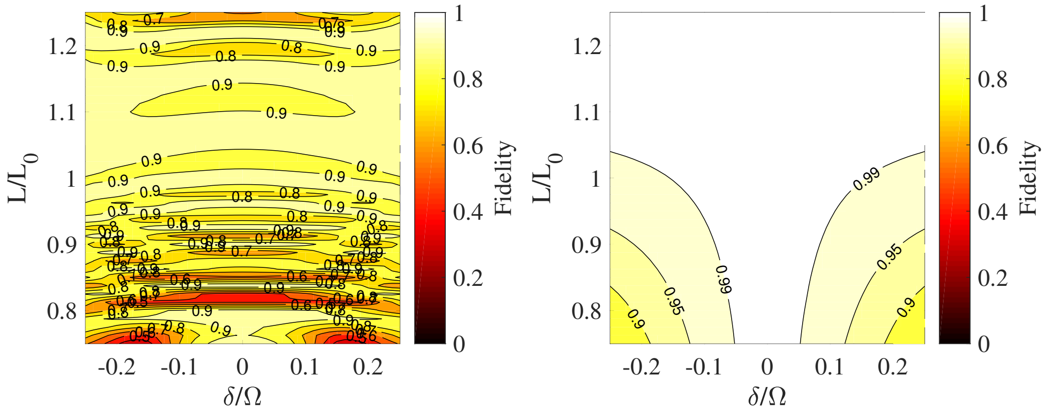

**(c)** All BB1 pulses

**(d)** BB1 pulses and a DD rectangular-pulse sequence

**Figure 7.7: Numerical simulation of a Ramsey experimental sequence with systematic control errors.** The contour plots show the simulated Ramsey experiment fidelity expected for the final state to be in the state $|1\rangle$. $\Delta L/L_0$ denotes a relative pulse length error. $\delta/\Omega$ denotes a relative detuning with respect to a Rabi frequency. Here, these simulations do not take the qubit dephasing into account to study the error contributions of the pulse length error and the detuning error. (a) There is no pulse during a free evolution time. (b) The UR-14 sequence is repeated 10 times as a DD pulse sequence during a free evolution time. The area of 0.99 fidelity is the same for (a) and (b). (c) All pulses as in (b) are replaced by composite pulses called BB1. The Ramsey experimental fidelity becomes more sensitive to the errors. (d) BB1 pulses are applied to the pulses that are not a part of the DD sequence, and the UR-14 sequence uses rectangular pulses. Here, the area of 0.99 fidelity is broadened in both errors.

The simulations of the single-pulse fidelity of either the $\frac{\pi}{2}$ pulse or $\pi$ pulse are shown in Fig. 7.6. When the BB1 sequence is employed, the pulse length error and the detuning error are less sensitive to both errors, as shown by the area of 0.99 fidelity.

Now, the composite pulses are applied to a Ramsey measurement sequence. In Fig. 7.7, the simulation results for Ramsey measurement sequences with/without a composite pulse sequence are shown. In this consideration, the qubit dephasing is not taken into account. Therefore, the error contributions are only the pulse length error and the detuning error. Fig. 7.7a and Fig. 7.7b show the Ramsey sequence fidelity plots with and without 10 sets of a UR-14 sequence, respectively. All pulses are still rectangular pulses. The fidelity plots between these two cases show similarity because the DD sequence does not change the error in the Ramsey sequence. In Fig. 7.7c, all pulses are replaced by BB1 pulses. The Ramsey sequence becomes more sensitive to both errors. The sequence fidelity can change markedly when the pulse length error is present. In the last case, shown in Fig. 7.7d, the BB1 sequence is only applied for the pulses that are not a part of the DD sequence, while the DD pulse sequence is still rectangular pulses. This method provides a benefit, which we can see by the larger area of 0.99 fidelity. Therefore, to directly apply the BB1 sequence to all coherent control pulses, it does not help to compensate for systematic errors such as the pulse length error and the detuning error. In contrast, the BB1 sequence can compensate for the errors when the composite pulses are not a part of the DD pulse sequence.

A Bell-state sequence, shown in Fig. 7.2, is also studied to understand the advantage of using composite pulses. The simulation results are shown in Fig. 7.8 for a Bell-state sequence with/without the BB1 sequence. In a method similar to the simulation of the Ramsey measurement, the qubit dephasing is not taken into account. Fig. 7.8a shows the Bell-state fidelity plot without any protection pulses and using only rectangular pulses. The fidelity is less sensitive to the pulse length error than to the detuning error. When 10 rectangular pulse sets of a UR-14 sequence are applied to the Bell-state sequence, shown in Fig. 7.8b, the fidelity plot does not change significantly. This result indicates that the DD pulse sequence does not change the error in the Bell-state sequence. In Fig. 7.8c, all pulses are replaced by BB1 pulses, which leads the Bell-state sequence to be more sensitive to both errors. In the last case, the BB1 sequence is removed from the DD pulse sequence; see Fig. 7.8d. The Bell-state sequence does not have any advantage, as shown in the similar case of the Ramsey experiment.

In summary, the composite pulse sequence does not always provide better error compensation in term of the systematic errors from the pulse length error and the detuning error. In particular, when it is applied to a dynamical decoupling pulse sequence, it can cause an experimental sequence to be more sensitive to pulse imperfections.

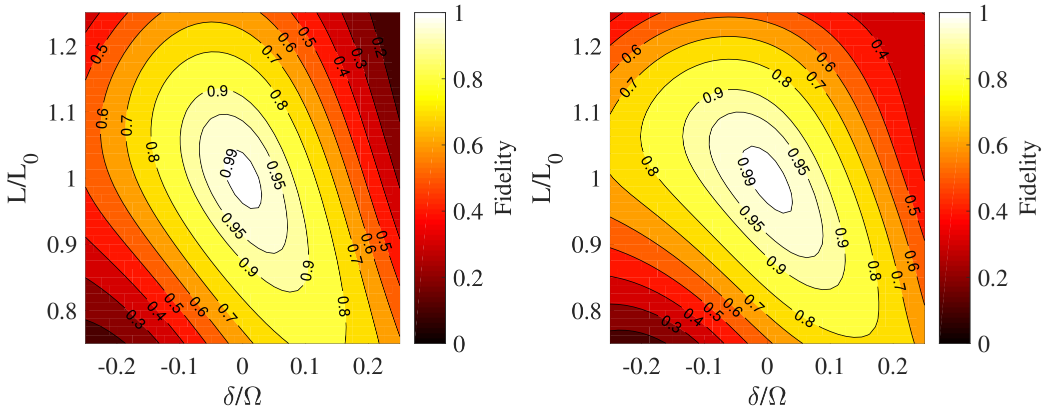

**(a)** Without any pulse **(b)** DD pulse sequence

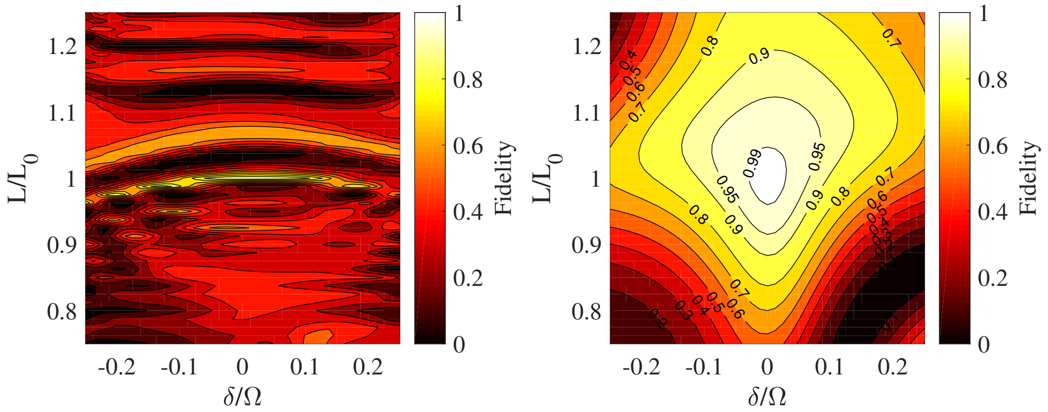

**(c)** All BB1 pulses **(d)** BB1 pulses and a DD rectangular-pulse sequence

**Figure 7.8: Numerical simulation of a Bell-state sequence with systematic control errors.** The contour plots show the Bell-state fidelity expected for the final state to be in the state $\frac{1}{\sqrt{2}}(|00\rangle + |11\rangle)$. $\Delta L/L_0$ denotes a relative pulse length error. $\delta/\Omega$ denotes a relative detuning with respect to the Rabi frequency. Here, these simulations do not take the qubit dephasing into account. (a) There is no pulse during a conditional evolution time. (b) The UR-14 sequence is repeated 10 times as a DD pulse sequence during a conditional evolution time. The area of 0.99 fidelity is approximately the same for (a) and (b). (c) All pulses in (b) are replaced by a BB1 sequence. The Bell-state fidelity becomes more sensitive to the errors. There are only small high-fidelity areas. (d) BB1 pulses are applied to all pulses that are not a part of the DD sequence, and the UR-14 sequence uses rectangular pulses. Here, the area of 0.99 fidelity is not significant compared with (a) and (b).

## 7.4 Two-Ion Coherent Dynamics

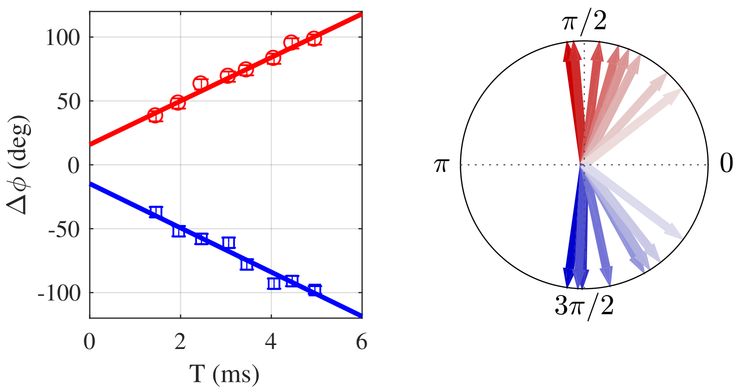

**Figure 7.9: $J$-coupling of a two-ion system.** The first ion acts as a control qubit, while the second ion acts as a target qubit. Each ion is protected simultaneously against dephasing by 10 sets of a UR-14 sequence. The RF powers are adjusted to have equal Rabi frequencies for the two ions. The axial trap frequency is $2\pi \cdot 122.99\,\mathrm{kHz}$. The plot on the left is the measured phase of the target qubit. The red data represent the control qubit in the state $|0\rangle$, and the blue data are for the state $|1\rangle$. The slopes of the linear fits show a $J$-coupling constant $J^{\text{two ions}}/2\pi = 48(2)\,\mathrm{Hz}$ corresponding to a CNOT gate time $\tau_{\mathrm{CNOT}}$ of $4.3(9)\,\mathrm{ms}$. The error bars represent statistical errors within one standard deviation for 60 repetitions. The right figure is for visualization of the measured phase of the target qubit in a phase diagram.

From section 7.2, the qubit cannot be protected completely because a DD pulse sequence can act as a band-pass filter, allowing magnetic noise to destroy coherent states. Now, the coupling constant for a two-ion system is remeasured while avoiding the noise components. The method to measure the coupling constant is described in section 7.1.1. Sideband cooling is also applied to keep the average phonon $\langle n \rangle < 10$. In Fig. 7.9, the plot shows the measured phase of the target qubit. Each ion is protected simultaneously against dephasing by 10 sets of a UR-14 sequence. The slopes of the linear fits show a $J$-coupling constant $J_{12}^{\text{two ions}}/2\pi = 48(2)\,\mathrm{Hz}$ corresponding to a CNOT gate time $\tau_{\mathrm{CNOT}}$ of $4.3(9)\,\mathrm{ms}$ at an axial trap frequency of $2\pi \cdot 122.99\,\mathrm{kHz}$. The $J$-coupling constant can be theoretically calculated by equation (2.47) as $J_{12}^{\text{Theory}}/2\pi = 44.85\,\mathrm{Hz}$ at a magnetic-field gradient of $19.105\,\mathrm{T/m}$. This means that our measurement is deviated by 1.6 standard deviations. The fit also shows offsets of the phase shift for both control states. The offsets are due to the use of the DD pulse sequence.

By obtaining the 2-ion $J$-coupling constant, the CNOT gate can be measured. The control qubit is prepared in either the state $|0\rangle_C$ or $|1\rangle_C$, and the target qubit is prepared in the state $|0\rangle_T$. The CNOT gate can be implemented as described in equation (7.9), where the second ion acts as the target qubit. The conditional evolution $U_{zz}(\frac{\pi}{2})$, corresponding to the CNOT gate time $\tau_{\mathrm{CNOT}}$ of $4.3(9)\,\mathrm{ms}$, is protected using

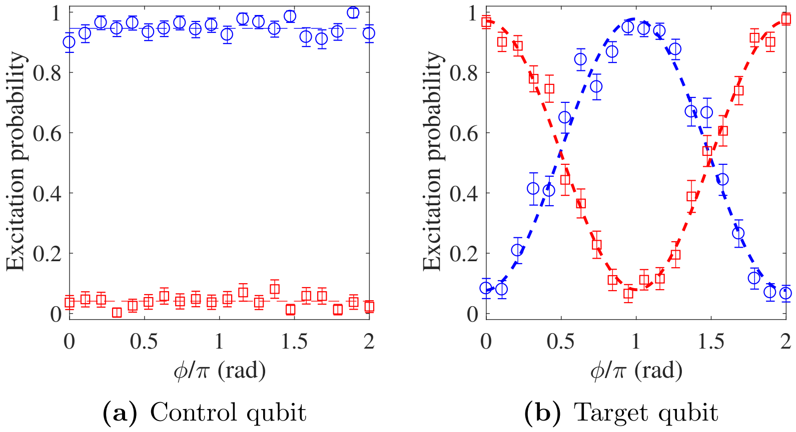

**(a)** Control qubit **(b)** Target qubit

**Figure 7.10: Measurement of the CNOT sequence of a two-ion system.** The implementation is according to equation (7.9) by preparing the control qubit in either the state $|0\rangle$ (red) or $|1\rangle$ (blue) and the target qubit in the state $|0\rangle$. Sideband cooling is applied for 80 ms in the center-of-mass mode. The conditional evolution time is 4.34 ms. During this time, both qubits are protected by 10 sets of a UR-14 sequence, simultaneously. (a) The final excitation probability of the control qubit is at 0.04(2) and 0.95(3). (b) The target qubit is probed by an additional $\pi/2$-pulse with a variable phase $\phi$. The red plot shows a contrast of 0.891(19) and a phase of $(0.489(10))\pi$. The blue plot shows a contrast of 0.900(19) and a phase of $(-0.497(10))\pi$. The error bars represent statistical errors within one standard deviation for 120 repetitions. That is, the average fidelity of a CNOT gate with a two-ion system is $F_{\mathrm{CNOT}} = 0.85(4)$, excluding SPAM errors.

10 sets of a UR-14 sequence applied to both ions simultaneously. After the CNOT gate, the target qubit is further rotated by a probe pulse, a $\pi/2$-pulse with varying phase. The control qubit does not undergo an additional pulse. With all considerations before this section, the improved CNOT is measured and shown in Fig. 7.10. The excitation probabilities of the control qubit do not reach either completely 0 or 1, possibly because the single-qubit pulse error accumulates over 140 $\pi$-pulses. When the control stays in the state $|0\rangle$, the measured phase of the probe pulse on the target qubit is similar to that with no conditional evolution. When the control stays in the state $|1\rangle$, the phase of the target qubit is flipped by a phase $\pi$. The accumulated fidelity is given by the product of the control ($F_C^{(1)}$) and target ($F_T^{(2)}$) qubit fidelity,

$$F_C^{(1)} = C_1, \tag{7.27}$$

$$F_T^{(2)} = C_2 \cos(\phi - \xi), \tag{7.28}$$

$$F_{\mathrm{CNOT}}^{(1,2)} = F_C^{(1)} \times F_T^{(2)}, \tag{7.29}$$

where $C_i$ represents the contrast of the excitation probability, $\phi$ represents the measured phase of the analyzed $\pi/2$-pulse, and $\xi$ represents the expected phase from the analyzed pulse, which is either $\frac{\pi}{2}$ or $-\frac{\pi}{2}$. That is, in our current experiment, the average fidelity of a CNOT gate with a two-ion system is $F_{\text{CNOT}} = 0.83(4)$. The average fidelity excluding SPAM errors is $F_{\text{CNOT}} = 0.85(4)$. The previous measurement with a two-ion system was $F_{\text{CNOT,CP}} = 0.59(5)$ [96]. Using two neighboring ions in a three-ion crystal, the fidelity was $F_{\text{CNOT,AK}} = 0.64(5)$ [27]. The previous two fidelities were reported including SPAM errors. These two fidelities are comparable, considering their errors.

Furthermore, the Bell state is also prepared and measured. The Bell state can be prepared through a Hadamard gate and a CNOT gate, as described in section 7.1.2. The improved Bell state is shown in Fig. 7.11. Using equation (7.16), the Bell-state creation in a two-ion system is quantified by an average fidelity of $F_{\text{Bell}} = 0.935(19)$. The fidelity without SPAM error is $F_{\text{Bell}} = 0.95(3)$. The old measurements gave fidelities of 0.64(4) [99], 0.59(7) [96], and 0.63(3) [83]. All old results were reported including SPAM errors. The observed Bell-state fidelity exceeds the Bell-state limit of 0.5, proving the existence of entanglement [174]. Nevertheless, the fidelity still does not reach unity. One might notice here that the Bell-state fidelity is slightly better than the CNOT fidelity given in the previous paragraph. This is due to the fact that the measurements were performed on two different days, which may have resulted in different noise contributions. These noise contributions are not completely negated by the DD-pulse sequence, resulting in the non-unity fidelity. In addition, the error of $\pi$-pulses can also limit the fidelity because of the accumulation of several pulses.

Additionally, the Bell-state fidelity is also studied with respect to the motional excitation of the two-ion system. The Bell state is prepared by a method similar to that mentioned in the previous paragraph. Dynamical decoupling pulses are also applied to prevent qubit dephasing, using 10 sets of a UR-14 sequence. To vary the motional excitation of the two-qubit system, the SBC is applied for different times. For each SBC time, the average motional excitation is determined by the method presented in section 5.2. The result is shown in Fig. 7.12. This experimental result suggests that the Bell-state fidelity does not depend on the motional excitation of the two-ion system.

Using the achievement of the Bell-state fidelity, we have extended our results to a SWAP gate. The SWAP gate consists of three consecutive CNOT gates, as follows.

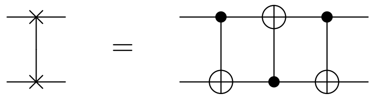

To demonstrate the SWAP gate, two ions are trapped and prepared in different initial states, $|0, +i\rangle$ and $|0,+\rangle$. The state $|0, +i\rangle$ is prepared by applying a single qubit rotation $R_2(\pi/2,0)$ and the state $|0,+\rangle$ is prepared by a Hadamard gate on the second qubit, where the first qubit is left in the state $|0\rangle$. The final excitation probabilities are measured by an additional $\pi/2$-pulse with varying phase on the first qubit. The oscillation can be expected from the initially prepared state of the second qubit.

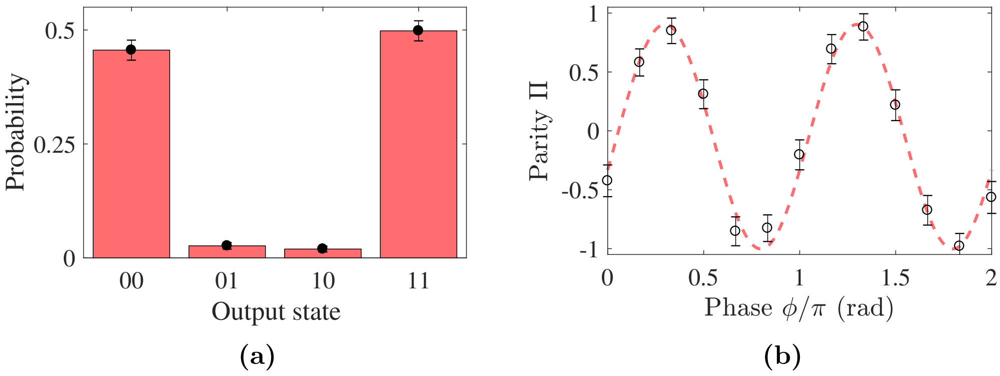

(a) (b)

**Figure 7.11: Measurement of the Bell-state sequence of a two-ion system.** This implementation uses the previous CNOT gate and a Hadamard gate on the control qubit to achieve a Bell state, $|\Phi^+\rangle = 1/\sqrt{2}(|00\rangle + |11\rangle)$. Sideband cooling is applied on both stretch ($2\pi \cdot 211.61\,\text{kHz}$) and center-of-mass ($2\pi \cdot 118.7\,\text{kHz}$) modes for 100 ms each. The gate time is 4.24 ms interleaved with 14 sets of a UR-14 sequence each for both ions, simultaneously. (a) The final state probability. (b) Applying another $\pi/2$-pulse with varying phase, the parity signal can be measured. The Bell-state fidelity is extracted from the final probability and the fit of the parity signal to be $F = 0.95(3)$. For this particular result, the parity phase is not correct because of the lack of $R_z(\theta)$ in the experimental sequence. The error bars represent statistical errors within one standard deviation for 84 repetitions.

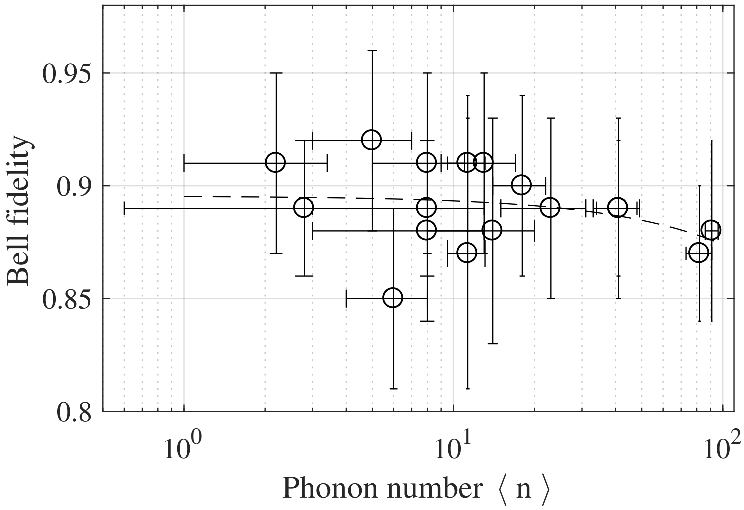

**Figure 7.12: Bell-state fidelity and motional excitation.** The Bell state is prepared by a method similar to that mentioned earlier. The difference is the SBC time applied to the SBC process. For each SBC time, the average motional excitation is determined by the method presented in section 5.2. This result suggests that the Bell-state fidelity does not depend on the motional excitation of the two-ion system. The horizontal and vertical error bars represent statistical errors within one standard deviation for 60 and 160 repetitions, respectively. The dashed line is to guide the eye by a linear fit.

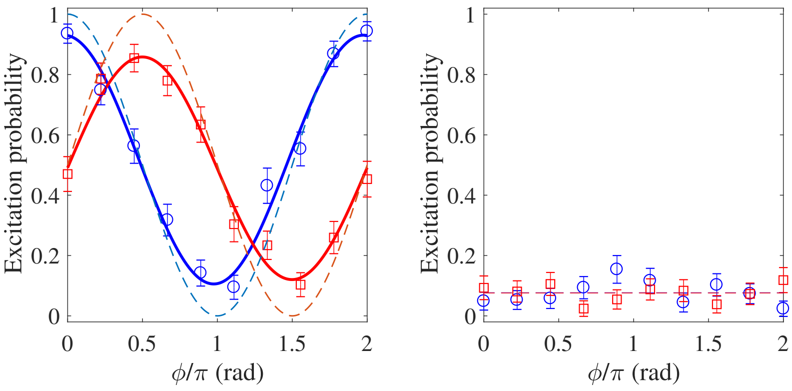

**(a)** Qubit 1 **(b)** Qubit 2

**Figure 7.13: Realization of a SWAP gate in a two-ion system.** The implementation takes three consecutive CNOT gates by preparing the qubits in either the state $|0,+i\rangle$ (blue) or $|0,+\rangle$ (red). The state $|0,+i\rangle$ is prepared by applying a single qubit rotation $R_2(\pi/2{,}0)$, and the state $|0{,}+\rangle$ is prepared by a Hadamard gate on the second qubit, where the first qubit is left in the state $|0\rangle$. Sideband cooling is applied in both stretch ($2\pi \cdot 211\,\mathrm{kHz}$) and center-of-mass ($2\pi \cdot 121\,\mathrm{kHz}$) modes for 50 ms and 100 ms, respectively. The conditional evolution time of each CNOT is 4.30 ms. During this time, both qubits are protected by 10 sets of a UR-10 sequence, simultaneously. Then, the total conditional evolution time is 12.9 ms using 300 DD-pulses. (a) The final excitation probability of qubit1 with a $\pi/2$ probe pulse of the blue data, fitted by a solid line, is a contrast of 0.83(3) with a phase of (-0.524(19))$\pi$. The red data give a contrast of 0.74(4) with a phase of (-0.002(21))$\pi$. The dashed lines show the expected oscillations of the given initial states. (b) The final excitation probabilities of qubit2, where the qubit is prepared in two different superposition states, are measured (without an additional $\pi/2$-pulse) as 0.08(3) (blue) and 0.08(4) (red). The error bars represent statistical errors within one standard deviation for 99 repetitions.

Fig. 7.13 shows the measured results of a SWAP gate. From these two initial states, the SWAP gate fidelities are $F_{\mathrm{SWAP}} = 0.70(8)$ and 0.65(9), by taking two-qubit gate fidelity. When the SPAM errors are removed, the SWAP gate fidelities are $F_{\mathrm{SWAP}} = 0.72(8)$ and 0.67(8). These two fidelities correspond to a CNOT gate fidelity $F_{\mathrm{CNOT}}$ between 0.87(6) to 0.90(5). They are also comparable to the CNOT fidelity within the same error shown in the previous three paragraphs.

The results for the improved Bell state and the SWAP gate lead us to more complex quantum algorithms, which will be presented in chapter 8 and 9. Nevertheless, the high-fidelity gate also needs to be considered further.

## 7.5 Detection Error

A qubit is interpreted to be in either a state $|0\rangle$ or $|1\rangle$ through the state-selective fluorescence detection of an ion in either of the two hyperfine states. When an EMCCD camera (or a detector) perceives fluorescence by probing the ion with a detection laser, we interpret the ion to be in the bright state or the excited state of the qubit transition, which means the qubit is in the state $|1\rangle$. Conversely, when an EMCCD camera does not perceive fluorescence, we interpret the ion to be in the dark state or the ground state. In practice, even in the dark state, an EMCCD camera can still perceive some background scattering light, which may come from reflections of electrodes or the vacuum recipient. In addition, the bright state of the $^{171}\mathrm{Yb}^+$ hyperfine state is not bright enough to confidently distinguish from the dark state with the current light collection system. The fluorescence histograms of the dark and bright states overlap. Formerly, in [96], the single threshold method was used to interpret experimental results. By introducing the double threshold method, as described in section 4.2.5, the two-qubit gate fidelity is improved by discarding the ambiguous events in the overlapping fluorescence histogram; see Fig. 7.14. In this example, when the single threshold method is used, the deduced fidelity is only 0.847(16), while the double threshold method gives a fidelity of 0.935(19) (0.95(3) excluding SPAM error). Therefore, it is important to further improve the light collection efficiency to be able to correctly interpret the experimental results.

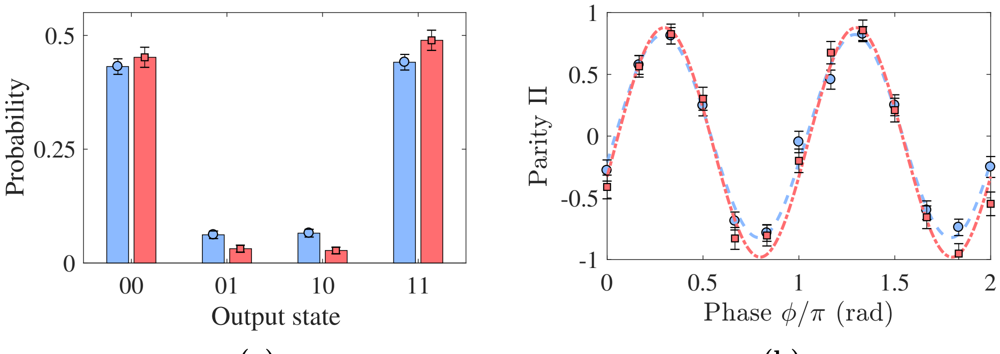

(a)

(b)

**Figure 7.14: Interpretation of a Bell state using the single/double threshold method.** This result is the same as that shown in Fig. 7.11, analyzed by the single (blue) or double (red) threshold method. The ambiguous part of the detection fluorescence can reduce the Bell-state fidelity from 0.935(19) (red) to 0.847(16) (blue). After correcting the SPAM error, the red plot has a Bell-state fidelity of 0.95(3).

## 7.6 Summary of Results and Outlook

In this chapter, the improved two-qubit gate fidelity is shown. Because the qubit dephasing time of the magnetic field-sensitive state, which is used for coherent operations, is shorter than as of the magnetic field-insensitive state by more than an order of magnitude, the dynamical decoupling pulse sequence is employed to protect against qubit dephasing. The DD pulse scheme can help against magnetic noise. However, DD pulse sequences can act as a band-pass filter to let some frequency pass with respect to their pulse interval. Therefore, the DD pulse sequence needs to be adjusted to avoid frequency components of magnetic noise, which can be different for each laboratory. In addition, the number of pulses cannot be too high because the pulse error accumulates to degrade the quantum gate fidelity. The compensation of the pulse error is not just simply employing the composite pulses in a DD sequence, as shown in the simulations. Moreover, the motional excitation of the two-ion system does not significantly affect the two-qubit gate fidelity. By implementing the double threshold method, the data analysis shows the Bell-state fidelity improved by more than 5 %. Taking all these results into consideration, the Bell-state fidelity is improved from 0.63(3) [83] to 0.935(19). After correcting the SPAM error, our current Bell-state fidelity is 0.95(3).

Even though we have improved the two-qubit gate fidelity to the 90 %-regime, this is still not enough. We still have a great deal of room to improve toward high-fidelity gates, which have been achieved using either laser [44, 45] or RF [35, 177] pulses. High-fidelity gates are necessary to perform more complex tasks, such as complicated quantum algorithms. One possibility is to employ the dressed state together with a magnetic-field gradient, which has been demonstrated to realize a two-qubit gate fidelity of 0.985(12) [60]. In addition, an optimum control technique can be considered to integrate the robust pulse and the DD pulse sequence.

# 8

# Quantum-Enhanced Deliberation Process

In the last few decades, computing power has drastically increased. The increasing computing power resulting from hardware advancements allows us to unlock new applications that require high computing power to process massive amounts of data, such as in the field of artificial intelligence [178]. Artificial intelligence technology is increasing its impact on our current society. A robot or a machine can learn to associate with some task by using massive amounts of data to train itself. By analyzing the data, machines are able to recognize patterns or detect abnormalities. The machines can be as good as humans at, for example, predicting heart attacks [179] and diagnosing pneumonia from a chest X-ray image [180]. A machine can also achieve superhuman efficiency, currently demonstrated by the game of Go [181, 182]. With a time limitation, an autonomous machine requires sufficient computing power to be able to make a decision fast enough to respond to a new situation. One method to speed up the decision-making algorithm underlying autonomous machines is to implement a quantum algorithm using a quantum processor.

In this chapter, a proof-of-principle demonstration of the speeding up of the decision-making process using a small-scale quantum processor is presented. This demonstration highlights the integration between artificial intelligence and quantum systems. This work has been published in Ref. [69].

## 8.1 Artificial Intelligence

Artificial intelligence (AI) is a field of study in which machines perform similar to intelligent beings. These include intellectual processes such as the ability to learn from past experience, to reason, or to discover a meaning. Machine learning is one of the core parts of AI. Machines can learn to associate with some task under supervision (supervised learning) [183]. Alternatively, machines can also learn without supervision by acquiring pattern identification ability with massive input data streams (unsupervised learning) [183]. Furthermore, machines can learn to interact with an arbitrary

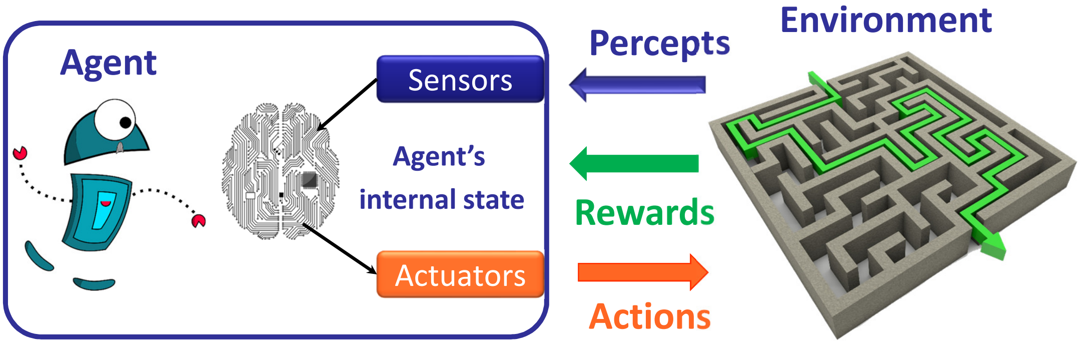

**Figure 8.1: Reinforcement learning scheme**. This is a typical model for an active learning agent. An agent wants to navigate in an environment, e.g., a maze. The agent has to be able to perceive what the environment looks like, so the agent must be equipped with sensors. To react back to the environment, the agent must also be equipped with actuators. To learn how to interact with the environment, the agent needs an internal state to process decisions to translate the sensors' information to actions. To learn the correct movements, a reward policy is required.

environment on their own.

In this work, we focus on autonomous learning. Autonomous learning is also called an active learning agent. A typical model is the reinforcement-learning (RL) model [183]. The RL model consists of perceptions, actions, and rewards (see Fig. 8.1). An agent has to have the ability to perceive the environment in which it wants to learn. The agent also has some actuators to take actions back into the environment. To learn how to interact with the environment, a reward scheme is implemented. The reward scheme, for simplicity, can be binary rewards, i.e., $\Lambda = \{0, 1\}$. When the agent takes actions correctly, it will gain reward points.

A general picture of autonomous learning scenarios for an agent and its environment is repeated in steps of a perception→action→reward sequence. For each step, the agent is triggered by a perception from its environment. In the agent's brain, it has a process for internal deliberation (or decision-making process) to select actions that would be likely to gain reward points. When an action is selected, the agent will perform that action and inspect the reward. Therefore, the agent can update its internal deliberation process, which means the agent "learns".

There are a number of algorithm to realize the decision-making process, for example, Q-Learning and state-action-reward-state-action (SARSA) [183]. In the following section, the so-called projective-simulation (PS) model, which is proposed in *Projective simulation for artificial intelligence* [184], is considered.

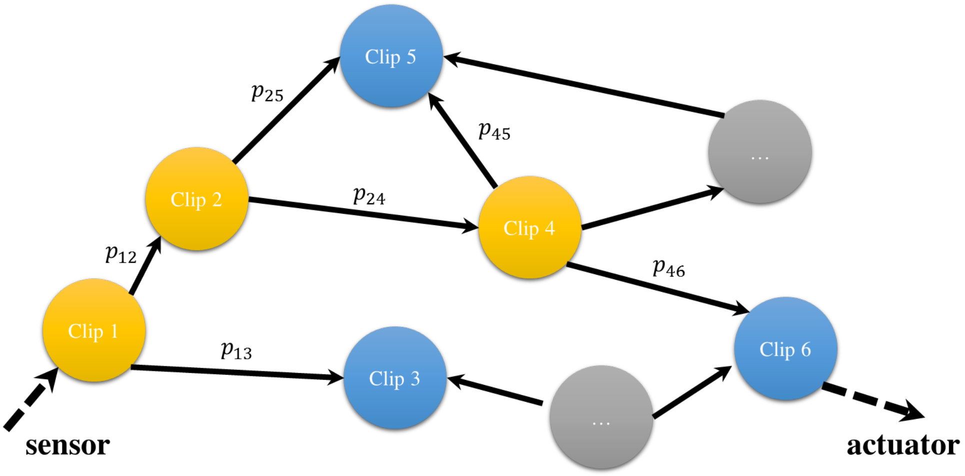

**Figure 8.2: An illustration model of Episodic & Compositional Memory**. Clips represent the network memory node, consisting of perception clips (yellow) and action clips (blue). The network nodes are all connected by a directed, weighted graph. A sensor triggers a perception clip. Then, a random walk using transition probabilities between clips is executed until hitting an action clip. $p_{ij}$ represents the transition probability from clip $i$ to clip $j$. The corresponding action will be performed in agent's environment through an actuator equipped on the agent. This figure has been adapted from Ref. [184].

## 8.2 Projective-Simulation Model

PS is an algorithm based on stochastic processing of past experience. This algorithm allows an agent to internally simulate future events based on its memorized events. The central component for a PS-based agent is a particular type of network memory called *episodic & compositional memory* (ECM). ECM is the memory of a collection of events. They consist of past personal experiences that occurred at a particular time and place. ECM can be represented by a directed[1], weighted graph, as shown in Fig. 8.2. In this work, each node of this network will be referred to as a *clip*. The clips represent the basic units of memory, consisting of not only memorized perceptions and actions but also various combinations of memorized perceptions and actions. These correspond to episodic experiences. In a standard PS model, we can assume that the network clip always contains clips as either individual perceptions or individual actions. Mathematically, the ECM is described by a connection between clip $i$ and

---

[1] A directed graph is graph of connected nodes (or vertices) in which all links (or edges) are directed from one vertex to another.

clip $j$ via a positive weight using a stochastic matrix

$$P = \begin{pmatrix} p_{11} & \cdots & p_{1j} \\ \vdots & \ddots & \vdots \\ p_{\mathrm{i}1} & \cdots & p_{\mathrm{ij}} \end{pmatrix}, \tag{8.1}$$

where $0 \leq p_{ij} \leq 1$, $\sum_i p_{ij} = 1 \ \forall \ j$, and $P$ represents the transition matrix with transition probabilities $p_{ij}$ between clip $c_i$ and clip $c_j$. The clip $c_i$ contains real non-negative probabilities. $i$ and $j$ are within the number of clips $N$; therefore, $i$,$j \in \{1,2,\ldots,N\}$.

Once a perception is perceived by the PS agent, the clip network memory initiates a random walk until hitting an action clip. The corresponding action will be coupled out to the environment, obtaining a reward or not, depending on the reward rule. These lead to an update of the $N \times N$ matrix $P$ by altering the probabilities, demonstrating the learning process. The random walk, which is the elementary process of the PS, is a well-established theoretical concept, known in randomized algorithms [185], providing several theoretical toolboxes for designing and analyzing the model. The random walk can further be extended to *quantum walks* [186], which has reported improvements polynomially and even exponentially with respect to hitting and mixing times [187–189].

There are different types of PS agents, in particular, PS agents based on *hitting* and *mixing*. For the hitting PS agent, a random walk is initiated from an initial perception clip, namely clip $c_1$. The first step is a random walk transition to clips $c_j$ with probabilities $p_{1j}$. Then, the resulting distribution $\{p_{1j}\}_j$ is sampled. If a sample provides an action, i.e., if the clip $c_k$ is “hit”, this action is selected as an output; otherwise, the walk continues on from the clip $c_k$. An advanced PS agent based on mixing is reflecting projective simulation (RPS) [190]. The Markov chain is first “mixed” using an appropriate number of steps. The mixing step or the mixing time depend on the spectral gap $\delta$ within the Markov chain $P$, determined by the difference between the two largest eigenvalues of $P$ [190, 191]. The Markov chain is mixed until the stationary distribution is reached before taking a sample. This is the basis for the PS framework for learning.

In the following section, we will consider an advanced version of the PS agent, the RPS agent, in more detail.

## 8.3 Reflecting-Projective-Simulation Model

In this chapter, RPS agents are focused on, which are a mixing-based model for the deliberation process. This allows a speed-up of the quantum version of RPS agents with respect to their classical counterparts [190]. The central objective of the RPS is to couple actions out according to a specific distribution. The clip network of RPS agents is structured into several sub-networks, one for each perception clip. Each sub-network has its own transition matrix $P$. These matrices, in addition to being stochastic, specify ergodic Markov chains, which provide a unique stationary distribution. Therefore, $P\boldsymbol{\alpha} = \boldsymbol{\alpha}$, with eigenvector $\boldsymbol{\alpha}$ and eigenvalue $+1$. Starting from any initial perception state, continued application of the respective $P$ mixes the Markov chain, leaving the network in the stationary state.

Stationary distributions over the RPS agent clip space are generated as specified by $P$, as a part of the decision-making process. The matrix $P$ is updated as the agent learns. To ensure a desired subset of clips to be an output, additional specifiers – flags – are used. This ensures that a desired action will be output, while maintaining the relative probabilities of the actions. Flags or emoticon tags are defined in [184]. The flag mechanism eliminates iterated attempts of actions that did not yield rewards in recent time-steps, which can be thought of as short-term memory. Thus, a more efficient exploration of correct behavior can be achieved.

In the quantum version of RPS, a basis vector $|i\rangle$ in an $N$-dimensional Hilbert space $\mathcal{H}$ represents a clip $c_i$. In the most general case, a diffusion process, representing the mixing step, requires two copies of the original Hilbert space. The classical objects $P$ and $\boldsymbol{\alpha}$ are then substituted by a quantum walk operator and a quantum state on the doubled space $\mathcal{H} \otimes \mathcal{H}$. The quantum walk operator, called the Szegedy walk operator [191, 192], is a unitary operator $W(P)$. The quantum state $|\alpha'\rangle$ has a property of $W(P)|\alpha'\rangle = |\alpha'\rangle$. Both $W(P)$ and $|\alpha'\rangle$ depend on a set of unitaries $U_i$ in space $\mathcal{H}$. The unitary $U_i$ follows

$$U_i|0\rangle = \sum_j \sqrt{p_{ij}}|j\rangle \tag{8.2}$$

for some reference state $|0\rangle \in \mathcal{H}$; that is,

$$|\alpha'\rangle = \sum_i \sqrt{a_i}|i\rangle \otimes U_i|0\rangle. \tag{8.3}$$

The quantum RPS implementation has a crucial feature, which is an amplitude amplification similar to Grover's algorithm [9], but the amplitudes are not symmetric. The asymmetrical amplitude amplification incorporates the mixing of the Markov chain. In addition, this allows outputting actions after an average of $\mathcal{O}(1/\sqrt{\epsilon})$ calls to $W(P)$, where $\epsilon$ represents the probability of sampling an action from the stationary distribution.

After an initialization stage via the set of unitaries $U_i$ where $|\alpha'\rangle$ is prepared, a number of diffusion steps are applied. Each diffusion step consists of two elements. (i) First, a reflection over the states corresponding to actions in the first copy of $\mathcal{H}$ is described by an operation

$$\mathrm{ref}_{\mathcal{A}} = 2\sum_{i=1}^{n} |i\rangle\langle i| \otimes \mathbb{1} - \mathbb{1} \otimes \mathbb{1}, \tag{8.4}$$

where $\mathcal{A} = \mathrm{span}\{|1\rangle, \ldots, |n\rangle\}$ denotes the subspace of the clip network corresponding to actions. (ii) Second, an approximate reflection over the state $|\alpha'\rangle$, acting as the mixing, is applied. An approximate reflection operation is designed, as follows in Ref. [190],

$$\mathrm{ref}_{\alpha'} = 2|\alpha'\rangle\langle\alpha'| - \mathbb{1}. \tag{8.5}$$

The generalized quantum walk operator is defined as

$$W(P) = (\mathrm{ref}_{\alpha'})(\mathrm{ref}_{\mathcal{A}}). \tag{8.6}$$

In this second element, the operator takes $\mathcal{O}(1/\sqrt{\delta})$ calls to $W(P)$. Summing together, the diffusion steps are repeated $\mathcal{O}(1/\sqrt{\epsilon})$ times before measuring the resulting state in the basis $\{|i\rangle\}_{i=1,\ldots,N}$ because the probability of sampling an action (almost) to unity is amplified by the quantum RPS algorithm. To carry out the deliberation procedure using a Szegedy walk hence requires an average of $\mathcal{O}(1/\sqrt{\delta\epsilon})$ calls to $W(P)$. Conversely, an average of $\mathcal{O}(1/\delta)$ applications of $P$ to mix the Markov chain would be required by a classical RPS agent, as well as an average of $\mathcal{O}(1/\epsilon)$ samples to find an action. This indicates that Q-RPS agents can achieve a quadratic speed-up in reaction time.

### 8.3.1 Rank-One RPS

For current quantum computational architectures, the requirement of two copies of $\mathcal{H}$ is extremely demanding, in the aspect of frequently updated coherent conditional

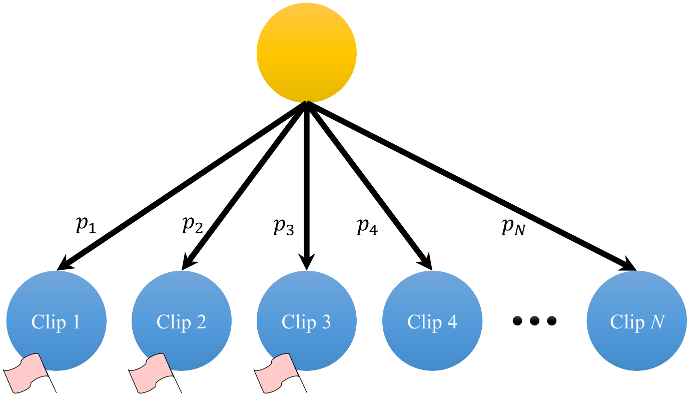

**Figure 8.3: An illustration of rank-one RPS.** Each perception-specific clip network contains only possible actions. Flags mark the desired actions. This is a one-to-one correspondence with the hitting-based basic PS using two-layered networks.

operations [193–195]. However, these requirements can be circumvented by considering the class of rank-one Markov chains. This is a special case where the entire Markov chain $P$ can be represented on a single copy of $\mathcal{H}$. That means a single unitary $U_P = U_i$ with $\forall i$, as all columns of $P$ are identical. This means the eigenvalues of Markov chain $P$ are (1,0, . . . ,0), and the spectral gap to mix the Markov chain is given by $\delta = 1$. Consequently, the network clip is simplified to each perception-specific clip network, containing only possible actions, and the Markov chain is mixed in one step ($\delta = 1$). To achieve the desired actions, flags are used. This is a one-to-one correspondence with the hitting-based basic PS using two-layered networks, as illustrated in Fig. 8.3.

Now, for a rank-one algorithm with the flagging mechanism, the action space $\mathcal{A}$ is limited to only the flagged actions $n$, where $n \ll N$. The corresponding probabilities within the stationary distribution are denoted by $a_1$,$a_2$, . . . ,$a_n$.

First, the current memory is initialized by the state $|\alpha\rangle$ as,

$$|\alpha\rangle = \sum_{i=1}^{N} \sqrt{a_i}|i\rangle. \tag{8.7}$$

Second, the diffusion steps $k$ are applied. The optimum number [9] of diffusion steps depends on the probability to find a flagged action within the stationary distribution. Thus, the optimum number is achieved by

$$k(\epsilon) = \text{round}\left(\frac{\pi}{4\sqrt{\epsilon}} - \frac{1}{2}\right), \tag{8.8}$$

where $\epsilon = \sum_{i=1,\dots,n} a_i$ represents the flagged action probability. In the rank-one case, the reflections over all actions of equation (8.4) are replaced by reflections over flagged actions,

$$\text{ref}_{\mathcal{A}} = 2\sum_{i=1}^{n} |i\rangle\langle i| - \mathbb{1}. \tag{8.9}$$

Third, the reflections $\text{ref}_\alpha$ over the stationary distribution $\alpha$ can be exact on one copy of $\mathcal{H}$ [193]. Finally, the agent takes a sample and checks whether the action is flagged. If the obtained action is marked by a flag, the action is coupled out; otherwise, the algorithm starts over.

When the number of actions $N$ is very large compared with the number of flagged actions $n$ and the environment is unfamiliar to the agent or has recently changed its rewarding rule, the probability of retrieving the flagged action $\epsilon$ may be remarkably small. In these cases, a quantum RPS has a huge advantage because a quantum RPS requires only an average call of $\mathcal{O}(1/\sqrt{\epsilon})$ samples until obtaining a flagged action, while a classical RPS requires $\mathcal{O}(1/\epsilon)$.

### 8.3.2 The Optimum Number of Diffusion Steps

The optimum number of diffusion steps in the quantum RPS is similar to the Grover iteration of the Grover search algorithm. It can be described by a geometric visualization. A diffusion step, which consists of two reflection operators, can be visualized as a starting vector $|\psi\rangle$ rotated in the two-dimensional space spanned by flagged and non-flagged solutions. Let $|A\rangle$ represent the non-flagged components and $|B\rangle$ represent the flagged components. Then,

$$\begin{aligned} |A\rangle &= \sum_{i\neq j} c_i |i\rangle, \\ |B\rangle &= \sum_{i=j} c_i |i\rangle, \end{aligned} \tag{8.10}$$

where $j$ represents flagged states and $c_i$ represents the state distribution within flagged and non-flagged states. The initial state $|\psi\rangle$ can be re-expressed as

$$|\psi\rangle = \sqrt{1-\epsilon}|A\rangle + \sqrt{\epsilon}|B\rangle, \tag{8.11}$$

with the probability of sampling flagged actions $\epsilon$. Using the geometric visualization shown in Fig. 8.4, the initial state $|\psi\rangle$ can be rewritten as

$$|\psi\rangle = \cos\left(\frac{\theta}{2}\right)|A\rangle + \sin\left(\frac{\theta}{2}\right)|B\rangle. \tag{8.12}$$

The reflection over the flagged state $U_j$ rotates the initial state $|\psi\rangle$ by angle $2\phi = \pi - \theta$. Then, the reflection over the original state $U_\psi$ further rotates the previous state $U_j|\psi\rangle$.

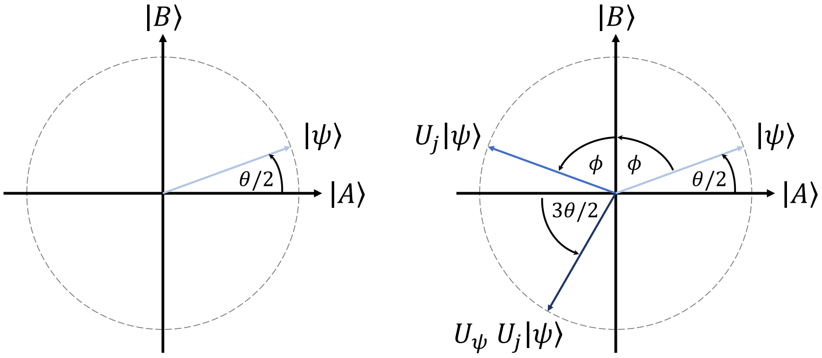

**Figure 8.4: Geometric visualization**. The initial state $|\psi\rangle$ is spanned by non-flagged and flagged states $|A\rangle$ and $|B\rangle$, respectively. Two reflection operators, as a diffusion step, rotate the initial vector by the reflection over flagged states $U_j$ and the reflection over the original state $U_\psi$. Using an optimum step, the state $|\psi\rangle$ will mostly overlap with the flagged state $|B\rangle$.

Therefore,

$$W|\psi\rangle = U_\psi U_j|\psi\rangle = (-1)\left(\cos\left(\frac{3\theta}{2}\right)|A\rangle + \sin\left(\frac{3\theta}{2}\right)|B\rangle\right). \tag{8.13}$$

It follows that continued application of diffusion steps rotates the state to

$$W^k|\psi\rangle = (-1)^k\left(\cos\left(\frac{2k+1}{2}\theta\right)|A\rangle + \sin\left(\frac{2k+1}{2}\theta\right)|B\rangle\right). \tag{8.14}$$

To have the initial state mostly overlapping with the flagged state, the state must by rotated by angle $\frac{\pi}{2}$. Thus,

$$\frac{\pi}{2} = \frac{2k+1}{2}\theta, \tag{8.15}$$

and

$$k = \frac{\pi}{2\theta} - \frac{1}{2}. \tag{8.16}$$

Because $\sin\left(\frac{\theta}{2}\right) = \sqrt{\epsilon}$, for small $\theta$, $\frac{\theta}{2} \approx \sqrt{\epsilon}$. Hence, the diffusion step $k$ is defined as shown in equation (8.8).

### 8.3.3 General Two-Qubit Rank-One RPS

In the mentioned scheme so far, we have focused on the case of the initial flagged probabilities in either $|00\rangle$ or $|01\rangle$, prepared by a product of two separable states between 2 qubits. In practice, the algorithm should be able to formulate an arbitrary state corresponding to the current network memory. According to Ref. [193], a four-clip state can be prepared by a four-clip probability unitary $U(\theta_1,\theta_2,\theta_3)$ with a probability distribution $(p_1,p_2,p_3,p_4)$, where

$$|\alpha\rangle = U(\theta_1,\theta_2,\theta_3)|0\rangle. \tag{8.17}$$

As a reminder, $\sum_j p_j = 1$. The unitary $U(\theta_1,\theta_2,\theta_3)$ is applied as follows

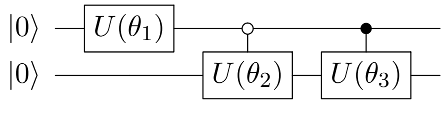

The first qubit takes a $Y$-rotation with a rotation angle $\theta_1$ and then makes two controlled $Y$-rotations to the second qubit, where the controls are in state $|0\rangle$ and $|1\rangle$, consecutively. (• represents the control state $|1\rangle$, and ∘ represents the control state $|0\rangle$.) The two controls rotate the second qubit with rotation angles $\theta_2$ and $\theta_3$, respectively. All rotation angles with respect to the stationary distribution are defined by

$$\theta_1 = 2\arccos\left(\sqrt{p_1 + p_2}\right), \tag{8.18}$$

$$\theta_2 = 2\arccos\left(\sqrt{\frac{p_1}{p_1 + p_2}}\right), \tag{8.19}$$

$$\theta_3 = 2\arccos\left(\sqrt{\frac{p_3}{p_3 + p_4}}\right). \tag{8.20}$$

The controlled $Y$-rotation is given by

$$U_{CY}^{(C,T)}(\theta) = \begin{pmatrix} 1 & 0 & 0 & 0 \\ 0 & 1 & 0 & 0 \\ 0 & 0 & \cos\left(\frac{\theta}{2}\right) & -\sin\left(\frac{\theta}{2}\right) \\ 0 & 0 & \sin\left(\frac{\theta}{2}\right) & \cos\left(\frac{\theta}{2}\right) \end{pmatrix}, \tag{8.21}$$

which is not directly achievable in this experiment. According to Ref. [79], the controlled $Y$-rotation can be interchanged with two CNOT operators and two $Y$-rotation operators, as expressed by

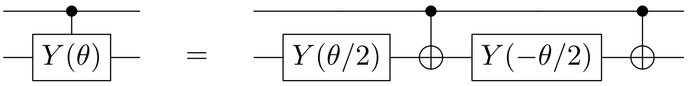

and

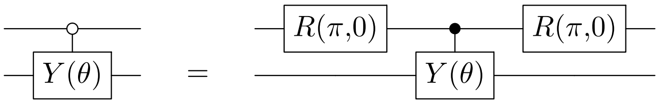

The standard controlled-unitary is sandwiched by two $\pi$-pulses to realize a controlled-$Y$ operator using control state $|0\rangle$. The single-qubit rotation $R(\theta,\phi)$ is defined in equation (2.7).

Using this scheme, we can prepare an arbitrary state for a 4-clip system to have a general two-qubit rank-one RPS.

### 8.3.4 Extended Space for Rank-One RPS and Higher Ranks

In this section, the clip-space is extended to an 8-clip system. To prepare this system, three qubits are required, using a unitary $U(\theta_1, \ldots, \theta_7)$ consisting of state probabilities

$\{p_1, \ldots, p_8\}$ [193]. The unitary $U(\theta_1, \ldots, \theta_7)$ is applied as

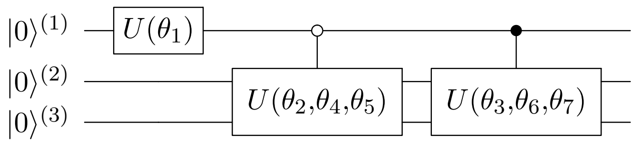

where

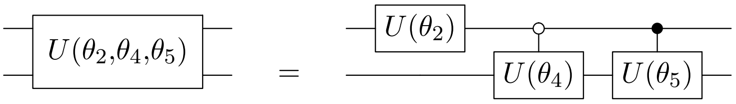

and

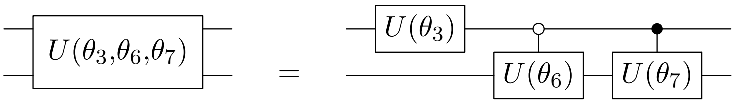

All rotation angles with respect to the stationary distribution are defined by

$$\theta_1 = 2\arccos\left(\sqrt{p_1+p_2+p_3+p_4}\right), \tag{8.22}$$

$$\theta_2 = 2\arccos\left(\sqrt{\frac{p_1+p_2}{p_1+p_2+p_3+p_4}}\right), \tag{8.23}$$

$$\theta_3 = 2\arccos\left(\sqrt{\frac{p_5+p_6}{p_5+p_6+p_7+p_8}}\right), \tag{8.24}$$

$$\theta_4 = 2\arccos\left(\sqrt{\frac{p_1}{p_1+p_2}}\right), \tag{8.25}$$

$$\theta_5 = 2\arccos\left(\sqrt{\frac{p_3}{p_3+p_4}}\right), \tag{8.26}$$

$$\theta_6 = 2\arccos\left(\sqrt{\frac{p_5}{p_5+p_6}}\right), \tag{8.27}$$

$$\theta_7 = 2\arccos\left(\sqrt{\frac{p_7}{p_7+p_8}}\right). \tag{8.28}$$

To extend to higher ranks, one would need an implementation of a quantum walk operator and an approximate reflection operator [193]. An implementation of a quantum walk operator can follow Ref. [196]. In addition, the quantum deliberation can be achieved through an approximate reflection operator, which is implemented by the phase detecting operator in a modification of Kitaev's phase detection algorithm [193, 197].

## 8.4 Experimental Implementation of Rank-One RPS

To demonstrate a quantum speedup of quantum-enhanced learning agents, the following features have to be confirmed:

1. the quadratically improved scaling of $\mathcal{O}(1/\sqrt{\epsilon})$,
2. the preservation of the tail of the stationary distribution.

As a reminder, the initial probability of finding a flagged action within the stationary distribution $\boldsymbol{\alpha}$ is denoted by $\epsilon$, where $\boldsymbol{\alpha} = (a_i)$ and $i \in \{1, \ldots, N\}$. Here, the tail is defined by the first $n$ components within $\boldsymbol{\alpha}$. Thus, the preservation means

$$\frac{a_j}{a_k} = \frac{b_j}{b_k}, \tag{8.29}$$

such that $\forall j,k \in \{1,\ldots,n\}$, and $b_j$ denotes the final probability after the application of the diffusion operator, when the agent obtains the flagged action labeled $j$. The central aim of the RPS is to output the actions according to a specific distribution, which is updated, indirectly, as the ECM network is modified throughout the learning process. To preserve the tail of the stationary distribution, the increasing probability of the flagged actions does not destroy what an agent has updated and learned in the ECM network. Using the quantum RPS algorithm, the overall probability of obtaining a flagged action is therefore enhanced,

$$\tilde{\epsilon} \equiv \sum_{i=1}^{n} b_i > \sum_{i=1}^{n} a_j \; = \epsilon. \tag{8.30}$$

The final relative probabilities of the flagged actions are preserved according to the tail of $\boldsymbol{\alpha}$, as conceptually illustrated in Fig. 8.5.

In the rank-one RPS case, a three-dimensional Hilbert space is the simplest implementation to demonstrate the quantum advantage. For the ion-trap system, each ion represents a qubit. Thus, at least two ions or two qubits are required to represent that space. Two different flagged actions are represented by two states, denoted $|00\rangle$ and $|01\rangle$. One additional state for all non-flagged actions, which are denoted by $|10\rangle$ and $|11\rangle$, is also required[2].

The stationary state, i.e., the previous knowledge the agent has learned, is prepared

---

[2] The implementation does not need to strictly follow this definition. This is an example representation. However, if one would like to use another representation, one would need to adjust the previous knowledge (the state preparation) and the diffusion operator, accordingly.

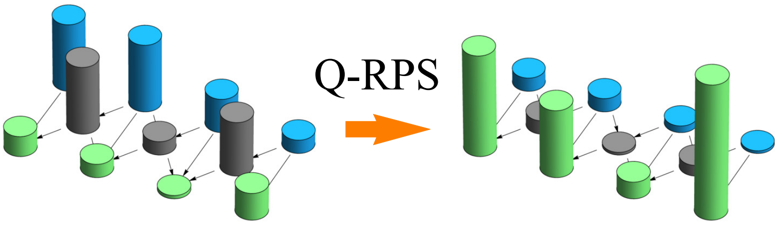

**Figure 8.5: Illustration of quantum RPS algorithm**. Quantum RPS agents enhance the relative probability of desired actions compared with other clips within the stationary distribution before a sampling clip is checked. The probabilities are visualized by the amplitude of each column. The desired actions are represented by green columns, the undesired clips are represented by gray columns, and the perception clips are represented by blue columns.

using two independent RF pulses,

$$\begin{aligned}|\alpha\rangle &= U_P(\theta_1,\theta_2)|00\rangle \\ &= R^{(1)}\left(\theta_1,\frac{\pi}{2}\right)R^{(2)}\left(\theta_2,\frac{\pi}{2}\right)|00\rangle,\end{aligned} \tag{8.31}$$

where $R_{(j)}(\theta,\phi)$ is a single-qubit rotation on qubit $j$, as defined in equation (2.4). The stationary distribution within the stationary state is defined by

$$\theta_1 = 2\arccos\left(\sqrt{\epsilon}\right), \tag{8.32}$$

$$\theta_2 = 2\arccos\left(\sqrt{\frac{a_{00}}{\epsilon}}\right), \tag{8.33}$$

where $\epsilon$ represents the total probability of the flagged action, defined by

$$\epsilon = a_{00} + a_{01} \tag{8.34}$$

and $a_j$ represents the probability of obtaining a two-qubit computational basis $j$.

The reflection over the flagged actions add the relative phase of $-1$ to all basis states corresponding to flagged actions. Then, the reflection over the flagged actions, $\mathrm{ref}_{\mathcal{A}}$, is a simple rotation around the $z$-axis with rotation angle $(-\pi)$ with respect to the first qubit,

$$\begin{aligned}\mathrm{ref}_{\mathcal{A}} &= R_z^{(1)}(-\pi), \\ &= \exp\left[-\mathrm{i}\frac{\pi}{2}\sigma_z^{(1)}\right],\end{aligned} \tag{8.35}$$

where $R_z^{(j)}(\theta)$ represents a $Z$ rotation and is defined in equation (2.4).

Another necessary reflection is the reflection over the stationary distribution, $\mathrm{ref}_\alpha$. It consists of a CNOT gate and single-qubit rotations, which depend on $\theta_1$ and $\theta_2$. This is given by

$$\begin{aligned}\mathrm{ref}_\alpha = {} & R^{(1)}\left(\theta_1 - \pi, \frac{\pi}{2}\right) R^{(2)}\left(\theta_2 + \frac{\pi}{2}, \frac{\pi}{2}\right) U_{\mathrm{CNOT}} \\ & \times R^{(1)}\left(-\theta_1 - \pi, \frac{\pi}{2}\right) R^{(2)}\left(-\theta_2 - \frac{\pi}{2}, \frac{\pi}{2}\right),\end{aligned} \tag{8.36}$$

The two reflections, denoted equation (8.35) and equation (8.36) presented above, perform a diffusion operator described by

$$\mathcal{D} = (\mathrm{ref}_\alpha)(\mathrm{ref}_\mathcal{A}). \tag{8.37}$$

This is equivalent to performing two calls of $U_P$ and $U_P^\dagger$ [193]. The preparation of the stationary state and the total gate sequence for a single diffusion step is illustrated in Fig. 8.6. The quantum RPS algorithm is performed in terms of a quadratically smaller average number of calls to diffusion operator $\mathcal{D}$ (calls to $U_P$) until a flagged action is sampled. A sample size of $1/\tilde{\epsilon}$ on average is required, which is determined by the initial preparation of $|\alpha\rangle$ and $k$ diffusion steps. The average number of calls to $U_P$

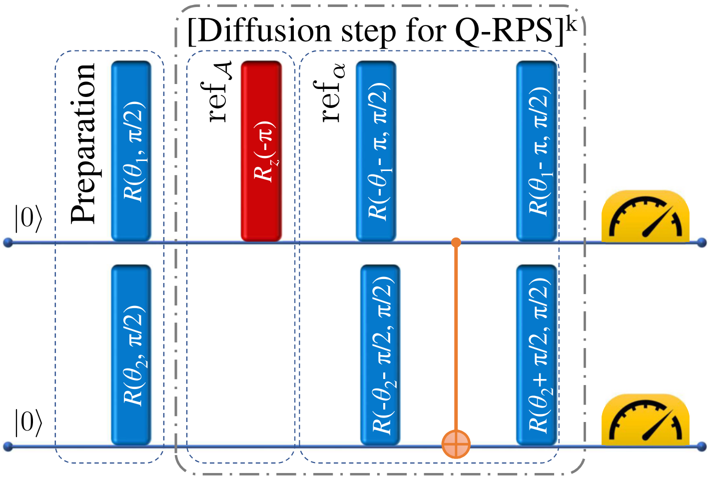

**Figure 8.6: Quantum circuit for rank-one Q-RPS using two-qubit system**. The stationary state is prepared using equation (8.31), (8.32), and (8.33). The diffusion step, consisting of reflections over the flagged actions ($\mathrm{ref}_\mathcal{A}$) and the stationary distribution ($\mathrm{ref}_\alpha$) (shown once each), is repeated $k$ times, where $\mathrm{ref}_\mathcal{A}$, $\mathrm{ref}_\alpha$, and $k$ are given by equation (8.35), (8.36), and (8.8), respectively. The specific pulse sequence implementing this circuit is explained later in equation (8.39).

to correctly sample a flagged action is referred to as the *'cost'* $\mathcal{C}$ in this work,

$$\mathcal{C} = \frac{\big(2k(\epsilon)+1\big)}{\tilde{\epsilon}}, \tag{8.38}$$

where $k(\epsilon)$ is defined in equation (8.8) and the simulated probability of obtaining a flagged action is defined in equation (8.30).

### 8.4.1 The Ion-Trap Setup

In this experiment, two ions are stored in a linear Paul trap. The ions are confined using axial and radial trap frequencies of $2\pi \cdot 123\,\mathrm{kHz}$ and $2\pi \cdot 525\,\mathrm{kHz}$, respectively. Each ion is addressed using a different VFG. By exposing full RF power, ions have two different Rabi frequencies, which means the ions perceive slightly different RF powers. The Rabi frequencies between the two ions can be made equal by appropriately adjusting the VFG amplitudes; see section 3.4. Hence, both ions have an equal Rabi frequency of $2\pi \cdot 20.92(3)\,\mathrm{kHz}$. Here, the qubit transition is the $\sigma^+$-transition, as described in equation (2.43). The experiment keeps track of the qubit transition frequencies by using the adaptive frequency correction technique, described in section 4.4. The ions are initially Doppler-cooled, and motional excitation is further reduced by employing RF sideband cooling. The RF sideband cooling is as described in chapter 5. Sideband cooling is applied on both modes, i.e., stretch mode and center-of-mass mode. This leads to an average motional excitation of $\langle n \rangle \leqslant 5$ for both modes.

The agent's memory is prepared by directly applying two RF pulses respective to each ion, as mentioned in equation (8.31). This is a coherent control using single-qubit rotation, given a rotation angle and phase as given in equation (8.31), (8.32), and (8.33). The reflection over the flagged actions requires a $Z$ rotation, which is not directly achievable in our experiment. The $Z$ rotation can be replaced by a equation (2.9). The diffusion operator includes a CNOT gate, which can be realized using a two-qubit $ZZ$-interaction from MAGIC [27]. A CNOT gate $U_{\mathrm{CNOT}}$ is applied as described in equation (7.9). When the diffusion operator is fully expanded using $U_{\mathrm{CNOT}}$ (equation (7.9)) and $R_z^{(i)}(\theta)$ (equation (2.9)), it can be optimized by combining appropriate single-qubit rotations together. Hence, the simplified diffusion operator can be described as,

$$\begin{aligned}\mathcal{D} &= (\mathrm{ref}_\alpha)(\mathrm{ref}_\mathcal{A}),\\ &= R^{(2)}\left(\theta_2,\frac{\pi}{2}\right) R^{(1)}\left(\theta_1,\frac{\pi}{2}\right) R_z^{(2)}\left(-\frac{\pi}{2}\right) R_z^{(1)}\left(\frac{\pi}{2}\right) U_{ZZ}\left(\frac{\pi}{2}\right) R^{(2)}\left(-\theta_2,\frac{\pi}{2}\right) R^{(1)}\left(\theta_1,\frac{\pi}{2}\right).\end{aligned} \tag{8.39}$$

The exact experimental sequence for the quantum RPS is shown in Fig. 8.7. From the

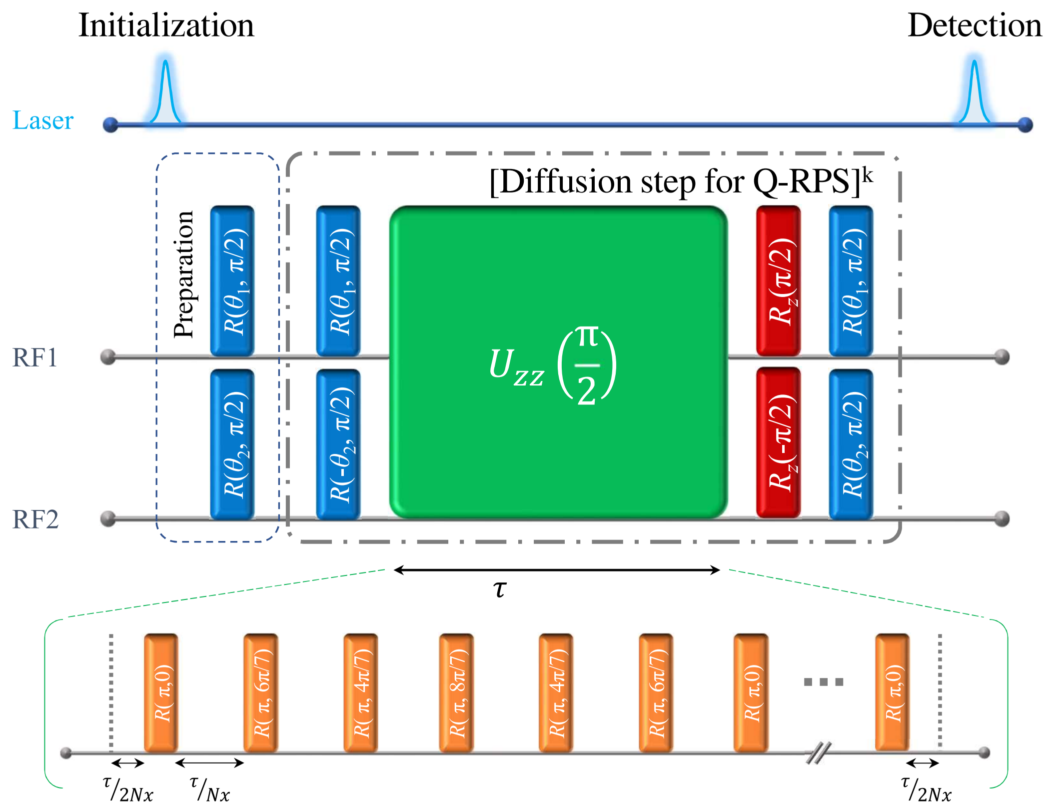

**Figure 8.7: Experimental sequence for quantum RPS**. The sequence is shown with respect to the time-axis along the horizontal line, reading from left to right. The qubits are first initialized to $|00\rangle$ by the preparation UV laser from the Doppler-cooled state. The qubits are then prepared in the stationary state using two RF pulses simultaneously, indicated by RF1 and RF2. Each single-qubit rotation RF pulse, represented in blue boxes, can be coherently controlled by the rotation angle and phase according to equation (2.7), (8.32), and (8.33). The conditional evolution $U_{zz}(\pi/2)$, indicated by a green box, is a part of the diffusion operator $\mathcal{D}$. The evolution of $\tau = 4.24\,\text{ms}$ is interleaved by dynamical decoupling pulses, shown in the bottom of the figure and as described in the text. The $Z$ rotation, represented by red boxes, is a collection of single-qubit pulses, as described in equation (2.9). $k$ iterations of the diffusion step depending on $\epsilon$ are applied to realize the quantum RPS algorithm. Finally, the detection UV laser is used again for state-selective detection at the end of the coherent manipulation.

Doppler-cooled state of the ions, the qubits are first initialized to $|00\rangle$ by the UV laser at 369 nm. The stationary state is then prepared (indicated as RF1 and RF2) using single-qubit rotation with an RF pulse (blue boxes). Then, the conditional evolution $U_{zz}(\pi/2)$ between two qubits is applied for $\tau = 4.24\,\text{ms}$. This interaction corresponds to a $J$-coupling between the two ions of $2\pi \cdot 48\,\text{Hz}$. The evolution is protected against decoherence by applying dynamical decoupling pulses. In this experiment, a UR pulse scheme is used; see section 4.3.5. For each set of UR pulses, the number of pulses can be adjusted. The UR-14 scheme with 14 $\pi$-pulses as one set is used. This pulse scheme is repeated ten times, for a total of 140 pulses. Within the UR-14 scheme, error correction is performed with appropriately chosen phase $\phi$:

$$\left(0, \frac{6\pi}{7}, \frac{4\pi}{7}, \frac{8\pi}{7}, \frac{4\pi}{7}, \frac{6\pi}{7}, 0,0, \frac{6\pi}{7}, \frac{4\pi}{7}, \frac{8\pi}{7}, \frac{4\pi}{7}, \frac{6\pi}{7}, 0\right).$$

The first seven pulses are shown in the lower part of Fig. 8.7, as the phases of the $\pi$-pulse are symmetric around the center. The pulse spacing is indicated by the arrows under the time axis of the UR-14 pulse scheme. At the end of the coherent manipulation, the UV laser is used again for state-selective detection on both qubits in the computational basis $\{|0\rangle,|1\rangle\}$. The relative frequencies for detecting the states $|00\rangle$, $|01\rangle$, $|10\rangle$, and $|11\rangle$ will be denoted as $b_{00}$, $b_{01}$, $b_{10}$, $b_{11}$, respectively, for discussion of the results. The double threshold method, as described in section 4.2.5, discards 10% of ambiguous measurement events. In summary, see Fig. 8.8, the process durations are as follows:

1. Doppler cooling: 30 ms
2. RF sideband cooling in stretch mode: 100 ms
3. RF sideband cooling in center-of-mass mode: 100 ms
4. Initialization to $|00\rangle$: 0.25 ms

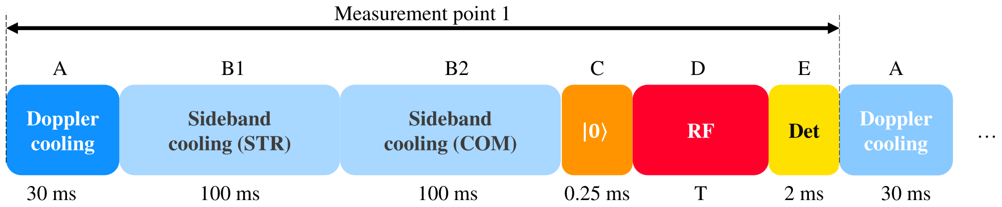

**Figure 8.8: The experimental sequence of the Q-RPS experiment.** The measurements consist of (A) Doppler cooling, (B) sideband cooling in STR mode (B1) and then COM mode (B2), (C) preparation of qubit state $|0\rangle$, (D) coherent RF manipulation, and (E) detection. The operation times for each sequence are indicated. The coherent RF manipulation uses a variable time $T$ between approximately 4 and 30 ms.

5. Coherent manipulation: 4−30 ms
6. State-selective detection: 2.0 ms

Next, the experimental results achieved using our ion trap are presented and discussed, together with the error analysis.

## 8.5 Experimental Results and Discussion

As mentioned above, to demonstrate the RPS features, two tests are performed:

1. the scaling of the average cost $\mathcal{C}$ with respect to the initial flagged probability $\epsilon$, and
2. the sampling ratio of the different flagged actions (equation (8.29)).

Furthermore, these experimental results also show that the implemented quantum RPS can amplify the asymmetric amplitude state distribution, in contrast to the standard Grover algorithm.

### 8.5.1 Scaling of Cost $\mathcal{C}$

After calibrating the RF power for coherent operation, each ion has an equal Rabi frequency of $2\pi \cdot 20.92(3)$ kHz on the $\sigma^+$-transition, which corresponds to a $\pi$-pulse time of 23.9 µs. A series of measurements is implemented using different initial flagged probabilities chosen from different numbers of diffusion steps, from $k = 1$ to $k = 7$. The probability $\epsilon$ is chosen to complete each diffusion step by considering the inverse function of equation (8.8). After performing the quantum RPS algorithm, the probabilities $b_{00}$ and $b_{01}$ are measured for each diffusion step to construct the cost according to equation (8.38). The experiment is repeated 1600 times for a given $\epsilon$. Fig. 8.9 shows the average cost $\mathcal{C}$ plotted against the initial flagged probability $\epsilon$. The red circles represent the experimental data. The error bars on the $y$-axis represent the measured statistical errors. The cost function also represents the algorithm complexity of the quantum RPS algorithm. The algorithm complexity can be described by an order of the number in the cost function as $\mathcal{O}(\epsilon^{-\xi})$. In the ideal case, the RPS gives $\xi = 1.0$ and the quantum RPS gives $\xi = 0.5$. The fit of the experimental data shows the cost decreases with respect to $\epsilon$ as $\xi = 0.57(5)$.

In the ideal case, the quantum RPS takes the complete number of diffusion steps, which brings the simulated flagged action probability close to unity ($\tilde{\epsilon} \approx 1$). Thus, one can substitute $k$ from equation (8.8) to equation (8.38) to achieve the ideal quantum

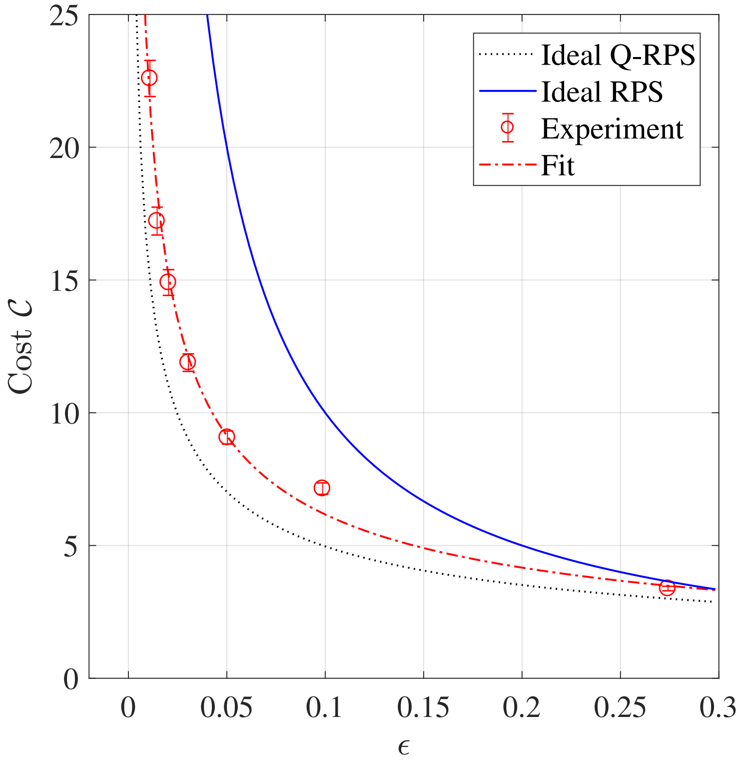

**Figure 8.9: Scaling characteristic of the learning agent's cost**. After preparation of the stationary state $|\alpha\rangle$, the quantum RPS algorithm is performed with diffusion step $k$ corresponding to each initial probability $\epsilon$. The resulting probabilities $\tilde{\epsilon}$ give the cost $\mathcal{C}$. Measurements are performed using $k = 1$ to $k = 7$ diffusion steps. The dashed black line and the solid blue line represent the calculation expected for an ideal quantum RPS ($\mathcal{O}(\epsilon^{-0.5})$) and ideal classical RPS ($\mathcal{O}(\epsilon^{-1.0})$), respectively. The red circles represent the experimental points averaged after 1600 repetitions. The error bars on the $y$-axis represent the measured statistical errors within one standard deviation. The fit to the experimental data (dot-dashed line) confirms the ($\mathcal{O}(\epsilon^{-0.57(5)})$) scaling behavior and hence is consistent with quantum RPS.

RPS cost,

$$\mathcal{C}_{QRPS}^{\text{ideal}} = \frac{\pi}{2\sqrt{\epsilon}}. \tag{8.40}$$

Within the classical RPS, the cost is calculated from the probability to sample a clip until hitting the flagged action,

$$\begin{aligned}\mathcal{C}_{RPS}^{\text{ideal}} &= \epsilon + 2\epsilon(1-\epsilon) + 3\epsilon(1-\epsilon)^2 + \dots \\ &= \sum_{j=1}^{\infty} j\epsilon(1-\epsilon)^{j-1} \\ &= \frac{1}{\epsilon}.\end{aligned} \tag{8.41}$$

The experimental data is in good agreement with the expected ideal quantum RPS. Furthermore, the experimental data outperforms the classical RPS baseline in the range of the chosen probabilities $\epsilon$. Despite the experimental imperfection causing the success probability $\tilde{\epsilon}$ to be between 0.66 and 0.89 from $k = 1$ to $k = 7$, the experimental result is good enough to obtain improved scaling and also to outperform the classical algorithm.

The deviation of the experimental data from the idealized predictions is discussed in the following section. Generally, the success probability $\tilde{\epsilon}$ after applying diffusion steps is not equal to unity, even in an ideal scenario without experimental imperfections; see Fig. 8.10. The success probability depends on the specific value of the initial probability $\epsilon$. This behavior originates from the step-wise increase in the quantum RPS algorithm according to the number of diffusion steps $k$, as defined in equation (8.8). The success probability can be fully achieved only when the number of diffusion step is an integer without rounding. The change in the ideal success probability with respect to deviations of $\epsilon$ from the given values becomes the largest for small numbers of diffusion steps ($k = 1$) and can drop down to 0.81. Increasing the number of diffusion steps, the precision of $\epsilon$ does not play an important role in the success probability, provided that the correct diffusion steps are performed. For example, the ideal success probability can be larger than 0.99, independent of the exact value of $\epsilon$, for a diffusion step of $k = 7$. Throughout this experiment, $\epsilon$ is chosen provided the number of diffusion steps is always close to an integer. Hence, the deviation from a unit success probability resulting from the theoretically chosen $\epsilon$ is negligible compared with other error sources.

In a real experiment, any state preparation can only be achieved with a certain accuracy. This results also in a certainty of $\epsilon$ and can lead to a non-optimal number of diffusion steps. Assuming an accuracy of $\epsilon \pm 1\%$ resulting from the preparation of two-qubit states, the effect is less than 5% on the success probability $\tilde{\epsilon}$ for the initial probability $\epsilon \gg 0.01$, corresponding to $k \leq 3$. In contrast, when the initial probability

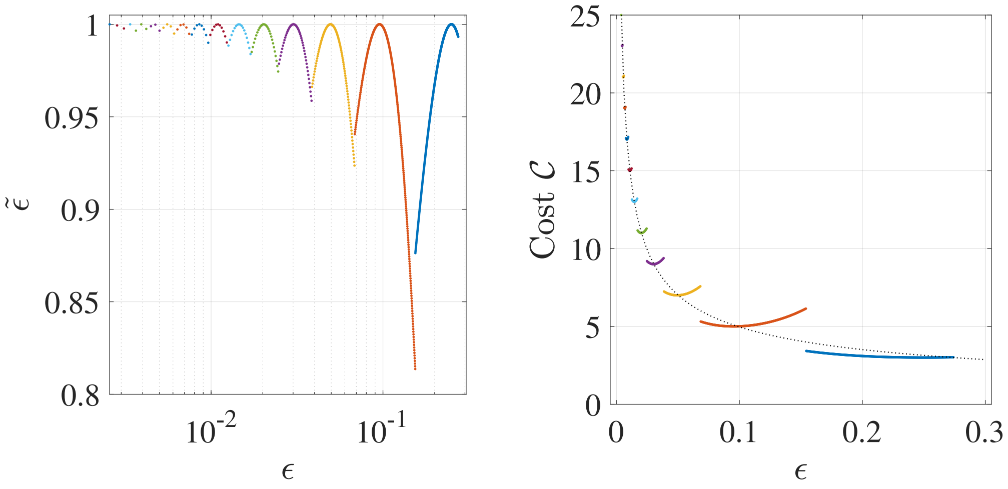

**(a)** **(b)**

**Figure 8.10: The quantum RPS using arbitrary initial probabilities**. The diffusion step $k$ in each plot is indicated by different colors, starting on the right side with $k = 1$. $k$ increases by one every time it changes a color to the left side. (a) The success probability depends on the step-wise increase of the diffusion step $k$; see equation (8.8). The success probability hits unity only if $k$ is an integer without rounding. For the worst possible scenario, the success probability can drop to approximately 0.81. (b) The cost is plotted against arbitrary initial probabilities in magenta points. This plot can be compared with the ideal quantum RPS cost (dotted line) in equation (8.40).

$\epsilon$ approaches $\approx 0.01$ from above, which corresponds to $k = 6$, then the success probability decreases to $\tilde{\epsilon} = 70\%$. This is caused by a non-optimal number of diffusion steps.

The accuracy of the two-qubit state preparation depends on the atomic transition frequency detuning $\Delta\omega$ of the RF pulses for single-qubit rotations, similar to the uncertainty $\Delta\Omega$ in the determination of the Rabi frequency $\Omega$. Using the adaptive frequency correction, as mentioned in section 4.4, the calibration of this experiment provides $|\Delta\omega/\Omega| < 0.05$ and $|\Delta\Omega/\Omega| = 0.0015$. These lead to an error in the initial probability $\epsilon$ of $\pm 2.5 \times 10^{-3}$ and a reduction of the success probability $\tilde{\epsilon}$ by less than 0.04. The errors associated with $\Delta\omega$ and $\Delta\Omega$ affect not only the state preparation but also the algorithm fidelity, as explained in the following section.

During this measurement, the bare atomic coherence $T_2^*$ time is approximately 0.5 ms, but each diffusion step requires a coherent manipulation time that is longer by an order of magnitude. To protect against qubit dephasing, a DD-pulse sequence is used during conditional evolution, which consists of 140 error-correcting RF $\pi$-pulses per diffusion step on each ion. Because of the high number of $\pi$-pulses, a small pulse error caused by detuning can limit the algorithm fidelity. For instance, the accumulated pulse error

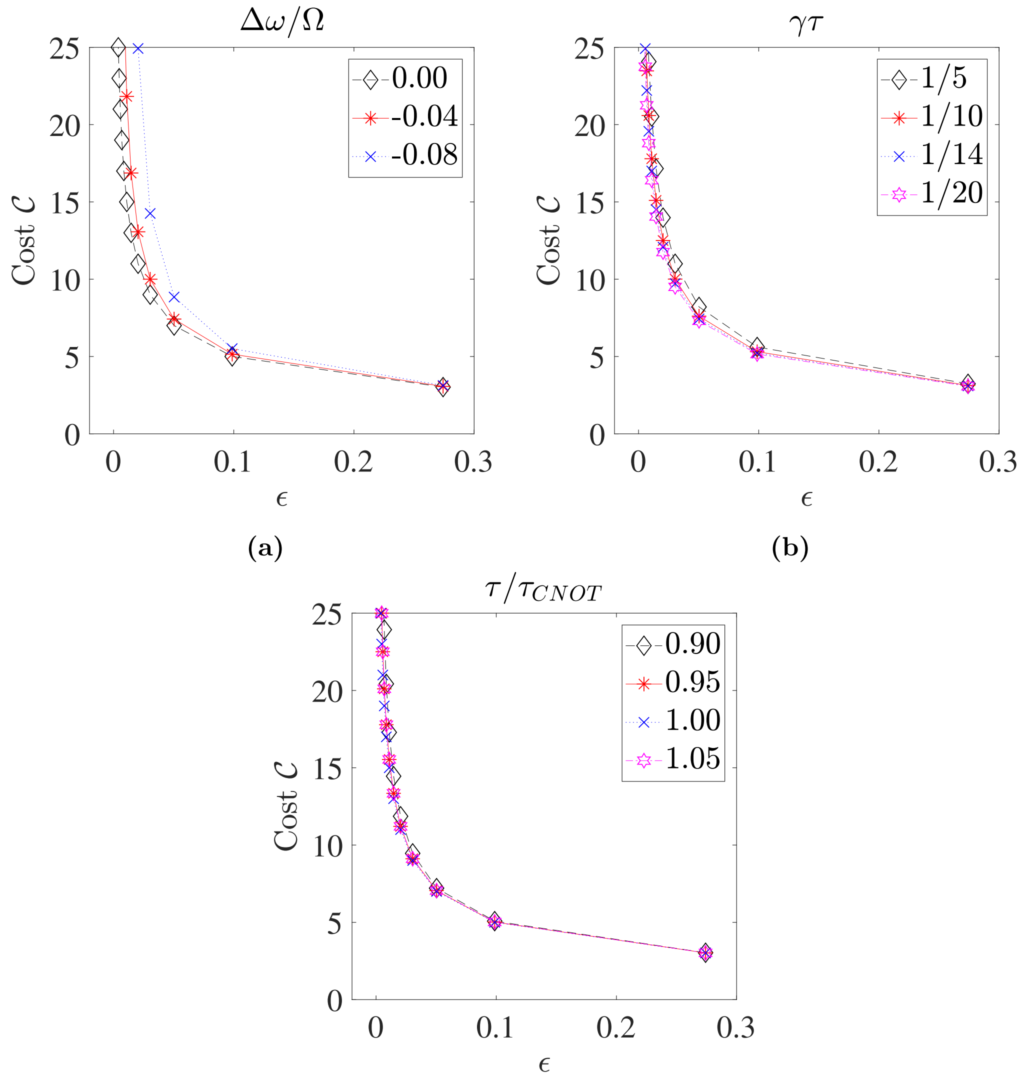

**(a)** **(b)**

**(c)**

**Figure 8.11: Error affecting scaling cost $\mathcal{C}$.** These plots are numerical calculations when each error contributes to the scaling cost. (a) The influence of the detuning $\Delta\omega/\Omega$ with respect to the cost function in the quantum RPS is shown for various detunings. (b) The influence of the decoherence effect $\gamma\tau$. (c) The influence of the interaction deviation with respect to the correct CNOT interaction time $\tau/\tau_{\text{CNOT}}$.

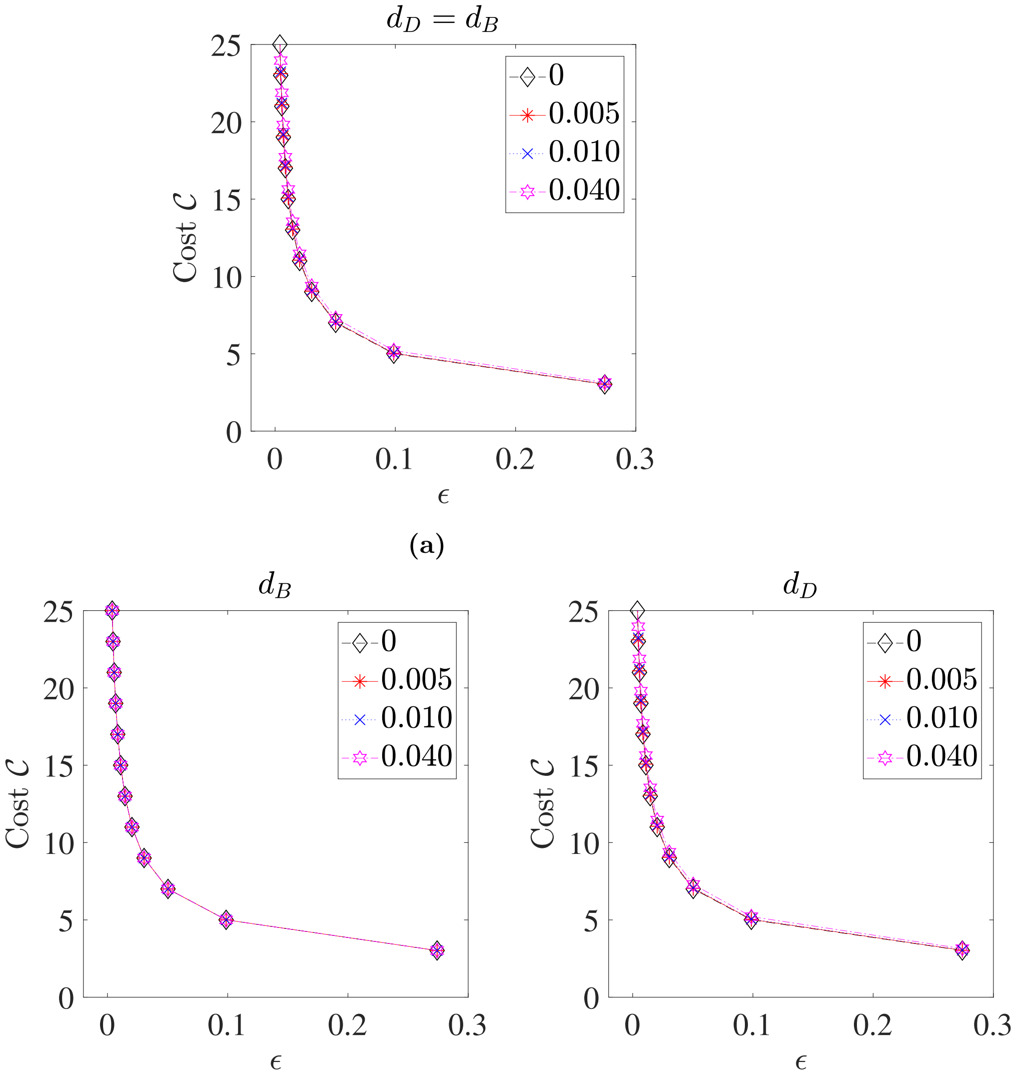

(a)

(b)

(c)

**Figure 8.12: Detection error affecting scaling cost $\mathcal{C}$.** These plots are numerical calculations when each detection error contributes to the scaling cost. (a) The influence of the symmetric detection error with respect to the cost function in the quantum RPS. (b) The influence of the asymmetric detection error when there is only an error for detecting bright to be dark and there is no error for detecting dark to be bright. (c) In contrast, the influence of the asymmetric detection error when there is only an error for detecting dark to be bright and there is no error for detecting bright to be dark.

**Figure 8.13: Detuning affects scaling cost $\mathcal{C}$.** The influence of the detuning with respect to the cost function in the quantum RPS is shown for various detunings, $\Delta\omega/\Omega \in \{0, -0.04, -0.08\}$. Black lines indicate the numerical simulations of the complete quantum RPS algorithm, taking different values of the relative detuning $\Delta\omega/\Omega$ into account. The simulation also includes experimentally determined dephasing and detection errors. Most of the experimental data (red circles) lie close to the $\Delta\omega/\Omega = -0.04$ line.

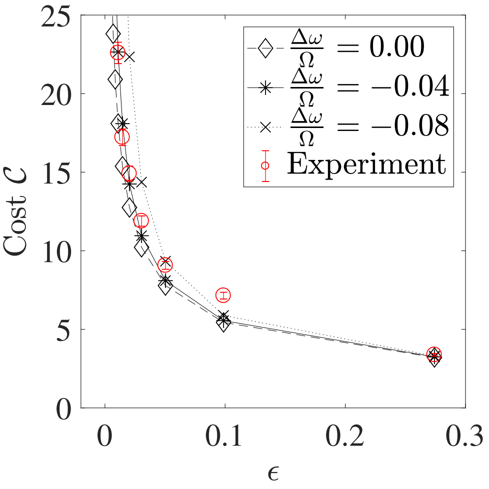

can be a potential error source for the success probability $\tilde{\epsilon} \approx 0.77$ when $k = 6$ and $\Delta\omega/\Omega = -0.04$. Even though the DD-pulses are applied, qubit dephasing is still present; however, its influence is less significant compared with the accumulated pulse error; see Fig. 8.11. This insignificance is similar to the detection error; see Fig. 8.12. To estimate the error caused by qubit dephasing, the success probability of a single diffusion step is considered. Assuming an exponential decay with $\gamma\tau \approx 1/14$ within a single diffusion step ($\tau \approx 4\,\mathrm{ms}$), the success probability would lead to $\tilde{\epsilon} \approx 0.90$ for $k = 6$, where $\gamma$ represents the experimentally diagnosed rate of dephasing and $\tau$ represents the coherent evolution time. In Fig. 8.13, the influence of the detuning with respect to the cost function in the quantum RPS is shown for various detunings. The algorithm, including the experimentally determined dephasing error together with detection errors of $\Delta\omega/\Omega \in \{0, -0.04, -0.08\}$, is numerically simulated. The experimental data are consistent with an average negative detuning of $\Delta\omega/\Omega = -0.04$. Note that the limited algorithm fidelity related to the detuning not only influences the single-qubit rotations, but also leads to errors during the conditional evolution when DD-pulses are applied.

### 8.5.2 Input and Output Ratio

For the second feature of the quantum RPS, the input ratio $r_i = a_{00}/a_{01}$ and the output ratio $r_f = b_{00}/b_{01}$ are studied. The studied ratio values lie between 0 and 2, while keeping $k(\epsilon)$ at $k = 1$ and $k = 3$ diffusion steps. Hence, the preparation with ratio values between 0.01 and 2.0 will not give probabilities that are too different from the two prepared probabilities. To prepare the initial distribution with the probabilities $a_{00}$ and $a_{01}$, single-qubit rotations are applied with rotation angles $\theta_1$ and $\theta_2$ for RF pulses, as given by equation (8.32) and (8.33). The respective diffusion step $k$ is applied to perform the quantum RPS. To obtain the statistics, the experiment is repeated

1600 times to estimate the probabilities $b_{00}$ and $b_{01}$. Fig. 8.14 shows the obtained output ratio $r_f$ plotted against the input ratio $r_i$ of the quantum RPS algorithm. The red and blue data points show the output ratio from $k = 1$ and $k = 3$ diffusion steps, respectively. They are fitted by a linear function with an offset and a slope as free parameters. The experimental data shows the trend as expected from the ideal quantum RPS, $r_f/r_i = 1$. The fitting slopes are 1.00(5) and 1.07(2) for $k = 1$ and $k = 3$, respectively. However, the experimental data show a $y$-offset from the expected trend line. Therefore, the ratio of the number of occurrences of the two actions obtained at the end of the deliberation process is maintained with respect to the relative probabilities of the initial stationary distribution. Even though there is an offset from the ideal result, the two linear fits show no significant difference between the two different diffusion steps ($k = 1$ and 3). This indicates that the offset error is not caused by the quantum algorithm itself. The detailed error analysis is presented

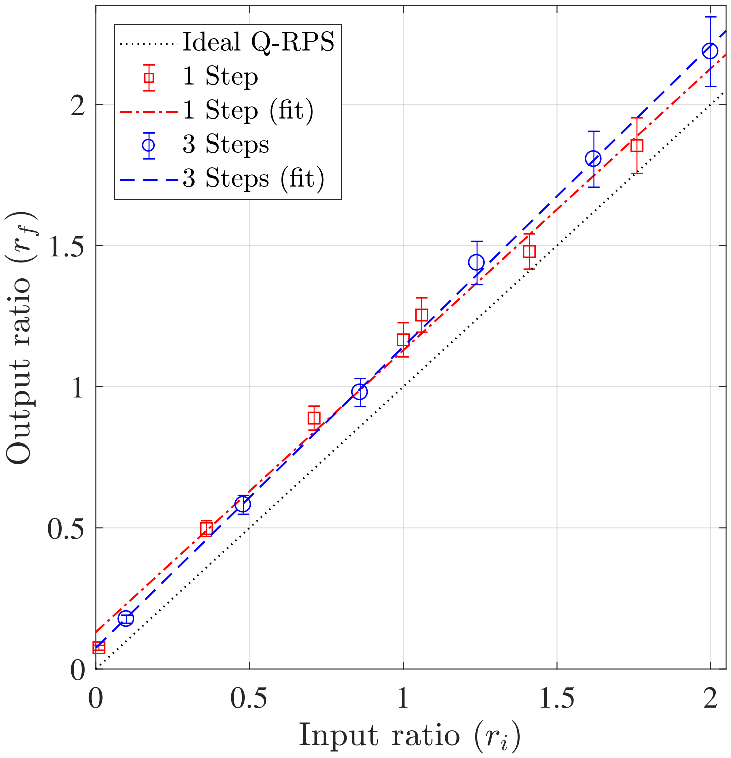

**Figure 8.14: Output ratio distribution**. The output ratio between two final flagged probabilities, $r_f = b_{00}/b_{01}$, is plotted against the input ratio between two initial flagged probabilities, $r_i = a_{00}/a_{01}$. The chosen probabilities take $k = 1$ (red square) and $k = 3$ (blue circle) diffusion steps. The black dashed line represents the behavior expected for the ideal quantum RPS. The red and blue dashed lines are the linear fits for the respective data set. Error bars represent statistical errors within one standard deviation.

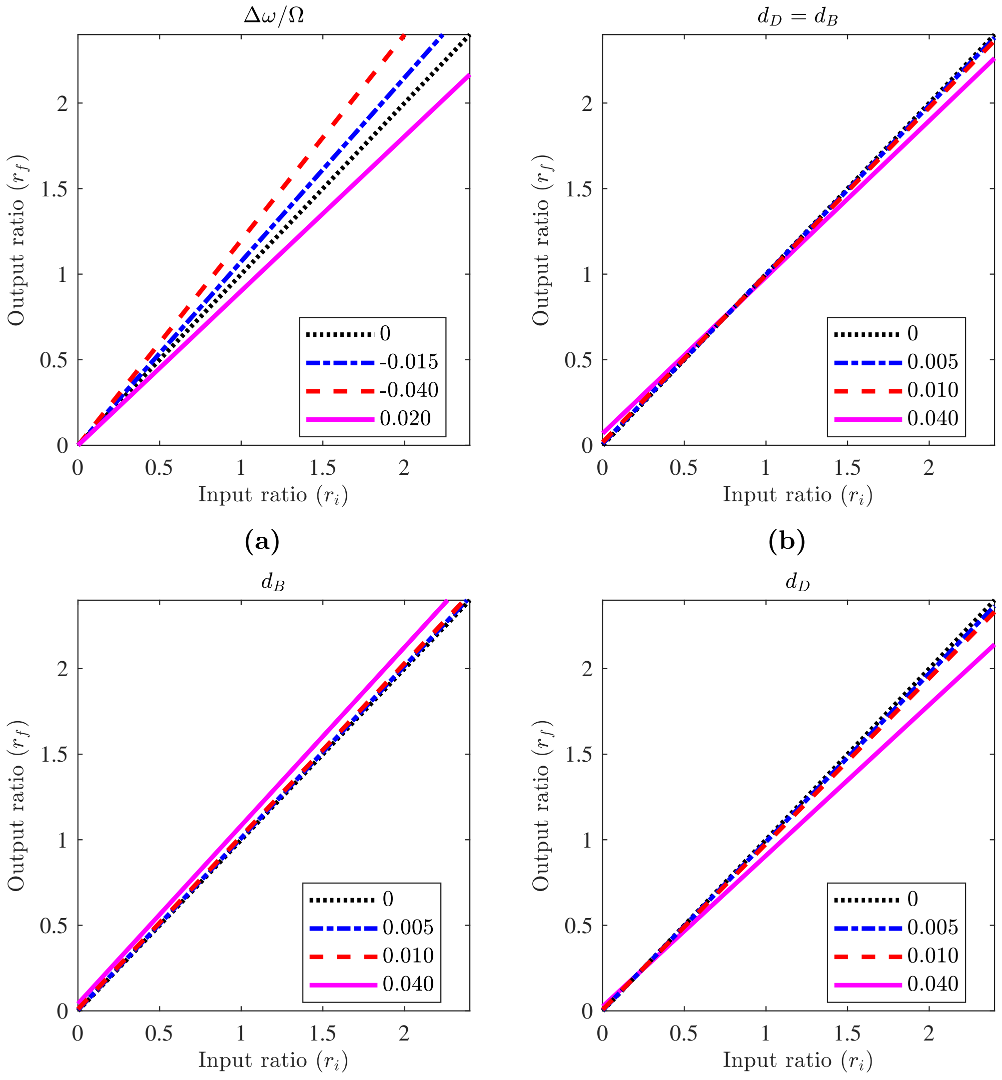

**(a)** **(b)** **(c)** **(d)**

**Figure 8.15: Error affecting output ratio distribution**. These plots are numerical calculations when each error contributes to the output distribution. (a) The influence of the detuning $\Delta\omega/\Omega$ with respect to the cost function in the quantum RPS. There is no influence resulting from decoherence and interaction time error. (b) The influence of symmetric detection error. (c) The influence of asymmetric detection error when only detecting bright as dark. (d) The influence of asymmetric detection error when only detecting dark as bright.

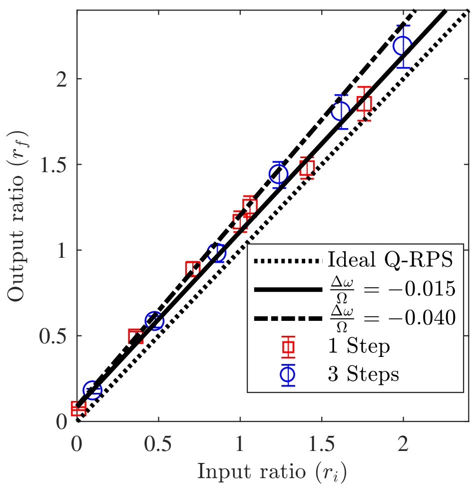

**Figure 8.16: Imbalanced detection**. The experimental data for the input and output ratios, represented by red squares and blue circles, are compared with simulations (solid and dash-dot black lines) of the Q-RPS algorithm, assuming a possible asymmetric detection error and detuning errors. The solid line presents the experimental data points corresponding to an expected output ratio assuming only an asymmetric detection error, where $d_\mathrm{B} = 0.06$ for bright ions and $d_\mathrm{D} = 0.03$ for dark ions, and detuning error $\Delta\omega/\Omega = -0.04$. The dash-dot line represents the same detection error, with a detuning error of $-0.015$.

as follows.

Each flagged probability is represented by the state $|00\rangle$ and $|01\rangle$, either in the beginning or at the end of the quantum RPS algorithm. The ratio is supposed to remain constant at $r_f/r_i = 1$; however, the experimental result shows deviations from $r_f/r_i = 1$, with a positive $y$-offset. That is, the measured probability $b_{00}$ of the state $|00\rangle$ increases with respect to the measured probability $b_{01}$ of the state $|01\rangle$. This characteristic is also present in the experimental result of the scaling feature in Fig. 8.9. During the measurements for the scaling investigation, the input ratio is fixed to $r_i = 1$; conversely, the observed output ratios vary by $0.98 \leq r_f/r_i \leq 1.33$. This is similar to the experimental result for the ratio feature, where the output ratios are larger than the input ratios.

The observed deviations of the output ratio are likely caused by an asymmetric detection error; see Fig. 8.15. The state detection relies on projective measurements of ions being either bright or dark, depending on the ions' resonance fluorescence. In the current setup, the fluorescence histograms indicating bright or dark ions are not separated well. The bright and dark states can be assigned with different errors, causing an asymmetric detection error for two-qubit state detection. Assuming the probability to detect a bright ion ($|1\rangle$) with a probability of $d_\mathrm{B} = 0.06$ as dark and a dark ion ($|0\rangle$) with a probability of $d_\mathrm{D} = 0.03$ as bright, this detection error explains the observed ratio results. This degree of detection error is possible in this experiment. Fig. 8.16 compares the measured output ratios with the calculated output ratios, assuming the mentioned detection errors and two different detuning errors $\Delta\omega/\Omega \in \{-0.04, -0.015\}$.

In Fig. 8.16, the experimental data, presented both for one and three diffusion steps, can be seen to be fitted well by the simulation when the experimentally determined detection error and detuning error of $-0.015$ are taken into account. In contrast, the simulation with a detuning error of $-0.04$ does not describe the experimental data well for both one diffusion step and three diffusion steps. This indicates that the detuning during these measurements remained at approximately $\Delta\omega/\Omega = -0.015$. The detuning error of $-0.015$, describing both results for different diffusion steps, indicates that the main contribution error in the ratio feature is the unbalanced detection error. Furthermore, when the input ratio is either very small or very large, these ratios lead to either $a_{00}$ or $a_{01}$, close to the preparation accuracy. By comparing with the preparation accuracy of $2.5 \times 10^{-3}$, the preparation error gives more significant contribution in the extreme case. In this experiment, intermediate ratios are chosen, which lead to insignificant error contribution to the preparation error. Similarly, because the small number of diffusion steps requires a smaller number of dynamical decoupling pulses, the detuning plays a less prominent role in these measurements. Considering in terms of the success probabilities $\tilde{\epsilon}$, the $k = 1$ and $k = 3$ cases achieve average success probabilities of 0.87 and 0.86, respectively. The detuning during these ratio feature measurements is indeed less than $\Delta\omega/\Omega = -0.04$, compared with $\tilde{\epsilon} = 0.77$ for $k = 3$ during the measurements investigating the scaling.

## 8.6 Summary of Experimental Results and Outlook

In this chapter, we presented the proof-of-principle experimental investigation of a quantum-enhanced deliberation (or decision-making) process, in which a learning agent is implemented in a prototype ion-trap quantum processor. The deliberation process can be further integrated with the reinforcement learning framework to realize an automated device, which is capable of learning how to interact with an environment. The presented scheme is centered on the projective simulation model [184] using a stochastic diffusion process. The diffusion process is governed by a (classical or quantum) random walk in an agent's memory. In this work, we focused on an advanced variant of the PS model based on mixing, the *reflecting projective simulation* model [190]. The RPS model allows the deliberation process for a quadratically sped-up quantum agent with respect to its classical counterpart. The implementation is demonstrated by a rank-one quantum RPS case, providing the scaling advantage of quantum speed-up without the need for an additional copy of the calculation space. In addition, the rank-one quantum RPS has a one-to-one correspondence with the hitting-based basic PS using two-layered networks, which has solved standard textbook problems, e.g., the invasion game, the grid-world problem, the mountain-car problem, and meta-learning [198–200], in reinforcement learning and advanced problems, e.g., robotic arm object manipulation, adaptive quantum experiments, and designing quantum experiments [70, 201, 202].

In this proof-of-principle experiment of a rank-one quantum RPS algorithm, the two main features of a quantum RPS have been verified. (i) The deliberation process of the quantum learning agent scales quadratically faster (compared with its classical counterpart), demonstrating up to 7 diffusion steps in the diffusion operator of the quantum RPS. This corresponds to an initial probability $\epsilon = 0.011$ to sample a desired action marked by a flag. The experimental results show the experimental uncertainties described by a qubit addressing error model as the main error contribution. In the range of the studied initial probabilities $\epsilon$, the demonstrated quantum agents always suppress the theoretical classical agents, even though there is qubit decoherence. (ii) The sampling ratio between the input probabilities $r_i = a_{00}/a_{01}$ and the output probabilities $r_f = b_{00}/b_{01}$ shows the preservation of the tail of the stationary distribution, regardless of the number of diffusion steps. The error model, describing the offset within the ratio result, suggests the effect of the asymmetric detection error.

Note that this experiment took the longest-ever conditional evolution time in our macroscopic linear Paul trap setup using computational qubits. During the coherent conditional evolution of 29.68 ms, the algorithm is protected by DD-pulse consisting of 980 $\pi$-pulses. This gate time is approximately 60 times longer than the coherence time $T_2^*$ of the bare-state qubit.

This experiment highlights the potential of a quantum computer in the field of quantum enhanced learning and artificial intelligence, enabling fast learning within a rapid-changing environment. This would be useful in a situation where reaction time is limited, for example, an AI-assisted emergency medical treatment, a high-frequency auto-trading system, or a high-speed driver-less vehicle.

From the presented toy-model of the quantum RPS algorithm, a possible extended study is complete reinforcement learning using quantum RPS agents. For a small toy-model, we could study an invasion game as an example problem. Furthermore, a practical use of the quantum RPS algorithm requires a larger perception space and action space. A general $N$-rank quantum RPS is required. A theoretical construction is given in detail in Ref. [193].

# 9

# Four-Ion System

One of the challenges in quantum information processing is to demonstrate a large qubit system that is able to perform complex quantum algorithms. Real-world calculations using quantum algorithms require a large number of qubits and multi-qubit operations. Therefore, this chapter begins by working with a four-ion system.

In our ion trap, the electrodes are not segmented, which means we cannot apply differential axial potentials to separate the ion crystal. That is, we have a static quantum register. A functionality that enables us to transfer a quantum state within a quantum register becomes an important element.

Here, we consider the possibility of demonstrating quantum teleportation. The spin-spin couplings for a four-ion system are measured for the first time using the MAGIC scheme. The techniques described in chapter 7 are applied in the experiments reported in this chapter. This implementation can be a stepping stone for a large-scale ion trap quantum computer in the future.

## 9.1 Spin-Spin Couplings of Four Ions

For a four-ion system ($N = 4$), the dimensionless matrix expressing the scaled deviation of an ion from its equilibrium position, as described in equation (2.48), is given by [86],

$$\boldsymbol{S} = \begin{pmatrix} 0.5 & 0.5 & 0.5 & 0.5 \\ -0.6742 & -0.2132 & 0.2132 & 0.6742 \\ 0.5 & -0.5 & -0.5 & 0.5 \\ -0.2132 & 0.6742 & -0.6742 & 0.2132 \end{pmatrix}, \tag{9.1}$$

and the vibrational modes $\omega_n = \sqrt{m_n}\omega_z$, with $m_n = \{1, 3, 5.81, 9.308\}$. Therefore, the coupling strength $\varepsilon$, see equation (2.48), resulting from the magnetic-field gradient of

19.105 T/m at the axial trap frequency of $2\pi \cdot 122.984\,\mathrm{kHz}$ is given by

$$\boldsymbol{\varepsilon} = \begin{pmatrix} 0.0166 & 0.0166 & 0.0166 & 0.0166 \\ -0.0098 & -0.0031 & 0.0031 & 0.0098 \\ 0.0044 & -0.0044 & -0.0044 & 0.0044 \\ -0.0013 & 0.0042 & -0.0042 & 0.0013 \end{pmatrix}. \tag{9.2}$$

Hence, the spin-spin coupling of a four-ion system is theoretically estimated using equation (2.47) to be

$$\boldsymbol{J}/2\pi = \begin{pmatrix} 0 & 32.36 & 23.58 & 18.48 \\ 32.36 & 0 & 30.97 & 23.58 \\ 23.58 & 30.97 & 0 & 32.36 \\ 18.48 & 23.58 & 32.36 & 0 \end{pmatrix} \mathrm{Hz}. \tag{9.3}$$

The spin-spin coupling matrix of a four-ion system is measured using a similar method to that for a two-ion system, as reported in section 7.4. The phase shift of the target qubit is observed with respect to the conditional evolution time, as described in section 7.4. Four ions are loaded to the trap and Doppler-cooled. Sideband cooling is applied in the center-of-mass mode of the first ion, resulting in an average phonon number $\langle n \rangle \approx 10$. The first ion is referred to as the ion that has the smallest Zeeman shift, visually in the left-most ion in the EMCCD image; see Fig. 9.1. The distances between ions are calculated from the ion addressing frequencies, as explained in equation (2.44). The exemplary addressing frequencies of 4 ions at a given of set trapping parameters are given in Tab. 9.1. The Rabi frequencies between ions are different, which is probably due to the orientation of the RF antenna with respect to the quantization axis (along the endcap electrodes) and/or the interference of the reflected RF of the vacuum recipient. The qubit resonance transitions of 4 ions are corrected simultaneously by directly measuring all qubit transitions using the adaptive frequency measurement, as described in section 4.4. Then, the ions are initialized in the state $|0000\rangle$. The spin-spin coupling matrix element $J_{ij}$ is measured by taking ion $i$ as the control qubit and ion $j$ as the target qubit. For example, the spin-spin coupling

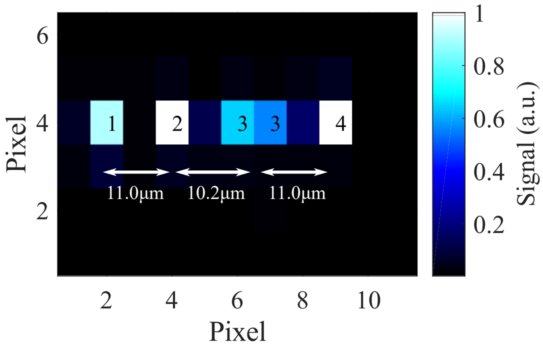

**Figure 9.1: An EMCCD image of a four-ion system.** The Doppler cooling image is orientated as it is seen from the front windows. The bright areas show Doppler cooling fluorescence of 4 ions using superpixels as 8 × 8 binning. The numbers in the bright areas are automatically assigned by the analysis algorithm to distinguish different ions. The numbers below the arrows indicate the separations between ions, estimated using equation (2.44).

**Table 9.1:** Addressing frequencies of 4 ions. The results are measured by coherent RF-optical double-resonance spectroscopy. The experimental parameters are a magnetic field offset of 0.85 mT (8.5 G), a magnetic-field gradient of 19.105(5) T/m, an axial trap frequency of $2\pi \cdot 122.984(10)$ kHz, and a radial trap frequency of $2\pi \cdot 524.75(8)$ kHz.

| #ion | $\omega_{\sigma^+}/2\pi$ (kHz) | $\Omega_{\sigma^+}/2\pi$ (kHz) | $\Omega_{\sigma^-}/2\pi$ (kHz) |
|---|---|---|---|
| 1 | 12 650 243.02(8) | 32.2(4) | 55.1(3) |
| 2 | 12 653 149.15(11) | 26.5(3) | 56.4(4) |
| 3 | 12 655 839.47(7) | 22.6(6) | 58.8(6) |
| 4 | 12 658 748.89(7) | 18.9(3) | 57.7(9) |

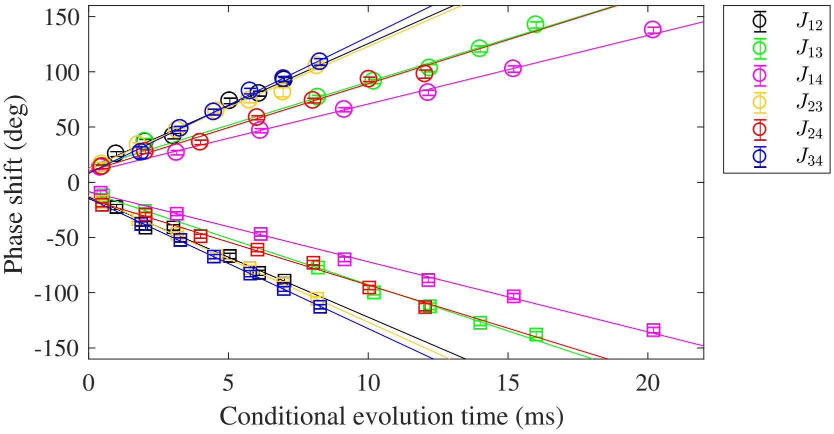

**Figure 9.2: The spin-spin coupling measurement of a four-ion system.** The spin-spin coupling element $J_{ij}$ is measured by taking ion $i$ as the control qubit and ion $j$ as the target qubit, with $i < j$. The circle markers represent the control qubit in the state $|0\rangle$, and the square markers represent the state $|1\rangle$. These two participant ions are protected simultaneously against dephasing by 7 sets of a UR-20 sequence. The RF powers are adjusted to have equal Rabi frequencies for the 2 ions. The error bars represent statistical errors within one standard deviation for 75 repetitions.

**Table 9.2:** Result of $J$-coupling of 4 ions. The experimental parameters are a magnetic field offset of 0.85 mT (8.5 G), a magnetic-field gradient of 19.105(5) T/m, an axial trap frequency of $2\pi \cdot 122.984(10)$ kHz, and a radial trap frequency of $2\pi \cdot 524.75(8)$ kHz. The interaction time $\tau_{\mathrm{CNOT}}$ does not include the interval of DD pulses of 7 sets of a UR-20 sequence.

| $J_{ij}/2\pi$ (Hz) | Measurement | Theory | Error | $\tau_{\mathrm{CNOT}}$ (ms) |
|---|---|---|---|---|
| $J_{12}$ | 30.8(17) | 32.36 | $1.0\sigma$ | 6.9(2) |
| $J_{13}$ | 22.5(6) | 23.58 | $1.8\sigma$ | 9.8(2) |
| $J_{14}$ | 17.4(5) | 18.48 | $2.2\sigma$ | 13.0(3) |
| $J_{23}$ | 31.3(12) | 30.97 | $1.0\sigma$ | 6.91(15) |
| $J_{24}$ | 21.9(8) | 23.58 | $2.1\sigma$ | 9.9(2) |
| $J_{34}$ | 33.6(19) | 32.36 | $1.0\sigma$ | 6.5(3) |

element $J_{23}$ is measured by taking ion 2 as the control qubit and ion 3 as the target qubit, while ions 1 and 4 are left in the state $|0\rangle$. The measurement results are shown in Fig. 9.2 and summarized in Tab. 9.2. The phase shift offsets are due to the employment of the DD pulse sequence, which is 7 sets of a UR-20 sequence.

The linear fits show that the data are separated into 3 groups: $J_{12}$, $J_{23}$, and $J_{34}$ are the nearest neighbor couplings. $J_{13}$ and $J_{24}$ are the second-nearest neighbor couplings. $J_{14}$ is the third nearest neighbor coupling. All experimental results are in good agreement with the theoretical calculation within 2.2 standard deviations. The corresponding CNOT gate times for each qubit pair are also given in Tab. 9.2.

## 9.2 Bell States in a Four-Qubit System

The Bell state of two different pairs within a four-ion system is studied. This is a similar study to that for a two-ion system, discussed in section 7.4.

First, the Bell state is prepared using ions 1 and 2. Sideband cooling is applied in the center-of-mass mode for the fourth ion at $2\pi \cdot 119.39$ kHz, resulting in an average phonon number $\langle n\rangle \approx 10$. Then, the ions are initialized in the state $|0000\rangle$ by the initialization laser. Thereafter, the coherent controls are applied only on ions 1 and 2. The applied gates and pulses are shown in the following circuit.

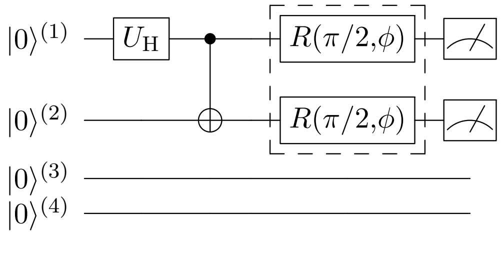

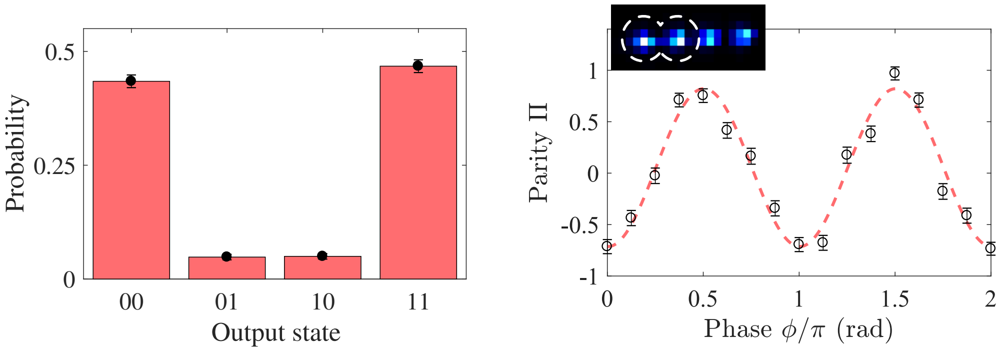

**(a)** **(b)**

**Figure 9.3: Measurement of a Bell state between ions 1 and 2 of a four-ion system.** As described in section 7.1.2, the implementation uses the CNOT gate and a Hadamard gate on the control qubit to create a Bell state, $|\Phi^+\rangle^{(1,2)} = 1/\sqrt{2}(|00\rangle^{(1,2)} + |11\rangle^{(1,2)})$. Sideband cooling is applied in the fourth ion's center-of-mass mode ($2\pi \cdot 119.39\,\text{kHz}$) for 80 ms. The gate time of 7.0 ms is interleaved with 4 sets of a UR-16 sequence each for both ions 1 and 2, simultaneously. (a) The final state probabilities for four possible output states. (b) By applying another $\pi/2$-pulse with varying phase, the parity signal is measured. The Bell-state fidelity is extracted using the final state probabilities and the fit of the parity signal as $F_{\text{Bell}}^{(1,2)} = 0.852(16)$, excluding SPAM error. The error bars represent statistical errors within one standard deviation for 120 repetitions.

The dashed box indicates that the $\pi/2$-pulses are either applied or not. The $\pi/2$-pulses are applied for the Bell-state parity measurement. The CNOT gate time $\tau_{\text{CNOT}}^{(1,2)}$ of 7.0 ms is interleaved with 4 sets of a UR-16 sequence applied to both ions simultaneously.

Fig. 9.3 shows the measurement result of the Bell state between ions 1 and 2. The Bell-state fidelity is $F_{\text{Bell}}^{(1,2)} = 0.852(16)$. This fidelity is smaller than the Bell-state fidelity of a two-ion system, see section 7.4. Because the CNOT gate time is longer than that for the two-ion case, the noise components may accumulate with longer time, especially if they are not completely protected against dephasing. Therefore, the fidelity of a four-ion system is less than that of a two-ion system.

Now, the Bell state is prepared using ions 2 and 4. The applied gates and pulses are in the following circuit.

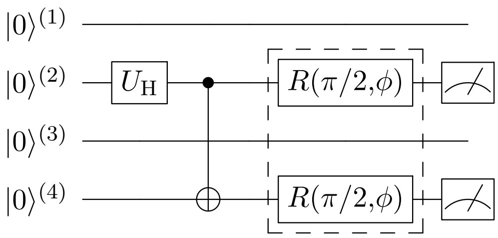

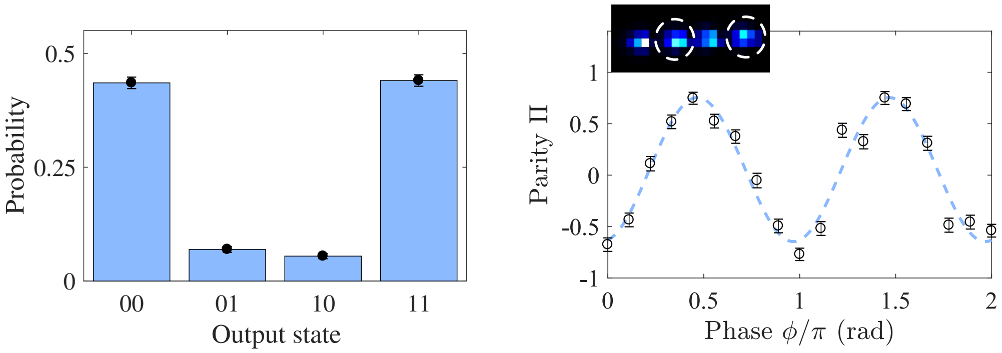

**(a)** **(b)**

**Figure 9.4: Measurement of a Bell state between ions 2 and 4 of a four-ion system.** As described in section 7.1.2, this implementation uses the CNOT gate and a Hadamard gate on the control qubit to create a Bell state, $|\Phi^+\rangle^{(2,4)} = 1/\sqrt{2}(|00\rangle^{(2,4)} + |11\rangle^{(2,4)})$. Sideband cooling is applied in the fourth ion's center-of-mass mode ($2\pi \cdot 119.39\,\mathrm{kHz}$) for 80 ms. The gate time of 9.9 ms is interleaved with 6 sets of a UR-16 sequence each for both ions 2 and 4, simultaneously. (a) The final state probabilities for four possible output states. (b) By applying another $\pi/2$-pulse with varying phase, the parity signal is measured. The Bell-state fidelity is extracted using the final state probabilities and the fit of the parity signal as $F_{\mathrm{Bell}}^{(2,4)} = 0.805(14)$, excluding SPAM error. The error bars represent statistical errors within one standard deviation for 150 repetitions.

Similar to the Bell state using ions 1 and 2, the CNOT gate time $\tau_{\mathrm{CNOT}}^{(2,4)}$ is changed to 9.9 ms. During the CNOT gate time, the qubits are protected using 6 sets of a UR-16 sequence applied to both ions simultaneously. The experimental result is shown in Fig. 9.4. The Bell-state fidelity after correcting for SPAM error is $F_{\mathrm{Bell}}^{(2,4)} = 0.805(14)$. This is a non-nearest neighbor interaction, which takes a longer time than the Bell state between ions 1 and 2. Therefore, the fidelity is smaller than in the previous case.

## 9.3 Towards Quantum Teleportation

Quantum teleportation is not the process of an object disappearing from one place and reappearing at some distant location, as shown in science-fiction movies. On the contrary, quantum teleportation provides a mechanism to faithfully transfer quantum information using previously shared quantum entanglement between the sending and receiving node and classical communication [203]. Thus, quantum teleportation is not a method of transportation, but of communication.

The first realization of quantum teleportation was demonstrated in a single-photon system [204]. The polarization state of single photons was transferred from Alice to Bob by destroying Alice's original unknown state. In an atomic system, the first two realizations were demonstrated in an ion trap experiment using three $\mathrm{Be}^+$ ions [205] and three $\mathrm{Ca}^+$ ions [206]. Furthermore, a demonstration using two systems with different physical natures, photons and an atom ensemble, has also been experimentally realized [207], connecting flying and stationary qubits. The most recent recorded distance for quantum teleportation is the space-based linked communication between a ground observatory and a low-Earth-orbit satellite, the Micius satellite, using a single photon over distances of up to 1400 km [208].

In our consideration, a quantum state can be transferred from one qubit to another within a string of ions coupled with the MAGIC-based long-range interaction. This technique can be used in a static qubit system to relocate a quantum state, which can be useful in ion traps without segmented electrodes or vacancy-center systems.

### 9.3.1 Teleportation Protocol

Initially, Alice has two particles: particle 1 is initialized in an arbitrary state $|\Psi\rangle^{(1)}$, and particle 2 is initialized as an auxiliary particle. Bob has another auxiliary particle, particle 3. Particles 2 and 3 are entangled together in the Bell state $|\Phi^+\rangle^{(2,3)}$. There is neither classical nor quantum correlation between particle 1 and the entangled pair; therefore, measurements of the entangled pair cannot yield any information regarding the state $|\Psi\rangle^{(1)}$. Teleportation can be essentially achieved by performing a joint Bell-state measurement between the unknown state and that of one of the entangled pair.

The particle 1 is given by

$$|\Psi\rangle^{(1)} = \alpha|0\rangle^{(1)} + \beta|1\rangle^{(1)}, \tag{9.4}$$

in which $\alpha$ and $\beta$ are the normalized factors. Then, the total state is expressed by

$$\begin{aligned} |\xi\rangle^{(1,2,3)} &= |\Psi\rangle^{(1)}|\Phi^+\rangle^{(2,3)}, && (9.5)\\ &= (\alpha|0\rangle + \beta|1\rangle)^{(1)}\frac{1}{\sqrt{2}}\left(|00\rangle + |11\rangle\right)^{(2,3)}, && (9.6)\\ &= \frac{\alpha}{\sqrt{2}}(|0\rangle^{(1)}|0\rangle^{(2)}|0\rangle^{(3)} + |0\rangle^{(1)}|1\rangle^{(2)}|1\rangle^{(3)})\\ &+ \frac{\beta}{\sqrt{2}}(|1\rangle^{(1)}|0\rangle^{(2)}|0\rangle^{(3)} + |1\rangle^{(1)}|1\rangle^{(2)}|1\rangle^{(3)}). && (9.7) \end{aligned}$$

The last equation (9.7) can be rewritten using the four Bell states as

$$\begin{aligned} |\xi\rangle^{(1,2,3)} = &\frac{1}{2}|\Phi^+\rangle^{(1,2)}(\alpha|0\rangle^{(3)} + \beta|1\rangle^{(3)}) + \frac{1}{2}|\Psi^+\rangle^{(1,2)}(\beta|0\rangle^{(3)} + \alpha|1\rangle^{(3)})\\ &+ \frac{1}{2}|\Phi^-\rangle^{(1,2)}(\alpha|0\rangle^{(3)} - \beta|1\rangle^{(3)}) + \frac{1}{2}|\Psi^-\rangle^{(1,2)}(-\beta|0\rangle^{(3)} + \alpha|1\rangle^{(3)}). \end{aligned} \tag{9.8}$$

Here, all Bell states can be measured as equally likely, with probability 0.25. To reconstruct the unknown state $|\Psi\rangle^{(1)}$ in particle 3 after the joint Bell-state measurement, additional unitary transformations are applied corresponding to which Bell state has been measured. Then, the final state of particle 3 is reconstructed as

$$|\Psi\rangle^{(3)} = \alpha|0\rangle^{(3)} + \beta|1\rangle^{(3)}. \tag{9.9}$$

Hence, the quantum teleportation circuit of a four-ion system to transfer the quantum state from ion 1 to ion 4 can be expressed as follows.

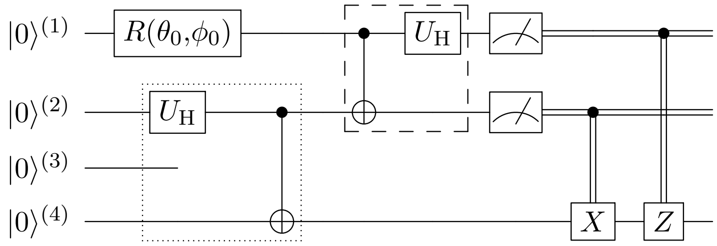

The state to be teleported is prepared by a single qubit rotation, $R(\theta_0,\phi_0)$. The dotted box creates a Bell state between ions 2 and 4, $|\Phi^+\rangle^{(2,4)}$. The dashed box is for the joint Bell-state measurement. The teleported state can be measured from ion 4 after applying the Pauli $X$ and $Z$ conditioned by the outcome of ions 1 and 2. The double lines represent classical wires.

According to this scheme, we have to control 3 qubits simultaneously. Moreover, ions need to interact to create the Bell state while keeping another ion as a quantum memory. The mentioned requirements can be fulfilled by our quantum toolbox [58, 96] using either a recoding into a memory qubit or a selective recoupling (SR) pulse [209].

### 9.3.2 Recoding Qubit Transition

To switch off the qubit interaction, the magnetic field-sensitive $\sigma^+$ (or $\sigma^-$) qubit can be recoded into a magnetic field-insensitive $\pi$ qubit. This recoding can be achieved by simply applying 3 RF $\pi$-pulses, consecutively [58, 96]. For a four-ion system or any multi-ion system, the $\pi$-transition pulses are not truly global for all ions because of the quadratic Zeeman effect for the transition ${}^2\mathrm{S}_{1/2}\,(F=0) \leftrightarrow {}^2\mathrm{S}_{1/2}\,(F=1, m_F=0)$. The addressing frequencies of the $\pi$-transition between the first and last ion differ by approximately $2\pi \cdot 31\,\mathrm{kHz}$ for the current magnetic field configuration. A rectangular RF pulse cannot resonantly address all ions, which affects the efficiency of the qubit recoding. The BB1 sequence, consisting of composite pulses, is considered experimentally and numerically here.

Considering that a Ramsey experiment is varied by the evolution time in a single-ion experiment, the qubit is prepared in a superposition state using a $\pi/2$-pulse of the $\sigma^+$-basis. The recoding pulse sequence is applied to recode in the $\pi$-basis, as expressed by

$$R_{\pi}^{BB1}(\pi,0)R_{\sigma^+}^{Rec}(\pi,0)R_{\pi}^{BB1}(\pi,0). \tag{9.10}$$

Here, the superscript indicates the RF pulse type, a rectangular pulse or a BB1-pulse sequence. The subscript indicates the associated transition. Now, the qubit is recoded in the superposition of the $\pi$-basis states; then, the qubit is evolved by the free evolution time interleaved with 10 sets of a UR-14 sequence. At the end of the evolution time, the qubit is recoded back to the $\sigma^+$-basis and probed by a $\pi/2$-pulse of the $\sigma^+$-basis, which brings the final excitation probability to either 0 or 1. The total experimental sequence is shown in Fig. 9.5.

Fig. 9.6 shows the result of the recoded Ramsey measurement. The recoding is performed using the resonant and detuned $\pi$-transition addressing frequencies. The non-resonant recoding is detuned by $-10$ kHz, imitating a multi-qubit system. The contrasts of the Ramsey fringes of the resonant and non-resonant recoding are 0.89(3) and 0.74(4), respectively. The non-resonant recoding gives a smaller Ramsey contrast, indicating insufficiency of the given composite pulses to protect the qubit memory. In a four-ion system, the detuned frequency would be $> 15$ kHz, which indicates that this method is not good enough. The limitation could be due to the current Rabi frequency; see Fig. 9.7. The error is too large for a good error compensation. Therefore, the SR pulse, as a qubit interaction control, will be selected in the four-ion experiment. An optimal control technique [210] to design a recoding sequence with a larger detuning could be considered in future experiments.

### 9.3.3 Bell State and Quantum Memory

Using the knowledge acquired from the investigations reported in section 9.2 and 9.3.2, we can prepare a Bell state between ions 2 and 4 and apply the SR technique to ion 1 to realize a quantum memory. The experiment follows the quantum circuit below.

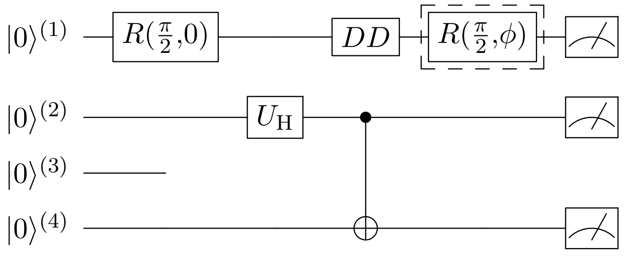

The first test is to prepare a memory using ion 1 in a superposition state with a $\pi/2$-pulse. Then, ions 2 and 4 are entangled by a Hadamard gate and a CNOT gate.

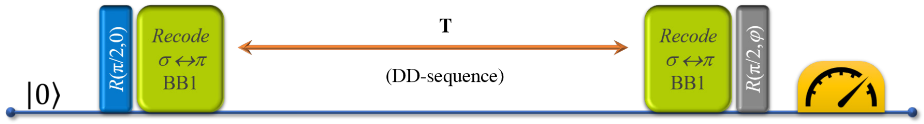

**Figure 9.5: The experimental sequence of a recoded Ramsey measurement.** The qubit is initialized in the state $|0\rangle$ and prepared in the superposition state by a $\pi/2$-pulse (blue) using the $\sigma^+$-basis. The recoding sequence (green) is performed, as shown in equation (9.10), to change to the $\pi$-basis. Thereafter, the qubit is evolved by the free evolution time $T$ with or without the DD-sequence, as desired. Before the probe pulse, the qubit is recoded back to the $\sigma^+$-basis. The probe $\pi/2$-pulse (gray) of the $\sigma^+$-transition is applied with a phase of either 0 or $\pi$.

**Figure 9.6: Measurement of a recoded Ramsey measurement.** The experimental sequence follows the description in Fig. 9.5. The free evolution time is varied from 0 to 40 ms interleaved with 10 sets of a UR-14 sequence. The Rabi frequencies on the $\pi$ and $\sigma^+$-transition are $2\pi \cdot 39.15$ kHz and $2\pi \cdot 33.09$ kHz, respectively. The circle and square data represent the phase 0 and $\pi$ of the probe pulse, respectively. The blue data show that the recoding is resonantly applied on the $\pi$-transition, while the red data is detuned by $-10$ kHz. Dashed lines indicate the average probabilities of the respective results. The Ramsey contrast of the resonant and non-resonant recoding are 0.89(3) and 0.74(4), respectively. These two results exclude SPAM errors.

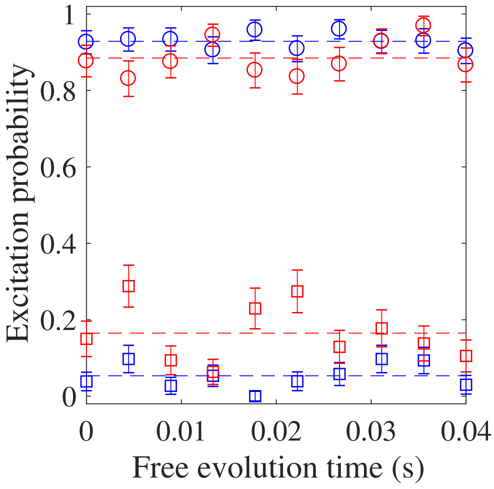

**Figure 9.7: Numerical simulation of a $\pi$-pulse using BB1 sequence with systematic control errors.** The pulse fidelity of 0.99 is indicated by the white area. This is based on the simulation shown in Fig. 7.6d, considering the larger error landscape.

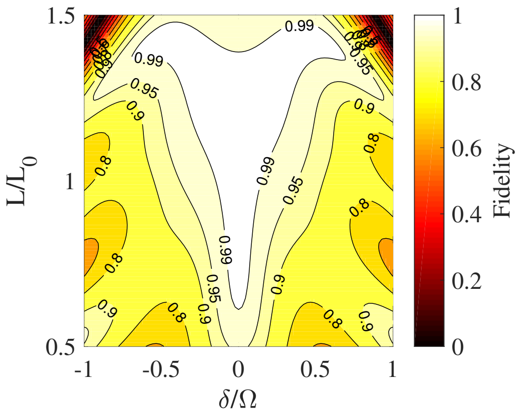

During the CNOT gate (which takes 9.9 ms), ion 1 needs to be protected against noise and isolated from interaction with the other ions. The same DD-pulse sequence from the CNOT between ions 2 and 4 is applied to ion 1 with an additional $R(\pi,\pi/2)$ in the center of the DD sequence as the SR pulse; for details, see Fig. 9.8. The probe pulse is shown in the dashed box before performing state-selective detection. We have three coherent control sources, which are adjusted by the VFG amplitudes to equalize the Rabi frequencies between all ions.

Fig. 9.9 shows the experimental results for obtaining the Bell state between qubits 2 and 4 while preserving the memory in qubit 1. The Bell state is prepared by the CNOT gate time of 9.9 ms interleaved with 6 sets of a UR-14 sequence. The exact DD sequence with a SR pulse is also applied to qubit 1 after preparing the superposition state. The excitation probability with respect to the probe pulse phase of qubit 1 is measured, and the result is shown by the blue plot. The blue line shows a contrast of 0.71(5) and a phase of (-0.42(3))$\pi$, while the Bell-state fidelity prepared during the blue data is 0.85(4), excluding SPAM error. The memory in the blue data can be protected, but not completely. Here, the memory has a phase shift of 0.07$\pi$, which can be removed by the red data, shown below.

The red data takes single qubit rotations into account, including the time for the Hadamard gate and the phase correction pulses of the Bell state. Adding these times to the DD sequence of the memory qubit, the excitation probability of qubit 1 is plotted in the red data. The red line shows a contrast of 0.87(3) and a phase of (-0.505(13))$\pi$, while the Bell-state fidelity prepared during the blue data is 0.79(2), excluding SPAM error. Now, the memory phase of the red data agrees well with the expected phase of the memory qubit within one standard deviation. Therefore, the matching sequence time is very important when preparing the experimental sequence.

Moreover, the Bell state between ions 1 and 2, while preserving the memory of ion 4, is also demonstrated. This experiment shows how well we can analyze the joint Bell-state measurement. The experiment follows the quantum circuit below.

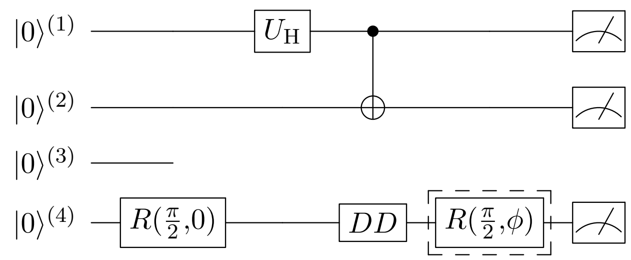

The experimental result is shown in Fig. 9.10. The CNOT gate takes 6.9 ms interleaved with 4 sets of a UR-16 sequence. Similar to the previous result, the same DD sequence with the SR pulse is applied to the quantum memory in qubit 4. Here, the sequence time is already corrected. The Bell-state fidelity between qubits 1 and 2 is achieved at 0.91(4) , without SPAM error, while the memory of qubit 4 has a contrast of 0.88(4)

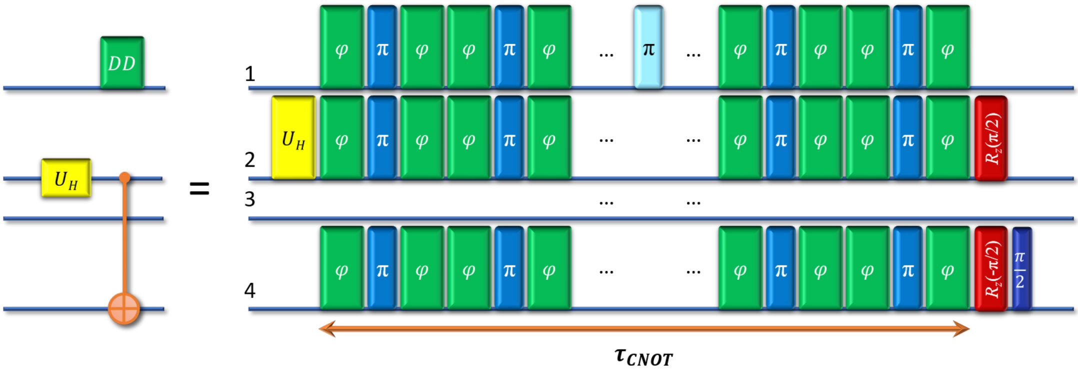

**Figure 9.8: The experimental sequence of preparing a Bell state and a quantum memory.** Ion 1, which serves as a quantum memory, needs to be protected during the Bell-state evolution between ions 2 and 4. The light-blue $\pi$-pulse in the center of the DD sequence indicates the SR pulse, $R(\pi,\pi/2)$. The spin-spin interaction is indicated by green boxes. To complete the Bell-state sequence, the Hadamard gate (yellow) and phase correction pulses (red and dark blue) are applied.

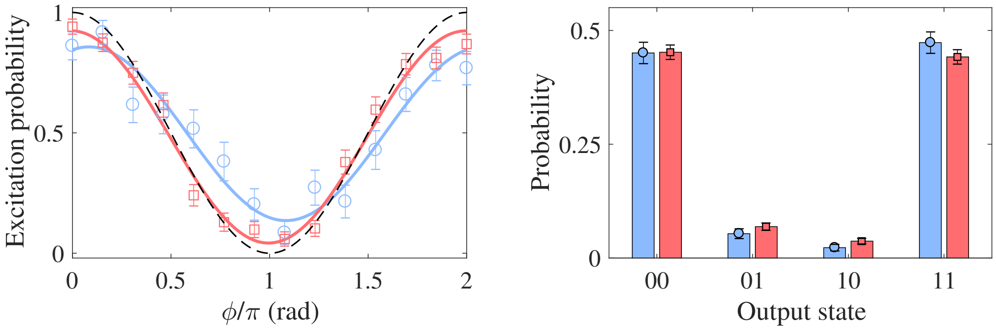

**(a)** Qubit 1 **(b)** Qubit 2 and 4

**Figure 9.9: Results of a quantum memory in a four-qubit system.** The memory qubit, qubit 1, is prepared in a superposition state by a $\pi/2$-pulse, after which qubits 2 and 4 are prepared in a Bell state interleaved with 6 sets of a UR-14 sequence. During the CNOT gate time of 9.9 ms in the Bell-state preparation, the memory qubit is also protected by the same DD sequence, with an additional SR pulse. (a) The excitation probability with respect to the probe pulse phase is plotted. The black dashed line represents a perfectly protected memory. The blue data take the same evolution time $\tau_{\text{CNOT}}$ in the DD sequence of the memory qubit, in addition to that for the Bell state. The red data take the same evolution time and the time spent for the Hadamard and the phase correction pulses. For the memory fidelity, solid lines show the fit of the corresponding results. The blue plot shows a contrast of 0.71(5) and a phase of (-0.42(3))$\pi$. The red plot shows a contrast of 0.87(3) and a phase of (-0.505(13))$\pi$. (b) The blue and red results give Bell-state fidelities of 0.85(4) and 0.79(2) , respectively. All results exclude SPAM errors. The error bars represent statistical errors within one standard deviation for 50 and 120 repetitions, respectively.

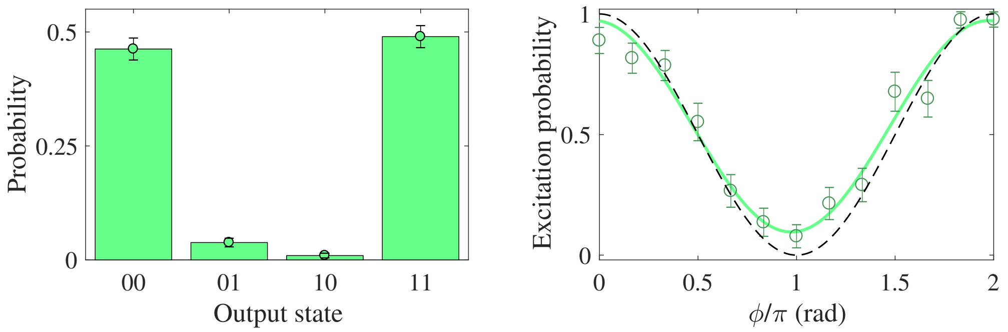

**(a)** Qubit 1 and 2

**(b)** Qubit 4

**Figure 9.10: Results of a quantum memory in a four-qubit system.** The memory qubit, qubit 4, is prepared in a superposition state by a $\pi/2$-pulse, after which qubits 1 and 2 are prepared in a Bell state interleaved with 4 sets of a UR-16 sequence. The CNOT gate time is 6.9 ms. (a) The Bell-state fidelity between qubits 1 and 2 after correcting SPAM error is 0.91(4). (b) The memory of qubit 4 shows a contrast of 0.88(4) and a phase of (-0.53(2))$\pi$. The black dashed line represents a perfectly protected memory. The error bars represent statistical errors within one standard deviation for 50 repetitions.

and a phase of (-0.53(2))$\pi$.

In the last two experiments, the Bell-state fidelities are comparable (or slightly better) to the ones obtained in section 9.2 within one standard deviation. With quantum memory as a part of the quantum register, these results show no significant differences, indicating that the SR pulse technique works well. Nevertheless, the memory qubit, in both cases, is not fully protected, which is shown by the non-unity of the measured contrast. One reason might be that the DD sequence cannot completely compensate for dephasing, which requires further investigation.

### 9.3.4 Quantum Teleportation Preliminary Result

The previous sub-section shows that we have enough ingredients to perform the teleportation protocol. The implementation, following the circuit presented in section 9.3.1, is shown below.

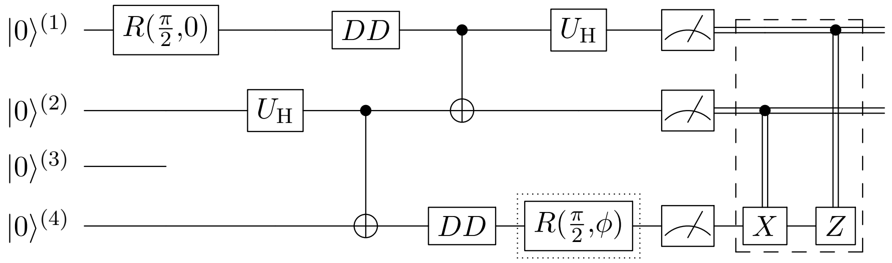

**Figure 9.11: The experimental preliminary result for quantum teleportation.** The superposition state of ion 1 is teleported to ion 4 and observed by a probe $\pi/2$-pulse. Two CNOT gates between ions 2 and 4 and ions 1 and 2 are applied for $\tau^{(2,4)}_{\mathrm{CNOT}} = 10.95\,\mathrm{ms}$ and $\tau^{(1,2)}_{\mathrm{CNOT}} = 5.54\,\mathrm{ms}$, respectively. During $\tau^{(2,4)}_{\mathrm{CNOT}}$ and $\tau^{(1,2)}_{\mathrm{CNOT}}$, 14 sets of a UR-26 sequence and 12 sets of a UR-22 sequence are applied to protect the qubits. The excitation probability is measured for qubit 4, showing a contrast of 0.56(5) and a phase of $(0.51(3))\pi$. The error bars represent statistical errors within one standard deviation for 60 repetitions. The black dashed line represents perfectly teleported memory. The measured phase is shifted by the phase $\pi$, which is due to the missing control Pauli-$Z$ in the analysis script.

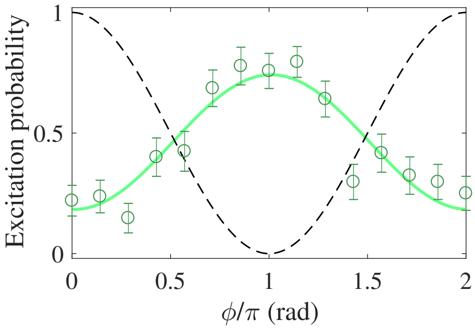

The dotted box indicates the probe pulse. The dashed box indicates the conditional Pauli operators, depending on the state of qubits 1 and 2. From the measured probabilities, the analysis script applies only the conditional Pauli-$X$ to the teleported qubit.

Three coherent control sources are adjusted by the VFG amplitudes to equalize the Rabi frequencies between all ions at $2\pi\cdot 29.33(3)\,\mathrm{kHz}$. The four-ion system is sideband-cooled by the center-of-mass of the first ion for 80 ms. The state $|0000\rangle$ is initialized by the preparation laser. The memory qubit (ion 1) is prepared by a $\pi/2$-pulse. The first CNOT between ions 2 and 4, $\tau^{(2,4)}_{\mathrm{CNOT}}$, takes 10.95 ms interleaved by 14 sets of a UR-26 sequence. The second CNOT between ions 1 and 2, $\tau^{(1,2)}_{\mathrm{CNOT}}$, takes 5.54 ms interleaved by 12 sets of a UR-22 sequence. The probe pulse is applied to ion 4 by a $\pi/2$-pulse of varying phase. The preliminary result is shown in Fig. 9.11. The excitation probability of ion 4 shows a contrast of 0.56(5) and a phase of $(0.51(3))\pi$. Here, the contrast of ion 4 indicates the success of the teleportation protocol. However, the measured phase is shifted by the phase $\pi$, which is due to the missing control Pauli-$Z$ in the analysis script. Furthermore, the SR pulses could also influence the phase of the quantum memory.

Currently, the superposition state is only an example to test quantum teleportation in our system. Arbitrary states are still required to be studied. Further investigations worth considering include (a) trying to improve the protocol fidelity by improving each Bell-state gate, (b) starting the experiment from the ground-state cooling, and (c) preparing an arbitrary state to be teleported.

## 9.4 Summary of Experimental Results and Outlook

In this chapter, we discussed some essential ingredients for experiments with a four-ion system in a non-segmented linear ion trap. The spin-spin couplings between all 4 ions have been measured. They all agree with the theoretical calculation within 2.2 standard deviations. The Bell state between a pair of nearest neighbors and second-nearest neighbors has been demonstrated. This is possible by the long-range interaction in our MAGIC scheme. Furthermore, while creating an entangled pair, another qubit can serve as a quantum memory. This memory qubit can be protected with the same DD sequence as the one applied to the Bell-state operations. The memory qubit is required to be isolated from the qubit interaction because of the always-on coupling within the MAGIC scheme, which can be achieved by the selective recoupling pulse technique. Here, the demonstration also indicates that we can perform experiments with 3 qubits simultaneously using 3 coherent control sources. This control can be achieved by a synchronization circuit, explained in Ref. [103].

To perform quantum information processing in a non-segmented linear trap, the quantum state transfer within a quantum register is also an important element. This chapter shows an example of a quantum state transfer using a quantum teleportation scheme. A preliminary result shows that it is possible to transfer a superposition state from one end to another end of a quantum register. There is still an open question of whether any arbitrary state can be teleported, which requires further investigation.

To quantify the teleported memory, the quantum state tomography can be considered. The teleportation fidelity can also be compared when the ground state cooling is applied. The qubit coherence is currently protected against dephasing by a DD-pulse sequence, which we could try to achieve by continuous DD (or a dressed state). The technique from this experiment can be applied to a larger system, for example, a full quantum byte or across quantum registers. In addition, if the teleportation protocol is performed with stronger spin-spin coupling, the operation time of the state transfer by this method could be shorter than the ion shuttling operation. Furthermore, the teleportation protocol can be extended to implement a quantum gate using teleportation [211].

# 10

# Summary and Outlook

Trapped ion systems are one of the promising candidates for building a large-scale, universal quantum computer. The work presented in this dissertation has explored several topics regarding the realization of a trapped-ion-based quantum processor using radio-frequency-driven hyperfine qubits in a static magnetic field gradient:

- decreasing motional excitation level near the motional ground state in a one- and two-ion system using RF radiation;
- investigation of possible sources of the qubit dephasing;
- investigation of the limitation of the fidelity of two-qubit gates;
- realization of a quantum algorithm to enhance the decision-making process for a type of machine learning methods;
- realization of a quantum algorithm to transfer a quantum state within a static quantum register.

The experimental techniques to study systems of spin-coupled qubits have been developed. All experimental demonstrations were performed with $^{171}\mathrm{Yb}^+$ ions detained in a macroscopic linear Paul trap with a permanent magnet magnetic field gradient [27, 83]. Computations can be tailored by coherent RF pulses and by tuning the experimental parameters [58]. Each qubit, represented by one physical ion, is encoded into two hyperfine levels of the ground state $^2\mathrm{S}_{1/2}$, which are the magnetic-field-sensitive state $|^2\mathrm{S}_{1/2}\,(F=0)\,\rangle$ and $|^2\mathrm{S}_{1/2}\,(F=1, m_F=+1)\,\rangle$, and it can be individually addressed and controlled by RF pulses near $2\pi \cdot 12.6\,\mathrm{GHz}$.

We have demonstrated near-ground-state cooling achieved by the sideband cooling of a single Doppler-cooled ion with a combination of radio-frequency and a repumping laser. The average phonon number after sideband cooling has achieved at $\langle n \rangle = 0.30(12)$ corresponding to the motional ground state occupation of 77 %. This is at the theoretical limit due to the current heating rate of our experiment. The success of sideband cooling has accomplished by optimizing the laser intensity of the repumping optical transition, as it has been also shown by the simulation of the rate equation model. This experiment used two methods to determine the average phonon number, which were the observation of the decay of the Rabi oscillation using a manipulation frequency on the qubit resonance and the excitation probability of the sideband of the RF-optical double-resonance spectrum. The average phonon number of a low motional level state was determined by observing the excitation probability of the sideband spectrum while the average phonon number of a highly excited motional level state was determined by observing the decay of the Rabi oscillation. For a two-ion system, this study is the first demonstration of sympathetic sideband cooling using RF radiation of two individually addressable identical isotopes of the same species. We investigated the average phonon numbers of each individual ion after performing the sideband cooling on different motional modes and ions. The cooling method was performed at an axial trap frequency similar to a trap potential frequency of neutral atom trap experiments, therefore the method could be applied to many neutral atom experiments and also hyperfine state trapped ion experiments using the availability of commercial RF devices.

During the course of improving the fidelity of our quantum gates, we have outlined four categories of possible sources of qubit dephasing: the incoherence of qubit controls, the fluctuation of magnetic fields, the fluctuation of electric fields, and the delocalization of an ion in a magnetic field gradient. The incoherence of qubit controls such as RF pulses of the qubit coherent control and the light-induced decoherence [108] were completely ruled out as sources of dephasing. Moreover, when we used either the Helmholtz coils or the permanent magnets to generate a magnetic field offset for the Zeeman splitting, the qubit coherence time has not been significantly different. That means we also ruled out the noise from the offset field. Furthermore, ambient magnetic fields were negated by an active magnetic-field stabilization, which can compensate frequency components up to 700 Hz. However, the field-stabilization system was not operating at full potential due to the location of the magnetic sensor. The sensor could not be placed close to where ions are located, but it could only be placed outside the vacuum chamber and at a distance of approximately 30 cm from where the ions are trapped. Ions' movement in a magnetic field gradient caused by the fluctuation of electric fields can be interpreted as magnetic noise. Micromotion compensation and passive filtering of DC potentials lowered the heating rate by one order of magnitude, but they have not changed the qubit coherence time. UV lasers could charge exposing materials such as the RF trap electrodes, the vacuum recipient, and the window of the objective viewport. These could cause a change of the static potential which has been counteracted by the adaptive frequency correction of the qubit addressing frequencies, therefore, it was negligible. Additionally, the transverse coherence time of an ion near the motional ground state was also similar to the coherence time of the Doppler cooled state. By having considered various sources, we have come to a conclusion that the likely important sources of dephasing are (i) vibration of magnets and (ii) fluctuations of the magnetic field of the permanent magnets. The cylindrical permanent magnets have been mounted on the endcap electrodes without any rigid fix, which might allow a small movement of the magnets. The temperature of the trap could be more than 370 K, as mentioned in Ref. [159], which might induce fluctuations of magnetization.

We have improved the fidelity of our two-qubit gates, shown by a CNOT gate and a Bell gate of a two-qubit system. However, we have not found the main source of the qubit dephasing as summarized in the previous paragraph. In the meanwhile, we have protected qubit states against the qubit dephasing using the dynamical decoupling pulse sequences. However, DD pulse sequences can act as a band-pass filter to let some frequency components of magnetic field pass with respect to their pulse interval. These noise components can destroy the qubit coherence. Therefore, the sequence has been required to be adjusted to avoid frequency components of magnetic noise, which can be different for each laboratory. Additionally, the pulse error can accumulate limiting the number of pulses used in a DD sequence. Composite pulse sequences could be employed to improve the robustness of a simple pulse in terms of the detuning error from the qubit resonance and the pulse rotation error, however, they cannot be applied directly to the DD sequence as shown by our simulation. Furthermore, we have studied the effect of the motional excitation on the Bell-state fidelity, and there was no significant effect. Lastly, we improved the Bell-state fidelity by 5 % due to the implementation of the double threshold method to reduce the detection error. Altogether, as a result of this work the Bell-state fidelity has been improved from 0.63(3) [83] to 0.935(19). After correcting the SPAM error, the Bell-state fidelity has achieved at 0.95(3). This is not at the high-fidelity level yet, we still need to improve the fidelity further. To my knowledge, the best of two-qubit MW gate using hyperfine qubits has the fidelity of 0.997(1), which has been achieved by an oscillating magnetic field gradient [177].

With all improvements, we have experimentally demonstrated the proof-of-principle quantum enhanced deliberation process with a quantum learning agent implemented by a quantum processor. This unit of the deliberation process is an essential element in the reinforcement learning framework, which is one of the pillars of machine learning techniques as a sub-field of artificial intelligence. The reinforcement learning framework can realize an automated machine capable to learn how to interact with an environment. We have implemented our deliberation process using the reflecting projective simulation model [190] based on a stochastic diffusion process of the memory of an agent. This model allows a quadratic speed-up of the deliberation process for quantum agents with respect to their classical counterparts. The two primary features of a quantum reflecting projective simulation algorithm have been verified: (i) quadratically faster scaling of the deliberation process using the quantum learning agent compared with its classical counterpart and (ii) preservation of the tail of the stationary distribution representing the memory of agents. Besides the experimental demonstration, our error model has completely described the errors in our experimental results, which came from the qubit decoherence, the addressing error, and the asymmetric detection error. This demonstration highlights the potential of a quantum processing unit in the field of quantum-enhanced learning and artificial intelligence enabling fast learning within a rapidly changing environment.

We have further discussed some essential ingredients for a static quantum register using a small-scale register of four ions. We demonstrated this system to prepare tools and techniques before extending to a large-scale quantum processor. We have measured the spin-spin couplings in the magnetic gradient induced coupling scheme between four ions for the first time, that they all agree well with the theoretical calculation within 2.2 standard deviations. The Bell state between a pair of nearest-neighbor and second-nearest-neighbor have been demonstrated together with another qubit serving as a quantum memory, even though the MAGIC scheme has the always-on interaction between ions. The isolation of the memory qubit has been achieved by the selective decoupling pulse technique. Additionally, we have used the quantum teleportation protocol to assist performing quantum information processing in a static quantum register, which has been implemented by a non-segmented ion trap. A preliminary result has shown that it was possible to transfer a superposition state from one end to another end of a quantum register. The fidelity of the teleported memory has achieved at 0.56(5) which has been mainly limited by the fidelity of a two-qubit gate. We still need further investigations on the quantum state transfer of any arbitrary state and as well the improvement of the protocol fidelity.

We still must keep searching for possible noise sources as well as techniques to extend the qubit coherence time to be able to perform higher-fidelity operations in the future. Passive magnetic field shielding can reduce magnetic noise from an environment [36]. In addition, the dressed-state qubits have been proven to obtain the fidelity of a two-qubit gate of 0.985(12) [60] in a comparable experimental setup. We can even further extend the level of dressed state to the double-dressed state picture [212], which has theoretically shown the noise robustness for a phase gate and a Mølmer–Sørensen gate. Alternatively, we could use the optimal control technique to design a two-qubit gate integrated with a dynamical decoupling pulse scheme. In the near future, when we have a new ion trap which could provide a much larger magnetic field gradient compared with the current setup, then the trap parameters could be improved. The sideband cooling will be faster. The spin-spin coupling will be larger, which will reduce the gate time of two-qubit and multi-qubit gates. The total manipulation time of a quantum algorithm would be reduced allowing the implementation of more complex algorithms and more operations if we could have a comparable qubit coherence time with the current setup. By improving the trap material, the heating rate and the magnetic field noise caused by permanent magnets, which might come from the fluctuation of the magnetization, could be reduced.

When we open the vacuum recipient, we could consider investigating the following: the vibration of the permanent magnets and the temperature effect of the permanent magnet on the qubit coherence time. Moreover, we should consider installing a pressure gauge and a magnetic field sensor inside the vacuum recipient.

In micro-structured traps [13, 213, 214], the higher magnetic field gradient is possible to achieve. This technique also allows ions to be placed near an RF source, which is advantageous for the single-qubit manipulation. This will require significantly lower RF powers, which will reduce the amplitude fluctuation of RF pulses. Furthermore, photodetectors could be fabricated directly to the trap chip [215], which will improve the detection fidelity.

To achieve a fault-tolerant universal quantum computer, the number of qubits must be increased and all errors must be lower than the error-correction threshold. Therefore, quantum error correction or topological qubits will be applied, when a large qubit system is achieved and the gates, preparation, and readout are at high fidelity. However, the topological qubits still need more experimental evidence to be conclusive. The techniques implemented here throughout this work together with the techniques mentioned above and the concept of the dressed states offer a promising future for an ion-based fault-tolerant quantum computer.

# A

# List of Publications

## Publications

The work described in this dissertation has given to the following publications:

1. “Speeding-up the decision making of a learning agent using an ion trap quantum processor”, **T. Sriarunothai**, S. Wölk, G. S. Giri, N. Friis, V. Dunjko, H. J. Briegel, and Ch. Wunderlich, arXiv: 1709.01366 (2017) (submitted to QST).
2. “Radio frequency sideband cooling and sympathetic cooling of trapped ions in a static magnetic field gradient”, **T. Sriarunothai**, G. S. Giri, S. Wölk, and Ch. Wunderlich, Journal of Modern Optics 65, 5-6 (2017).

Further publications:

1. “Consistency test for quantum process tomography”, S. Wölk, **T. Sriarunothai**, G. S. Giri, and Ch. Wunderlich, arXiv: 1808.10336 (2018) (submitted to NJP).
2. “Versatile microwave-driven trapped ion spin system for quantum information processing”, C. Piltz, **T. Sriarunothai**, S. S. Ivanov, S. Wölk, and Ch. Wunderlich, Science Advances 2, e1600093 (2016).
3. “State selective detection of hyperfine qubits”, S. Wölk, C. Piltz, **T. Sriarunothai**, and Ch. Wunderlich, Journal of Physics B 48, 075101 (2015).
4. “A trapped-ion-based quantum byte with $10^{-5}$ next-neighbour cross-talk”, C. Piltz, **T. Sriarunothai**, A. F. Varón, and Ch. Wunderlich, Nature Communications 5, 4679 (2014).

## Oral Presentations

1. “Speeding-up the decision making of a learning agent using an ion trap quantum processor”
   DPG-Frühjahrstagung 2018 (DPG Spring Meeting), Erlangen, Germany
   (March 5-9, 2018)

2. “Speeding up a Coherent Quantum Fourier Transform using 3-Qubit Conditional Gates”
   619. WE-Heraeus-Seminar on Quantum Speed Limits, Bad Honnef, Germany
   (June 8-10, 2016)

3. “Investigation of Hyperfine Qubit Dephasing in Trapped Ions”
   DPG-Frühjahrstagung 2016 (DPG Spring Meeting), Hannover, Germany
   (February 29 - March 4, 2016)

4. “Experimental realization of the Quantum Fourier Transform based on multiple coupling”
   DPG-Frühjahrstagung 2015 (DPG Spring Meeting), Heidelberg, Germany
   (March 23-27, 2015)

## Posters

1. “Speeding up a Coherent Quantum Fourier Transform using 3-Qubit Conditional Gates”
   619. WE-Heraeus-Seminar on Quantum Speed Limits, Bad Honnef, Germany
   (June 8-10, 2016)

2. “A Quantum Toolbox and Experimental Realization of the Quantum Fourier Transform with Trapped Ions”
   Quantum Information Processing and Communication (QIPC2015)
   University of Leeds, Leeds, United Kingdom
   (September 13-18, 2015)

# B

# List of Devices

## Experimental control

| | |
|---|---|
| DSP | Jäger GmbH ADwin-Pro<br>- Pro-CPU-T9<br>- Ethernet computer link<br>- 2x DIO 32<br>- AIN8/12<br>- AOUT8/16 |
| Experiment sequence | National Instruments LabVIEW 2015 |
| DAC | PLUG-IN Electronics USB-3112 |
| Frame grabber card | BitFlow Neon-CLB CameraLink |

## Paul trap

| | |
|---|---|
| Function Generator | Stanford Research Systems DS345 |
| Power amplifier | Kalmus 714FC-CE |
| RF Helical resonator | Prague University Ivo Polak's design |
| Permanent magnets | Magnetic Component Engineering (UK) Ltd<br>SmCo tubes S2869 [83] |

## VFG synchronization

| | |
|---|---|
| Atomic clock | Stanford Research Systems FS725 |
| 4-way Power splitter | Mini-Circuits ZCSC-3-R3+ |
| Schmitt trigger | In-house [103] |
| Data flip-flop | In-house [102] |
| TTL Fan-out | In-house [103] |

## RF control chain

| | |
|---|---|
| RF sequence | In-house VFG-150 Versatile Frequency Generator |
| RF power amplifier | Globes 10W PA Elisra (+35dB) |
| RF power amplifier | Microwave Amplifiers Ltd AM43-12.4-12.8-43-43 (+45dB) |
| RF pre-amplifier | Mini-Circuits ZFL-500LN+ |
| RF pre-amplifier | Mini-Circuits ZX60-183A+ |
| RF pre-amplifier | Mini-Circuits ZX60-14012L+ |
| Power supply (for AM43) | TOELLNER TOE 8851-16 |
| RF low-loss cable | Elspec Phase Master 300 PM300-SMA11-SMA11-1500 |
| Dual loop PLL oscillator | MITEQ DLCRO-010-12568-3-15P |
| MW switch | Narda SPST S213D |
| 3-way Power cominer/splitter | Mini-Circuits ZFRSC-183-S+ |
| 3-way Power cominer/splitter | Mini-Circuits ZFRSC-2-1W+ |
| 4-way Power cominer/splitter | Mini-Circuits ZCSC-3-R3+ |
| High-pass filter | Mini-Circuits SHP-50+ |
| MW mixer (double-balanced) | Macom M79 |
| MW mixer (double-balanced) | Mini-Circuits ZX05-153LH+ |
| MW mixer (SSB) | Maki SSB-0618MXW-2 |
| MW attenuator (-10dB) | Elisra MW21110 |
| MW attenuator (-6dB) | Mini-Circuits BW-S6W2+ |
| MW attenuator (-3dB) | Mini-Circuits BW-S3W2+ |
| MW isolator | AtlanTecRF ACI-20240-SF-SF (5W) |
| MW isolator | TKI Ferrit IC 12,5 (1W) |
| MW isolator | TKI Ferrit IC 12,5-10W (10W) |
| MW isolator | (Unknown) MW 11218 |
| MW isolator | MSC Microwave Ltd MCSM 0616 P-0190-08 (25W) |
| MW isolator | Raditek RADI-10-15-S3-1WR-60W Fwd-g18 (60W) |
| MW isolator | UIY UIYCI1220A10T13SF (60W) |
| MW termination | api technologies corp. 50W SMA termination TS180M-50W |

## Vacuum Components

| | |
|---|---|
| Ion Getter Pump | StarCell VacIon Varian 919-0110 20l/s |
| Vacuum Controller | Varian MiniVac Controller 2008 Model 929-0290 |

## Helmholtz Coils

| | |
|---|---|
| 3-channel power supply | Low residual ripple power supply Toellner TOE 8733-2 |

### Optical Resonator

| | |
|---|---|
| CF Windows (369 laser) | Kurt J. Lesker Company UV Quartz DN16CF VPZL-133Q |
| Lemo cable | Lemo cable Lemo Gmbh FGG.1B.306.CLAD52 |
| Lemo connector (6 pins) | Air-tight connector Lemo Gmbh HGG.1B.306.CLLSV |
| Lemo connector | Air-tight connector Lemo Gmbh HGP.00.250.CTLSV |
| Pressure measurement | In-house $\mu$Trap MPX4100A [107] |

### AOM Components

| | |
|---|---|
| Acousto-optic modulator | AOM (old) 65 MHz IntraAction ASM-702B8M |
| Acousto-optic modulator | AOM (new) 90 MHz ISOMET AOM 1206C-833 |
| Acousto-optic modulator | AOM 960 MHz Brimrose TEF-1050-50-369 |
| AOM driver (SUB-D9 port) | Brimrose VFF-1050-50SPS-B1/B2-C1 |
| Acousto-optic modulator | AOM 115 MHz Crystal Technology 31110-125 |
| Voltage-controlled oscillator | VCO (for old AOM 65 MHz) Mini-Circuits ZX95-100-S+ |
| Voltage-controlled oscillator | VCO Mini-Circuits ZX95-200-S+ |
| Five-Axis Kinetic mount | Newport Five-Axis Aligner 9081-M |
| Stable mounting | Radiant Dyes RD-PDT-B |

### Lasers

| | |
|---|---|
| Laser diode (369 nm) | Nichia NDU1113E 20 mW |
| Laser diode (399 nm) | Unknown |
| Laser diode (638 nm) | Thorlabs Mitsubishi ML520G54-01 110 mW |
| Laser diode (935 nm) | eagleyard photonics EYP-RWE-0980-08020-1500-SOT02-0000 (serial AG-02607) 1 mW |
| Optical fiber | Polarization-maintaining type Thorlabs PM-S350MHP |
| Fiber collimator | Schäfter+Kirchhoff 60FC-4-A11-01 |
| Electro-optic modulator (EOM) | Photline NIR-MPX800 for 935 laser |

### Ion Detection

| | |
|---|---|
| EMCCD Camera | Andor iXon Ultra 890 DU-897U-CS0-EXF X-8188 |
| EMCCD software | Andor Solis 64bit 4.28.30001.0 |
| Photo-multiplier tube | Hamamatsu R5600P |

# C

# Ytterbium Ion

The detailed information about the energy structure of ytterbium ions is summarized in tables C.1, C.2, and C.3. It is visualized in Fig. C.1. Our optical repumping scheme depopulates the state $|^2D_{3/2}\rangle$ and $|^2F_{7/2}\rangle$ using the 935-nm and the 638-nm laser. There are two known alternative repumping schemes, shown in figures C.2 and C.3. The scheme in Fig. C.2 could be an alternative choice for our future experiments because the natural lifetime of the state $|^1D[3/2]_{3/2}\rangle$ is much shorter than of the state $|^1D[5/2]_{5/2}\rangle$.

**Table C.1:** Yb II energy levels and their lifetime. The energy levels are the calculated values provided by the atomic database from NIST. The experimental observation of the hyperfine splittings was performed using $^{171}\mathrm{Yb}^+$ions. N/A means the experimental data is not available.

| Term | Energy ($\mathrm{cm}^{-1}$) [216] | Hyperfine splitting $\Delta/2\pi$ (GHz) | Lifetime | Ref. |
|---|---|---|---|---|
| $^2S_{1/2}$ | 0 | 12.642 812 118 466(2) | - | [93, 217] |
| $^2P_{1/2}$ | 27 061.82 | 2.1049(13) | 8.12(2) ns | [149, 218] |
| $^2P_{3/2}$ | 30 392.23 | 1.7508(10) | 6.15(9) ns | [219, 220] |
| $^2D_{3/2}$ | 22 960.80 | 0.86(2) | 52.7(24) ms | [26, 221] |
| $^2D_{5/2}$ | 24 332.69 | 0.191(2) | 7.2(3) ms | [222, 223] |
| $^2F_{7/2}$ | 21 418.75 | 3.620(2) | $5.4^{+9.3}_{-3.6}$ yr | [224–226] |
| $^3D[3/2]_{1/2}$ | 33 653.86 | 2.2095(11) | 37.7(5) ns | [26, 227] |
| $^3D[1/2]_{1/2}$ | 33 378.89 | N/A | N/A | |
| $^1D[3/2]_{3/2}$ | 34 575.37 | N/A | 28.6(4) ns | [227] |
| $^1D[5/2]_{5/2}$ | 37 077.59 | 0.321(18) | $< 172$ ms | [220, 222] |

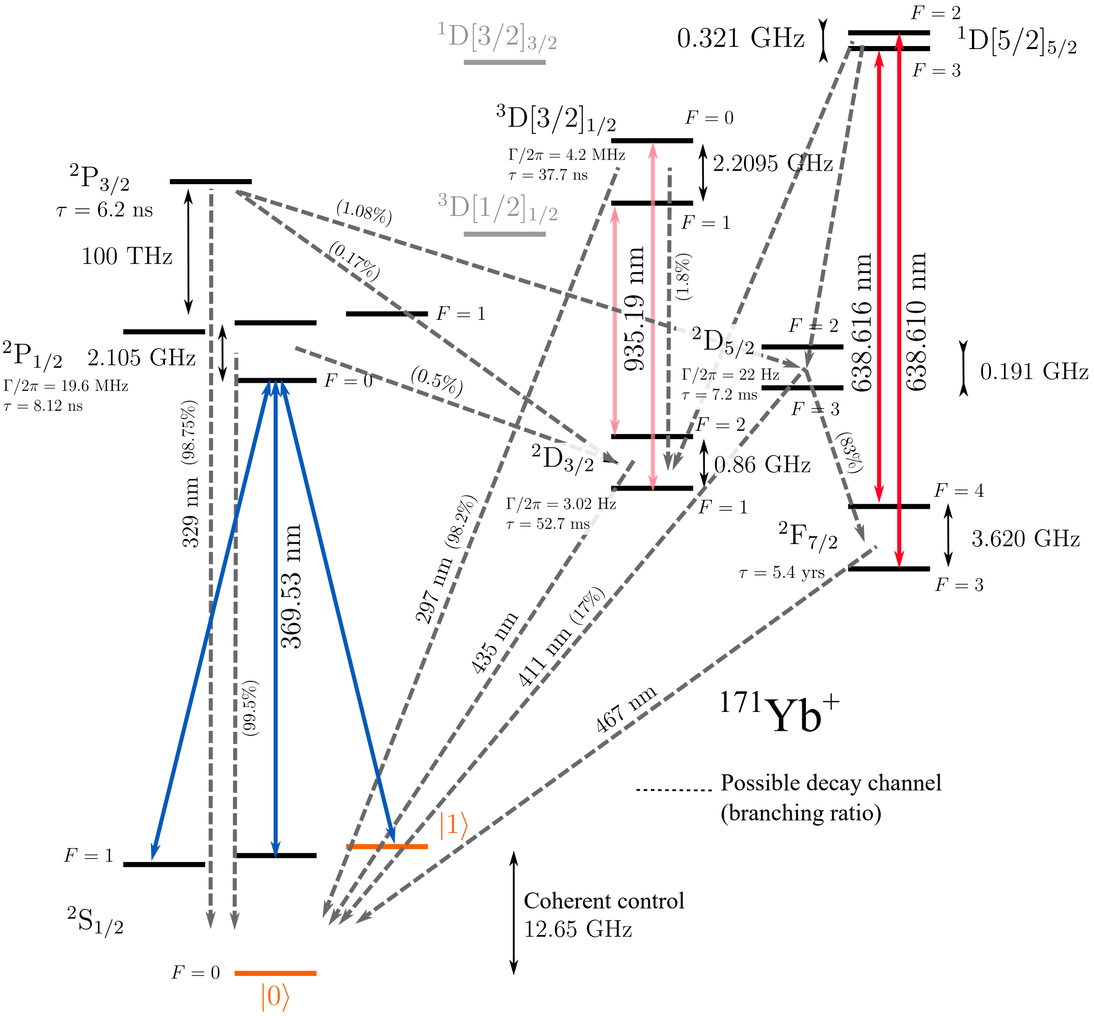

**Figure C.1: Energy level structure of $^{171}$Yb$^+$.** The schematic, not to scale, shows optical transitions for Doppler cooling and repumping, indicated by color arrows. Significant decay channels are shown by dashed lines. Numbers in round parentheses show the branching ratio for each possible channel. The main qubit states are highlighted in orange. Our optical repumping scheme depopulates the state $|^2D_{3/2}\rangle$ and $|^2F_{7/2}\rangle$ using the 935-nm and the 638-nm laser. (Adapted from Ref. [236].)

**Table C.2:** Yb II transitions. The upper shows our main transitions with the corresponding laser wavelength in vacuum. The lower shows the other known transitions with their references. The energy differences are provided by the atomic database from NIST.

| Transition | Linewidth | $\Delta E$ (cm$^{-1}$) [216] | Wavelength (nm) | Ref. |
|---|---|---|---|---|
| $^2\mathrm{S}_{1/2} \leftrightarrow {}^2\mathrm{P}_{1/2}$ | 19.6 MHz | 27 061.82 | 369.5 | [227, 228] |
| $^2\mathrm{D}_{3/2} \leftrightarrow {}^3\mathrm{D}[3/2]_{1/2}$ | 4.2 MHz | 10 693.06 | 935.2 | [227, 228] |
| $^2\mathrm{F}_{7/2} \leftrightarrow {}^1\mathrm{D}[5/2]_{5/2}$ | $> 0.9$ Hz | 15 658.84 | 638.6 | [222, 225, 228] |
| $^2\mathrm{S}_{1/2} \leftrightarrow {}^1\mathrm{D}[3/2]_{3/2}$ | 5.4 MHz | 34 575.37 | 289.139 | [216, 227, 228] |
| $^2\mathrm{S}_{1/2} \leftrightarrow {}^3\mathrm{D}[3/2]_{1/2}$ | 4.2 MHz | 33 653.86 | 297.056 | [228, 229] |
| $^2\mathrm{S}_{1/2} \leftrightarrow {}^2\mathrm{P}_{3/2}$ | 25.8 MHz | 30 392.23 | 328.937 | [228] |
| $^2\mathrm{S}_{1/2} \leftrightarrow {}^2\mathrm{D}_{5/2}$ | 22.9 Hz | 24 332.69 | 410.97 | [222, 223] |
| $^2\mathrm{S}_{1/2} \leftrightarrow {}^2\mathrm{D}_{3/2}$ | 3.02 Hz | 22 960.80 | 435 | [225, 230] |
| $^2\mathrm{S}_{1/2} \leftrightarrow {}^2\mathrm{F}_{7/2}$ | 0.9 nHz | 21 418.75 | 467 | [224, 225] |
| $^2\mathrm{D}_{3/2} \leftrightarrow {}^3\mathrm{D}[1/2]_{1/2}$ | N/A | 16 418.09 | 609.1 | [231] |
| $^2\mathrm{F}_{7/2} \leftrightarrow {}^1\mathrm{D}[3/2]_{3/2}$ | 5.4 MHz | 13 156.62 | 760.072 | [227, 232, 233] |
| $^2\mathrm{F}_{7/2} \leftrightarrow {}^2\mathrm{D}_{5/2}$ | 22.9 Hz | 2913.94 | $3.43 \times 10^3$ | [222, 234] |

**Table C.3:** Yb II branching ratio.

| Initial state | Final state | Ratio | Ref. |
|---|---|---|---|
| $^2\mathrm{P}_{1/2}$ | $^2\mathrm{S}_{1/2}$ | 0.994 99(15) | [26] |
|  | $^2\mathrm{D}_{3/2}$ | 0.005 01(15) |  |
| $^2\mathrm{D}_{5/2}$ | $^2\mathrm{F}_{7/2}$ | 0.83(3) | [222] |
|  | $^2\mathrm{S}_{1/2}$ | 0.17(3) |  |
| $^2\mathrm{P}_{3/2}$ | $^2\mathrm{S}_{1/2}$ | 0.9875(6) | [220] |
|  | $^2\mathrm{D}_{3/2}$ | 0.0017(1) |  |
|  | $^2\mathrm{D}_{5/2}$ | 0.0108(5) |  |
| $^3\mathrm{D}[3/2]_{1/2}$ | $^2\mathrm{S}_{1/2}$ | 0.982* | [235] |
|  | $^2\mathrm{D}_{3/2}$ | 0.018* |  |

*Calculated values

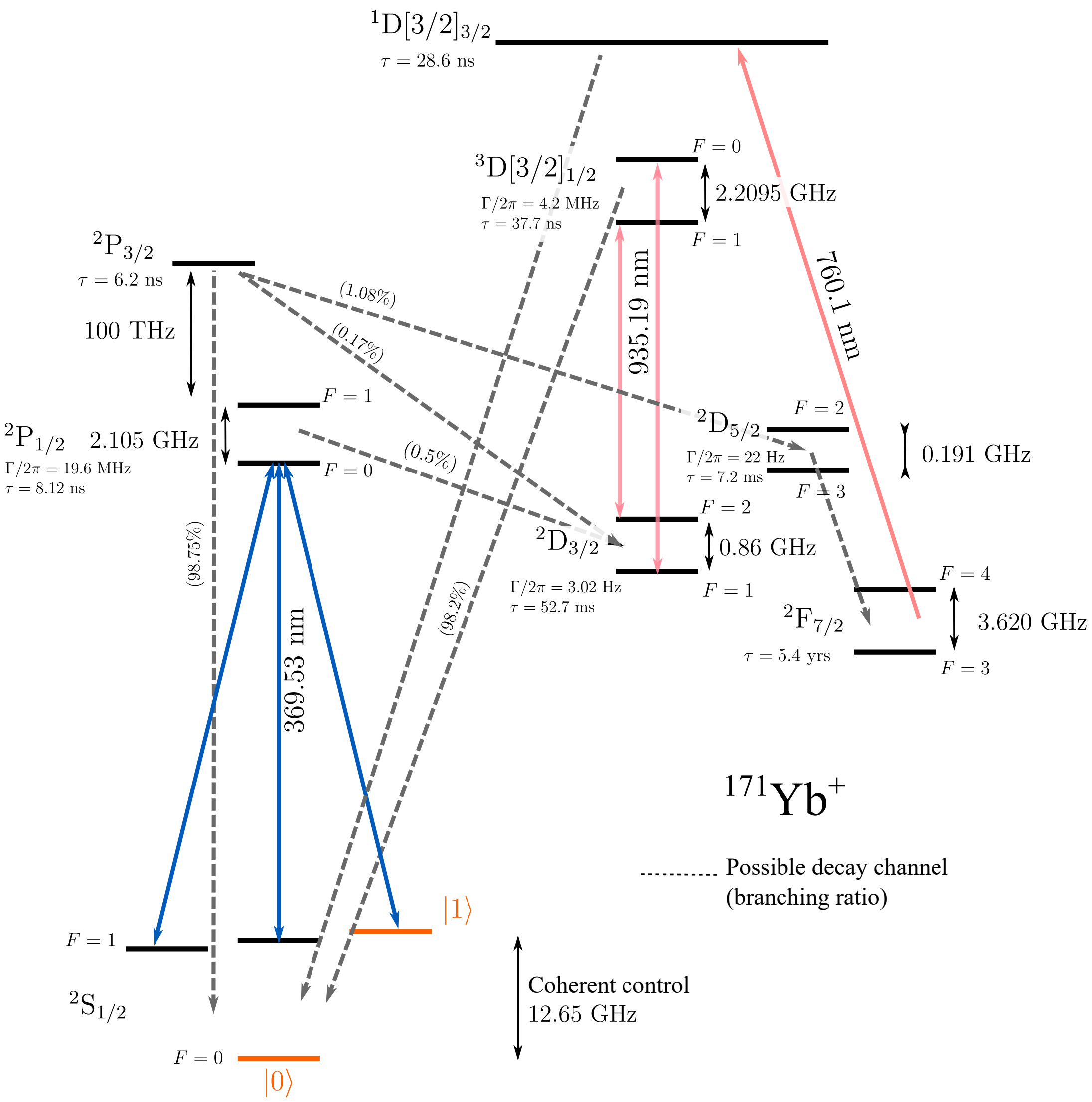

**Figure C.2: Alternative repumping scheme 1.** This scheme has been used in Japanese National Research Laboratory of Metrology [232] and German National Metrology Institute (PTB) [233]. This is an alternative repumping scheme from the long-lifetime state $|^2F_{7/2}\rangle$. This method could be a better choice because the state $|^1D[3/2]_{3/2}\rangle$ has the natural lifetime much shorter compared to the state $|^1D[5/2]_{5/2}\rangle$, which is used in our repumping scheme, see Fig. C.1 or Fig. 3.1.

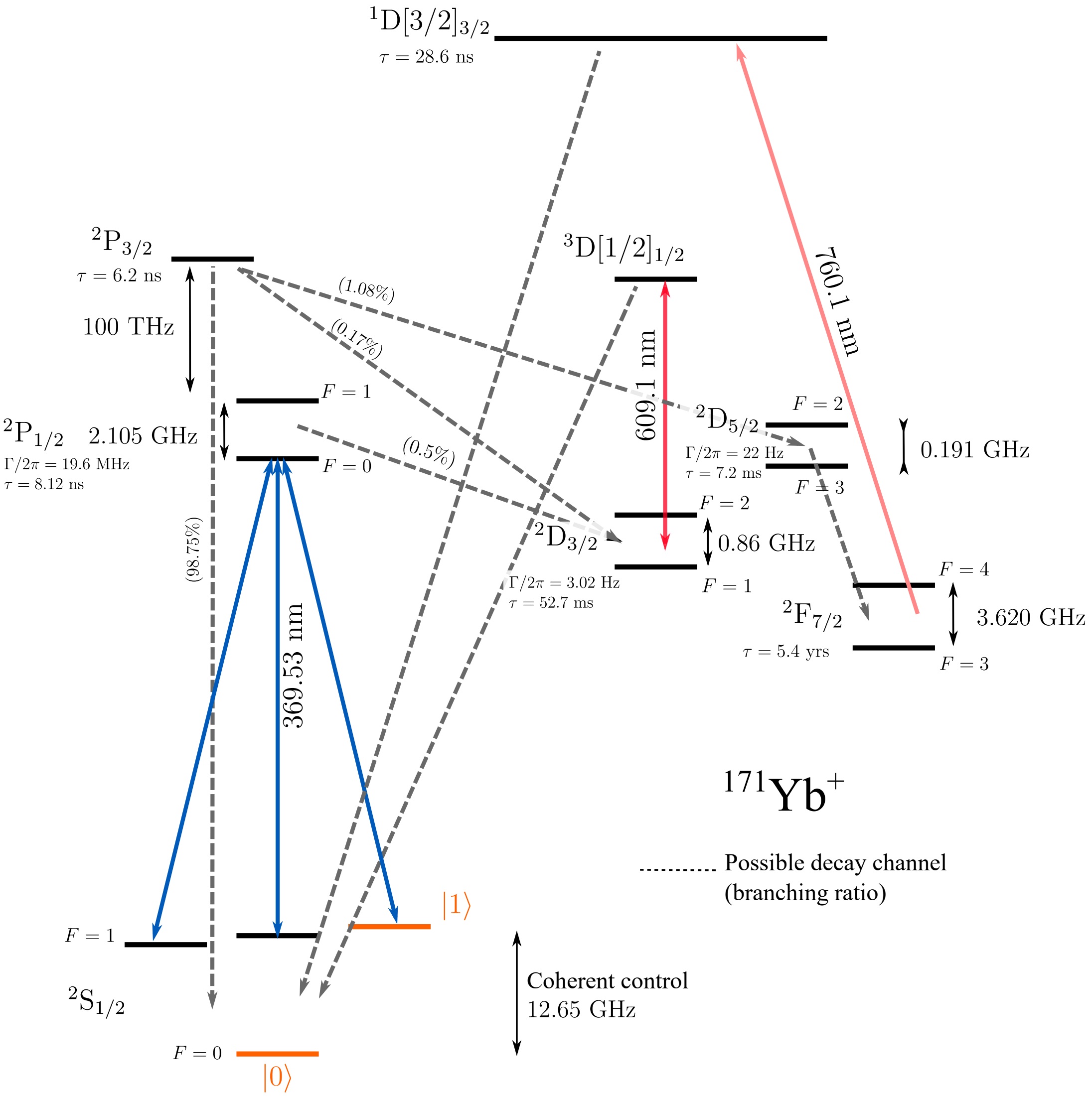

**Figure C.3: Alternative repumping scheme 2.** The laser at 609 nm has been introduced to depopulate the state $|^2\mathrm{D}_{3/2}\rangle$ in Ref. [231] from CSIRO National Measurement Laboratory (Australia). However, there is still a chance to be in the state $|^2\mathrm{D}_{5/2}\rangle$, then the laser at 760 nm is necessary. Since then there is only this research group reporting about the use of the 609-nm laser. We still need more information on the natural lifetime of the state $|^3\mathrm{D}[1/2]_{1/2}\rangle$.

# D

# Simulation Scripts

All simulation scripts use a MATLAB package from Ref. [237]. The scripts are written in MATLAB R2017a. The scripts are available on our shared hard drive.

## D.1 Rate Equation Model for SBC

The following MATLAB scripts are used in section 5.1.1.

```
function out=RE_SBC(Omega, TrpF, Gam, tSBCmax)
%This programm solves the rate equations for the population of the phonon
%numbers. One can obtain with it the phonon population distribution at
%every time between the span given by the tspan variable
%The input parameters are
%Omega, the rabi Oscilation frequency in Hz. (not the angular frequency)
%TrpF, the trap frequency in Hz. (not the angular frequency)
%Gam, the decay rate in Hz. (not the angular frequency)
%
%The output out gives the average phonon number a the end of the
%sideband cooling process that happens at max(tspan).
%
%The initial population is given by a thermal distribution whose average
%population number is set by nz0.
%
% Andres F Varon May 2013

% tspan = [0, 20e-3];
tspan = [0, tSBCmax]; % upto tSBCmax s

% nz0=150*120e3/TrpF; %The initial ocupation Number is related to the
%                     %initial energy
nz0=100; %The initial ocupation Number is related to the
                    %initial energy

[nz, p0]=population_n(nz0);

Omega=2*pi*Omega;
TrpF=2*pi*TrpF;
```

```
Gam=2*pi*Gam;

OmegaTxT=num2str(Omega/(2*pi*1e3), '%.0f');
GammaTxT=num2str(Gam/(2*pi*1e3), '%.0f');
TrapTxT=num2str(TrpF/(2*pi*1e3), '%.0f');
tTxT=num2str(max(tspan)*1e3, '%.0f');


ode = @(t,p) RateEquations(t, p,  Omega, TrpF, Gam);
[t,p] = ode45(ode, tspan, p0);

for m=1:size(p,1)
    p(m,:)=p(m,:)/sum(p(m,:));
end

t=t*1e3;

n=0:size(p,2)-1;
X=meshgrid(n, 1:size(p,1));
n_av=sum(X.*p,2);
n_zoom=0:floor(min(n_av)*8);
out=n_av(size(p,1));

txt=['\Omega_{MW}=2\pi\times' OmegaTxT ' kHz '];
txt=[txt '  \Gamma_{369}=2\pi\times' GammaTxT ' kHz'];
txt=[txt '  \omega_{z}=2\pi\times' TrapTxT ' kHz'];
txt=[txt '   t_{max}=' tTxT ' ms'];

clf;
annotation('textbox', [0.06 0.95 0.9 .05], 'String', txt);

subplot('Position', [0.06 0.575 0.4 .33])
imagesc(t, n_zoom, transpose(p(:,n_zoom+1)));
set(gca,'YDir','normal')
title('Phonon Population');
xlabel('t (ms)')
ylabel('n');

subplot('Position', [0.56 0.575 0.4 .33])
plot(t,n_av, 'LineWidth',2);
title('Average phonon number');
xlabel('t (ms)')
ylabel('\langle n \rangle');

subplot('Position', [0.06 0.1 0.4 .33])
plot(n,p(1,:), 'LineWidth',2);
title(['Population at t='  num2str(t(1)) ' ms']);
legend(['\langle n \rangle=' num2str(n_av(1),'%.1f')]);
xlabel('n')
ylabel('Phonon Population');

subplot('Position', [0.56 0.1 0.4 .33])
[nz, p0]=population_n(n_av(size(p,1)));
```

```
plot(nz,p0, 'LineWidth',2, 'Color', 'r');
hold on
plot(n_zoom,p(size(p,1),n_zoom+1), 'LineWidth',2);
hold off
title(['Population at t='  num2str(t(size(p,1))) ' ms']);
legend('Thermal Dist', ['\langle n \rangle=' ...
                        num2str(n_av(size(p,1)), '%.1f')])
xlabel('n')
ylabel('Phonon Population');

name_str=['Om' OmegaTxT 'kHz_G' GammaTxT ...
            'kHz_v' TrapTxT 'kHz_t' tTxT 'ms'];
% cd('./Cooling_Simulation2');
print('-dpdf', name_str);
% print('-dmeta',  name_str);
savefig([name_str '.fig'])
save(name_str, 'p','t', 'txt', 'OmegaTxT', 'GammaTxT', 'TrapTxT', 'tTxT');
% cd('../');
```

```
function [nz, Pnz]=population_n(avnz)

%%%%%%%%%%%%%%%%%%%%%%%%%%%%%%%%%%%%%%%%%%%%%%%%%%%%%%%%%%%%%%%%%%%%%%%%%%%%%%
%This funcion calculates the thermal distribution for an average ocupation
%number naver.
%For a phonon number nz (given as vector) it is assigned a Probability
%Pnz (also given as a vestor)
%
%Andres F. Varon Sep. 2011
%%%%%%%%%%%%%%%%%%%%%%%%%%%%%%%%%%%%%%%%%%%%%%%%%%%%%%%%%%%%%%%%%%%%%%%%%%%%%%

%We truncate the Thermal distribution.
nzmax=avnz*10;
nz=0:nzmax;

%calculates the thermal population probability
Pnz=1/(avnz+1)*(avnz/(avnz+1)).^nz;

%We force the normalization (due to the truncation):
Pnz=Pnz/sum(Pnz);
```

```
function dpdt = RateEquations(t, p, Omega, TrpF, Gam)
%RateEquations define the evolution of the vibrational
%populations in the onset of Side Band Cooling

%Trap Gradient
Gradient=19; %T/m

%Constants definitions
m=171*1.6605e-27; %kg mass of 171
mub=9.27400915e-24;% Bohr Magneton J/T.
```

```
h=6.62606896e-34;% Planck Constant Js.
hbar=h/(2*pi);

%Size of the ground function
Dz=sqrt(hbar./(2*m*TrpF));

%Effective eta (Microwave)
etaeff=Dz*mub/hbar*Gradient./TrpF;

%Eta due to the laser transition
lambda=369.5e-9; %wavelength in m
% eta=2*pi*Dz/lambda;
eta=2*pi*Dz/lambda * cos(pi/4) ; % laser at 45 deg: eta = eta*cos(pi/4)

%p=(p+min(p));
p=p.*(p>0);
p=p/sum(p);
dpdt=zeros(size(p));

CR_fa = CoolRate(1, Omega, etaeff, eta, Gam, TrpF);
HR =    HeatRate(0, Omega, etaeff, eta, Gam, TrpF);
dpdt(1) = p(2)*CR_fa - p(1)*HR;

for m=2:max(size(p))-1
    CR_fa=  CoolRate(m  , Omega, etaeff, eta, Gam, TrpF);
    CR=     CoolRate(m-1, Omega, etaeff, eta, Gam, TrpF);
    HR=     HeatRate(m-1, Omega, etaeff, eta, Gam, TrpF);
    HR_fb=  HeatRate(m-2, Omega, etaeff, eta, Gam, TrpF);
    dpdt(m) = p(m+1)*CR_fa - p(m)*(CR+HR) + p(m-1)*HR_fb;
end

m=max(size(p));
CR=CoolRate(m-1, Omega, etaeff, eta, Gam, TrpF);
HR_fb=HeatRate(m-2, Omega, etaeff, eta, Gam, TrpF);
dpdt(m)=-p(m)*CR+p(m-1)*HR_fb;

if sum(dpdt)>1e-3
    sum(dpdt)
end
```

```
function out = CoolRate(n, Omega, etaeff, eta, Gam, TrpF)
%Gives the cooling rate for sideband cooling when the microwave
%is in resonance with the red side band

OmL = Gam;
etaL = eta;

GamP = 2*pi*19.6e6;
GamP = GamP*(1/4); % from to pump to |P,F=1> and fall to |S,F=0>


Om  = OmegaRSB(Omega,n, etaeff);
```

```
GamCC = OmL^2/(4*GamP);
out=Om^2*GamCC/(GamCC^2+2*Om^2);


GamRC = OmegaRSB(OmL,n, etaL)^2/(4*GamP);
Om=OmegaC(Omega,n, etaeff);
out=out+Om^2*GamRC/(GamRC^2+2*Om^2+4*(1*TrpF)^2);


end
```

```
function out=HeatRate(n, Omega, etaeff, eta, Gam, TrpF)

OmL = Gam;
etaL = eta;

GamP = 2*pi*19.6e6;
GamP = GamP*(1/4);  % from to pump to |P,F=1> and fall to |S,F=0>


GamBC = OmegaBSB(OmL,n, etaL)^2/(4*GamP);
Om=OmegaC(Omega,n, etaeff);
out=Om^2*GamBC/(GamBC^2+2*Om^2+4*(1*TrpF)^2);


GamCC = OmL^2/(4*GamP);
Om=OmegaBSB(Omega,n, etaeff);
out=out+Om^2*GamCC/(GamCC^2+2*Om^2+4*(2*TrpF)^2);

end
```

```
function out = OmegaBSB(Omega, n, etaeff)
%Omega_n calculates the Rabi frequency for a system between the
%levels n and n+1
if n>=0
    out=(n+1-(n^2+n)/2*etaeff^2+(n^3-n)/12*etaeff^4)/sqrt(n+1);
    out=etaeff*Omega*exp(-etaeff^2/2)*out;

else
    out=0;
end

end
```

```
function out = OmegaC(Omega, n, etaeff)
%OmegaC calculates the Rabi frequency for the carrier

out=Omega*(1-etaeff^2*n+1/4*etaeff^4*n*(n-1));
```

```

end
```

```
function out = OmegaRSB(Omega, n, etaeff)
%Omega_n calculates the Rabi frequency for a system between the
%vibrational levels n and n-1
if n>=1
    out=(n-(n^2-n)/2*etaeff^2+(n*(n-1)*(n-2))/12*etaeff^4)/sqrt(n);
    out=etaeff*Omega*exp(-etaeff^2/2)*out;

else
    out=0;
end

end
```

## D.2 Composite Pulse Sequence

The following MATLAB scripts are used in section 7.3. This is for a study of errors in the BB1 pulse sequence.

```
function sim_CompositePulse_v2( )

caseName = {'plain','BB1'};
caseID = 2;

step = 41;

inPsi = 1; % initial state |0>
rabiOmega = 2*pi*30e3;

% theta = pi/2;
theta = pi;
% theta = random('Uniform',0,pi,1,1);

phi = 0;

%%
% nOp = 5; % number of applied pulses
nOp = 1; % number of applied pulses

disp(['theta = ' num2str(theta*180/pi) ' deg'])


state_F = 1;
eta = 0.25;
```

```
% eta = 1;

del = [-eta:2*eta/(step-1):eta]*rabiOmega;
l = [-eta:2*eta/(step-1):eta]+state_F;

fidelity = [];
for k=1:step
    for j=1:step
        Delta = del(j);
        L = l(k);
        switch caseName{caseID}
            case 'plain'
                fidelity(k,j) = rotation1(inPsi,rabiOmega, ...
                                theta,phi,Delta,L, nOp); % plain pulse
            case 'BB1'
                fidelity(k,j) = rot_BB1(inPsi,rabiOmega, ...
                                theta,phi,Delta,L, nOp); % plain pulse
        end
    end
end

% rotation1(inPsi,rabiOmega,theta,phi,0,1, nOp)

%%
h = figure(6787); clf;
hold on;

set(h,'PaperUnits','centimeters');
xSize=12;
ySize=10;
% scaleXY = 1.25;
scaleXY = 1;
set(h,'PaperSize', scaleXY*[xSize ySize]);
set(h,'PaperPosition',[0 0 scaleXY*xSize scaleXY*ySize]);

fontsize=scaleXY*16;
fontname='Times';
markSize = scaleXY*8;

%%
[c,hc] = contourf( del./rabiOmega, l, fidelity );
hc.LevelList = [0.99 0.95 0.9:-0.1:0];
clabel(c,hc)
cb = contourcbar;
colormap('Hot');
caxis([0 1]);
cb.FontName = fontname;
cb.FontSize = fontsize;

% title(['Pulse Fidelity'])
xlabel('\delta/\Omega')
ylabel('L/L_0')

```

```
zlab = get(cb,'ylabel')';
set(zlab,'String',['Fidelity'],'FontSize',fontsize,'FontName',fontname);

a = gca;
a.Box = 'on';
a.FontSize = fontsize;
a.FontName = fontname ;

% print('-dpdf', ['simu_pi_' caseName{caseID}]) ;

end
```

```
function F = rotation1( inPsi, rabiOmega, theta , phi , ...
                        detuningRabi, length , nOp)

debug = 0;


f = length;
Delta = detuningRabi;

%%------------------------------
%%
%need module from [Computer Physics Communications 179 (2008) 430]
% addpath('D:\Users\Chronos\Documents\00_AT_Work\Research\ ...
%           Siegen\Research\Program_scripts\MatlabModules\QUBIT4MATLAB');


%%------------------------------
%%

ident = eye(2);             %define the identity
sigma_x=[0 1; 1 0];         %Pauli matrix X
sigma_y=[0 -1i; 1i 0];      %Pauli matrix Y
sigma_z=[1 0 ; 0 -1];       %Pauli matrix Z

if(inPsi == 1)
    ini_ket = ket([1 0]);

elseif(inPsi == 2)
    ini_ket = ket([0 1]);

elseif(inPsi == 3)
    ini_ket = ket([1 1]);

end

% nOp = 100;

R_op = R(rabiOmega, theta , phi ,Delta,f);
R_op_ideal = R(rabiOmega, theta , phi ,0,1);
fin_ket_ideal = (R_op_ideal)^nOp * ini_ket;
```

```

fin_ket = (R_op)^nOp * ini_ket;

F = abs( braket( fin_ket, fin_ket_ideal) ) ;

end

%=====================================================
%=====================================================
```

```
function F = rot_BB1( inPsi, rabiOmega, theta , phi , ...
                                detuningRabi, length , nOp)

debug = 0;


f = length;
Delta = detuningRabi;

%%-------------------------------
%%
%need module from [Computer Physics Communications 179 (2008) 430]
% addpath('D:\Users\Chronos\Documents\00_AT_Work\Research\ ...
%            Siegen\Research\Program_scripts\MatlabModules\QUBIT4MATLAB');


%%-------------------------------
%%

ident = eye(2);             %define the identity
sigma_x=[0 1; 1 0];         %Pauli matrix X
sigma_y=[0 -1i; 1i 0];      %Pauli matrix Y
sigma_z=[1 0 ; 0 -1];       %Pauli matrix Z

if(inPsi == 1)
    ini_ket = ket([1 0]);

elseif(inPsi == 2)
    ini_ket = ket([0 1]);

elseif(inPsi == 3)
    ini_ket = ket([1 1]);

end

% nOp = 100;

R_op = R(rabiOmega, theta , phi ,Delta,f);
R_op_ideal = R(rabiOmega, theta , phi ,0,1);
fin_ket_ideal = (R_op_ideal)^nOp * ini_ket;

fin_ket = (R_op)^nOp * ini_ket;
```

```

F = abs( braket( fin_ket, fin_ket_ideal) ) ;

end

%====================================================
%====================================================
function P=QRot(rabiOmega, theta,phi,Delta,f);
%time evolution of an arbitrary pulse with possible errors

Omega=rabiOmega;

%definition of Pauli spin operators
sigma_x=[0 1; 1 0];
sigma_y=[0 -1i; 1i 0];
sigma_z=[1 0 ; 0 -1];
ident=[1 0; 0 1];

theta=f*theta*sqrt(Omega^2+Delta^2)/Omega;

if Delta==0
    nperp=1;
    nz=0;
else
%   nperp=sqrt(Omega^2/Delta^2/(1+Omega^2/Delta^2));
    nperp=Omega/sqrt(Omega^2+Delta^2);
%   nz=sqrt(1/(1+Omega^2/Delta^2));
    nz=Delta/sqrt(Omega^2+Delta^2);
end;

P= cos(theta/2)*ident + ...
    1i*sin(theta/2)*(nperp*(cos(phi)*sigma_x-sin(phi)*sigma_y)+nz*sigma_z);

end


%%
function P=R(rabiOmega, theta,phi,Delta,f)

% Use RWR BB1

Rot = QRot(rabiOmega, 0.5*theta,phi,Delta,f);

phi1 = acos(-theta/(4*pi));
phi2 = 3*phi1;

Rp = QRot(rabiOmega, pi , phi1 ,Delta,f);
R2p = QRot(rabiOmega, 2*pi , phi2 ,Delta,f);

W = Rp * R2p * Rp ;

P = Rot * W * Rot;

```

```
end
```

## D.3 DD Pulse Sequence

The following MATLAB scripts are used in section 7.3. This is for a study of errors and a UR pulse sequence in a Ramsey experiment.

```
function sim_RamseyDD_fidelity_2()
%%
caseDD = 2;

% step = 15;
step = 41;

Omega = 2*pi*30e3;
state_F = 1.0;
eta = 0.25;

URorder = 14;
URsetPulse = 10;


inputStr = '|0>';inPsi = 1;
% inputStr = '|1>';inPsi = 2;
% inputStr = '|0>+|1>';inPsi = 3;
% inputStr = '|0>+i|1>';inPsi = 4;



n = URorder*URsetPulse;


%%
del = [-eta:2*eta/(step-1):eta]*Omega;
l = [-eta:2*eta/(step-1):eta]+state_F;

fidelity = [];
parfor k=1:step
    for j=1:step

        Delta = del(j);
        L = l(k);

        switch caseDD
            case 0
                [fidelity(k,j)] = ramsey_bare(inPsi,Delta,L,Omega);
                % without any pulse
%                 [fidelity(k,j)] = ramsey_SE(inPsi,URorder,URsetPulse ...
```

```
%                                 ,Delta,L,Omega); % with only a spin echo
            case 1
                [fidelity(k,j)] = ramsey_UR(inPsi,UROrder,URsetPulse ...
                    ,Delta,L,Omega); % all plain pulses
            case 2
                [fidelity(k,j)] = ramsey_UR_BB1(inPsi,URorder ...
                    ,URsetPulse,Delta,L,Omega); % all BB1 pulses
            case 3
                [fidelity(k,j)] = ramsey_UR_BB1_nonDD_BB1(inPsi ...
                    ,URorder,URsetPulse,Delta,L,Omega);
                % BB1 pulses to normal rotations and No BB1 in DD-seq
        end

    end
end


%%
% save(['Out_dephasedQTele_sim_KDD' num2str(n) '_IN_' ...
%         num2str(inPsi)],'del','l','fidelity');

h = figure(6785); clf;
hold on;

set(h,'PaperUnits','centimeters');
xSize=12;
ySize=10;
% scaleXY = 1.25;
scaleXY = 1;
set(h,'PaperSize', scaleXY*[xSize ySize]);
set(h,'PaperPosition',[0 0 scaleXY*xSize scaleXY*ySize]);

fontsize=scaleXY*16;
fontname='Times';
markSize = scaleXY*8;


% contourf( del./Omega, l, fidelity )
% contourcbar
% caxis([0 1]);

[c,hc] = contourf( del./Omega, l, fidelity );
    clabel(c,hc)
    cb = contourcbar;
    colormap('Hot');
    caxis([0 1]);
    cb.FontName = fontname;
    cb.FontSize = fontsize;

    if( caseDD ~= 2 )
        hc.LevelList = [0.99 0.95 0.9:-0.1:0];
    end

```

```


% title(['Bell23: Fidelity, KDD ' num2str(n) ' pulses, IN: ' inputStr])
% title(['simu_Ramsey_DD_case_' num2str(caseDD)],'Interpreter','none')
xlabel('\delta/\Omega')
ylabel('L/L_0')

a = gca;
a.Box = 'on';
a.FontSize = fontsize;
a.FontName = fontname ;

print('-dpdf', ['simu_Ramsey2_DD_case_' num2str(caseDD)]) ;

end
```

```
function [fidelity_all] = ramsey_bare(inPsi,Delta,f,Omega)

err = [Delta, f];

mode_debug = 0;


%%------------------------------
%need module from [Computer Physics Communications 179 (2008) 430]
% addpath('D:\Users\Chronos\Documents\00_AT_Work\Research\ ...
%           Siegen\Research\Program_scripts\MatlabModules\QUBIT4MATLAB');
%%------------------------------


ident = eye(2);              %define the identity
sigma_x=[0 1; 1 0];          %Pauli matrix X
sigma_y=[0 -1i; 1i 0];       %Pauli matrix Y
sigma_z=[1 0 ; 0 -1];        %Pauli matrix Z


%%

% psi_ini = ket([1 0]); % |0>

switch inPsi
    case 1
        ketIn1 = ket([1 0]); % |0>
    case 2
        ketIn1 = ket([0 1]); % |1>
    case 3
        ketIn1 = ket([1 1]); % |0> + |1>
    case 4
        ketIn1 = ket([1 +1i]); % |0> + i|1>
end

psi_ini = ketIn1;
```

```


R_halfpi1 = R(pi/2,0,Delta,f,Omega);
% R_halfpi2 = R(pi/2,pi,Delta,f,Omega); % end |0>
R_halfpi2 = R(pi/2,0,Delta,f,Omega);  % end |1>




op = R_halfpi2 * R_halfpi1 ;
psi_fin = op * psi_ini ;

prob_0 = abs(bra([1 0]) * psi_fin )^2 ;
prob_1 = abs(bra([0 1]) * psi_fin )^2 ;


% fidelity_all = abs(bra([1 0]) * psi_fin );
fidelity_all = abs(bra([0 1]) * psi_fin );



end % end main



%%
function theta = PHI_pulse( seq_of_n_pulses )

n = seq_of_n_pulses;
if( mod(n,4) == 0 )
    m = n/4;
    theta = pi/m ;  % This can be + and -. Here we just choose plus.
                        % rotation in radian

elseif( mod(n,4) == 2 )
    m = (n-2)/4;
    theta = (2*pi*m)/(2*m+1) ;
    % This can be + and -. Here we just choose plus.
    % rotation in radian
else
    error('Error in calculation of the angle in UR_DD_pulse')
end

end

%%
function phase = phaseUR( seq_of_n_pulses, phi2 )

n = seq_of_n_pulses;

phase = [];
for k = 1:n
    p = (k-1)*(k-2)/2*PHI_pulse(n) + (k-1)*phi2 ;
```

```
    phase = [phase ; p];
end

phase = mod(phase, 2*pi);

end

%%
function P=R(theta,phi,Delta,f,Omega)
%time evolution of an arbitrary pulse with possible errors



%definition of Pauli spin operators
sigma_x=[0 1; 1 0];
sigma_y=[0 -1i; 1i 0];
sigma_z=[1 0 ; 0 -1];
ident=[1 0; 0 1];


theta=f*theta*sqrt(Omega^2+Delta^2)/Omega;

if Delta==0
    nperp=1;
    nz=0;
else
    nperp=Omega/sqrt(Omega^2+Delta^2);
    nz=Delta/sqrt(Omega^2+Delta^2);
end

P=cos(theta/2)*ident+1i*sin(theta/2)* ...
    (nperp*(cos(phi)*sigma_x-sin(phi)*sigma_y)+nz*sigma_z);

end
```

```
function [fidelity_all] = ramsey_UR(inPsi,URorder,URsetPulse,Delta,f,Omega)

err = [Delta, f];

mode_debug = 0;


%%-------------------------------
%need module from [Computer Physics Communications 179 (2008) 430]
% addpath('D:\Users\Chronos\Documents\00_AT_Work\Research\ ...
%          Siegen\Research\Program_scripts\MatlabModules\QUBIT4MATLAB');
%%-------------------------------


ident = eye(2);             %define the identity
sigma_x=[0 1; 1 0];         %Pauli matrix X
sigma_y=[0 -1i; 1i 0];      %Pauli matrix Y
```

```
sigma_z=[1 0 ; 0 -1];       %Pauli matrix Z


%%

% psi_ini = ket([1 0]); % |0>

switch inPsi
    case 1
        ketIn1 = ket([1 0]); % |0>
    case 2
        ketIn1 = ket([0 1]); % |1>
    case 3
        ketIn1 = ket([1 1]); % |0> + |1>
    case 4
        ketIn1 = ket([1 +1i]); % |0> + i|1>
end

psi_ini = ketIn1;


R_halfpi1 = R(pi/2,0,Delta,f,Omega);
% R_halfpi2 = R(pi/2,pi,Delta,f,Omega); % end |0>
R_halfpi2 = R(pi/2,0,Delta,f,Omega);  % end |1>



%% UR_pulse
seq_of_n_pulses = URorder;
phi_UR = PHI_pulse( seq_of_n_pulses );
phase = phaseUR( seq_of_n_pulses, phi_UR );

DDseq1=phase;

UR = ident;
for l=1:length(DDseq1)
    UR=R(pi,DDseq1(l),Delta,f,Omega)*UR;
end

UR = UR^URsetPulse ; % Set of UR pulse

op = R_halfpi2 * UR * R_halfpi1 ;
psi_fin = op * psi_ini ;

prob_0 = abs(bra([1 0]) * psi_fin )^2 ;
prob_1 = abs(bra([0 1]) * psi_fin )^2 ;


fidelity_all = abs(bra([0 1]) * psi_fin );



end % end main
```

```
%%
function theta = PHI_pulse( seq_of_n_pulses )

n = seq_of_n_pulses;
if( mod(n,4) == 0 )
    m = n/4;
    theta = pi/m ;  % This can be + and -. Here we just choose plus.
                        % rotation in radian

elseif( mod(n,4) == 2 )
    m = (n-2)/4;
    theta = (2*pi*m)/(2*m+1) ;
    % This can be + and -. Here we just choose plus.
    % rotation in radian
else
    error('Error in calculation of the angle in UR_DD_pulse')
end

end

%%
function phase = phaseUR( seq_of_n_pulses, phi2 )

n = seq_of_n_pulses;

phase = [];
for k = 1:n
    p = (k-1)*(k-2)/2*PHI_pulse(n) + (k-1)*phi2 ;
    phase = [phase ; p];
end

phase = mod(phase, 2*pi);

end

%%
function P=R(theta,phi,Delta,f,Omega)
%time evolution of an arbitrary pulse with possible errors



%definition of Pauli spin operators
sigma_x=[0 1; 1 0];
sigma_y=[0 -1i; 1i 0];
sigma_z=[1 0 ; 0 -1];
ident=[1 0; 0 1];


theta=f*theta*sqrt(Omega^2+Delta^2)/Omega;

```

```
if Delta==0
    nperp=1;
    nz=0;
else
    nperp=Omega/sqrt(Omega^2+Delta^2);
    nz=Delta/sqrt(Omega^2+Delta^2);
end

P=cos(theta/2)*ident+1i*sin(theta/2)*...
    (nperp*(cos(phi)*sigma_x-sin(phi)*sigma_y)+nz*sigma_z);

end
```

```
function [fidelity_all] = ...
            ramsey_UR_BB1(inPsi,URorder,URsetPulse,Delta,f,Omega)

err = [Delta, f];

mode_debug = 0;


%%------------------------------
%need module from [Computer Physics Communications 179 (2008) 430]
% addpath('D:\Users\Chronos\Documents\00_AT_Work\Research\ ...
%            Siegen\Research\Program_scripts\MatlabModules\QUBIT4MATLAB');
%%------------------------------


ident = eye(2);             %define the identity
sigma_x=[0 1; 1 0];         %Pauli matrix X
sigma_y=[0 -1i; 1i 0];      %Pauli matrix Y
sigma_z=[1 0 ; 0 -1];       %Pauli matrix Z


%%

% psi_ini = ket([1 0]); % |0>

switch inPsi
    case 1
        ketIn1 = ket([1 0]); % |0>
    case 2
        ketIn1 = ket([0 1]); % |1>
    case 3
        ketIn1 = ket([1 1]); % |0> + |1>
    case 4
        ketIn1 = ket([1 +1i]); % |0> + i|1>
end

psi_ini = ketIn1;


```

```
R_halfpi1 = R_BB1(pi/2,0,Delta,f,Omega);
% R_halfpi2 = R_BB1(pi/2,pi,Delta,f,Omega); % end |0>
R_halfpi2 = R_BB1(pi/2,0,Delta,f,Omega);  % end |1>



%% UR_pulse
seq_of_n_pulses = URorder;
phi_UR = PHI_pulse( seq_of_n_pulses );
phase = phaseUR( seq_of_n_pulses, phi_UR );

DDseq1=phase;

UR = ident;
for l=1:length(DDseq1)
    UR=R_BB1(pi,DDseq1(l),Delta,f,Omega)*UR;
end

UR = UR^URsetPulse ; % Set of UR pulse

op = R_halfpi2 * UR * R_halfpi1 ;
psi_fin = op * psi_ini ;

prob_0 = abs(bra([1 0]) * psi_fin )^2 ;
prob_1 = abs(bra([0 1]) * psi_fin )^2 ;


fidelity_all = abs(bra([0 1]) * psi_fin );



end % end main



%%
function theta = PHI_pulse( seq_of_n_pulses )

n = seq_of_n_pulses;
if( mod(n,4) == 0 )
    m = n/4;
    theta = pi/m ;  % This can be + and -. Here we just choose plus.
                    % rotation in radian

elseif( mod(n,4) == 2 )
    m = (n-2)/4;
    theta = (2*pi*m)/(2*m+1) ;
    % This can be + and -. Here we just choose plus.
    % rotation in radian
else
    error('Error in calculation of the angle in UR_DD_pulse')
end

```

```
end

%%
function phase = phaseUR( seq_of_n_pulses, phi2 )

n = seq_of_n_pulses;

phase = [];
for k = 1:n
    p = (k-1)*(k-2)/2*PHI_pulse(n) + (k-1)*phi2 ;
    phase = [phase ; p];
end

phase = mod(phase, 2*pi);

end

%%
function P=R(theta,phi,Delta,f,Omega)



%definition of Pauli spin operators
sigma_x=[0 1; 1 0];
sigma_y=[0 -1i; 1i 0];
sigma_z=[1 0 ; 0 -1];
ident=[1 0; 0 1];


theta=f*theta*sqrt(Omega^2+Delta^2)/Omega;

if Delta==0
    nperp=1;
    nz=0;
else
    nperp=Omega/sqrt(Omega^2+Delta^2);
    nz=Delta/sqrt(Omega^2+Delta^2);
end

P=cos(theta/2)*ident+1i*sin(theta/2)*...
     (nperp*(cos(phi)*sigma_x-sin(phi)*sigma_y)+nz*sigma_z);

end

function P=R_BB1(theta,phi,Delta,f,Omega)

% Use RWR BB1

Rot = R(0.5*theta,phi,Delta,f,Omega);

phi1 = acos(-theta/(4*pi));
phi2 = 3*phi1;

```

```
Rp = R( pi , phi1 ,Delta,f,Omega);
R2p = R( 2*pi , phi2 ,Delta,f,Omega);

W = Rp * R2p * Rp ;

P = Rot * W * Rot;

end
```

```
function [fidelity_all] = ...
            ramsey_UR_BB1_nonDD_BB1(inPsi,URorder,URsetPulse,Delta,f,Omega)

err = [Delta, f];

mode_debug = 0;


%%------------------------------
%need module from [Computer Physics Communications 179 (2008) 430]
% addpath('D:\Users\Chronos\Documents\00_AT_Work\Research\ ...
%           Siegen\Research\Program_scripts\MatlabModules\QUBIT4MATLAB');
%%------------------------------


ident = eye(2);             %define the identity
sigma_x=[0 1; 1 0];         %Pauli matrix X
sigma_y=[0 -1i; 1i 0];      %Pauli matrix Y
sigma_z=[1 0 ; 0 -1];       %Pauli matrix Z


%%

% psi_ini = ket([1 0]); % |0>

switch inPsi
    case 1
        ketIn1 = ket([1 0]); % |0>
    case 2
        ketIn1 = ket([0 1]); % |1>
    case 3
        ketIn1 = ket([1 1]); % |0> + |1>
    case 4
        ketIn1 = ket([1 +1i]); % |0> + i|1>
end

psi_ini = ketIn1;


R_halfpi1 = R_BB1(pi/2,0,Delta,f,Omega);
% R_halfpi2 = R_BB1(pi/2,pi,Delta,f,Omega); % end |0>
R_halfpi2 = R_BB1(pi/2,0,Delta,f,Omega);  % end |1>

```

```


%% UR_pulse
seq_of_n_pulses = URorder;
phi_UR = PHI_pulse( seq_of_n_pulses );
phase = phaseUR( seq_of_n_pulses, phi_UR );

DDseq1=phase;

UR = ident;
for l=1:length(DDseq1)
    UR=R(pi,DDseq1(l),Delta,f,Omega)*UR;
end

UR = UR^URsetPulse ; % Set of UR pulse

op = R_halfpi2 * UR * R_halfpi1 ;
psi_fin = op * psi_ini ;

prob_0 = abs(bra([1 0]) * psi_fin )^2 ;
prob_1 = abs(bra([0 1]) * psi_fin )^2 ;


fidelity_all = abs(bra([0 1]) * psi_fin );



end % end main



%%
function theta = PHI_pulse( seq_of_n_pulses )

n = seq_of_n_pulses;
if( mod(n,4) == 0 )
    m = n/4;
    theta = pi/m ;  % This can be + and -. Here we just choose plus.
                        % rotation in radian

elseif( mod(n,4) == 2 )
    m = (n-2)/4;
    theta = (2*pi*m)/(2*m+1) ;
    % This can be + and -. Here we just choose plus.
    % rotation in radian
else
    error('Error in calculation of the angle in UR_DD_pulse')
end

end

%%
function phase = phaseUR( seq_of_n_pulses, phi2 )
```

```

n = seq_of_n_pulses;

phase = [];
for k = 1:n
    p = (k-1)*(k-2)/2*PHI_pulse(n) + (k-1)*phi2 ;
    phase = [phase ; p];
end

phase = mod(phase, 2*pi);

end

%%
function P=R(theta,phi,Delta,f,Omega)



%definition of Pauli spin operators
sigma_x=[0 1; 1 0];
sigma_y=[0 -1i; 1i 0];
sigma_z=[1 0 ; 0 -1];
ident=[1 0; 0 1];


theta=f*theta*sqrt(Omega^2+Delta^2)/Omega;

if Delta==0
    nperp=1;
    nz=0;
else
    nperp=Omega/sqrt(Omega^2+Delta^2);
    nz=Delta/sqrt(Omega^2+Delta^2);
end

P=cos(theta/2)*ident+1i*sin(theta/2)*...
     (nperp*(cos(phi)*sigma_x-sin(phi)*sigma_y)+nz*sigma_z);

end

function P=R_BB1(theta,phi,Delta,f,Omega)

% Use RWR BB1

Rot = R(0.5*theta,phi,Delta,f,Omega);

phi1 = acos(-theta/(4*pi));
phi2 = 3*phi1;

Rp = R( pi , phi1 ,Delta,f,Omega);
R2p = R( 2*pi , phi2 ,Delta,f,Omega);

W = Rp * R2p * Rp ;
```

```

P = Rot * W * Rot;

end
```

## D.4 Bell State using DD Sequence

The following MATLAB scripts are used in section 7.3. This is for a study of errors and a UR pulse sequence in a Bell-state generation.

```
function Fidelity=Bell2qubits_Bare(Delta,f);
% function Fidelity=Bell2qubits_Bare();
%need module from [Computer Physics Communications 179 (2008) 430]


%perfect pulses
% Delta=0;
% f=1;

%experimental parameters
%---------------------------
J=2*pi*[0 50; 50 0];

T1=4.5e-3; % 5 ms for Bell gate


ident=[1 0; 0 1];

CNOTideal=U_CNOT;
Bell_ideal = U_CNOT * kron(U_H,ident);

%------------------------------------------------------------------



%identitiy of the two-qubit system
IDENT=kron(ident,ident);

%the definition of the bases are:
% |00> |01> |10> |11>

%prepared initial state
%-----------------------------------------------

initial_state=kron(ket([1 0]), ket([1 0])); % |00>

%conditional evolutions
%---------------------------------------------
```

```
E1=PHI(T1,J);



Had1 = -1i*kron(R(pi/2,3*pi/2,Delta,f),ident) * kron(R(pi,0,Delta,f),ident);
R1=kron(ident,R(pi/2,pi/2,Delta,f));

Yp90 = R(pi/2,pi/2,Delta,f) ;
Yn90 = R(pi/2,-pi/2,Delta,f) ;
Xp90 = R(pi/2,pi,Delta,f) ;
Xn90 = R(pi/2,0,Delta,f) ;

Zp90 = Yp90 * Xn90 * Yn90 ;
Zn90 = Yp90 * Xp90 * Yn90 ;

RZ1 = kron( Zn90, Zp90 );

R2=kron(ident,R(pi/2,3*pi/2,Delta,f));

Bellgate= exp(-1i*pi/4) * R2*RZ1*E1*R1*Had1 ; % bare Bell


%-------------------------------------------------------
final_state=Bellgate*initial_state;

% printv(final_state)   % When test the function!

%abs(final_state).^2
%bar([0:3],abs(final_state).^2);


%normalize the final state
N=sum((final_state.*conj(final_state)))* ...
            sum((final_state.*conj(final_state)));
final_state=1/N*final_state;

desired_state=Bell_ideal*initial_state;
%desired_state=[0.5+0.5*i;0;0;-0.5+0.5*i];

Fidelity=sum((desired_state.*conj(final_state)))* ...
            sum((final_state.*conj(desired_state)));

%end;

%=====================================================


function P=R(theta,phi,Delta,f);

%definition of Pauli spin operators
sigma_x=[0 1; 1 0];
sigma_y=[0 -i; i 0];
sigma_z=[1 0 ; 0 -1];
```

```
ident=[1 0; 0 1];

Omega=2*pi*30e3;
theta=f*theta*sqrt(Omega^2+Delta^2)/Omega;

if Delta==0
    nperp=1;
    nz=0;
else
    nperp=Omega/sqrt(Omega^2+Delta^2);
    nz=Delta/sqrt(Omega^2+Delta^2);
end;

P=cos(theta/2)*ident+1i*sin(theta/2)*...
    (nperp*(cos(phi)*sigma_x-sin(phi)*sigma_y)+nz*sigma_z);

%end;
%---------------------------------------------

function U=PHI(T,J);

%definition of Pauli spin operators
%sigma_x=[0 1; 1 0];
%sigma_y=[0 -i; i 0];
sigma_z=[1 0 ; 0 -1];
%ident=[1 0; 0 1];

U=expm(1i*T/2*(J(1,2)*kron(sigma_z,sigma_z)));
```

```
function Fidelity=Bell2qubits_UR(Delta,f);
% function Fidelity=Bell2qubits_UR();
%need module from [Computer Physics Communications 179 (2008) 430]


URorder = 14;
URsetPulse = 10;


% %perfect pulses
% Delta=0;
% f=1;

%experimental parameters
%---------------------------
J=2*pi*[0 50; 50 0];

T1=5e-3; % 5 ms for Bell gate


ident=[1 0; 0 1];

CNOTideal=U_CNOT;
```

```
Bell_ideal = U_CNOT * kron(U_H,ident);

%---------------------------------------------------------------



%identitiy of the two-qubit system
IDENT=kron(ident,ident);

%the definition of the bases are:
% |00> |01> |10> |11>

%prepared initial state
%----------------------------------------------

initial_state=kron(ket([1 0]), ket([1 0])); % |00>

%conditional evolutions
%--------------------------------------------


seq_of_n_pulses = URorder;
phi_UR = PHI_pulse( seq_of_n_pulses );
phase = phaseUR( seq_of_n_pulses, phi_UR );

DDseq1 = [];
for k = 1:URsetPulse
    DDseq1=[DDseq1 ; phase];
end

tau1=T1/2/length(DDseq1);
E1=IDENT;
for l=1:length(DDseq1)
  E1=PHI(tau1,J)*kron(R(pi,DDseq1(l),Delta,f),R(pi,DDseq1(l),Delta,f))*...
      PHI(tau1,J)*E1;
end


if( URorder==0 )
    E1=PHI(T1,J);
end


Had1 = -1i*kron(R(pi/2,3*pi/2,Delta,f),ident)*kron(R(pi,0,Delta,f),ident);
R1=kron(ident,R(pi/2,pi/2,Delta,f));

Yp90 = R(pi/2,pi/2,Delta,f) ;
Yn90 = R(pi/2,-pi/2,Delta,f) ;
Xp90 = R(pi/2,pi,Delta,f) ;
Xn90 = R(pi/2,0,Delta,f) ;

Zp90 = Yp90 * Xn90 * Yn90 ;
Zn90 = Yp90 * Xp90 * Yn90 ;
```

```

RZ1 = kron( Zn90, Zp90 );

R2=kron(ident,R(pi/2,3*pi/2,Delta,f));

Bellgate= exp(-1i*pi/4) * R2*RZ1*E1*R1*Had1 ; % bare Bell


%-------------------------------------------------------
final_state=Bellgate*initial_state;

% printv(final_state)    % When test the function!

%abs(final_state).^2
%bar([0:3],abs(final_state).^2);


%normalize the final state
N=sum((final_state.*conj(final_state)))*...
        sum((final_state.*conj(final_state)));
final_state=1/N*final_state;

desired_state=Bell_ideal*initial_state;
%desired_state=[0.5+0.5*i;0;0;-0.5+0.5*i];

Fidelity=sum((desired_state.*conj(final_state)))*...
            sum((final_state.*conj(desired_state)));

end

%=====================================================


function P=R(theta,phi,Delta,f);

    %definition of Pauli spin operators
    sigma_x=[0 1; 1 0];
    sigma_y=[0 -i; i 0];
    sigma_z=[1 0 ; 0 -1];
    ident=[1 0; 0 1];

    Omega=2*pi*30e3;
    theta=f*theta*sqrt(Omega^2+Delta^2)/Omega;

    if Delta==0
        nperp=1;
        nz=0;
    else
        nperp=Omega/sqrt(Omega^2+Delta^2);
        nz=Delta/sqrt(Omega^2+Delta^2);
    end;

    P=cos(theta/2)*ident+1i*sin(theta/2)*...
```

```
                (nperp*(cos(phi)*sigma_x-sin(phi)*sigma_y)+nz*sigma_z);


end
%---------------------------------------------

function U=PHI(T,J);

    %definition of Pauli spin operators
    %sigma_x=[0 1; 1 0];
    %sigma_y=[0 -i; i 0];
    sigma_z=[1 0 ; 0 -1];
    %ident=[1 0; 0 1];

    U=expm(1i*T/2*(J(1,2)*kron(sigma_z,sigma_z)));
end



%%
function theta = PHI_pulse( seq_of_n_pulses )

    n = seq_of_n_pulses;
    if( mod(n,4) == 0 )
        m = n/4;
        theta = pi/m ;  % This can be + and -. Here we just choose plus.
                            % rotation in radian

    elseif( mod(n,4) == 2 )
        m = (n-2)/4;
        theta = (2*pi*m)/(2*m+1) ;
        % This can be + and -. Here we just choose plus.
        % rotation in radian
    else
        error('Error in calculation of the angle in UR_DD_pulse')
    end

end


function phase = phaseUR( seq_of_n_pulses, phi2 )

    n = seq_of_n_pulses;

    phase = [];
    for k = 1:n
        p = (k-1)*(k-2)/2*PHI_pulse(n) + (k-1)*phi2 ;
        phase = [phase ; p];
    end

    phase = mod(phase, 2*pi);

end
```

```
function Fidelity=Bell2qubits_UR_BB1(Delta,f);
% function Fidelity=Bell2qubits_UR();
%need module from [Computer Physics Communications 179 (2008) 430]



URorder = 14;
URsetPulse = 10;


%perfect pulses
% Delta=0;
% f=1;

%experimental parameters
%---------------------------
J=2*pi*[0 50; 50 0];

T1=5e-3; % 5 ms for Bell gate


ident=[1 0; 0 1];

CNOTideal=U_CNOT;
Bell_ideal = U_CNOT * kron(U_H,ident);

%--------------------------------------------------------------



%identitiy of the two-qubit system
IDENT=kron(ident,ident);

%the definition of the bases are:
% |00> |01> |10> |11>

%prepared initial state
%---------------------------------------------

initial_state=kron(ket([1 0]), ket([1 0])); % |00>

%conditional evolutions
%-------------------------------------------


seq_of_n_pulses = URorder;
phi_UR = PHI_pulse( seq_of_n_pulses );
phase = phaseUR( seq_of_n_pulses, phi_UR );

DDseq1 = [];
for k = 1:URsetPulse
    DDseq1=[DDseq1 ; phase];
end
```

```

tau1=T1/2/length(DDseq1);
E1=IDENT;
for l=1:length(DDseq1)
  E1=PHI(tau1,J)*kron(R(pi,DDseq1(l),Delta,f),R(pi,DDseq1(l),Delta,f))*...
      PHI(tau1,J)*E1;
end


% UR = UR^URsetPulse ; % Set of UR pulse


Had1 = -1i*kron(R(pi/2,3*pi/2,Delta,f),ident)*kron(R(pi,0,Delta,f),ident);
R1=kron(ident,R(pi/2,pi/2,Delta,f));

Yp90 = R(pi/2,pi/2,Delta,f) ;
Yn90 = R(pi/2,-pi/2,Delta,f) ;
Xp90 = R(pi/2,pi,Delta,f) ;
Xn90 = R(pi/2,0,Delta,f) ;

Zp90 = Yp90 * Xn90 * Yn90 ;
Zn90 = Yp90 * Xp90 * Yn90 ;

RZ1 = kron( Zn90, Zp90 );

R2=kron(ident,R(pi/2,3*pi/2,Delta,f));

Bellgate= exp(-1i*pi/4) * R2*RZ1*E1*R1*Had1 ; % bare Bell


%-------------------------------------------------------
final_state=Bellgate*initial_state;

% printv(final_state)   % When test the function!

%abs(final_state).^2
%bar([0:3],abs(final_state).^2);


%normalize the final state
N=sum((final_state.*conj(final_state)))*...
        sum((final_state.*conj(final_state)));
final_state=1/N*final_state;

desired_state=Bell_ideal*initial_state;
%desired_state=[0.5+0.5*i;0;0;-0.5+0.5*i];

Fidelity=sum((desired_state.*conj(final_state)))*...
            sum((final_state.*conj(desired_state)));

end

%=====================================================
```

```


function P=QRot(theta,phi,Delta,f);

    %definition of Pauli spin operators
    sigma_x=[0 1; 1 0];
    sigma_y=[0 -i; i 0];
    sigma_z=[1 0 ; 0 -1];
    ident=[1 0; 0 1];

    Omega=2*pi*30e3;
    theta=f*theta*sqrt(Omega^2+Delta^2)/Omega;

    if Delta==0
        nperp=1;
        nz=0;
    else
        nperp=Omega/sqrt(Omega^2+Delta^2);
        nz=Delta/sqrt(Omega^2+Delta^2);
    end;

    P=cos(theta/2)*ident+1i*sin(theta/2)*...
            (nperp*(cos(phi)*sigma_x-sin(phi)*sigma_y)+nz*sigma_z);

end
%--------------------------------------------

function U=PHI(T,J);

    %definition of Pauli spin operators
    %sigma_x=[0 1; 1 0];
    %sigma_y=[0 -i; i 0];
    sigma_z=[1 0 ; 0 -1];
    %ident=[1 0; 0 1];

    U=expm(1i*T/2*(J(1,2)*kron(sigma_z,sigma_z)));
end



%%
function theta = PHI_pulse( seq_of_n_pulses )

    n = seq_of_n_pulses;
    if( mod(n,4) == 0 )
        m = n/4;
        theta = pi/m ;  % This can be + and -. Here we just choose plus.
                            % rotation in radian

    elseif( mod(n,4) == 2 )
        m = (n-2)/4;
        theta = (2*pi*m)/(2*m+1) ;
        % This can be + and -. Here we just choose plus.
```

```
            % rotation in radian
        else
            error('Error in calculation of the angle in UR_DD_pulse')
        end

end


function phase = phaseUR( seq_of_n_pulses, phi2 )

    n = seq_of_n_pulses;

    phase = [];
    for k = 1:n
        p = (k-1)*(k-2)/2*PHI_pulse(n) + (k-1)*phi2 ;
        phase = [phase ; p];
    end

    phase = mod(phase, 2*pi);

end


function P=R(theta,phi,Delta,f)

% Use RWR BB1

Rot = QRot(0.5*theta,phi,Delta,f);

phi1 = acos(-theta/(4*pi));
phi2 = 3*phi1;

Rp = QRot( pi , phi1 ,Delta,f);
R2p = QRot( 2*pi , phi2 ,Delta,f);

W = Rp * R2p * Rp ;

P = Rot * W * Rot;

end
```

```
function Fidelity=Bell2qubits_BB1_DDnoBB1(Delta,f);
% function Fidelity=Bell2qubits_Bare();
%need module from [Computer Physics Communications 179 (2008) 430]

%perfect pulses
% Delta=0;
% f=1;

URorder = 14;
URsetPulse = 10;

```

```

%experimental parameters
%---------------------------
J=2*pi*[0 50; 50 0];

T1=5e-3; % 5 ms for Bell gate


ident=[1 0; 0 1];

CNOTideal=U_CNOT;
Bell_ideal = U_CNOT * kron(U_H,ident);

%---------------------------------------------------------------



%identitiy of the two-qubit system
IDENT=kron(ident,ident);

%the definition of the bases are:
% |00> |01> |10> |11>

%prepared initial state
%----------------------------------------------
initial_state=kron(ket([1 0]), ket([1 0])); % |00>

%conditional evolutions
%--------------------------------------------
seq_of_n_pulses = URorder;
phi_UR = PHI_pulse( seq_of_n_pulses );
phase = phaseUR( seq_of_n_pulses, phi_UR );

DDseq1 = [];
for k = 1:URsetPulse
    DDseq1=[DDseq1 ; phase];
end

tau1=T1/2/length(DDseq1);
E1=IDENT;
for l=1:length(DDseq1)
  E1=PHI(tau1,J)...
      *kron(QRot(pi,DDseq1(l),Delta,f),QRot(pi,DDseq1(l),Delta,f))...
      *PHI(tau1,J)*E1;
end



Had1 = -1i*kron(R(pi/2,3*pi/2,Delta,f),ident)*kron(R(pi,0,Delta,f),ident);
R1=kron(ident,R(pi/2,pi/2,Delta,f));

Yp90 = R(pi/2,pi/2,Delta,f) ;
Yn90 = R(pi/2,-pi/2,Delta,f) ;
```

```
Xp90 = R(pi/2,pi,Delta,f) ;
Xn90 = R(pi/2,0,Delta,f) ;

Zp90 = Yp90 * Xn90 * Yn90 ;
Zn90 = Yp90 * Xp90 * Yn90 ;

RZ1 = kron( Zn90, Zp90 );

R2=kron(ident,R(pi/2,3*pi/2,Delta,f));

Bellgate= exp(-1i*pi/4) * R2*RZ1*E1*R1*Had1 ; % bare Bell


%-----------------------------------------------------------
final_state=Bellgate*initial_state;

% printv(final_state)    % When test the function!

%abs(final_state).^2
%bar([0:3],abs(final_state).^2);


%normalize the final state
N=sum((final_state.*conj(final_state)))*...
        sum((final_state.*conj(final_state)));
final_state=1/N*final_state;

desired_state=Bell_ideal*initial_state;
%desired_state=[0.5+0.5*i;0;0;-0.5+0.5*i];

Fidelity=sum((desired_state.*conj(final_state)))*...
            sum((final_state.*conj(desired_state)));

%end;

%=========================================================


function P=QRot(theta,phi,Delta,f);

%definition of Pauli spin operators
sigma_x=[0 1; 1 0];
sigma_y=[0 -i; i 0];
sigma_z=[1 0 ; 0 -1];
ident=[1 0; 0 1];

Omega=2*pi*30e3;
theta=f*theta*sqrt(Omega^2+Delta^2)/Omega;

if Delta==0
    nperp=1;
    nz=0;
else
```

```
    nperp=Omega/sqrt(Omega^2+Delta^2);
    nz=Delta/sqrt(Omega^2+Delta^2);
end;

P=cos(theta/2)*ident+1i*sin(theta/2)*...
    (nperp*(cos(phi)*sigma_x-sin(phi)*sigma_y)+nz*sigma_z);


%end;
%---------------------------------------------

function U=PHI(T,J);

%definition of Pauli spin operators
%sigma_x=[0 1; 1 0];
%sigma_y=[0 -i; i 0];
sigma_z=[1 0 ; 0 -1];
%ident=[1 0; 0 1];

U=expm(1i*T/2*(J(1,2)*kron(sigma_z,sigma_z)));


function P=R(theta,phi,Delta,f)

% Use RWR BB1

Rot = QRot(0.5*theta,phi,Delta,f);

phi1 = acos(-theta/(4*pi));
phi2 = 3*phi1;

Rp = QRot( pi , phi1 ,Delta,f);
R2p = QRot( 2*pi , phi2 ,Delta,f);

W = Rp * R2p * Rp ;

P = Rot * W * Rot;

function theta = PHI_pulse( seq_of_n_pulses )

    n = seq_of_n_pulses;
    if( mod(n,4) == 0 )
        m = n/4;
        theta = pi/m ;  % This can be + and -. Here we just choose plus.
                            % rotation in radian

    elseif( mod(n,4) == 2 )
        m = (n-2)/4;
        theta = (2*pi*m)/(2*m+1) ;
        % This can be + and -. Here we just choose plus.
        % rotation in radian
    else
        error('Error in calculation of the angle in UR_DD_pulse')
```

```
    end




function phase = phaseUR( seq_of_n_pulses, phi2 )

    n = seq_of_n_pulses;

    phase = [];
    for k = 1:n
        p = (k-1)*(k-2)/2*PHI_pulse(n) + (k-1)*phi2 ;
        phase = [phase ; p];
    end

    phase = mod(phase, 2*pi);
```

# E

# Magnetic-Field Sensor

One of our three-dimensional magnetic-field sensors is an in-house assembly device based on a Honeywell HMC1053 sensor chip [238]. The sensing type is based on magnetoresistive technology. It is chosen for strong field withstanding and fast response. The circuit is designed and assembled by Simon Spitzer. The schematic can be found in appendix G.1.

The sensor is calibrated by placing it in the center of a circular Helmholtz coil pair. The Helmholtz coil pair has a radius $R$ and a separation $d$ of 6.6 cm, see Fig. E.1a. From the Biot-savart law, the magnetic field in the center of a circular Helmholtz coil $B_z(z)$ is given by [239]

$$B_z(z) = N\frac{\mu_0 I R^2}{2}\left(\frac{1}{(R^2+(\frac{d}{2}-z)^2)^{3/2}}+\frac{1}{(R^2+(\frac{d}{2}+z)^2)^{3/2}}\right), \tag{E.1}$$

where $N$ represents the number of turns of each circular coil, $\mu_0$ represents the vacuum permeability, and $I$ represents the applied current. Using Helmholtz configuration, the magnetic field is uniformly distributed in between two coils. In addition, the Helmholtz configuration gives a broad area of a homogeneous magnetic field, which means a small

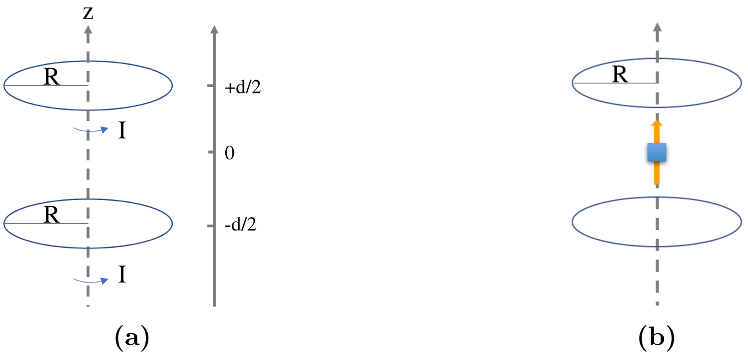

**Figure E.1: Calibration of a magnetic-field sensor.** (a) The schematic of two circular coils in Helmholtz configuration. (b) The schematic of the calibration. The response signal from a sensor can be calibrated with the calculated magnetic field at a given current.

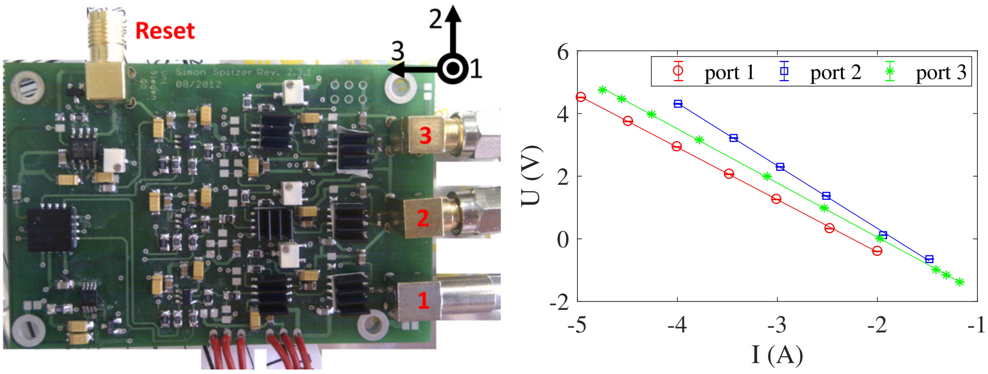

**(a)** **(b)**

**Figure E.2: Magnetic-field sensor and the respond signal.** (a) The magnetic-field sensor on a PCB board. The black square in the left is the sensor chip (HMC1053). The magnetic-field signal is given through 3 SMA ports with the respective direction as shown in the label. (b) When putting the sensor with each respective direction in the calibration coils, the respond signals $U$ are recorded in voltage by a multimeter while changing the current through the coils. From the slopes of linear fits, the conversion factors of port 1, 2, and 3 are $-73.4(4)\,\mu\mathrm{T/V}$, $-61.3(7)\,\mu\mathrm{T/V}$, and $-70.9(2)\,\mu\mathrm{T/V}$, respectively.

error for the calibration. The magnetic-field sensor is placed as shown in Fig. E.1b.

Providing the variation current $I$ through the Helmholtz coil, the magnetic field can be calculated and the potential respond signal $U$ of the sensor for a given port can also be measured. The magnetic-field components with respect to the sensor chip are shown in Fig. E.2a. From the slopes of linear fits, shown in Fig. E.2b, the conversion factors of port 1, 2, and 3 are

$$\begin{aligned}\mathrm{Port1} &= -73.4(4)\,\mu\mathrm{T/V},\\ \mathrm{Port2} &= -61.3(7)\,\mu\mathrm{T/V},\\ \mathrm{Port3} &= -70.9(2)\,\mu\mathrm{T/V}.\end{aligned}$$

The frequency bandwidth of the magnetic-field sensor has also been tested. Fig. E.3 shows the frequency response. The sensor is tested using a constant amplitude of a given frequency to a small coil aligned around the sensor. This coil has 2 turns ($N = 2$) and a diameter of 5.1 cm resulting an inductance of below 20 µH. Then the relative reading amplitude of the sensor is measured at the corresponding frequency. At the −3-dB point, this sensor can respond up to approximately 40 kHz. However, the reading amplitude is not a flat line after approximately 700 Hz.

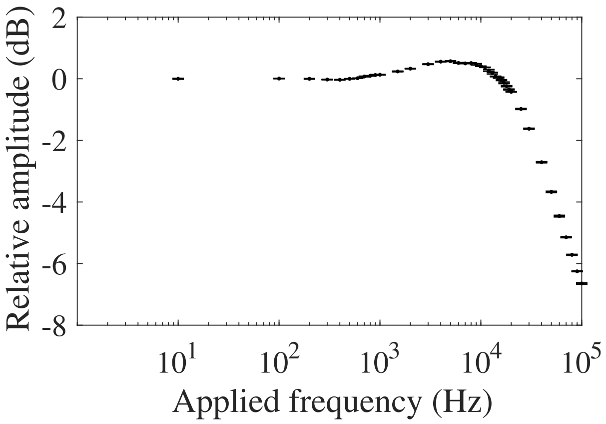

**Figure E.3: Frequency bandwidth of in-house magnetic-field sensor (HMC1053).** By applying a constant amplitude of a given frequency to a small coil with $N = 2$, the relative reading amplitude of the sensor is measured. At the −3-dB point, this sensor can respond up to approximately 40 kHz. However, after approximately 700 Hz, the reading amplitude becomes noticeably frequency dependent.

# F

# Feedback Control

Proportional-integral (PI) controls are commonly used in industry and laboratory equipment. They are control loop feedback mechanisms underlying all stabilization methods used in this dissertation. A PI controller continuously evaluates an error signal $e(t)$ as the difference between a set point value and measured process variable. Using the error signal, a PI controller applies a correction signal based on proportional and integral terms, to negate external influences on a system.

The correction signal as a control function $u(t)$ is given by [240]

$$u(t) = K_p e(t) + K_i \int_0^t e(t') dt', \tag{F.1}$$

$$= K_p \left( e(t) + \frac{1}{T_i} \int_0^t e(t') dt' \right), \tag{F.2}$$

where $K_p$ and $K_i$ are the gain coefficients for the proportional and integral terms, respectively, and $T_i$ represents the integration time. The general scheme of a feedback system is illustrated in Fig. F.1. The process variable ($y(t)$) is the system parameter that needs to be controlled. It is provided by a sensor measuring the system such as a temperature sensor. The process variable is compared to the set point ($r(t)$), which is the desired value of the process variable such as 310 K for a temperature control system. Then, the difference ($u(t)$) between the process variable and the set point is used by the compensator, realized by either hardware or software, for the control system algorithm, to determine the actuator output, e.g. changing the temperature of a heat source. For example, if the temperature is reading below the set point, a heat source is driven to increase the temperature of the system and it starts over from reading the process variable. This is a closed loop control system.

The proportional term depends only on the error signal. It is amplified by the proportional gain ($K_p$). Generally, when the proportional gain is increased, the speed of the control system response is increased. However, if the gain is too large, the process variable will oscillate and the system will go out of control.

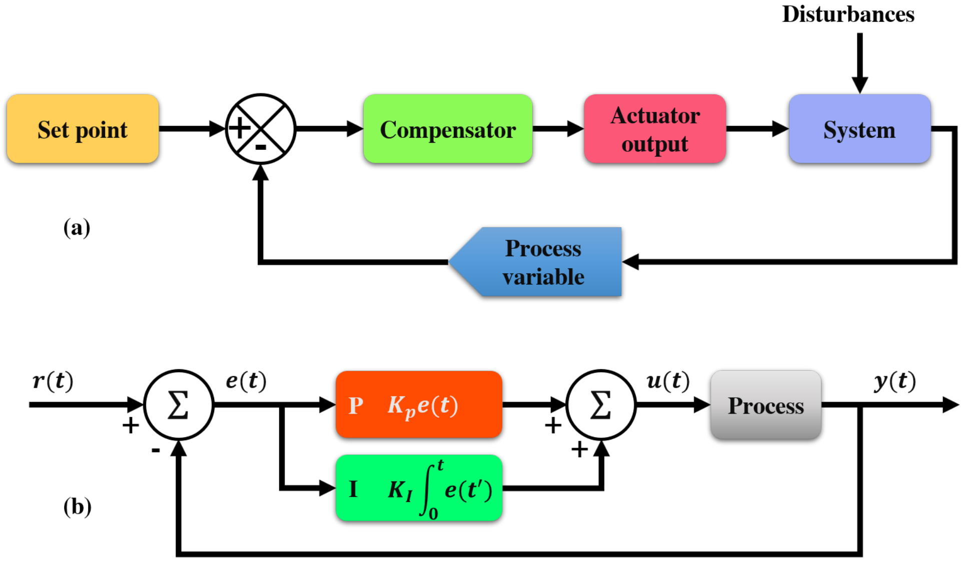

**Figure F.1: The schematic of PI control loop system.** We want to stabilize the process variable ($y(t)$) around the set point ($r(t)$), the desired value of the process variable. The value of the process variable is provided by a sensor, measuring on a system. The process variable is then compared to the set point giving the error signal ($e(t)$) as the difference between the two. The error signal is used by the compensator for the control system algorithm, to determine the actuator output acting on the system. The overview is shown in (a) and the proportional and integral terms are specified in (b) as the orange and green box, respectively.

The integral term integrates the error signal over time. As a result it even a small error will increase this term slowly. It is amplified by the integral gain ($K_i$). This will compensate the steady state of the error signal to the set point.

# G

# Electronics Files

The following files describe the electronics circuits and designs, which have been used in the active magnetic field stabilization project. They are in eagle-file format which can be opened by Eagle 5.1.0 or Autodesk Eagle 9.0.1.

## G.1 Magnetic-Field Sensor

- Circuit for HMC1053
  `//Misc_files/b_sensor.brd`
  `//Misc_files/b_sensor.sch`

## G.2 PI Feedback Control

- Power panel for PI control rack supply
  `//Misc_files/stromversorgung_r2_1.brd`
  `//Misc_files/stromversorgung_r2_1.sch`
- PI control
  `//Misc_files/pi_reg.brd`
  `//Misc_files/pi_reg.sch`
- PI control revision
  `//Misc_files/pi_reg_revised.brd`
  `//Misc_files/pi_reg_revised.sch`

## G.3 Current Driver

- Circuit for a current driver with modulation input
  `//Misc_files/LM675_submitted.brd`
  `//Misc_files/LM675_submitted.sch`

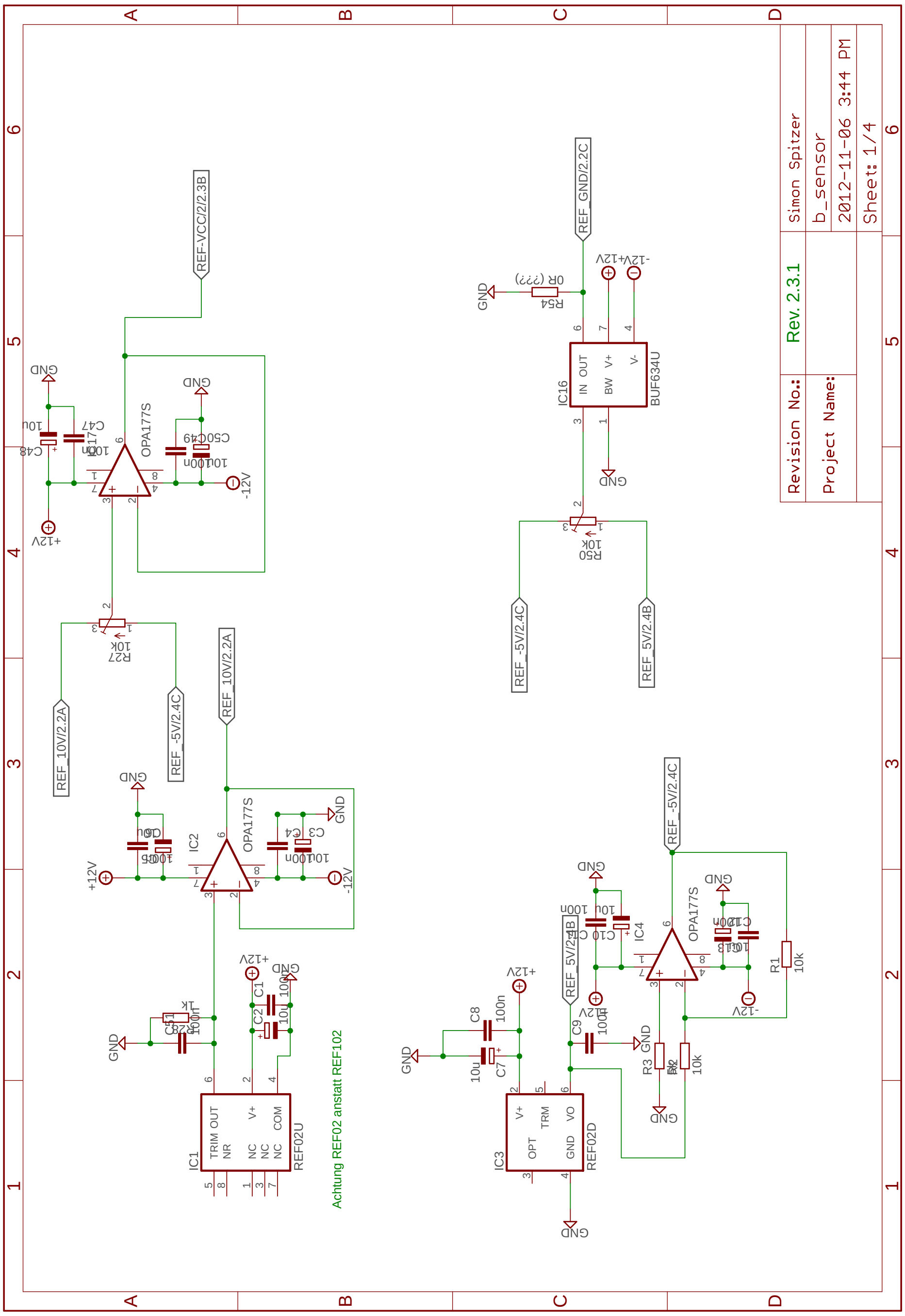

**Figure G.1: b_sensor.** page 1

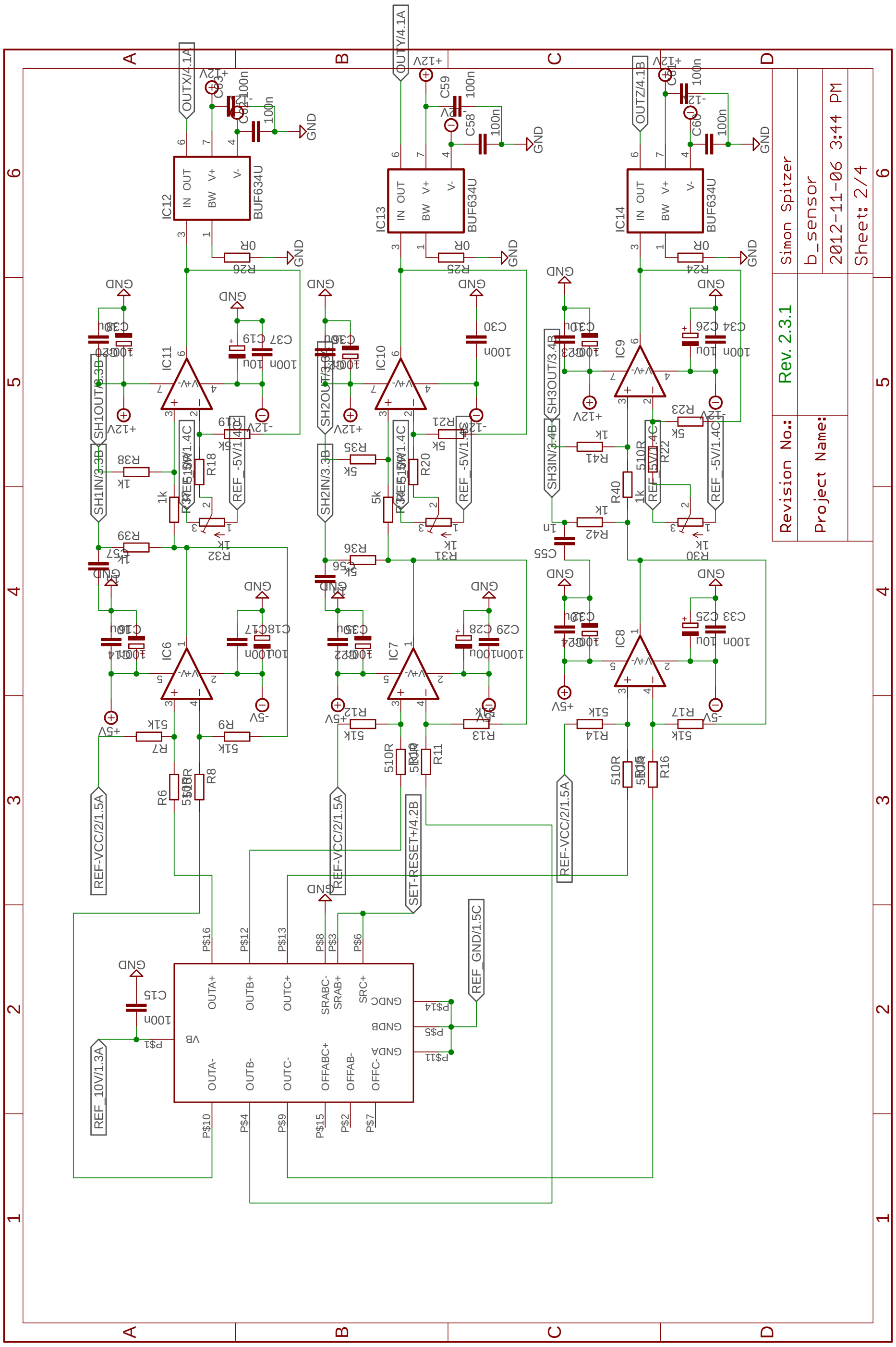

**Figure G.2: b_sensor.** page 2

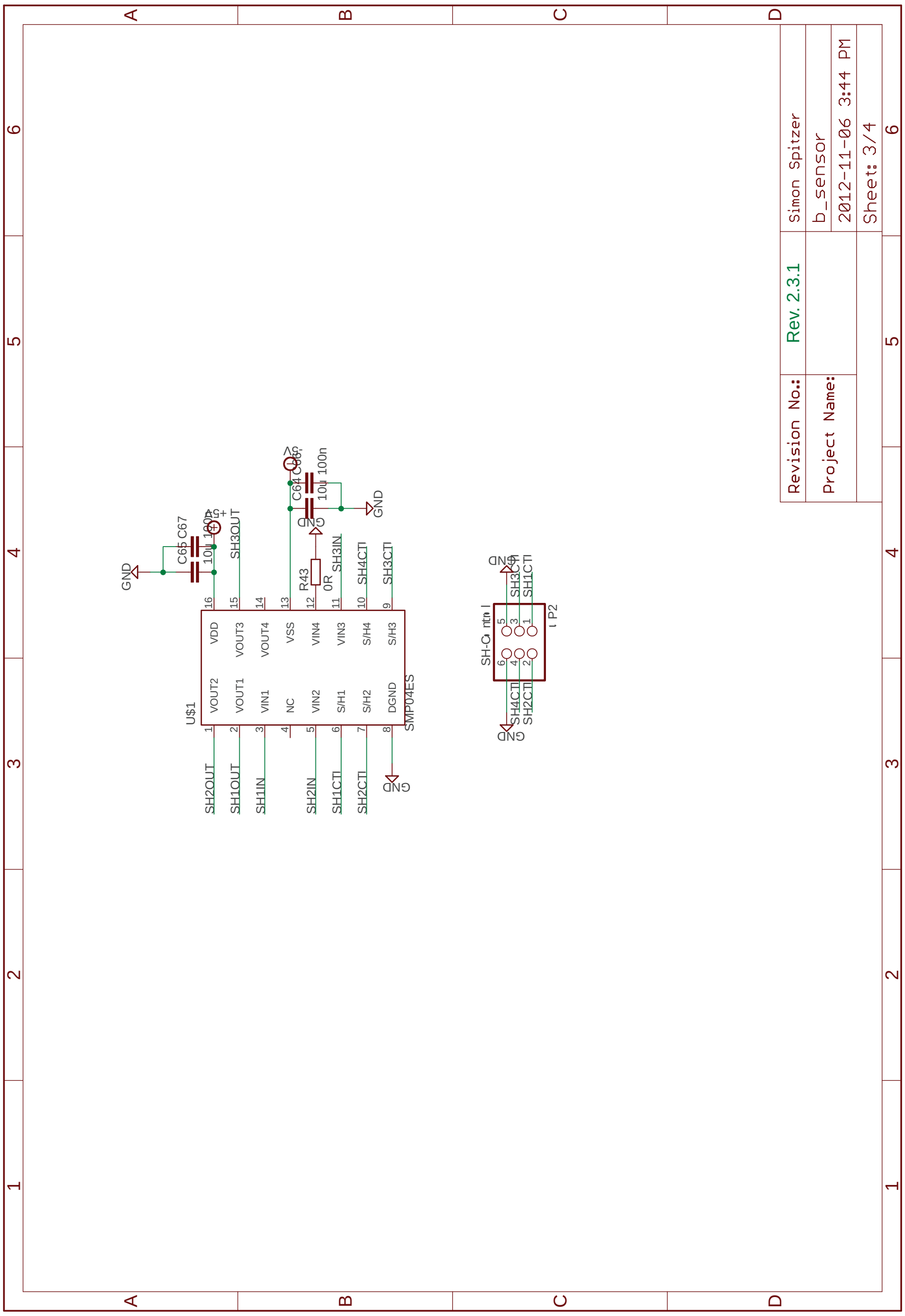

**Figure G.3: b_sensor.** page 3

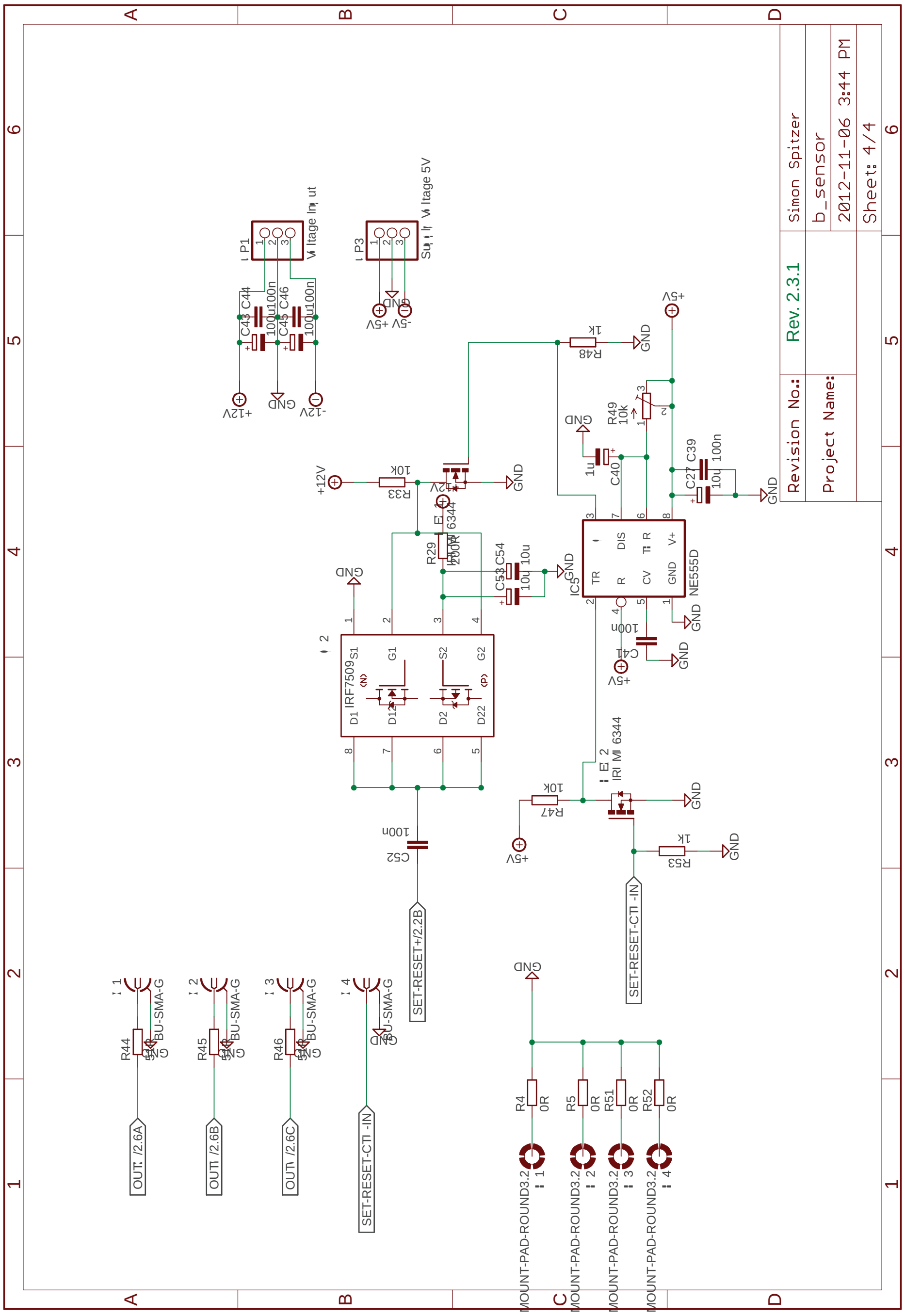

Figure G.4: b_sensor. page 4

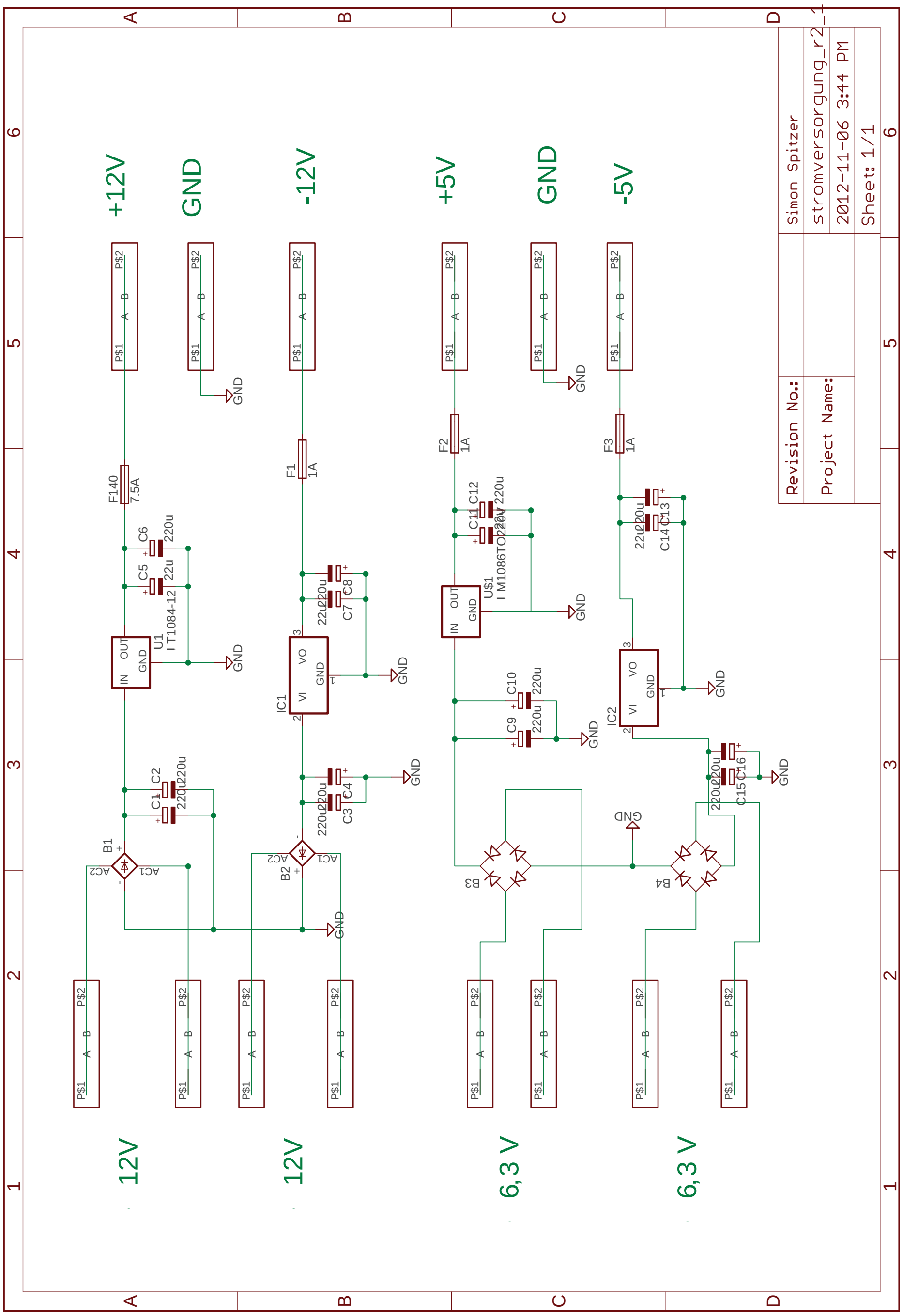

Figure G.5: stromversorgung_r2_1.

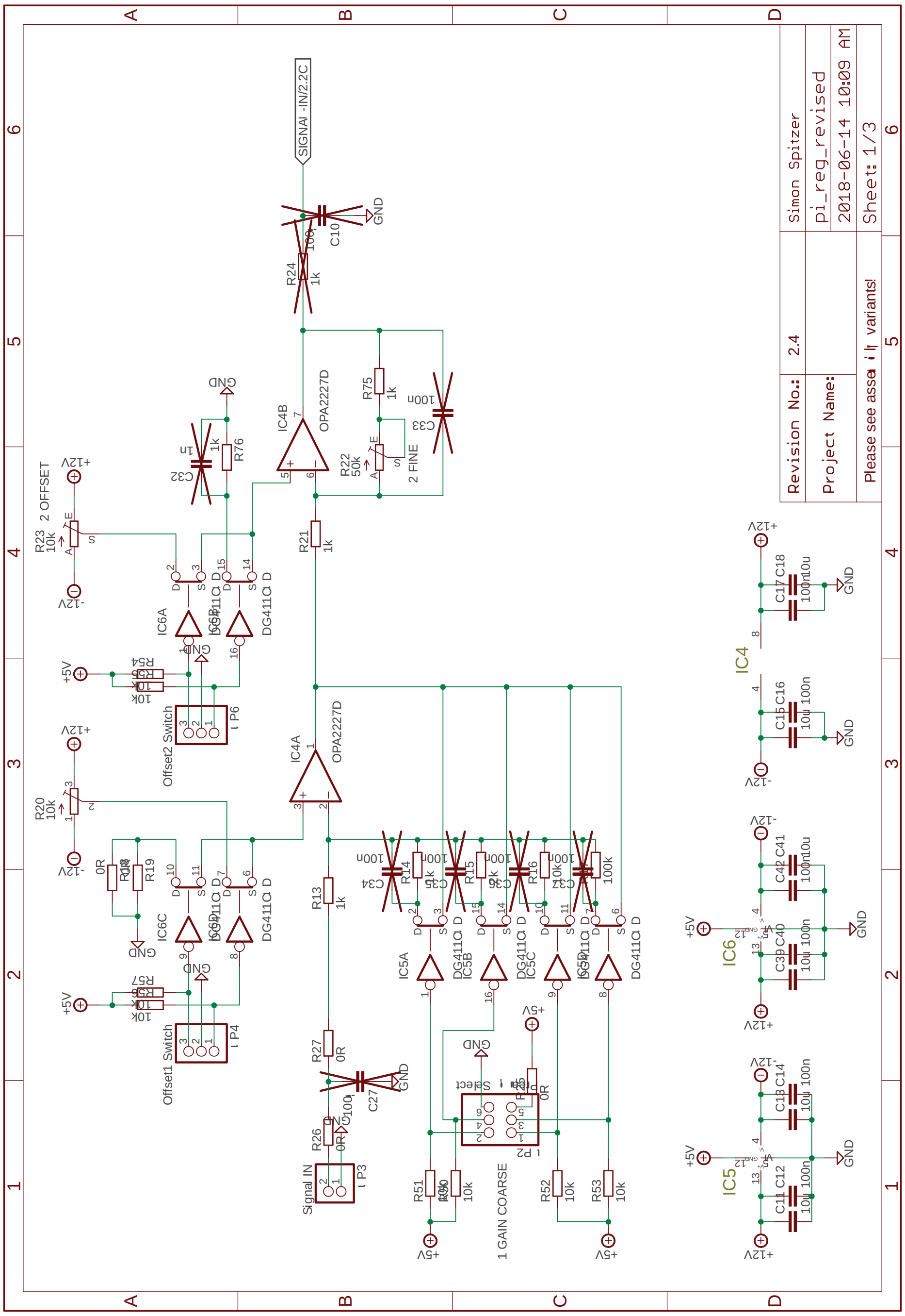

**Figure G.6: pi_reg_revised.** page 1

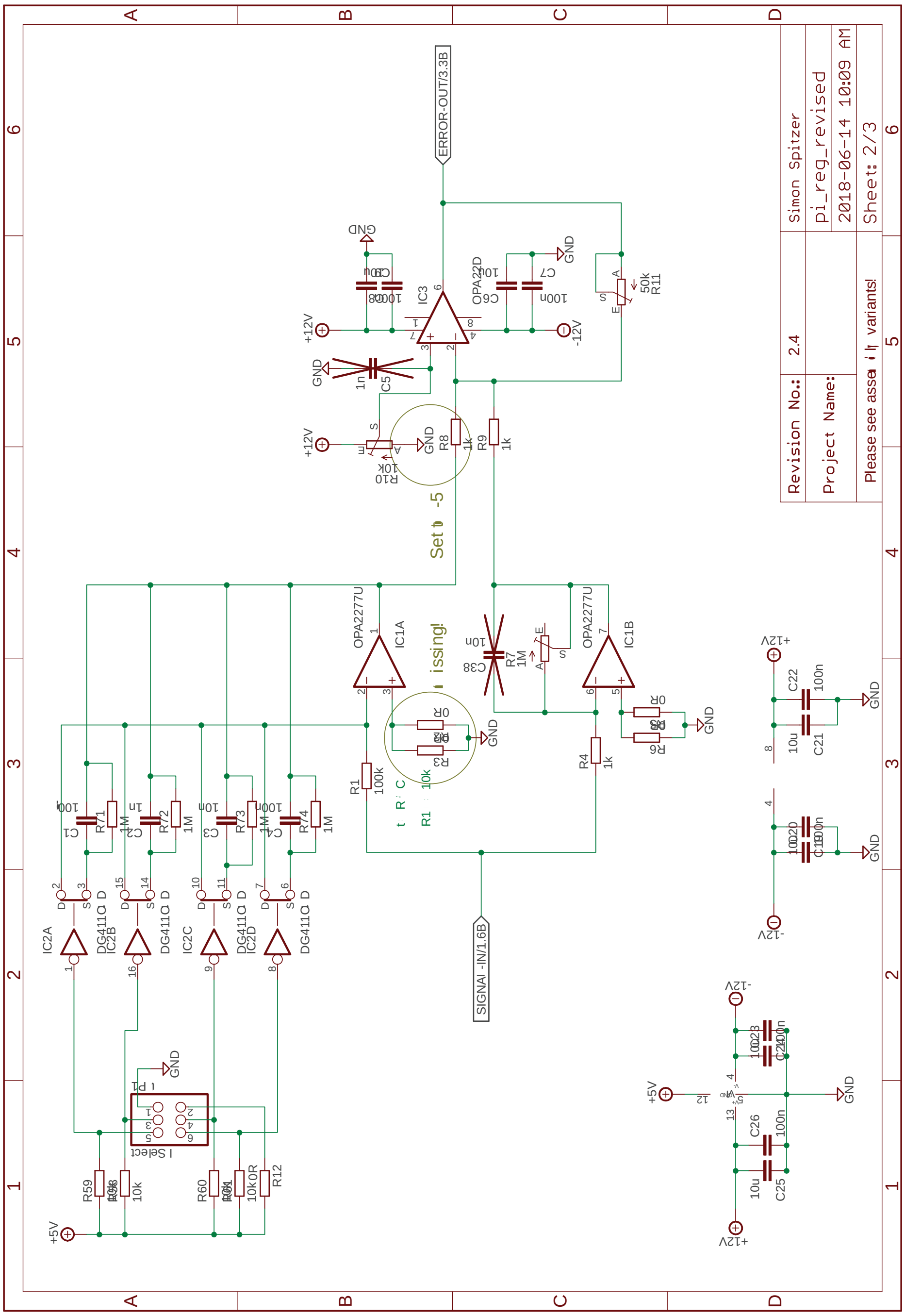

**Figure G.7: pi_reg_revised.** page 2

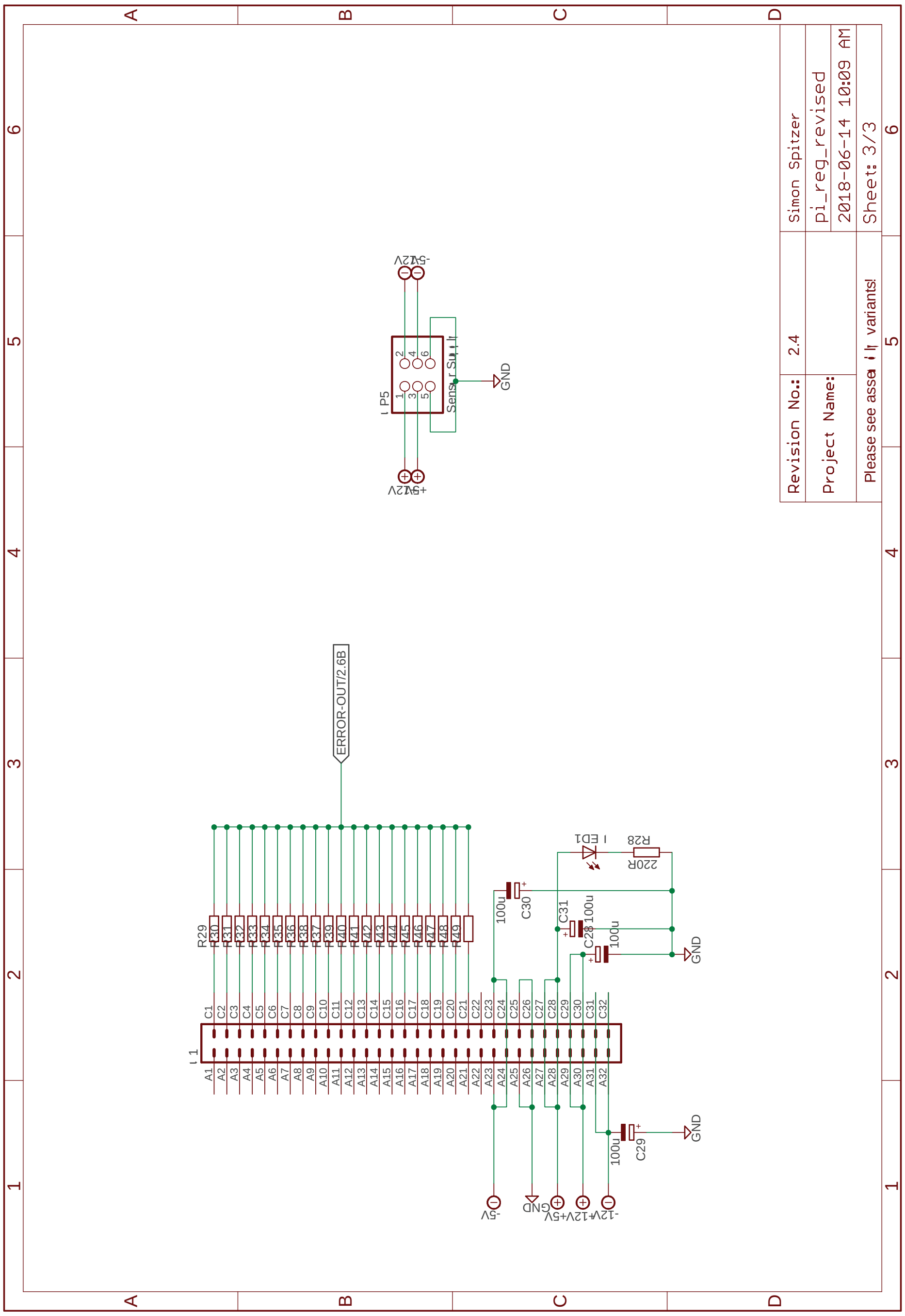

**Figure G.8: pi_reg_revised.** page 3

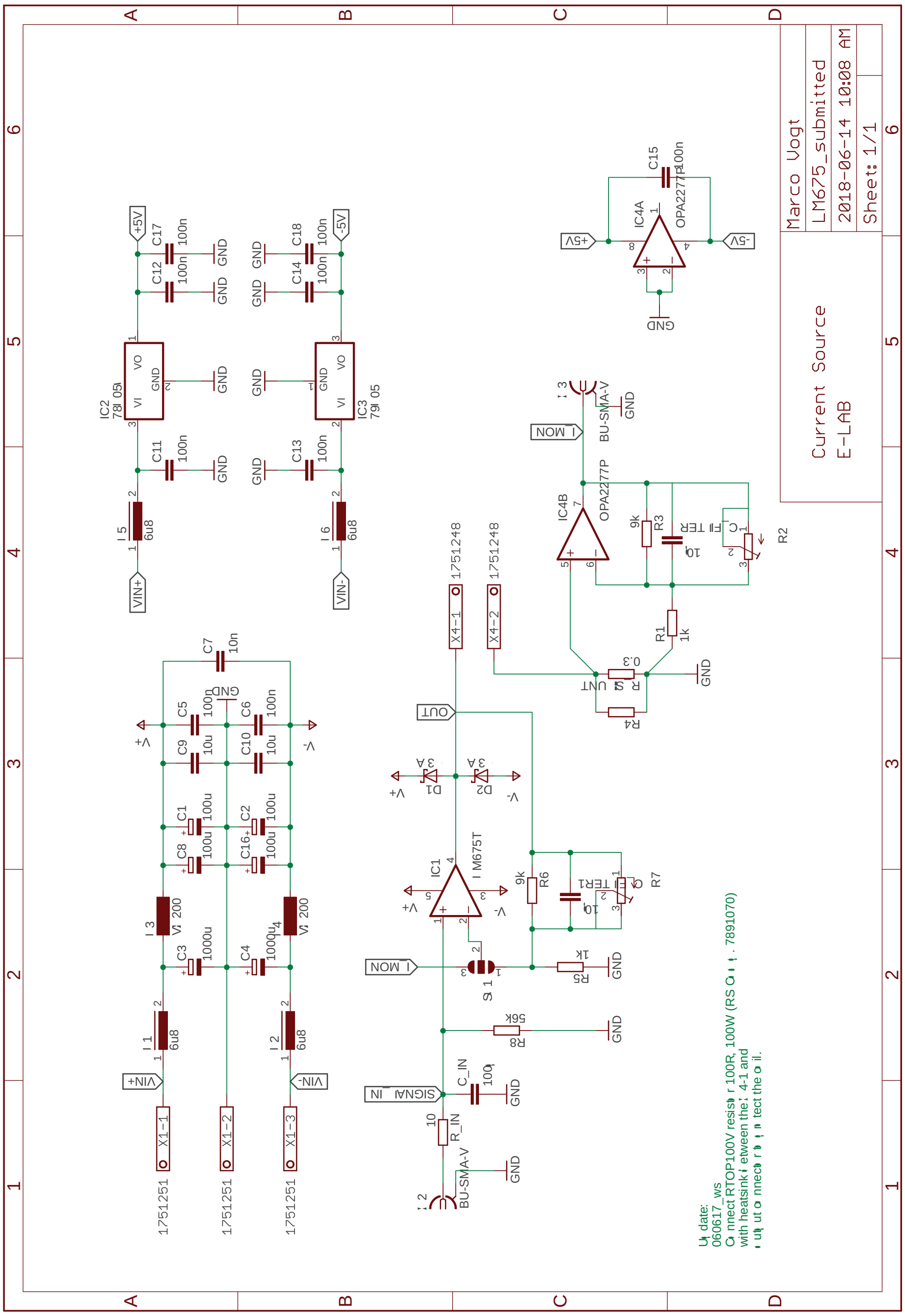

Figure G.9: LM675_submitted.

# H

# Mechanical Drawing

## H.1 New Housing Lid of 369 Optical Resonator

The drawing for the mechanical workshop can be found in the following:

- Lid of 369 optical resonator
  `//Misc_files/LT-1_369_resonator.pdf`

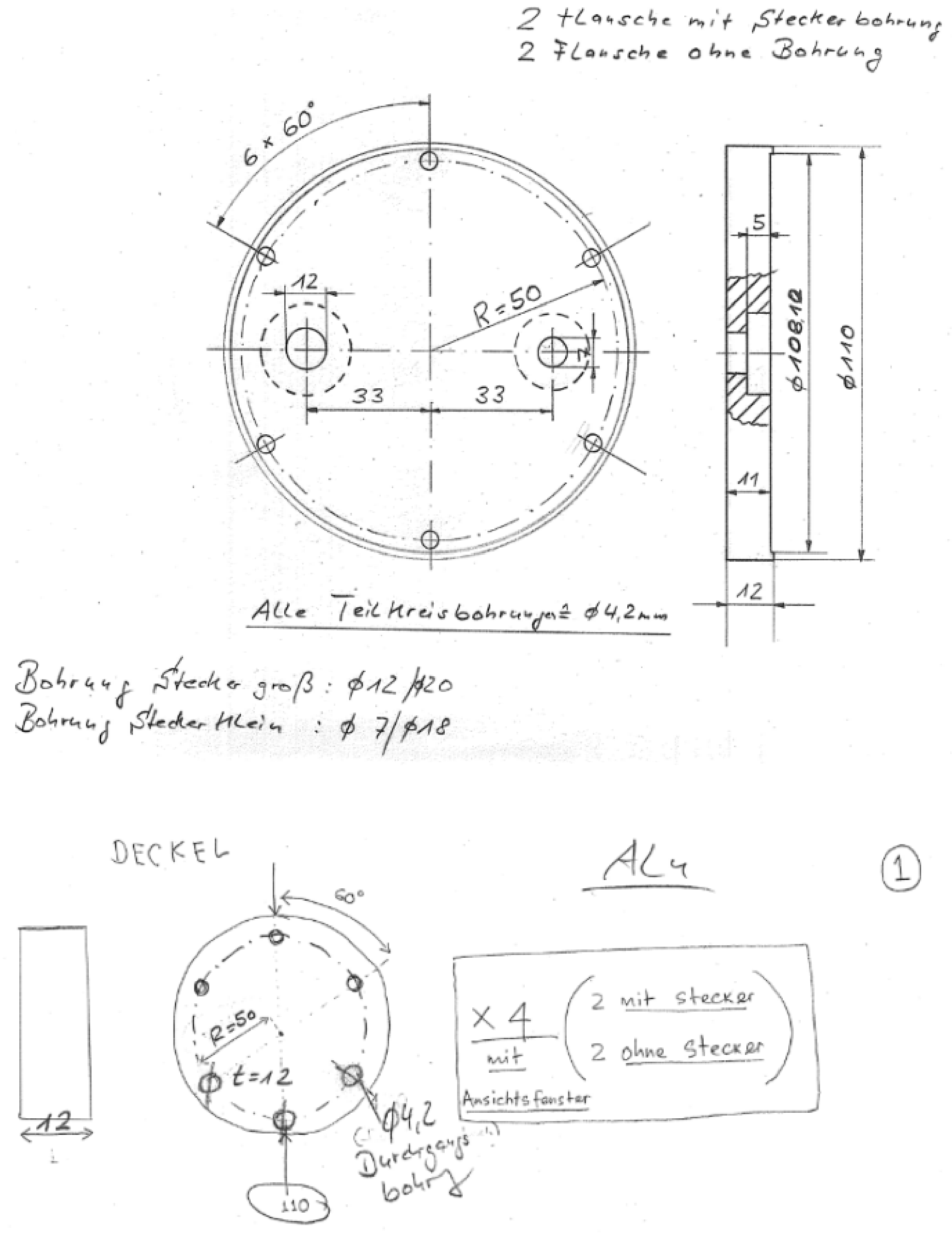

Figure H.1: Redesign of the housing lid of the 369 optical resonator.

# I

# Technical Information

## I.1 RF Qubit-Control Chain

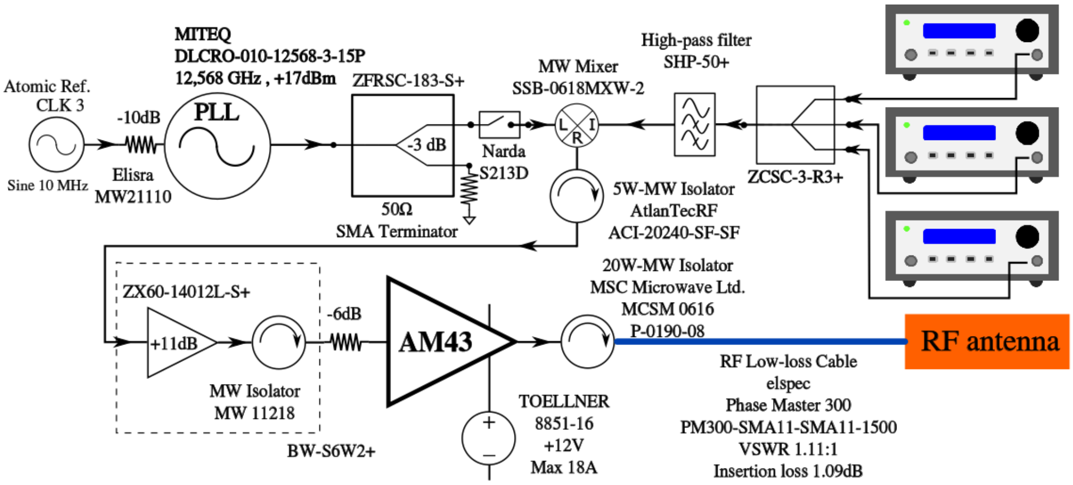

**Figure I.1: Schematic of RF qubit-control chain.** This schematic shows detailed components from Fig. 3.3. Three qubit-control signals from three VFGs are combined by a 4-way power combiner and mixed using a single-sideband double-balanced mixer with the frequency 12.568 GHz, which is generated by a phase-locked loop (PLL) oscillator. The PLL oscillator is also synchronized with the atomic clock reference. To be able to completely switch off the high frequency, a MW switch is installed before the mixer. After the mixer, the signals become the range to manipulate the qubit transitions with controllable frequency, amplitude, and phase. The signal is amplified by a pre-amplifier as an option, indicated by the dashed box, and further amplified by a power amplifier (AM43). The isolators are inserted for back-reflection protection. Finally, the RF control signals are sent through a low-loss and phase-stable cable to the RF antenna.

## I.2 VCO calibration

The calibration result from Fig. 3.4 is fitted by a degree-7 polynomial, where $y = \sum_{i=0}^{7} p_i x^i$. The fitting coefficients are (with 95% confidence bounds):

$$
\begin{aligned}
p_0 &= 4.375 \times 10^4 (4.188 \times 10^4, 4.562 \times 10^4) \\
p_1 &= -6.281 \times 10^5 (-6.511 \times 10^5, -6.051 \times 10^5) \\
p_2 &= 3.596 \times 10^6 (3.483 \times 10^6, 3.708 \times 10^6) \\
p_3 &= -1.026 \times 10^7 (-1.054 \times 10^7, -9.98 \times 10^6) \\
p_4 &= 1.457 \times 10^7 (1.42 \times 10^7, 1.494 \times 10^7) \\
p_5 &= -8.257 \times 10^6 (-8.509 \times 10^6, -8.005 \times 10^6) \\
p_6 &= 7.393 \times 10^6 (7.317 \times 10^6, 7.469 \times 10^6) \\
p_7 &= 8.541 \times 10^7 (8.54 \times 10^7, 8.542 \times 10^7).
\end{aligned}
$$

## I.3 Helmholtz Coils Current Settings

The magnetic field offset in our experiment are set by three Helmholtz coils, as summarized in Tab. I.1.

**Table I.1:** The setting current of the Helmholtz coils. These coils were supplied by in-house current drivers. Now a commercial 3 channel power supply, Toellner TOE 8733-2, is using.

| Coil Name | I (A) |
|---|---|
| Big 1+2 | -0.308 |
| Small Up+Down | -1.68 |
| Round C+W | -0.116 |

## I.4 Compensation Electrodes Settings

The compensation electrodes are optimized with respect to the minimization micromotion of a single ion. The offset potentials are summarized in Tab. I.2.

**Table I.2:** The setting potential of the trap compensation electrodes.

| Electrode Name | Supplied Voltage (V) |
|---|---|
| RF-side | -90.1 |
| Under RF-side | -65.5 |
| Under Viewport Windows | -22.65 |

# Acknowledgments

I am grateful to have received a lot of support from many wonderful people over years in Siegen. I would like to express my sincere gratitude to all those who gave me the possibility to complete my dissertation.

First of all, I would like to thank Prof. Dr. Christof Wunderlich for his supervision, wise suggestions, and all kinds of support during my PhD. I greatly appreciate the opportunity to work in the exciting field of quantum information science, in which I have been interested in for many years. He always gave me the necessary freedom to work with pleasure.

The results of this work would not have been possible without the support of the Linear Trap team. It is in this spirit that I would like to express my gratitude to all my colleges: Dr. Andrés Varón, Dr. Christian Piltz, Dr. Gouri Shankar Giri, Dr. Sabine Wölk, Lukas Bogunia, Sodbileg Erdenebayar (aka Scott), Patrick Barthel, and Patrick Huber. This work has partially been supported with the collaboration with the theoretical physicists Prof. Dr. Hans J. Briegel, Dr. Nicolai Friis, and Dr. Vedran Dunjko.

I would like to thank to our postdocs, Dr. Andrés Varón, Dr. Gouri Shankar Giri, Dr. Michael Johanning, Dr. Sabine Wölk, Dr. Ivan Boldin, and Dr. Delia Kaufmann for all fruitful discussions, endless of questions, encouragements, sharing their experiences, and various kinds of help.

My direct predecessors, Christian and Andrés, taught me everything I need to operate as well as diagnose our experiment. I appreciate their time to help me learn my way around. I wish Patrick B. and Patrick H. all the best in their implementations for further great achievements as the successors of the Linear Trap setup. I would like to thank again Gouri, Michael, Ivan, Patrick B., Patrick H. for proofreading and discussions. Thank you for your corrections and your suggestions. Furthermore, I would like as well to thank Timm F. Gloger and Peter Kaufmann for nice discussions and exchanging ideas.

Special thanks also go to Gudrun Bingener who gave me a lot of help in the bureaucracy and administration as well as her good humor. I also thank the electronics workshop (Michael Ziolkowski, Simon Spitzer, Marco Vogt, Jens Winter, and Stefan Heidbrink) and the mechanical workshop (Guido Schmidt) for their assistance and guidance. In addition, I thank all members of the experimental quantum optics group who have been open-minded and made wonderful working environment.

I gratefully acknowledge Development and Promotion of Science and Technology Tal-

ent Project (DPST) to initiate my journey in Science.

Besides, other people outside the working group have contributed significantly to the success of this work. I am also incredibly grateful for the support of my family and friends throughout this process. Thank you wholeheartedly to my parents for worrying and supporting me for all time. I greatly appreciate Nithiwadee (Pound) Thaicharoen and Suthira (Praer) Owlarn who have been helpful and about the days of frustration. The Thai student community in Siegen, Pakkanan (Yäm) Sae-ngow, Pimpika (Pim) Boonchan, Supanut (New) Vathanyupracha, Padipat (Mew) Pluemworasawat, Natwadee (Poon) Kesprayoon, Nantana (Nan) Anuntkosol, Pannapa (Gift) Huayhongtong, Santanee (Ann) Manomat, and the Pfeifer family, has been incredibly supportive friends as well as throughout frustrated days during my years in Siegen. It has never made me really miss Thai cuisine. I must thank Thai Studenten-Verein in Deutschland unter der Schirmherrschaft S.M. des Königs e.V. (TSVD) and the Office of Educational Affairs which have connected me to the Thai student society in Germany. They made me very happy to be able to meet a big branch of companions; Maylada (Aomsin) Phathikuldilok, Nithi (Big) Rungtanapirom, Supakorn (Ply) Ounsiri, Chompunud (Pink) Phiromjit, Suthira (Praer) Owlarn, Wachiraporn (Fon) Wanichnopparat, Suphawit (Dew) Udomrungkhajornchai, Thanaporn (Bee) Yamsuan, Piyanut (Dao) Pinyou, Pimpussorn (Prim) Anutchatchawan, Kunaree (Guitar) Wongrach, Krittiya (May) Tongkoom, Ruj (Ruddy) Kasetsuwan, and to all my other friends whom are not listed here. It really has been so much fun!

Thank you!
Theeraphot Sriarunothai
04.09.2018 in Siegen

# Bibliography

[1] J. Preskill, "Quantum Computing in the NISQ Era and Beyond," Quantum **2**, 79 (2018).

[2] J. P. Dowling and G. J. Milburn, "Quantum Technology: The Second Quantum Revolution," Philosophical Transactions of the Royal Society A: Mathematical, Physical and Engineering Sciences **361**, 1655 (2003).

[3] A. M. Turing, "On Computable Numbers, with an Application to the Entscheidungsproblem," (Oxford University Press (OUP), 1937) pp. 230–265.

[4] R. P. Feynman, "Simulating Physics with Computers," International Journal of Theoretical Physics **21**, 467 (1982).

[5] D. Deutsch, "Quantum Theory, the Church-Turing Principle and the Universal Quantum Computer," (The Royal Society, 1985) pp. 97–117.

[6] E. Bernstein and U. Vazirani, "Quantum Complexity Theory," in *Proceedings of the twenty-fifth annual ACM symposium on Theory of computing - STOC '93* (ACM Press, 1993).

[7] P. W. Shor, "Algorithms for Quantum Computation: Discrete Logarithms and Factoring," in *Proceedings 35th Annual Symposium on Foundations of Computer Science* (IEEE Comput. Soc. Press, 1994).

[8] P. W. Shor, "Polynomial-Time Algorithms for Prime Factorization and Discrete Logarithms on a Quantum Computer," SIAM Journal on Computing **26**, 1484 (1997).

[9] L. K. Grover, "A Fast Quantum Mechanical Algorithm for Database Search," in *Proceedings of the Twenty-eighth Annual ACM Symposium on Theory of Computing*, STOC '96 (ACM, New York, NY, USA, 1996) pp. 212–219.

[10] D. P. Divincenzo, "Topics in Quantum Computers," in *Mesoscopic Electron Transport* (Springer Netherlands, 1997) pp. 657–677.

[11] D. P. DiVincenzo, "The Physical Implementation of Quantum Computation," Fortschritte der Physik **48**, 771 (2000).

[12] D. Kielpinski, C. Monroe, and D. J. Wineland, "Architecture for a Large-scale Ion-Trap Quantum Computer," Nature **417**, 709 (2002).

[13] B. Lekitsch, S. Weidt, A. G. Fowler, K. Mølmer, S. J. Devitt, C. Wunderlich, and W. K. Hensinger, "Blueprint for a Microwave Trapped Ion Quantum Computer," Science Advances **3**, e1601540 (2017).

[14] K. R. Brown, J. Kim, and C. Monroe, "Co-Designing a Scalable Quantum Computer with Trapped Atomic Ions," npj Quantum Information **2** (2016), 10.1038/npjqi.2016.34.

[15] I. Bloch, "Quantum Coherence and Entanglement with Ultracold Atoms in Optical Lattices," Nature **453**, 1016 (2008).

[16] M. Saffman, T. G. Walker, and K. Mølmer, "Quantum Information with Rydberg Atoms," Rev. Mod. Phys. **82**, 2313 (2010).

[17] C. Neill, P. Roushan, K. Kechedzhi, S. Boixo, S. V. Isakov, V. Smelyanskiy, A. Megrant, B. Chiaro, A. Dunsworth, K. Arya, R. Barends, B. Burkett, Y. Chen, Z. Chen, A. Fowler, B. Foxen, M. Giustina, R. Graff, E. Jeffrey, T. Huang, J. Kelly, P. Klimov, E. Lucero, J. Mutus, M. Neeley, C. Quintana, D. Sank, A. Vainsencher, J. Wenner, T. C. White, H. Neven, and J. M. Martinis, "A Blueprint for Demonstrating Quantum Supremacy with Superconducting Qubits," Science **360**, 195 (2018).

[18] J. L. O'Brien, "Optical Quantum Computing," Science **318**, 1567 (2007).

[19] M. D. Shulman, O. E. Dial, S. P. Harvey, H. Bluhm, V. Umansky, and A. Yacoby, "Demonstration of Entanglement of Electrostatically Coupled Singlet-Triplet Qubits," Science **336**, 202 (2012).

[20] L. Dong, X. Rong, J. Geng, F. Shi, Z. Li, C. Duan, and J. Du, "Scalable Quantum Computation Scheme based on Quantum-Actuated Nuclear-Spin Decoherence-Free Qubits," Phys. Rev. B **96** (2017), 10.1103/physrevb.96.205149.

[21] C. Monroe, D. M. Meekhof, B. E. King, W. M. Itano, and D. J. Wineland, "Demonstration of a Fundamental Quantum Logic Gate," Phys. Rev. Lett. **75**, 4714 (1995).

[22] N. M. Linke, D. Maslov, M. Roetteler, S. Debnath, C. Figgatt, K. A. Landsman, K. Wright, and C. Monroe, "Experimental Comparison of Two Quantum Computing Architectures," Proceedings of the National Academy of Sciences **114**, 3305 (2017).

[23] F. Schmidt-Kaler, S. Gulde, M. Riebe, T. Deuschle, A. Kreuter, G. Lancaster, C. Becher, J. Eschner, H. H. ffner, and R. Blatt, "The Coherence of Qubits based on Single Ca ions," Journal of Physics B: Atomic, Molecular and Optical Physics **36**, 623 (2003).

[24] T. Hannemann, D. Reiss, C. Balzer, W. Neuhauser, P. E. Toschek, and C. Wunderlich, "Self-Learning Estimation of Quantum States," Phys. Rev. A **65**, 050303 (2002).

[25] C. Balzer, A. Braun, T. Hannemann, C. Paape, M. Ettler, W. Neuhauser, and C. Wunderlich, "Electrodynamically Trapped $Yb^+$ Ions for Quantum Information Processing," Phys. Rev. A **73**, 041407 (2006).

[26] S. Olmschenk, K. C. Younge, D. L. Moehring, D. N. Matsukevich, P. Maunz, and C. Monroe, "Manipulation and Detection of a Trapped $Yb^+$ Hyperfine Qubit," Phys. Rev. A **76** (2007), 10.1103/physreva.76.052314.

[27] A. Khromova, C. Piltz, B. Scharfenberger, T. F. Gloger, M. Johanning, A. F. Varón, and C. Wunderlich, "Designer Spin Pseudomolecule Implemented with Trapped Ions in a Magnetic Gradient," Phys. Rev. Lett. **108**, 220502 (2012).

[28] M. D. Barrett, B. DeMarco, T. Schaetz, V. Meyer, D. Leibfried, J. Britton, J. Chiaverini, W. M. Itano, B. Jelenković, J. D. Jost, C. Langer, T. Rosenband, and D. J. Wineland, "Sympathetic Cooling of $^9Be^+$ and $^{24}Mg^+$ for Quantum Logic," Phys. Rev. A **68**, 042302 (2003).

[29] C. Wunderlich and C. Balzer, "Quantum Measurements and New Concepts for Experiments with Trapped Ions," in *Advances In Atomic, Molecular, and Optical Physics* (Elsevier, 2003) pp. 293–372.

[30] M. R. Dietrich, A. Avril, R. Bowler, N. Kurz, J. S. Salacka, G. Shu, B. B. Blinov, J. R. Danielson, and T. S. Pedersen, "Barium Ions for Quantum Computation," in *AIP Conference Proceedings* (AIP, 2009).

[31] D. J. Berkeland, "Quantum Information with Trapped Strontium Ions," Los Alamos Science **27**, 178 (2002).

[32] M. G. Raizen, J. M. Gilligan, J. C. Bergquist, W. M. Itano, and D. J. Wineland, "Ionic Crystals in a Linear Paul Trap," Phys. Rev. A **45**, 6493 (1992).

[33] P. C. Haljan, P. J. Lee, K.-A. Brickman, M. Acton, L. Deslauriers, and C. Monroe, "Entanglement of Trapped-Ion Clock States," Phys. Rev. A **72** (2005), 10.1103/physreva.72.062316.

[34] N. Timoney, I. Baumgart, M. Johanning, A. F. Varon, M. B. Plenio, A. Retzker, and C. Wunderlich, "Quantum Gates and Memory using Microwave-Dressed States," Nature **476**, 185 (2011).

[35] T. P. Harty, D. T. C. Allcock, C. J. Ballance, L. Guidoni, H. A. Janacek, N. M. Linke, D. N. Stacey, and D. M. Lucas, "High-Fidelity Preparation, Gates, Memory, and Readout of a Trapped-Ion Quantum Bit," Phys. Rev. Lett. **113**, 220501 (2014).

[36] T. Ruster, C. T. Schmiegelow, H. Kaufmann, C. Warschburger, F. Schmidt-Kaler, and U. G. Poschinger, "A Long-Lived Zeeman Trapped-Ion Qubit," Appl. Phys. B **122**, 254 (2016).

[37] Y. Wang, M. Um, J. Zhang, S. An, M. Lyu, J.-N. Zhang, L.-M. Duan, D. Yum, and K. Kim, "Single-Qubit Quantum Memory Exceeding Ten-Minute Coherence Time," Nature Photonics **11**, 646 (2017).

[38] T. Monz, P. Schindler, J. T. Barreiro, M. Chwalla, D. Nigg, W. A. Coish, M. Harlander, W. Hänsel, M. Hennrich, and R. Blatt, "14-Qubit Entanglement: Creation and Coherence," Phys. Rev. Lett. **106**, 130506 (2011).

[39] J. G. Bohnet, B. C. Sawyer, J. W. Britton, M. L. Wall, A. M. Rey, M. Foss-Feig, and J. J. Bollinger, "Quantum Spin Dynamics and Entanglement Generation with Hundreds of Trapped Ions," Science **352**, 1297 (2016).

[40] N. Friis, O. Marty, C. Maier, C. Hempel, M. Holzäpfel, P. Jurcevic, M. B. Plenio, M. Huber, C. Roos, R. Blatt, and B. Lanyon, "Observation of Entangled States of a Fully Controlled 20-Qubit System," Phys. Rev. X **8**, 021012 (2018).

[41] R. Blatt and D. Wineland, "Entangled States of Trapped Atomic Ions," Nature **453**, 1008 (2008).

[42] R. Noek, G. Vrijsen, D. Gaultney, E. Mount, T. Kim, P. Maunz, and J. Kim, "High Speed, High Fidelity Detection of an Atomic Hyperfine Qubit," Opt. Lett. **38**, 4735 (2013).

[43] N. Akerman, N. Navon, S. Kotler, Y. Glickman, and R. Ozeri, "Universal Gate-Set for Trapped-Ion Qubits using a Narrow Linewidth Diode Laser," New J. Phys. **17**, 113060 (2015).

[44] C. J. Ballance, T. P. Harty, N. M. Linke, M. A. Sepiol, and D. M. Lucas, "High-Fidelity Quantum Logic Gates Using Trapped-Ion Hyperfine Qubits," Phys. Rev. Lett. **117**, 060504 (2016).

[45] J. P. Gaebler, T. R. Tan, Y. Lin, Y. Wan, R. Bowler, A. C. Keith, S. Glancy, K. Coakley, E. Knill, D. Leibfried, and D. J. Wineland, "High-Fidelity Universal Gate Set for $^9\mathrm{Be}^+$ Ion Qubits," Phys. Rev. Lett. **117**, 060505 (2016).

[46] F. Mintert and C. Wunderlich, "Ion-Trap Quantum Logic Using Long-Wavelength Radiation," Phys. Rev. Lett. **87**, 257904 (2001).

[47] F. Mintert and C. Wunderlich, "Erratum: Ion-Trap Quantum Logic Using Long-Wavelength Radiation [Phys. Rev. Lett.PRLTAO0031-900787, 257904 (2001)]," Phys. Rev. Lett. **91** (2003), 10.1103/physrevlett.91.029902.

[48] C. Ospelkaus, C. E. Langer, J. M. Amini, K. R. Brown, D. Leibfried, and D. J. Wineland, "Trapped-Ion Quantum Logic Gates Based on Oscillating Magnetic Fields," Phys. Rev. Lett. **101**, 090502 (2008).

[49] C. Ospelkaus, U. Warring, Y. Colombe, K. R. Brown, J. M. Amini, D. Leibfried, and D. J. Wineland, "Microwave Quantum Logic Gates for Trapped Ions," Nature **476**, 181 (2011).

[50] A. Braun, “Addressing Single Yb$^+$ Ions: A New Scheme for Quantum Computing in Linear Ion Traps,” Ph.D. thesis, Universität Siegen (2007).

[51] M. Johanning, A. Braun, N. Timoney, V. Elman, W. Neuhauser, and C. Wunderlich, “Individual Addressing of Trapped Ions and Coupling of Motional and Spin States Using rf Radiation,” Phys. Rev. Lett. **102** (2009), 10.1103/physrevlett.102.073004.

[52] C. Piltz, T. Sriarunothai, A. F. Varón, and C. Wunderlich, “A Trapped-Ion-Based Quantum Byte with $10^{-5}$ Next-Neighbour Cross-Talk,” Nature Communications **5** (2014), 10.1038/ncomms5679.

[53] K. Lake, S. Weidt, J. Randall, E. D. Standing, S. C. Webster, and W. K. Hensinger, “Generation of Spin-Motion Entanglement in a Trapped Ion using Long-Wavelength Radiation,” Phys. Rev. A **91**, 012319 (2015).

[54] B. J. Scharfenberger, “Seitenbandkühlung von gespeicherten Ytterbium-Ionen im Mikrowellenregime,” Ph.D. thesis, Universität Siegen (2012).

[55] S. Weidt, J. Randall, S. C. Webster, E. D. Standing, A. Rodriguez, A. E. Webb, B. Lekitsch, and W. K. Hensinger, “Ground-State Cooling of a Trapped Ion Using Long-Wavelength Radiation,” Phys. Rev. Lett. **115**, 013002 (2015).

[56] S. Erdenebayar, “Microwave Sideband Cooling of Trapped Ytterbium Ions in a Linear Paul Trap,” Masterarbeit, Universität Siegen (2016).

[57] T. Sriarunothai, G. S. Giri, S. Wölk, and C. Wunderlich, “Radio Frequency Sideband Cooling and Sympathetic Cooling of Trapped Ions in a Static Magnetic Field Gradient,” Journal of Modern Optics **65**, 560 (2018).

[58] C. Piltz, T. Sriarunothai, S. S. Ivanov, S. Wölk, and C. Wunderlich, “Versatile Microwave-Driven Trapped Ion Spin System for Quantum Information Processing,” Science Advances **2**, e1600093 (2016).

[59] S. C. Webster, S. Weidt, K. Lake, J. J. McLoughlin, and W. K. Hensinger, “Simple Manipulation of a Microwave Dressed-State Ion Qubit,” Phys. Rev. Lett. **111**, 140501 (2013).

[60] S. Weidt, J. Randall, S. Webster, K. Lake, A. Webb, I. Cohen, T. Navickas, B. Lekitsch, A. Retzker, and W. Hensinger, “Trapped-Ion Quantum Logic with Global Radiation Fields,” Phys. Rev. Lett. **117** (2016), 10.1103/physrevlett.117.220501.

[61] A. Y. Kitaev, “Fault-Tolerant Quantum Computation by Anyons,” Annals of Physics **303**, 2 (2003).

[62] R. Raussendorf and J. Harrington, “Fault-Tolerant Quantum Computation with High Threshold in Two Dimensions,” Phys. Rev. Lett. **98**, 190504 (2007).

[63] R. L. Willett, C. Nayak, K. Shtengel, L. N. Pfeiffer, and K. W. West, "Magnetic-Field-Tuned Aharonov-Bohm Oscillations and Evidence for Non-Abelian Anyons at $\nu = 5/2$," Phys. Rev. Lett. **111**, 186401 (2013).

[64] C. W. von Keyserlingk, S. H. Simon, and B. Rosenow, "Enhanced Bulk-Edge Coulomb Coupling in Fractional Fabry-Perot Interferometers," Phys. Rev. Lett. **115**, 126807 (2015).

[65] A. M. Steane, "Error Correcting Codes in Quantum Theory," Phys. Rev. Lett. **77**, 793 (1996).

[66] J. Preskill, "Reliable Quantum Computers," Proceedings of the Royal Society A: Mathematical, Physical and Engineering Sciences **454**, 385 (1998).

[67] A. M. Steane, "Overhead and Noise Threshold of Fault-Tolerant Quantum Error Correction," Phys. Rev. A **68** (2003), 10.1103/physreva.68.042322.

[68] V. Dunjko and H. J. Briegel, "Machine Learning & Artificial Intelligence in the Quantum Domain: A Review of Recent Progress," Reports on Progress in Physics **81**, 074001 (2018).

[69] T. Sriarunothai, S. Wölk, G. S. Giri, N. Friis, V. Dunjko, H. J. Briegel, and C. Wunderlich, "Speeding-Up the Decision Making of a Learning Agent using an Ion Trap Quantum Processor," (2017), arXiv:1709.01366 .

[70] M. Tiersch, E. J. Ganahl, and H. J. Briegel, "Adaptive Quantum Computation in Changing Environments using Projective Simulation," Sci. Rep. **5**, 12874 (2015).

[71] A. Seif, K. A. Landsman, N. M. Linke, C. Figgatt, C. Monroe, and M. Hafezi, "Machine Learning Assisted Readout of Trapped-Ion Qubits," (2018), arXiv:1804.07718 .

[72] D. J. Bernstein, J. Buchmann, and E. Dahmen, eds., *Post-Quantum Cryptography* (Springer Berlin Heidelberg, 2009).

[73] M. Herrero-Collantes and J. C. Garcia-Escartin, "Quantum Random Number Generators," Rev. Mod. Phys. **89**, 015004 (2017).

[74] S. Jordan, "Quantum Algorithm Zoo," [Online] Available: 14.08.2018 (2011), updated 13.06.2018.

[75] C. Wunderlich, "Conditional Spin Resonance with Trapped Ions," in *Laser Physics at the Limits*, edited by H. Figger, C. Zimmermann, and D. Meschede (Springer Berlin Heidelberg, Berlin, Heidelberg, 2002) pp. 261–273.

[76] M. A. Nielsen and I. L. Chuang, *Quantum Computation and Quantum Information: 10th Anniversary Edition*, 10th ed. (Cambridge University Press, New York, NY, USA, 2011).

[77] J. Johansson, P. Nation, and F. Nori, "QuTiP 2: A Python Framework for the Dynamics of Open Quantum Systems," Computer Physics Communications **184**, 1234 (2013).

[78] J. Jones, R. Hansen, and M. Mosca, "Quantum Logic Gates and Nuclear Magnetic Resonance Pulse Sequences," Journal of Magnetic Resonance **135**, 353 (1998).

[79] A. Barenco, C. H. Bennett, R. Cleve, D. P. DiVincenzo, N. Margolus, P. Shor, T. Sleator, J. A. Smolin, and H. Weinfurter, "Elementary Gates for Quantum Computation," Phys. Rev. A **52**, 3457 (1995).

[80] H. Dehmelt, "Radiofrequency Spectroscopy of Stored Ions I: Storage," in *Advances in Atomic and Molecular Physics*, Vol. 3, edited by D. Bates and I. Estermann (Academic Press, 1968) pp. 53–72.

[81] H. Dehmelt, "Radiofrequency Spectroscopy of Stored Ions II: Spectroscopy," in *Advances in Atomic and Molecular Physics*, Vol. 5, edited by D. Bates and I. Estermann (Academic Press, 1969) pp. 109–154.

[82] W. Paul and H. Steinwedel, "Notizen: Ein neues Massenspektrometer ohne Magnetfeld," Zeitschrift für Naturforschung A **8** (1953), 10.1515/zna-1953-0710.

[83] A. Khromova, "Quantum Gates with Trapped Ions using Magnetic Gradient Induced Coupling," Ph.D. thesis, Universität Siegen (2012).

[84] N. W. McLachlan, *Theory and Application of Mathieu Functions* (Clarendon Press, 1947).

[85] A. Steane, "The Ion Trap Quantum Information Processor," Applied Physics B: Lasers and Optics **64**, 623 (1997).

[86] D. F. V. James, "Quantum Dynamics of Cold Trapped Ions with Application to Quantum Computation," Applied Physics B **66**, 181 (1998).

[87] Y. Stalgies, I. Siemers, B. Appasamy, T. Altevogt, and P. E. Toschek, "The Spectrum of Single-atom Resonance Fluorescence," EPL (Europhysics Letters) **35**, 259 (1996).

[88] H. C. Nägerl, D. Leibfried, H. Rohde, G. Thalhammer, J. Eschner, F. Schmidt-Kaler, and R. Blatt, "Laser Addressing of Individual Ions in a Linear Ion Trap," Phys. Rev. A **60**, 145 (1999).

[89] F. Schmidt-Kaler, H. Häffner, M. Riebe, S. Gulde, G. P. T. Lancaster, T. Deuschle, C. Becher, C. F. Roos, J. Eschner, and R. Blatt, "Realization of the Cirac–Zoller Controlled-NOT Quantum Gate," Nature **422**, 408 (2003).

[90] D. Leibfried, B. DeMarco, V. Meyer, D. Lucas, M. Barrett, J. Britton, W. M. Itano, B. Jelenković, C. Langer, T. Rosenband, and D. J. Wineland, "Experimental Demonstration of a Robust, High-Fidelity Geometric Two Ion-Qubit Phase Gate," Nature **422**, 412 (2003).

[91] B. B. Blinov, D. Leibfried, C. Monroe, and D. J. Wineland, "Quantum Computing with Trapped Ion Hyperfine Qubits," Quantum Information Processing **3**, 45 (2004).

[92] J. Walraven, "Atomic Physics," [Online] Available: November 4, 2016 (2016), university of Amsterdam.

[93] P. T. H. Fisk, M. J. Sellars, M. A. Lawn, and G. Coles, "Accurate Measurement of the 12.6 GHz "Clock" Transition in Trapped $^{171}$Yb$^{+}$ Ions," IEEE Transactions on Ultrasonics, Ferroelectrics and Frequency Control **44**, 344 (1997).

[94] C. H. Balzer, "Zur Dynamik eines beobachteten einzelnen Quantensystems," Ph.D. thesis, Universität Hamburg (2003).

[95] N. F. Ramsey, "A Molecular Beam Resonance Method with Separated Oscillating Fields," Phys. Rev. **78**, 695 (1950).

[96] C. M. Piltz, "Maßgeschneiderte Spin-Spin-Kopplung und Quanten-Fouriertransformation mit gespeicherten Yb$^{+}$-Ionen in einem Magnetfeldgradienten," Ph.D. thesis, Universität Siegen (2016).

[97] C. J. Foot, *Atomic Physics*, Oxford Master Series in Physics (OUP Oxford, 2004).

[98] L. Viola and S. Lloyd, "Dynamical Suppression of Decoherence in Two-State Quantum Systems," Phys. Rev. A **58**, 2733 (1998).

[99] C. Piltz, B. Scharfenberger, A. Khromova, A. F. Varón, and C. Wunderlich, "Protecting Conditional Quantum Gates by Robust Dynamical Decoupling," Phys. Rev. Lett. **110**, 200501 (2013).

[100] D. Eiteneuer, "Bau und Charakterisierung einer Ytterbium-Quelle für mikrostruktierte Ionenfallen," Masterarbeit, Universität Siegen (2009).

[101] T. Hannemann, *VFG-150 Versatile Frequency Generator* (2005).

[102] T. F. Gloger, "Mikrowellenquelle mit phasenkohärenter Frequenzumschaltung zur Quantenzustandsmanipulation," Masterarbeit, Universität Siegen (2011).

[103] P. Barthel, "Microwave-Dressed States for Quantum Gates with $^{171}$Yb$^{+}$-Ions," Masterarbeit, Universität Siegen (2016).

[104] W. Demtröder, *Laser Spectroscopy: Basic Concepts and Instrumentation*, 3rd ed., Advanced texts in physics (Springer, Berlin ; New York, 2003).

[105] J. Reuner, "Aufbau frequenzstabilisierter Diodenlasersysteme mit Emissionswellenlängen bei 399 nm, 638 nm und 935 nm," Masterarbeit, Universität Siegen (2007).

[106] C. M. Piltz, "Aufbau von Laserlichtquellen und Optik zur Speicherung und Kühlung von Ytterbium$^+$-Ionen," Masterarbeit, Universität Siegen (2010).

[107] P. Kaufmann, "Präzise Wellenlängenmessung und Computer-Steuerung für Experimente mit gespeicherten Yb$^+$-Ionen," Diplomarbeit, Universität Siegen (2012).

[108] C. Balzer, T. Hannemann, D. Reiss, W. Neuhauser, P. E. Toschek, and C. Wunderlich, "Light-Induced Decoherence in the Driven Evolution of an Atom," Laser Physics **12**, 729 (2002).

[109] K. F. Riley, *Mathematical Methods for Physics and Engineering: A Comprehensive Guide* (Cambridge University Press, 2006).

[110] C. Schneider, "Entwicklung eines Objektivs hoher numerischer Apertur zum Nachweis der Resonanzfluoreszenz einzelner gespeicherter Ionen," Masterarbeit, Universität Siegen (2007).

[111] *Real-Time Development Tool for ADwin Systems (ADbasic Version 6.00)*, Jäger Computergesteuerte Messtechnik GmbH (2015).

[112] P. Huber, "Adaptive Frequency Measurement for Radio Frequency Driven Trapped Ion Qubits," Masterarbeit, Universität Siegen (2017).

[113] L. Bogunia, "Optimierung der Kohärenzeigenschaften und der Detektionseffizienz eines Qubits basierend auf gespeicherten Ytterbium$^+$-Ionen," Masterarbeit, Universität Siegen (2013).

[114] A. Dwyer, *Handbook of PI and PID Controller Tuning Rules* (Imperial College Press Distributed by World Scientific Pub. Co, London Singapore, 2009).

[115] R. E. March, A. W. McMahon, F. A. Londry, R. L. Alfred, J. F. Todd, and F. Vedel, "Resonance Excitation of Ions Stored in a Quadrupole Ion Trap. Part 1. A Simulation Study," International Journal of Mass Spectrometry and Ion Processes **95**, 119 (1989).

[116] M. Johanning, A. Braun, D. Eiteneuer, C. Paape, C. Balzer, W. Neuhauser, and C. Wunderlich, "Resonance-Enhanced Isotope-Selective Photoionization of YbI for Ion Trap Loading," Applied Physics B **103**, 327 (2011).

[117] D. J. Wineland and H. Dehmelt, "Proposed $10^{14}\delta\nu < \nu$ Laser Fluorescence Spectroscopy on Tl$^+$ Mono-Ion Oscillator III (Sideband Cooling)," Bull. Am. Phys. Soc. **20**, 637 (1975).

[118] T. Hänsch and A. Schawlow, "Cooling of Gases by Laser Radiation," Optics Communications **13**, 68 (1975).

[119] D. J. Wineland, R. E. Drullinger, and F. L. Walls, "Radiation-Pressure Cooling of Bound Resonant Absorbers," Phys. Rev. Lett. **40**, 1639 (1978).

[120] D. J. Wineland and W. M. Itano, "Laser Cooling of Atoms," Phys. Rev. A **20**, 1521 (1979).

[121] S. Stenholm, "The Semiclassical Theory of Laser Cooling," Rev. Mod. Phys. **58**, 699 (1986).

[122] D. Leibfried, R. Blatt, C. Monroe, and D. Wineland, "Quantum Dynamics of Single Trapped Ions," Rev. Mod. Phys. **75**, 281 (2003).

[123] C. Monroe, D. M. Meekhof, B. E. King, S. R. Jefferts, W. M. Itano, D. J. Wineland, and P. Gould, "Resolved-Sideband Raman Cooling of a Bound Atom to the 3D Zero-Point Energy," Phys. Rev. Lett. **75**, 4011 (1995).

[124] C. Wunderlich, G. Morigi, and D. Reiß, "Simultaneous Cooling of Axial Vibrational Modes in a Linear Ion Trap," Phys. Rev. A **72**, 023421 (2005).

[125] I. Baumgart, "Optimierte Präparation eines $^{171}\mathrm{Yb}^{+}$-Ions in den Zustand $^{2}\mathrm{S}_{1/2}, F = 0$," Diplomarbeit, Universität Siegen (2008).

[126] S. Wölk, C. Piltz, T. Sriarunothai, and C. Wunderlich, "State Selective Detection of Hyperfine Qubits," Journal of Physics B: Atomic, Molecular and Optical Physics **48**, 075101 (2015).

[127] N. V. Vitanov, T. F. Gloger, P. Kaufmann, D. Kaufmann, T. Collath, M. T. Baig, M. Johanning, and C. Wunderlich, "Fault-Tolerant Hahn-Ramsey Interferometry with Pulse Sequences of Alternating Detuning," Phys. Rev. A **91** (2015), 10.1103/physreva.91.033406.

[128] P. Kaufmann, T. F. Gloger, D. Kaufmann, M. Johanning, and C. Wunderlich, "High-Fidelity Preservation of Quantum Information During Trapped-Ion Transport," Phys. Rev. Lett. **120** (2018), 10.1103/physrevlett.120.010501.

[129] P. Kaufmann, T. F. Gloger, D. Kaufmann, M. Johanning, and C. Wunderlich, "Unbiased State Probability Distribution Reconstruction," (in preparation) (2018).

[130] I. I. Rabi, "Space Quantization in a Gyrating Magnetic Field," Phys. Rev. **51**, 652 (1937).

[131] E. L. Hahn, "Spin Echoes," Phys. Rev. **80**, 580 (1950).

[132] S. Meiboom and D. Gill, "Modified Spin-Echo Method for Measuring Nuclear Relaxation Times," Review of Scientific Instruments **29**, 688 (1958).

[133] A. A. Maudsley, “Modified Carr-Purcell-Meiboom-Gill Sequence for NMR Fourier Imaging Applications,” Journal of Magnetic Resonance (1969) **69**, 488 (1986).

[134] K. Khodjasteh and D. A. Lidar, “Fault-Tolerant Quantum Dynamical Decoupling,” Phys. Rev. Lett. **95**, 180501 (2005).

[135] A. M. Souza, G. A. Álvarez, and D. Suter, “Robust Dynamical Decoupling for Quantum Computing and Quantum Memory,” Phys. Rev. Lett. **106**, 240501 (2011).

[136] G. T. Genov, D. Schraft, N. V. Vitanov, and T. Halfmann, “Arbitrarily Accurate Pulse Sequences for Robust Dynamical Decoupling,” Phys. Rev. Lett. **118**, 133202 (2017).

[137] A. D. Ludlow, M. M. Boyd, J. Ye, E. Peik, and P. O. Schmidt, “Optical Atomic Clocks,” Rev. Mod. Phys. **87**, 637 (2015).

[138] J. Bernard, L. Marmet, and A. Madej, “A Laser Frequency Lock Referenced to a Single Trapped Ion,” Optics Communications **150**, 170 (1998).

[139] G. Barwood, K. Gao, P. Gill, G. Huang, and H. Klein, “Development of Optical Frequency Standards Based upon the $^2\mathrm{S}_{1/2}$–$^2\mathrm{D}_{5/2}$ Transition in $^{88}\mathrm{Sr}^+$ and $^{87}\mathrm{Sr}^+$,” IEEE Transactions on Instrumentation and Measurement **50**, 543 (2001).

[140] E. Peik, T. Schneider, and C. Tamm, “Laser Frequency Stabilization to a Single Ion,” Journal of Physics B: Atomic, Molecular and Optical Physics **39**, 145 (2005).

[141] C. Roos, T. Zeiger, H. Rohde, H. C. Nägerl, J. Eschner, D. Leibfried, F. Schmidt-Kaler, and R. Blatt, “Quantum State Engineering on an Optical Transition and Decoherence in a Paul Trap,” Phys. Rev. Lett. **83**, 4713 (1999).

[142] J. D. Thompson, T. G. Tiecke, A. S. Zibrov, V. Vuletić, and M. D. Lukin, “Coherence and Raman Sideband Cooling of a Single Atom in an Optical Tweezer,” Phys. Rev. Lett. **110**, 133001 (2013).

[143] J. Eschner, G. Morigi, F. Schmidt-Kaler, and R. Blatt, “Laser Cooling of Trapped Ions,” J. Opt. Soc. Am. B **20**, 1003 (2003).

[144] W. D. Phillips, “Nobel Lecture: Laser Cooling and Trapping of Neutral Atoms,” Rev. Mod. Phys. **70**, 721 (1998).

[145] D. M. Segal and C. Wunderlich, “Chapter 3: Cooling Techniques for Trapped Ions,” in *Physics with Trapped Charged Particles* (IMPERIAL COLLEGE PRESS, 2014) pp. 43–81.

[146] L. Emsley and G. Bodenhausen, “Phase Shifts Induced by Transient Bloch-Siegert Effects in NMR,” Chemical Physics Letters **168**, 297 (1990).

[147] W. Vogel and R. L. de Matos Filho, "Nonlinear Jaynes-Cummings Dynamics of a Trapped Ion," Phys. Rev. A **52**, 4214 (1995).

[148] I. Marzoli, J. I. Cirac, R. Blatt, and P. Zoller, "Laser Cooling of Trapped Three-Level Ions: Designing Two-Level Systems for Sideband Cooling," Phys. Rev. A **49**, 2771 (1994).

[149] S. Olmschenk, D. Hayes, D. N. Matsukevich, P. Maunz, D. L. Moehring, K. C. Younge, and C. Monroe, "Measurement of the Lifetime of the $6p\ ^2P^o_{1/2}$ Level of Yb$^+$," Phys. Rev. A **80**, 022502 (2009).

[150] D. Wineland, C. Monroe, W. Itano, D. Leibfried, B. King, and D. Meekhof, "Experimental Issues in Coherent Quantum-State Manipulation of Trapped Atomic Ions," J. Res. Natl. Inst. Stand. Technol. **103**, 259 (1998).

[151] G. Morigi, J. Eschner, J. I. Cirac, and P. Zoller, "Laser Cooling of Two Trapped Ions: Sideband Cooling Beyond the Lamb-Dicke Limit," Phys. Rev. A **59**, 3797 (1999).

[152] H. Rohde, S. T. Gulde, C. F. Roos, P. A. Barton, D. Leibfried, J. Eschner, F. Schmidt-Kaler, and R. Blatt, "Sympathetic Ground-State Cooling and Coherent Manipulation with Two-Ion Crystals," Journal of Optics B: Quantum and Semiclassical Optics **3**, S34 (2001).

[153] C. J. Ballance, V. M. Schäfer, J. P. Home, D. J. Szwer, S. C. Webster, D. T. C. Allcock, N. M. Linke, T. P. Harty, D. P. L. A. Craik, D. N. Stacey, A. M. Steane, and D. M. Lucas, "Hybrid Quantum Logic and a Test of Bell's Inequality using Two Different Atomic Isotopes," Nature **528**, 384 (2015).

[154] M. Guggemos, D. Heinrich, O. A. Herrera-Sancho, R. Blatt, and C. F. Roos, "Sympathetic Cooling and Detection of a Hot Trapped Ion by a Cold One," New J. Phys. **17**, 103001 (2015).

[155] B. Roth, P. Blythe, and S. Schiller, "Motional Resonance Coupling in Cold Multispecies Coulomb Crystals," Phys. Rev. A **75**, 023402 (2007).

[156] J. E. Goeders, C. R. Clark, G. Vittorini, K. Wright, C. R. Viteri, and K. R. Brown, "Identifying Single Molecular Ions by Resolved Sideband Measurements," J. Phys. Chem. A **117**, 9725 (2013).

[157] D. C. Marinescu, *Classical and Quantum Information* (Academic Press, 2011).

[158] J. P. Home, "Chapter 4 - Quantum Science and Metrology with Mixed-Species Ion Chains," in *Advances in Atomic, Molecular, and Optical Physics*, Advances In Atomic, Molecular, and Optical Physics, Vol. 62, edited by E. Arimondo, P. R. Berman, and C. C. Lin (Academic Press, 2013) pp. 231–277.

[159] F. Pokorny, “Experimental Setup for Trapping Strontium Rydberg Ions,” Masterarbeit, Leopold-Franzens-Universität Innsbruck (2014).

[160] L. Deslauriers, S. Olmschenk, D. Stick, W. K. Hensinger, J. Sterk, and C. Monroe, “Scaling and Suppression of Anomalous Heating in Ion Traps,” Phys. Rev. Lett. **97**, 103007 (2006).

[161] J. Chiaverini and J. M. Sage, “Insensitivity of the Rate of Ion Motional Heating to Trap-Electrode Material Over a Large Temperature Range,” Phys. Rev. A **89**, 012318 (2014).

[162] Y. Kawai, K. Shimizu, A. Noguchi, S. Urabe, and U. Tanaka, “Surface-Electrode Trap with an Integrated Permanent Magnet for Generating a Magnetic-Field Gradient at Trapped Ions,” Journal of Physics B: Atomic, Molecular and Optical Physics **50**, 025501 (2016).

[163] J. Welzel, F. Stopp, and F. Schmidt-Kaler, “Spin and Motion Dynamics with Zigzag Ion Crystals in Transverse Magnetic Field Gradients,” (2018), arXiv:1801.03391 .

[164] N. V. Vitanov, “Arbitrarily Accurate Narrowband Composite Pulse Sequences,” Phys. Rev. A **84**, 065404 (2011).

[165] J. P. Home, D. Hanneke, J. D. Jost, J. M. Amini, D. Leibfried, and D. J. Wineland, “Complete Methods Set for Scalable Ion Trap Quantum Information Processing,” Science **325**, 1227 (2009).

[166] K. Kim, M.-S. Chang, S. Korenblit, R. Islam, E. E. Edwards, J. K. Freericks, G.-D. Lin, L.-M. Duan, and C. Monroe, “Quantum Simulation of Frustrated Ising Spins with Trapped Ions,” Nature **465**, 590 (2010).

[167] D. Nigg, M. Müller, E. A. Martinez, P. Schindler, M. Hennrich, T. Monz, M. A. Martin-Delgado, and R. Blatt, “Quantum Computations on a Topologically Encoded Qubit,” Science **345**, 302 (2014).

[168] T. Sleator and H. Weinfurter, “Realizable Universal Quantum Logic Gates,” Phys. Rev. Lett. **74**, 4087 (1995).

[169] J. R. West, D. A. Lidar, B. H. Fong, and M. F. Gyure, “High Fidelity Quantum Gates via Dynamical Decoupling,” Phys. Rev. Lett. **105**, 230503 (2010).

[170] S. Kotler, N. Akerman, Y. Glickman, A. Keselman, and R. Ozeri, “Single-Ion Quantum Lock-In Amplifier,” Nature **473**, 61 (2011).

[171] I. Baumgart, “Erzeugung von robusten magnetfeldabhängigen Qubitzuständen für hochpräzise Magnetometrie,” Ph.D. thesis, Universität Siegen (2017).

[172] T. Hannemann, C. Wunderlich, M. Plesch, M. Ziman, and V. Buzek, "Scrutinizing Single-Qubit Quantum Channels: Theory and Experiment with Trapped Ions," (2009), arXiv:1711.05225 .

[173] J. J. Sakurai, *Modern Quantum Mechanics (Revised Edition)* (Addison Wesley, 1993).

[174] C. A. Sackett, D. Kielpinski, B. E. King, C. Langer, V. Meyer, C. J. Myatt, M. Rowe, Q. A. Turchette, W. M. Itano, D. J. Wineland, and C. Monroe, "Experimental Entanglement of Four Particles," Nature **404**, 256 (2000).

[175] L. M. K. Vandersypen and I. L. Chuang, "NMR techniques for Quantum Control and Computation," Rev. Mod. Phys. **76**, 1037 (2005).

[176] S. Wimperis, "Broadband and Narrowband Composite Excitation Sequences," Journal of Magnetic Resonance (1969) **86**, 46 (1990).

[177] T. P. Harty, M. A. Sepiol, D. T. C. Allcock, C. J. Ballance, J. E. Tarlton, and D. M. Lucas, "High-Fidelity Trapped-Ion Quantum Logic Using Near-Field Microwaves," Phys. Rev. Lett. **117**, 140501 (2016).

[178] J. Moor, "The Dartmouth College Artificial Intelligence Conference: The Next Fifty Years," AI Magazine **27**, 87 (2006).

[179] S. F. Weng, J. Reps, J. Kai, J. M. Garibaldi, and N. Qureshi, "Can Machine-Learning Improve Cardiovascular Risk Prediction using Routine Clinical Data?" PLOS ONE **12**, 1 (2017).

[180] P. Rajpurkar, J. Irvin, K. Zhu, B. Yang, H. Mehta, T. Duan, D. Ding, A. Bagul, C. Langlotz, K. Shpanskaya, M. P. Lungren, and A. Y. Ng, "CheXNet: Radiologist-Level Pneumonia Detection on Chest X-Rays with Deep Learning," CoRR **abs/1711.05225** (2017), arXiv:1711.05225 .

[181] D. Silver, A. Huang, C. J. Maddison, A. Guez, L. Sifre, G. van den Driessche, J. Schrittwieser, I. Antonoglou, V. Panneershelvam, M. Lanctot, S. Dieleman, D. Grewe, J. Nham, N. Kalchbrenner, I. Sutskever, T. Lillicrap, M. Leach, K. Kavukcuoglu, T. Graepel, and D. Hassabis, "Mastering the Game of Go with Deep Neural Networks and Tree Search," Nature **529**, 484 (2016).

[182] D. Silver, J. Schrittwieser, K. Simonyan, I. Antonoglou, A. Huang, A. Guez, T. Hubert, L. Baker, M. Lai, A. Bolton, Y. Chen, T. Lillicrap, F. Hui, L. Sifre, G. van den Driessche, T. Graepel, and D. Hassabis, "Mastering the Game of Go without Human Knowledge," Nature **550**, 354 (2017).

[183] S. J. Russell, P. Norvig, and E. Davis, *Artificial Intelligence: A Modern Approach*, 3rd ed., Prentice Hall series in artificial intelligence (Prentice Hall, Upper Saddle River, 2010).

[184] H. J. Briegel and G. D. l. Cuevas, "Projective Simulation for Artificial Intelligence," Scientific Reports **2**, 400 (2012).

[185] R. Motwani and P. Raghavan, *Randomized Algorithms* (Cambridge University Press, Cambridge ; New York, 1995).

[186] Y. Aharonov, L. Davidovich, and N. Zagury, "Quantum Random Walks," Phys. Rev. A **48**, 1687 (1993).

[187] A. M. Childs, R. Cleve, E. Deotto, E. Farhi, S. Gutmann, and D. A. Spielman, "Exponential Algorithmic Speedup by a Quantum Walk," in *Proceedings of the Thirty-fifth Annual ACM Symposium on Theory of Computing*, STOC '03 (ACM, New York, NY, USA, 2003) pp. 59–68.

[188] J. Kempe, "Discrete Quantum Walks Hit Exponentially Faster," in *Approximation, Randomization, and Combinatorial Optimization.. Algorithms and Techniques*, edited by S. Arora, K. Jansen, J. D. P. Rolim, and A. Sahai (Springer Berlin Heidelberg, Berlin, Heidelberg, 2003) pp. 354–369.

[189] H. Krovi, F. Magniez, M. Ozols, and J. Roland, "Quantum Walks can Find a Marked Element on any Graph," Algorithmica **74**, 851 (2016).

[190] G. D. Paparo, V. Dunjko, A. Makmal, M. A. Martin-Delgado, and H. J. Briegel, "Quantum Speedup for Active Learning Agents," Phys. Rev. X **4**, 031002 (2014).

[191] M. Szegedy, "Quantum Speed-Up of Markov Chain Based Algorithms," in *45th Annual IEEE Symposium on Foundations of Computer Science* (IEEE, 2004).

[192] F. Magniez, A. Nayak, J. Roland, and M. Santha, "Search via Quantum Walk," SIAM Journal on Computing **40**, 142 (2011).

[193] V. Dunjko, N. Friis, and H. J. Briegel, "Quantum-Enhanced Deliberation of Learning Agents using Trapped Ions," New Journal of Physics **17**, 023006 (2015).

[194] N. Friis, V. Dunjko, W. Dür, and H. J. Briegel, "Implementing Quantum Control for Unknown Subroutines," Phys. Rev. A **89**, 030303 (2014).

[195] N. Friis, A. A. Melnikov, G. Kirchmair, and H. J. Briegel, "Coherent Controlization using Superconducting Qubits," Sci. Rep. **5**, 18036 (2015).

[196] T. Loke and J. Wang, "Efficient Quantum Circuits for Szegedy Quantum Walks," Annals of Physics **382**, 64 (2017).

[197] A. Y. Kitaev, "Quantum measurements and the Abelian Stabilizer Problem," Electronic Colloquium on Computational Complexity (ECCC) **3** (1996).

[198] J. Mautner, A. Makmal, D. Manzano, M. Tiersch, and H. J. Briegel, "Projective Simulation for Classical Learning Agents: A Comprehensive Investigation," New Generation Computing **33**, 69 (2015).

[199] A. A. Melnikov, A. Makmal, and H. J. Briegel, "Projective Simulation Applied to the Grid-World and the Mountain-Car Problem," Artificial Intelligence Research **3** (2014), 10.5430/air.v3n3p24.

[200] A. Makmal, A. A. Melnikov, V. Dunjko, and H. J. Briegel, "Meta-Learning within Projective Simulation," IEEE Access **4**, 2110 (2016).

[201] S. Hangl, E. Ugur, S. Szedmak, and J. Piater, "Robotic Playing for Hierarchical Complex Skill Learning," in *Proceedings 2016 IEEE/RSJ International Conference on Intelligent Robots and Systems (IROS)* (IEEE, 2016) p. 2799.

[202] A. A. Melnikov, H. Poulsen Nautrup, M. Krenn, V. Dunjko, M. Tiersch, A. Zeilinger, and H. J. Briegel, "Active Learning Machine Learns to Create New Quantum Experiments," Proceedings of the National Academy of Sciences **115**, 1221 (2018).

[203] C. H. Bennett, G. Brassard, C. Crépeau, R. Jozsa, A. Peres, and W. K. Wootters, "Teleporting an Unknown Quantum State via Dual Classical and Einstein-Podolsky-Rosen Channels," Phys. Rev. Lett. **70**, 1895 (1993).

[204] D. Bouwmeester, J.-W. Pan, K. Mattle, M. Eibl, H. Weinfurter, and A. Zeilinger, "Experimental Quantum Teleportation," Nature **390**, 575 (1997).

[205] M. D. Barrett, J. Chiaverini, T. Schaetz, J. Britton, W. M. Itano, J. D. Jost, E. Knill, C. Langer, D. Leibfried, R. Ozeri, and D. J. Wineland, "Deterministic Quantum Teleportation of Atomic Qubits," Nature **429**, 737 (2004).

[206] M. Riebe, H. Häffner, C. F. Roos, W. Hänsel, J. Benhelm, G. P. T. Lancaster, T. W. Körber, C. Becher, F. Schmidt-Kaler, D. F. V. James, and R. Blatt, "Deterministic Quantum Teleportation with Atoms," Nature **429**, 734 (2004).

[207] J. F. Sherson, H. Krauter, R. K. Olsson, B. Julsgaard, K. Hammerer, I. Cirac, and E. S. Polzik, "Quantum Teleportation between Light and Matter," Nature **443**, 557 (2006).

[208] J.-G. Ren, P. Xu, H.-L. Yong, L. Zhang, S.-K. Liao, J. Yin, W.-Y. Liu, W.-Q. Cai, M. Yang, L. Li, K.-X. Yang, X. Han, Y.-Q. Yao, J. Li, H.-Y. Wu, S. Wan, L. Liu, D.-Q. Liu, Y.-W. Kuang, Z.-P. He, P. Shang, C. Guo, R.-H. Zheng, K. Tian, Z.-C. Zhu, N.-L. Liu, C.-Y. Lu, R. Shu, Y.-A. Chen, C.-Z. Peng, J.-Y. Wang, and J.-W. Pan, "Ground-to-Satellite Quantum Teleportation," Nature **549**, 70 (2017).

[209] D. W. Leung, I. L. Chuang, F. Yamaguchi, and Y. Yamamoto, "Efficient Implementation of Coupled Logic Gates for Quantum Computation," Phys. Rev. A **61**, 042310 (2000).

[210] N. Timoney, V. Elman, S. Glaser, C. Weiss, M. Johanning, W. Neuhauser, and C. Wunderlich, “Error-Resistant Single-Qubit Gates with Trapped Ions,” Phys. Rev. A **77**, 052334 (2008).

[211] D. Gottesman and I. L. Chuang, “Demonstrating the Viability of Universal Quantum Computation using Teleportation and Single-Qubit Operations,” Nature **402**, 390 (1999).

[212] I. Cohen, S. Weidt, W. K. Hensinger, and A. Retzker, “Multi-Qubit Gate with Trapped Ions for Microwave and Laser-Based Implementation,” New Journal of Physics **17**, 043008 (2015).

[213] P. J. Kunert, D. Georgen, L. Bogunia, M. T. Baig, M. A. Baggash, M. Johanning, and C. Wunderlich, “A Planar Ion Trap Chip with Integrated Structures for an Adjustable Magnetic Field Gradient,” Applied Physics B **114**, 27 (2013).

[214] D. Kaufmann, T. Collath, M. T. Baig, P. Kaufmann, E. Asenwar, M. Johanning, and C. Wunderlich, “Thick-Film Technology for Ultra High Vacuum Interfaces of Micro-Structured Traps,” Applied Physics B **107**, 935 (2012).

[215] A. M. Eltony, S. X. Wang, G. M. Akselrod, P. F. Herskind, and I. L. Chuang, “Transparent Ion Trap with Integrated Photodetector,” Applied Physics Letters **102**, 054106 (2013).

[216] A. Kramida, Yu. Ralchenko, J. Reader, and and NIST ASD Team, NIST Atomic Spectra Database (ver. 5.5.6), [Online]. Available: `https://physics.nist.gov/asd` [2018, September 5]. National Institute of Standards and Technology, Gaithersburg, MD. (2018).

[217] M. J. Sellars, P. T. H. Fisk, M. A. Lawn, and G. Coles, “Further Investigation of a Prototype Microwave Frequency Standard Based on Trapped $^{171}$Yb$^{+}$Ions,” in *Proceedings of the 1995 IEEE International Frequency Control Symposium (49th Annual Symposium)* (IEEE, 1995).

[218] A.-M. Mårtensson-Pendrill, D. S. Gough, and P. Hannaford, “Isotope Shifts and Hyperfine Structure in the 369.4-nm 6s-6$p_{1/2}$ Resonance Line of Singly Ionized Ytterbium,” Phys. Rev. A **49**, 3351 (1994).

[219] E. H. Pinnington, G. Rieger, and J. A. Kernahan, “Beam-Laser Measurements of the Lifetimes of the 6$p$ Levels in Yb II,” Phys. Rev. A **56**, 2421 (1997).

[220] T. Feldker, H. Fürst, N. V. Ewald, J. Joger, and R. Gerritsma, “Spectroscopy of the $^2S_{1/2} \rightarrow ^2 P_{3/2}$ Transition in Yb II: Isotope Shifts, Hyperfine Splitting, and Branching Ratios,” Phys. Rev. A **97**, 032511 (2018).

[221] N. Yu and L. Maleki, “Lifetime Measurements of the 4$f^{14}$5$d$ Metastable States in Single Ytterbium Ions,” Phys. Rev. A **61**, 022507 (2000).

[222] P. Taylor, M. Roberts, S. V. Gateva-Kostova, R. B. M. Clarke, G. P. Barwood, W. R. C. Rowley, and P. Gill, “Investigation of the $^2S_{1/2}$–$^2D_{5/2}$ Clock Transition in a Single Ytterbium Ion,” Phys. Rev. A **56**, 2699 (1997).

[223] M. Roberts, P. Taylor, S. V. Gateva-Kostova, R. B. M. Clarke, W. R. C. Rowley, and P. Gill, “Measurement of the $^2S_{1/2}$–$^2D_{5/2}$ Clock Transition in a Single $^{171}$Yb$^+$ Ion,” Phys. Rev. A **60**, 2867 (1999).

[224] M. Roberts, P. Taylor, G. P. Barwood, W. R. C. Rowley, and P. Gill, “Observation of the $^2S_{1/2}$–$^2F_{7/2}$ Electric Octupole Transition in a Single $^{171}$Yb$^+$ Ion,” Phys. Rev. A **62**, 020501(R) (2000).

[225] M. Roberts, P. Taylor, G. P. Barwood, P. Gill, H. A. Klein, and W. R. C. Rowley, “Observation of an Electric Octupole Transition in a Single Ion,” Phys. Rev. Lett. **78**, 1876 (1997).

[226] P. Taylor, M. Roberts, G. M. Macfarlane, G. P. Barwood, W. R. C. Rowley, and P. Gill, “Measurement of the Infrared $^2F_{7/2}$–$^2D_{5/2}$ Transition in a Single $^{171}$Yb$^+$ Ion,” Phys. Rev. A **60**, 2829 (1999).

[227] R. W. Berends, E. H. Pinnington, B. Guo, and Q. Ji, “Beam-Laser Lifetime Measurements for Four Resonance Levels of Yb II,” Journal of Physics B: Atomic, Molecular and Optical Physics **26**, L701 (1993).

[228] W. F. Meggers, C. H. Corliss, and B. F. Scribner, *Tables of Spectral-Line Intensities Part I–Arranged by Elements*, 2nd ed., National Bureau of Standards Monograph 145 (Government Printing Office, Washington, DC, 1975) pp. 367–371.

[229] H. M. Meyer, M. Steiner, L. Ratschbacher, C. Zipkes, and M. Köhl, “Laser Spectroscopy and Cooling of Yb$^+$ Ions on a Deep-UV Transition,” Phys. Rev. A **85**, 012502 (2012).

[230] D. Engelke and C. Tamm, “Dark Times in the Resonance Fluorescence of Trapped $^{171}$Yb Ions caused by Spontaneous Quantum Jumps to the $^2$D3/2($F = 2$) State,” Europhysics Letters (EPL) **33**, 347 (1996).

[231] P. T. H. Fisk, M. A. Lawn, and C. Coles, “Laser Cooling of $^{171}$Yb$^+$Ions in a Linear Paul Trap,” Applied Physics B **57**, 287 (1993).

[232] K. Sugiyama, “Laser Cooling of Single174Yb$^+$Ions Stored in a RF Trap,” Japanese Journal of Applied Physics **38**, 2141 (1999).

[233] N. Huntemann, M. Okhapkin, B. Lipphardt, S. Weyers, C. Tamm, and E. Peik, “High-Accuracy Optical Clock Based on the Octupole Transition in $^{171}$Yb$^+$,” Phys. Rev. Lett. **108**, 090801 (2012).

[234] A. Bell, P. Gill, H. Klein, A. Levick, and W. Rowley, "Precision Measurement of the $^2F_{1/2}$–$^2D_{5/2}$ 3.43 $\mu$m Intervel in Trapped $^{172}Yb^+$," Journal of Modern Optics **39**, 381 (1992).

[235] B. C. Fawcett and M. Wilson, "Computed Oscillator Strengths, Landé g Values, and Lifetimes in Yb II," Atomic Data and Nuclear Data Tables **47**, 241 (1991).

[236] J. D. Wong Campos, "Demonstration of a Quantum Gate with Ultrafast Laser Pulses," Ph.D. thesis, University of Maryland (2017).

[237] G. Tóth, "QUBIT4MATLAB V3.0: A Program Package for Quantum Information Science and Quantum Optics for MATLAB," Computer Physics Communications **179**, 430 (2008).

[238] *1, 2 and 3 Axis Magnetic Sensors HMC1051/HMC1052L/HMC1053*, Honeywell International Inc. (2010).

[239] D. Griffiths, *Introduction to Electrodynamics* (Prentice Hall, Upper Saddle River, N.J, 1999).

[240] K. J. Aström, *Feedback Systems: An Introduction for Scientists and Engineers* (Princeton University Press, 2008).